# Récupération des Terres Rares (La, Ce, Nd) et métaux rares (Sn, Nb, W) à partir de résidus micacés issus de la production de kaolin

Q. Dehaine

Université de Lorraine
UMR 7359 GéoRessources CNRS-UL
Ecole Doctorale RP2E

Thèse de doctorat présentée en vue d'obtenir le titre de
**Docteur de l'Université de Lorraine** (Spécialité: *Géosciences*)

par **Quentin DEHAINE**

---

# Récupération des Terres Rares (La, Ce, Nd) et métaux rares (Sn, Nb, W) à partir de résidus micacés issus de la production de kaolin

***Rare Earths (La, Ce, Nd) and rare metals (Sn, Nb, W) recovery from micaceous waste of china clay production***

---

Thèse soutenue publiquement le 31 Mars 2016

**Membres du Jury:**

Hylke J. Glass, *Professor, University of Exeter, CSM* ..... Rapporteur
Claude Bazin, *Professeur, Université Laval* ..... Rapporteur
François Martin, *Professeur, Université Paul Sabatier* ..... Examinateur
Stéphane Brochot, *Docteur, CASPEO* ..... Examinateur
Michel Cathelineau, *Directeur de recherches CNRS, Laboratoire GéoRessources* .. Examinateur
Pierre Daniellou, *Industrial Manager Kaolin Activity, Imerys* ..... Invité
Lev Filippov, *Professeur, Université de Lorraine* ..... Directeur

Vandoeuvre-lès-Nancy, France
April 5, 2016

Le paradoxe de la science est qu'il n'y a qu'une réponse à ses méfaits et à ses périls: encore plus de science.

**Romain Gary**,
Charge d'âme

**Résumé**

L'approvisionnement en matières premières critiques minérales (CRMs), est un sujet préoccupant pour l'industrie européenne. Les granites à métaux rares, en raison de leurs faibles teneurs en métaux, ont toujours été considérés comme ayant une faible valeur économique mais, lorsqu'ils sont altérés, ils sont souvent exploités pour les minéraux industriels. L'objectif du présent travail est d'évaluer la potentialité des résidus micacés issus de la production de kaolin pour la récupération des Terres Rares légères (LREE), Nb, W et Sn, au travers du développement d'un procédé de valorisation de ces résidus dans le cas des kaolins de St Austell.

Le granite de St Austell, à l'origine des dépôts de kaolin, est composé de 6 types de granites ayant chacun leur propre cortège de minéraux accessoires. Ces derniers, libérés par le processus de kaolinisation, sont majoritairement pré-concentrés dans le résidu micacé du procédé de traitement de kaolin, notamment pour les zones couvrant le granite à biotite. Les teneurs en CRMs atteignent 170 ppm LREE (Ce, La, Nd), 140 ppm Sn, 94 ppm Nb et 70 ppm W, ceux-ci étant principalement distribués dans les fractions fines (-100 µm). Une approche statistique combinée aux observations minéralogiques a montré que les LREE sont uniquement portés par la monazite et que Sn, Nb et W sont respectivement portés par la cassiterite, le rutile et la wolframite.

La prise en compte de la variabilité des propriétés du flux de résidu considéré, tels que les teneurs, la granularité, etc., est primordiale. Le développement du multivariogramme a permis de résumer la variabilité globale de l'ensemble des propriétés considérées en une fonction unique soulignant les structures communes à ces propriétés.

Un procédé de traitement du résidu micacé combinant concentration gravimétrique (spirale, table à secousses, Falcon) et flottation a été testé sur les fractions 53-180 µm et -53 µm. Une modélisation par la méthode des plans d'expériences montre que le débit d'eau de lavage de la spirale est le facteur le plus significatif pour la récupération des minéraux denses. De la même manière, la modélisation des courbes de distribution par taille via des modèles de régression permet de mieux comprendre les mécanismes de séparation ayant lieu au sein de la spirale (effet de Bagnold, circulations secondaires). Jusqu'à 70% des minéraux denses peuvent être récupérés après trois passages de spirale tandis que le même niveau de récupération pour les LREE est obtenu en un seul passage. Le traitement du concentré de spirale par table à secousses permet d'obtenir un concentré à 1.6% LREE. La flottation de la monazite dans la fraction -53 µm est globalement plus performante que la séparation centrifuge (Falcon UF). L'utilisation de dispersant lors du deschlammage élimine l'effet néfaste des argiles et augmente l'efficacité de la flottation, en particulier avec l'oléate de sodium, permettant de récupérer jusqu'à 80% des LREE avec une teneur de 0.54% LREE.

Une méthode d'évaluation des ressources, intégrant les résultats de caractérisation et des tests de valorisation, est proposée afin de prédire les performances du procédé de récupération des CRMs, ce qui permettra d'aller vers l'établissement d'un modèle géométallurgique.

**Abstract**

During the last few years the supply of some critical raw materials (CRMs) such as the Light Rare Earth Elements (LREE) became a concern for the European industry. Rare metals granites have always been considered of poor economic value due to their low grades but, when altered, they are often exploited for their industrial minerals. This work addresses the recovery of LREE (La, Ce, Nd) and rare metals (Sn, Nb, W) from St Austell (UK) kaolin residues though the development of a dedicated beneficiation process.

The St Austell granite is composed of six major granite types, each one having its own accessory mineral assemblage. As a consequence of the kaolinisation process, these accessory minerals are partially liberated from the gangue which allows their pre-concentration in some residues of the kaolin production route. Results shows that when processing material from biotite granite, 40% to 60% of the CRMs goes to the micaceous residue stream with CRM grades around 170 ppm LREE, 140 ppm Sn, 94 ppm Nb et 70 ppm W. The overall CRMs grade increases in the fines fractions of the residue in which the majority of the CRMs are distributed. A combined statistical/mineralogical approach has allowed identifying monazite as the only LREE-bearing mineral as well as cassiterite, wolframite and rutile as the major host for Sn, Nb and W respectively.

Taking into account the variability of the properties of the residue treated such as grade or particle sizes is essential. A multivariate variographic approach has been developed to summarize the overall spatial variability of a set of properties by one structural function and thus highlight their common spatial structures.

A CRMs beneficiation process combining gravity (spiral, shaking table, Falcon) and flotation has been tested on the 53-180 µm and –53 µm fractions of the micaceous residue. Modelling of the influence of the operating parameters on spiral performance using the design of experiments methodology (DOE) shows that wash water flow rate as the most significant effect on heavy minerals recovery. Similarly, modelling size recovery curves through particle size distribution and DOE regression model fitting allow a better understanding of the effect of wash water on separation mechanism (Bagnold effect and secondary flows). Up to 70% heavy minerals recovery is achieved after three spiral passes at low wash water addition whereas the same recoveries are obtained for the LREE in only one pass. Processing of spiral concentrate by shaking table allow to obtain a 1.6% LREE concentrate. Froth flotation of monazite in the -53 µm fraction is generally more efficient than centrifugal separation (Falcon UF). The use of dispersant in the desliming step eliminates the negative effect of clay-coating and increases flotation efficiency, especially with sodium oleate, allowing to recover 80% of the LREE in the floated product with a 0.54% LREE grade.

A resources evaluation method, using results from characterisation and metallurgical testing, is proposed to predict the performance of spiral concentration and goes towards the development of a geometallurgical model.

# Forewords

### Organization of this manuscript

This manuscript includes one introductory chapter, a chapter dedicated to materials and methods, five chapters presenting the main results of this PhD work, a general discussion, a conclusion and seven appendices.

The five results chapters are presented under the form of scientific articles, published, submitted or to be submitted to international journals. These papers can be addressed independently from the rest of the manuscript, and have their own introduction, materials and methods and discussion with sometimes an independent bibliography (published articles only).

### Organisation de ce manuscrit

Ce manuscrit comporte un chapitre introductif, un chapitre dédié aux matériels et méthodes, cinq chapitres présentant les principaux résultats de cette thèse, une discussion générale, une conclusion et sept annexes.

La plupart des chapitres partagent des références bibliographiques communes, répertoriées en fin de manuscrit. Les cinq chapitres centraux sont organisés sous forme d'articles scientifiques, publiés ou soumis à des revues internationales ou en voie de soumission. Ces articles peuvent être abordés indépendamment du reste du manuscrit, et comporte une introduction, des matériels et méthodes et une discussion avec parfois leur propres références bibliographiques (articles publiés uniquement).

**Remerciements**

*Je remercie mon directeur de thèse Lev Filippov, pour l'attention et l'écoute dont il a fait preuve tout au long de ma thèse, pour son expertise et ses conseils avisés qui m'ont permis d'aller dans la bonne direction.*

*J'adresse mes plus vifs remerciements à Claude Bazin et Hylke J. Glass pour avoir accepté de rapporter ce mémoire ainsi qu'aux autres membres du jury: François Martin, Stéphane Brochot, Michel Cathelineau et Pierre Daniellou, pour avoir accepté d'évaluer ce travail de thèse.*

*Je souhaite remercier les membres du projet STOICISM au sein d'Imerys Ltd. UK, notamment David Moseley, Maretva Baricot et Becky Prall, pour la gestion du projet, et plus particulièrement Saeid Moradi, Pankaj Chauhan et Alex Coe qui ont assuré la préparation et l'envoi d'échantillons et pour l'aide apportée lors de mes nombreuses visites au Par Moor Center. Je tiens aussi à remercier les membres de l'équipe géologie, Jonathan Hodgins, Richard Hooper, Ben Thompson et Éric Sennavoine pour leur accueil chaleureux et leur aide lors des missions d'échantillonnage. Un grand merci également à Steve Lightfoot et Peter Budge pour le soutien logistique et technique lors de l'échantillonnage de l'usine de traitement.*

*Je suis reconnaissant envers Robert Joussemet, aka Bob, pour ses nombreux conseils et critiques concernant la concentration par gravité ainsi que son aide précieuse pendant les essais. Je remercie chaleureusement tout le personnel du bâtiment A. En particulier Christophe, Fred et Jean-Marie pour leur aide au cours de mes nombreuses manips' à la station STEVAL, les meilleures comme celles du vendredi car comme dit l'adage « manip' du vendredi, manip' pourrie » (Gauthier et al., 2015). Je tiens également à m'excuser pour les longues heures passées à tamiser, quarter, sécher près de 4 tonnes d'échantillons en cumulé pour l'ensemble de ses travaux ! Une bonne ambiance de travail et une bonne humeur générale facilitent grandement la vie au laboratoire. Aussi, je n'oublie pas mes voisines de bureau, les irréductibles du rez-de-chaussée: les chimistes Pabla et Christine, ainsi que Monique pour leur bonne humeur, le café (et les gâteaux) qui aident à tenir le rythme au quotidien. J'adresse mes plus vifs remerciements à mes amis de thèse ayant déjà soutenu ou qui soutiendront bientôt. Un grand merci donc à Agathe, Guillaume & Guillaume, Léo, Mathilde, Olga, Oumar, Patrice, Rémi, Sébastien, Viacheslav et Zineb ainsi qu'aux étudiants que j'ai pu encadrer lors de projets labos ou stages master: Khan, Alix, Baptiste, Eglantine et Cecilia. Enfin je remercie également les chercheurs avec qui j'ai eu l'occasion de collaborer et d'échanger au cours de ces 3 années, Jean Jacques Royer, Inna Filippova, Jacques Yvon, Philippe Marion et j'en oublie sûrement.*

*Je tiens à remercier mes parents, mes frères et sœurs ainsi que tous mes proches qui m'ont épaulé tout au long de ma scolarité et qui, j'en suis sûr, sont heureux de pouvoir dire que j'ai (enfin) terminé mes études ! Merci aussi à Floriane qui partage ma vie (et même mon travail sur la fin de cette thèse), qui m'a soutenu (et supporté!) tout au long de ces 3 années.*

Ce travail a reçu le support financier du projet " *Sustainable Technologies for Industrial Minerals Calcined in Europe*" (STOICISM) du 7e Programme Cadre (FP7) européen, subvention NMP2-LA-2012-310645.

# Contents

# List of Figures

# List of Tables

# Chapter 1

# Introduction

## Contents



## 1.1 Scope of the study

The role of raw materials is fundamental to Europe's (EU) economy, as it has a direct influence on growth and jobs and they are essential for maintaining and improving quality of people's life. The number of materials used across products manufacturing

has significantly increase in the recent years and ensuring a safe and steady supply to certain raw materials is of growing concern within the EU and across the globe.

### 1.1.1 The European Raw Material Initiative

#### 1.1.1.1 Raw materials supply in Europe

EU has many raw material occurrences or deposits but their exploration and extraction faces accrued competition, a highly regulated environment and technological limitations regarding the access to mineral deposits (European Commission, 2008). Moreover, the EU is deeply dependant on raw material importation, which can be critical for the high-tech metals due to their economic value and their high supply risks. The production of some materials is concentrated in a small number of countries, *e.g.* in 2012, 97% of the global supply of Rare Earth Elements (Rare Earth Elements (REE)) was produced by China (Massari and Ruberti, 2013) which also produces 84% of tungsten global supply while 91% of niobium production was ensured by Brazil (US Geological Survey, 2013). Under these conditions the metal supply risk increases, such as the rush for tantalum in 2000 during the boom of mobile phones or, more recently, the significant increase in consumption of REEs (while their supply has suffered a severe diminution).

Given that our Earth's surface and subsurface have not been completely explored and is large enough to contain many hidden deposits, or that some large potential deposits are not currently considered because of technological limitations, it appears that it is not the geological availability but the criticality of mineral raw materials which must be considered as an issue (Rosenau-Tornow et al., 2009). The criticality of a material refers to its uncertainty or risk in supply that could affect the national economy. To address this situation the European Commission launched in November 2008 the "European Raw Material Initiative" with the first objective to identify critical raw materials at the European Union level (European Commission, 2008). The main difficulty in defining Critical Raw Material (CRM)s was to develop a methodology to assess criticality and to select raw materials which could be considered as critical using this methodology.

#### 1.1.1.2 Defining Critical Raw Materials

*Material availability*

The resources are defined by mining companies, which usually only define the reserves regarding their short to middle-term needs. Therefore the published reserves cannot be considered as reliable indicators of long-term availability. For some materials, mined as by-product, the availability is also conditioned by the major metal of the ore in which they occurred usually in low concentration. This by-product can generate additional revenue but in some cases they are considered to be impurities that can lower the product value or drive up production cost. Another consideration regarding the geological availability is that some metals can occur as accompanying element in some deposits, as the platinum group elements or PGMs (platinum, palladium, osmium, iridium ruthenium and rhodium) in ultramafic deposits or REE ores which are generally mined and processed for all these metals together. Technological develop-

ment can have an important impact on the future availability of certain materials by improving processing, manufacturing or recycling methods.

A more efficient use of resources and recycling thanks to technological advances could increase the existing reserves. That's why rather than using a static view of geological availability, a more dynamic model was chosen by the European Commission. This model take in consideration not only the general trends in reserves, but also technological developments and changes in the geopolitical-economic framework that impact on supply and demand of raw materials (European Commission, 2010).

*Main parameters and definition of criticality*

Previous studies all defined criticality on the basis of both supply risk and the associated impact on country's economy. In 2008, the Committee on Critical Mineral Impacts for the US Economy suggested in an expert report a framework for identifying critical minerals (Committee on Critical Mineral Impacts of the US Economy, 2008). In this report the raw materials are considered critical if there are both important in use and subject to potential supply restrictions. In agreement with this approach, the expert work group of the European Commission has also put forward a relative concept of criticality. They consider that a raw material is "critical" when the risk of supply shortage and their impact on the economy are higher than for most of the other raw material (European Commission, 2010).

This innovative approach uses three main indicators to determine criticality, *i.e.* the supply risk, the economic importance and the environmental country risk:

- The assessment of the supply risks for a raw material was achieved using widely recognised indexes which evaluate the level of concentration of worldwide production and are linked to the economic and political stability of the producing countries. The supply risks could also be linked to "company concentration". For example the high corporate concentration of mine production of niobium and tantalum means that a few companies control the global market, increasing the supply risk for these materials. However, the company concentration was not included in the assessment of supply risks because of the limited information regarding the studied materials (European Commission, 2010),

- The measurement of the economic importance of each candidate raw material was performed by breaking down its main uses and attributing to each of them the value added of the economic sector that has this raw material as input,

- The last indicator relates to the environmental country risk, *i.e.* the risk that measures might be taken by a country in order to protect its environment and thus endanger the supply of raw materials to the EU. The importance of this indicator is perfectly illustrated by the global supply of REE by China, which has decided in 2010 to drastically decrease its export quotas in order to protect its environment (Massari and Ruberti, 2013).

Based on the methodology described above, a raw material can be considered as critical if it is of high economic importance and faces both high supply and environmental risks.

#### 1.1.1.3 Applying the methodology : list of critical raw materials

First evaluations of the criticality of the 41 material candidates have been made using the previously described method (European Commission, 2010). In 2014, this evaluation has been extended to 54 non-energy, non-agricultural materials (European Commission, 2014). In total this new evaluation defines 20 Critical Raw Materials (CRMs), with more detail provided to the REE by splitting them into 'heavy' (HREE) and 'light' (LREE) categories and scandium (Figure 1.1). These evaluations are based on their economic importance for the EU economy (represented on the x-axis) and their supply risks (represented on the y-axis) only, since environmental country risks did not add significant changes. The results range from low (pulpwood, diatomite) to very high (vanadium, tungsten) economic importance and from very low to very high (LREE and HREE) supply risks.

Three groups of raw materials have been distinguished by the expert work group (European Commission, 2014), see Figure 1.1. The CRMs are located in the top right corner sub-group, *i.e.* every material with a supply risk superior to 1 and an economic importance higher than 5 is qualified as critical.

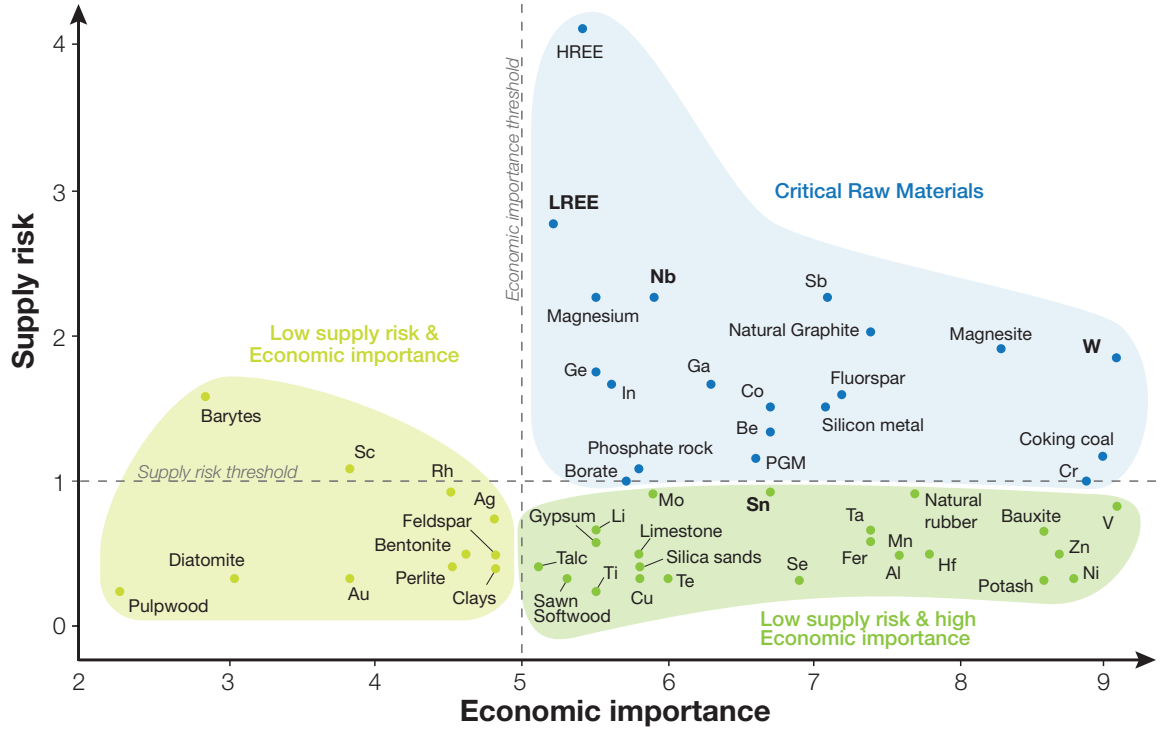


Figure 1.1: Criticality diagram based on the economic importance and supply risk, slightly modified from European Commission (2014).

Their high supply risk is mainly due to the high production concentration. Indeed, the share of the worldwide production is dominated by China (antimony, coking coal, fluorspar, gallium, germanium, indium, magnesium, natural graphite, phosphate rock, LREE, HREE, tungsten). For the remaining CRMs the worldwide production is divided between Brazil (niobium), Democratic Republic of Congo (cobalt), Kazakhstan (chromium), Russia (PGM), South Africa (chromium, PGM), Turkey (borates) and the United States (beryllium, borates), see Figure 1.2.

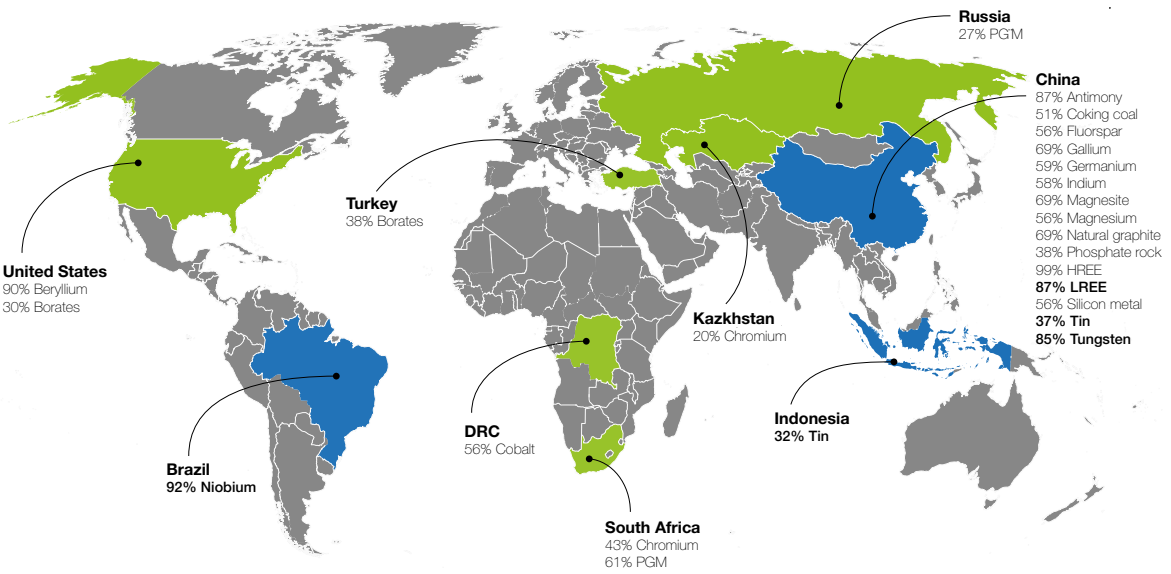


Figure 1.2: World map of major CRMs (and Sn) producers with critical metals of interest (LREE, Nb, W) and Sn highlighted in bold (European Commission, 2014; US Geological Survey, 2015).

The two other sub-groups are not considered as critical but it is important to notice that regarding the sub-group on the lower right corner (*i.e.* low supply risk and high economic importance materials) a small variation in the supply risk may result in a translation upward in the CRMs sub-group.

Although tin does not fall into the criticality zone, its economic importance is largely above the economic importance threshold whereas the associated supply risk is close to the supply risk threshold. As a result, comparatively small changes in tin supply risk can make this material move into the "critical" region. Thus tin can be properly considered as a "near-critical raw material" (Oakdene Hollins and Faunhofer ISI, 2014).

### 1.1.2 CRMs (LREE, Nb-Ta, W) and Sn consumption

All the CRMs of interest and Sn have a wide variety of uses, which have varied over time mainly in the metallurgical, electronics, automotive and chemical industry. Appendix A.1 lists the principal industrial applications of the CRMs of interest and Sn for each industry in which they are used.

*LREE*

The demand for rare earth elements has "skyrocketed" in recent years due to their increasing usage in numerous high-technology markets. The global market shares are distributed between high strength permanent magnets (21%), alloying agents in metals (21%), catalysts (19.5%), polishing (13%), glass (7%), phosphors for electronic displays (6.5%), ceramics (6%) and others (Kingsnorth, 2014b). The industrial application of LREE are numerous in economic areas such as aeronautic, automotive (hybrid and electric vehicles), defence, renewable energy technologies (wind turbine, solar panels),

medicine (medical imagery) and other economic areas for which they became essential. This wide variety of application for REE came from the configuration of their electrons in the atomic structure, which give them many desirable features: (1) ability of forming alloys with other metals, very strong and light magnetic materials; (2) valuable and distinctive optical properties, including fluorescence and emission of coherent light, essential for laser devices; (3) other unique nuclear, metallurgical, chemical, catalytic, electrical, magnetic, and optical properties (Massari and Ruberti, 2013). However, each REE has its particular uses as the lanthanides are not all interchangeable (Table 1.1). For instance La is the main REE used in nickel metal hybrid (NiMH) rechargeable batteries that powers many electronic products. Along with cerium (Ce), it is used in fluid cracking catalysts in the petroleum industry for the crude oil refining process. Ce is mainly used for autocatalysts and chemical catalysts as cerium carbonate and cerium oxide to increase effectiveness of chemical reactions and reduce the amount of platinum and other precious metal required. Glass and polishing is also a major use of Ce due to its ability to adsorb ultraviolet light. Neodymium (Nd) is mainly used for permanent magnets in neodymium-iron-boron (NIB) magnets for low temperature applications (Curie point at 310°C) and possesses a magnetic energy of up to 2.5 times greater than the former samarium-cobalt magnets (Walters and Lusty, 2011). According to Kingsnorth (2014b) demand of Nd (and praseodymium) for rare earth permanent magnets will be the market driver for the foreseeable future.

Table 1.1: Rare Earth Elements consumption by application (Lynas Corporation Ltd., 2010).

| Application | La (%) | Ce (%) | Pr (%) | Nd (%) | Sm (%) | Eu (%) | Gd (%) | Tb (%) | Dy (%) | Y (%) | Other (%) |
|---|---|---|---|---|---|---|---|---|---|---|---|
| Magnets | - | - | 23.4 | 69.4 | - | - | 2 | 0.2 | 5 | - | - |
| Battery alloys | 50 | 33.4 | 3.3 | 10 | 3.3 | - | - | - | - | - | - |
| Metal alloys | 26 | 52 | 5.5 | 16.5 | - | - | - | - | - | - | - |
| Auto catalysts | 5 | 90 | 2 | 3 | - | - | - | - | - | - | - |
| Petroleum re ning | 90 | 10 | - | - | - | - | - | - | - | - | - |
| Polishing compounds | 31.5 | 65 | 3.5 | - | - | - | - | - | - | - | - |
| Glass additives | 24 | 66 | 1 | 3 | - | - | - | - | - | 2 | 4 |
| Phosphors | 8.5 | 11 | - | - | - | 4.9 | 1.8 | 4.6 | - | 69.2 | - |
| Ceramics | 17 | 12 | 6 | 12 | - | - | - | - | - | 53 | - |
| Other | 19 | 39 | 4 | 15 | 2 | - | 1 | - | - | 19 | - |

*Sn*

Tin has been in use since ancient times and its consumption by different sectors is varying with time. Since 2000, consumption of tin for electronic soldering application increases in Asian countries, especially China and Japan (Angadi et al., 2015). Tin is primarily used worldwide, in descending order, in solders, tin plates, chemicals, tin alloys (brass, bronze, etc.) and float glass (Figure 1.3). Tin is employed in a wide range of specialised solders of higher or lower melting temperature, and physical properties to support the electronics and industrial sectors. Solders are used in almost every electronic product for conductive joints, and for traditional industrial applications such as joining copper water pipes. Tinplate (*i.e.* steel with a thin tin coating) is used in pack-

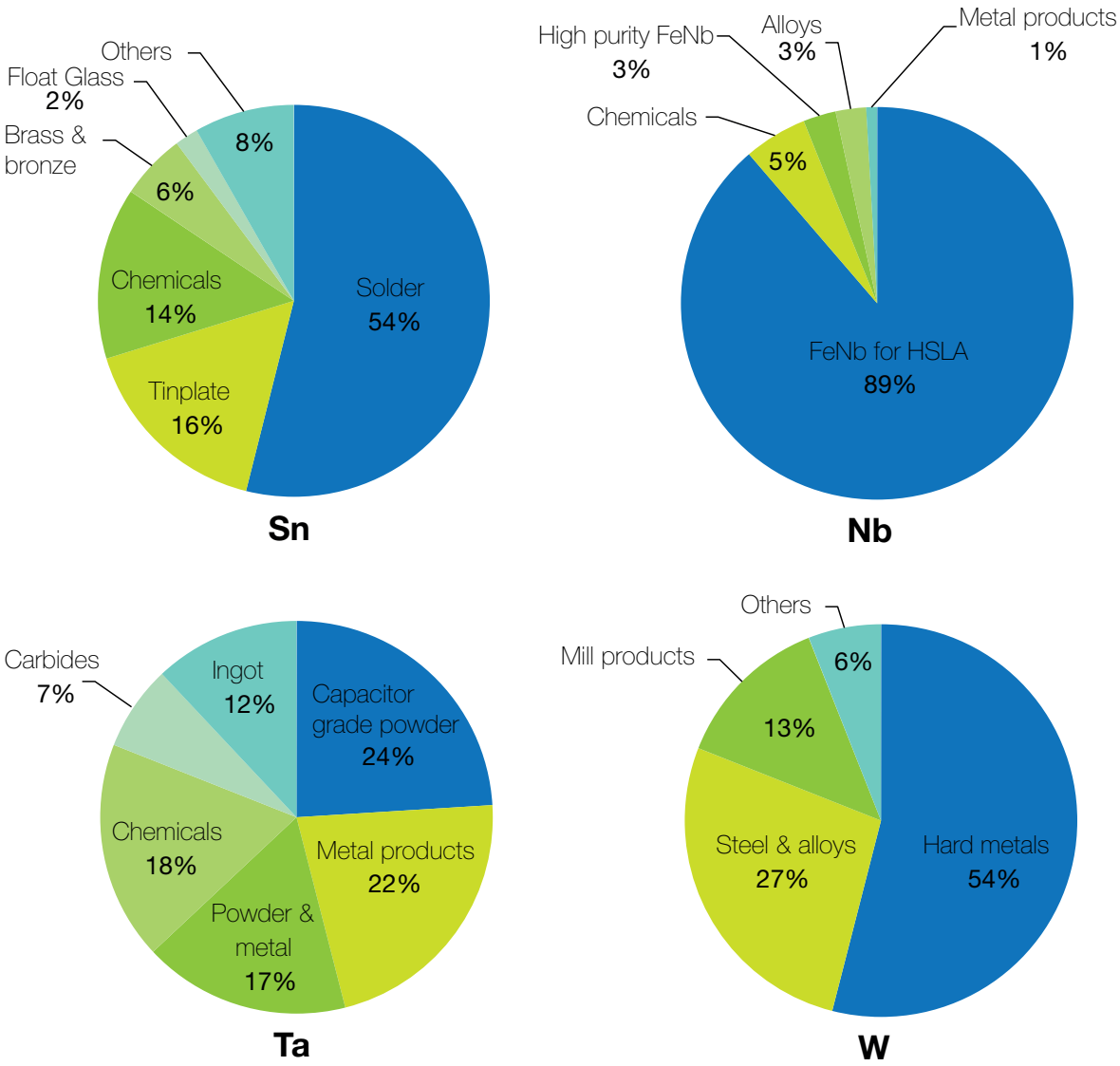


Figure 1.3: The main global uses of CRMs (Nb, Ta, W) and Sn in 2010 using data from (ITRI, 2010; Roskill Consulting Group, 2010; Schwela, 2010). Abbreviations are given in the text.

aging in the food industry for food and beverages (*e.g.* tin cans), product containers and various other items (ITRI, 2010). Tin chemicals represent also an important share of tin consumption, primarily used in organic compounds in PVC (doors, windows) to prevent degradation by heat and sunlight. Other uses of tin include non-smelting alloys of tin such as brass, bronze, pewter and even superconductor. Tin as also an essential role in the float glass technology for flat glass manufacturing process (De Cuyper and Delwasse, 1999).

*Nb-Ta*

Niobium and tantalum are vital components in a diverse range of products and applications due to their unique properties which include superconductivity, corrosion-resistance, very high melting temperature, shape memory properties, high coefficient of

capacitance and bio-compatibility (Shaw and Goodenough, 2011). The majority of niobium is consumed in the form of ferro-niobium (FeNb) utilised in the production of high strength low alloy steels (HSLA) used to manufacture vehicle bodies, railway tracks, ship pull, bridges or pipelines. The remaining share is used in manufacturing niobium chemicals, high purity ferro-niobium, niobium alloys and other niobium metal products (Schwela, 2010), see Figure 1.3. The end uses for tantalum are more balanced between capacitor-grade and metallurgical grade tantalum powder, metal products, tantalum chemicals, ingot and carbides (Figure 1.3). Tantalum powders are used in a wide range of applications, primarily for the production of capacitors in mobile phones, due to their ability to hold electric charge.

*W*

The unique properties of tungsten are a very high density and melting point, an extreme strength, a high wear resistance, a low coefficient of expansion, a high thermal and electrical conductivity (Pitfield and Brown, 2011). However the global end-uses of tungsten are less diverse comparing to the above-mentioned uses of other CRMs. Tungsten is primarily used worldwide, in descending order, in hard metal, steel and alloys, mill products and other products (Roskill Consulting Group, 2010), see Figure 1.3. The term hard metals refer to tungsten and cemented carbides used to manufacture very hard materials used for cutting, drilling and wear-resistant coatings in the metal-working, mining and petroleum industry. There is a wide variety of tungsten alloys, the more common being the steel alloys, such as high speed steel, heat resistant steel and tool steel used for metal cutting and other specialised engineering application where hardness and strength are required (Pitfield and Brown, 2011). The term mill products refer to tungsten wire, sheets or rods used in electrical application, electronics, notably in incandescent light bulb filaments, vacuum tubes and heating elements. Other applications include chemical products used as colouring agents in the porcelain industry or in catalysts, phosphors and absorbent gels, as reagents for chemical analysis during medical diagnosis, or as a corrosion inhibitors (Pitfield and Brown, 2011).

### 1.1.3 The STOICISM project

#### 1.1.3.1 Project summary

The European Seventh Framework Programme for Research (FP7) launched in mid-2011, offered to support large projects under the umbrella of Nanosciences, Nanotechnologies, Materials and New Production Technologies (NMP) including "NMP.2012. 4.1-1: New environmentally friendly approaches to mineral processing". It was recognized through the EU Raw Materials Initiative and Europe 2020 that there was also a need to improve all raw materials efficiency to remain as self-sufficient and self-sustainable as possible (EU, 2015).

Europe is a major global producer of industrial minerals with around 180 million tonnes per year of products extracted in the EU, with an estimated contribution of €10 billion to European Gross Domestic Product (GDP). In global terms, EU produces 35% of perlite, 20% of calcined kaolin and 20% of diatomite of world demand (EU, 2015). Key markets for these minerals are beverage filtration, coatings, plastic, rubber, cosmetics, insulation and construction materials. Any strategy based on sustainable

use of mineral resources has to reduce the impact on the environment through improved efficiency and effectiveness of the entire value chain of raw materials.

In this context the STOICISM (Sustainable Technologies for Calcined Industrial Minerals in Europe) project was launched in 2013 with 4-years duration, with the specific objective to enhance the competitiveness of the European industrial minerals industry by developing cleaner, more energy efficient extraction and processing technologies reducing the carbon footprint of several calcined industrial minerals, thereby looking at the whole supply chain from the extraction, beneficiation, waste valorisation and optimisation of the functionality for the end users.

Three industrial minerals, *i.e.* diatomaceous earth (DE), perlite and kaolin have been selected but results should be directly transferable to many other industrial minerals.

#### 1.1.3.2 Project partners and consortium structures

The STOICISM Consortium is led by a major industrial mineral producing company (Imerys minerals Ltd) and consists of 17 partners from 8 different European countries. Key contributors on this multidisciplinary platform include several universities, specialized SMEs & corporations, an industry association, as well as applied technology and research institutes. The project is structured in 9 work packages (WP) with associated tasks and with clearly identified milestones and outcomes. The 6 first work packages are complementary and correspond to the main steps of the whole industrial materials supply chain (Figure 1.4).

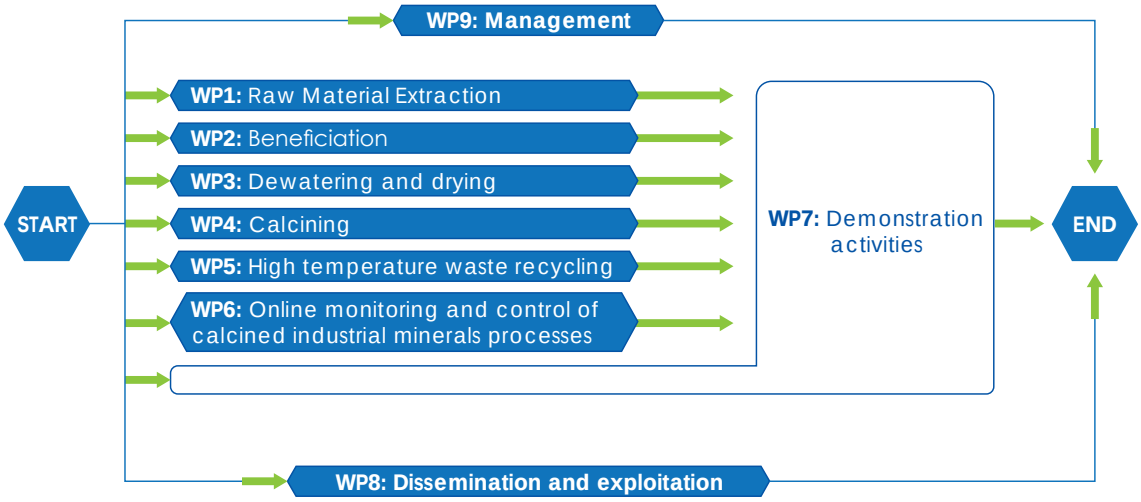


Figure 1.4: Consortium structure and list of work packages, after EU (2015).

This work is incorporated within the framework of WP2 "beneficiation" the leader of which is the *Université de Lorraine* (UL). The others partners involved in this work package are:

- Imerys Minerals Ltd, the wholly-owned UK entity of Imerys, world leader in mineral-based specialties for industry, active in 47 countries with more than 240 industrial locations. Imerys is the lead participant in the project and ensure that the industrial partnership, with its academic support, meets the aims and

objectives of the project on time and within the budget. They are involved in all of the Work Packages, thus providing leadership and continuity throughout the project.

- University of Exeter's Camborne School of Mines (CSM), which has an international reputation for research related to the understanding and management of the Earth's natural processes, mineral resources, energy, and the environment. The core of Exeter's involvement is participating in WP1 (Extraction) but it also participates across WP2, investigating opportunities for renewable energy.

The strategic objective of WP2 is to develop and apply new beneficiation techniques to allow the use of low quality DE, perlite and kaolin ore and to recover CRMs from waste streams. This is expected to reduce waste production and increase useful mine volumes. UL led this activity with support and input from Imerys and CSM. The specific objectives of WP2 are to:

1. Advance technological development of high intensity flotation devices for better flotation recovery with investigation of pulsation, vibration and ultrasonic fields. Thus a considerable diminution of energy and reagents consumption by unit volume of material processed will be obtained.
2. Develop a process for selective flocculation of DE to remove impurities.
3. Identify alternative and new uses for industrial mineral waste streams.
4. Identify processes to extract useful CRMs from raw materials and waste such as physical separation, advanced flotation technology, and embrittlement by high power electromagnetic pulses.
5. Assess opportunities for the use of renewable energy in the beneficiation process stages.

This PhD thesis is linked to the fourth objective through the task 2.6 untitled "CRM Recovery".

#### 1.1.3.3 Task 2.6 CRM Recovery

This task is dedicated to CRM recovery from waste streams of kaolin production of the St Austell kaolin workings of Imerys in Cornwall, UK. T2.6 itself is subdivided into specific subtasks:

- **T2.6.1 Analysis of materials streams and definition of the samples to be characterised:** analyse raw materials/waste streams and evaluate their availability to extract the critical CRMs.
- **T2.6.2 Identification of valuable minerals and metals:** identify the CRM-bearing minerals and the degree of dissemination in the ore and waste streams to evaluate the way of processing. The classical and advanced analytical techniques for mineral characterisation (XRD, high resolution SEM and TEM, etc.) will be used by UL to identify the mineral composition and mineral associations. University of Exeter will apply the new QEMSCAN technique to establish the mineral and size by size associations in order to direct to the best separation method.

- **T2.6.3 Feasibility studies of pre-concentration by physical methods and extraction of CRMs.** UL will test the physical separation techniques such as gravity (*i.e.*, centrifuge) and high intensity magnetic separation, advanced flotation technique and leaching (all available in STEVAL pilot plant) to extract the CRMs from various type of streams. For low grade rare metals-containing ore (W, Sn, Ta, Nb, REE) a high capacity pre-concentration method will be searched and tested.

- **T2.6.4 Feasibility studies on advanced flotation technique for low grade and fine grained ores:** For low grade and fine grained ores (or waste products) the high intensity flotation machine will be used. In order to decrease the reagent consumption, P4 will develop a new formulation of flotation reagents based on the synergistic effects in the mixed collector system. Thus, the combination of new formulations of surfactants with pulsed fields in the high intensity flotation machine will result in the enhanced separability of CRMs from waste streams. In particular it will allow rare metals (W, Ta and Nb) to be processed economically from low grade, high volume ores.

- **T2.6.5 "Go/No Go" evaluation:** UL will carry out a "Go/No Go" evaluation at M24.

- **T2.6.6 Validation of CRMs extraction methods at laboratory and pilot scale:** UL will validate the promising CRM extraction methods at laboratory and pilot scale.

- **T2.6.7 Assessment of scale-up potential for the technologies developed:** Imerys and UL will assess the potential for scale-up of the technologies developed based on the results of (M36-M42).

## 1.2 Geological background

The Cornubian granite province is well known for its historically important deposits of tin and base metals (Manning and Hill, 1990), and for its current international importance as a major producer of china clay (kaolin).

### 1.2.1 The Cornubian Sn-W province

Tin is distributed on the continents in relatively narrow continent-sized belts (Schuiling, 1967). For instance, most of tin deposits across Europe are related to Variscan granites (Figure 1.5). The major tin belt passes from the Cornubian massif (Redruth, Camborne, etc.) in UK through the French Massif Central (Echassières) and continues towards Italy with tertiary tin deposits (Elbe, Tuscany and Scilly). Other tin belts are also related to varsican granites, like the one which pass from Northen Portugal (Panasqueira) through Spain or the one around the Bohemian massif (Cinovec-Altenberg). Indeed most of these tin deposits are associated with Sn-W cupolas located at the top of tardi- to post-orogenic plutons emplaced at shallow depths (Jébrak and Marcoux, 2008).

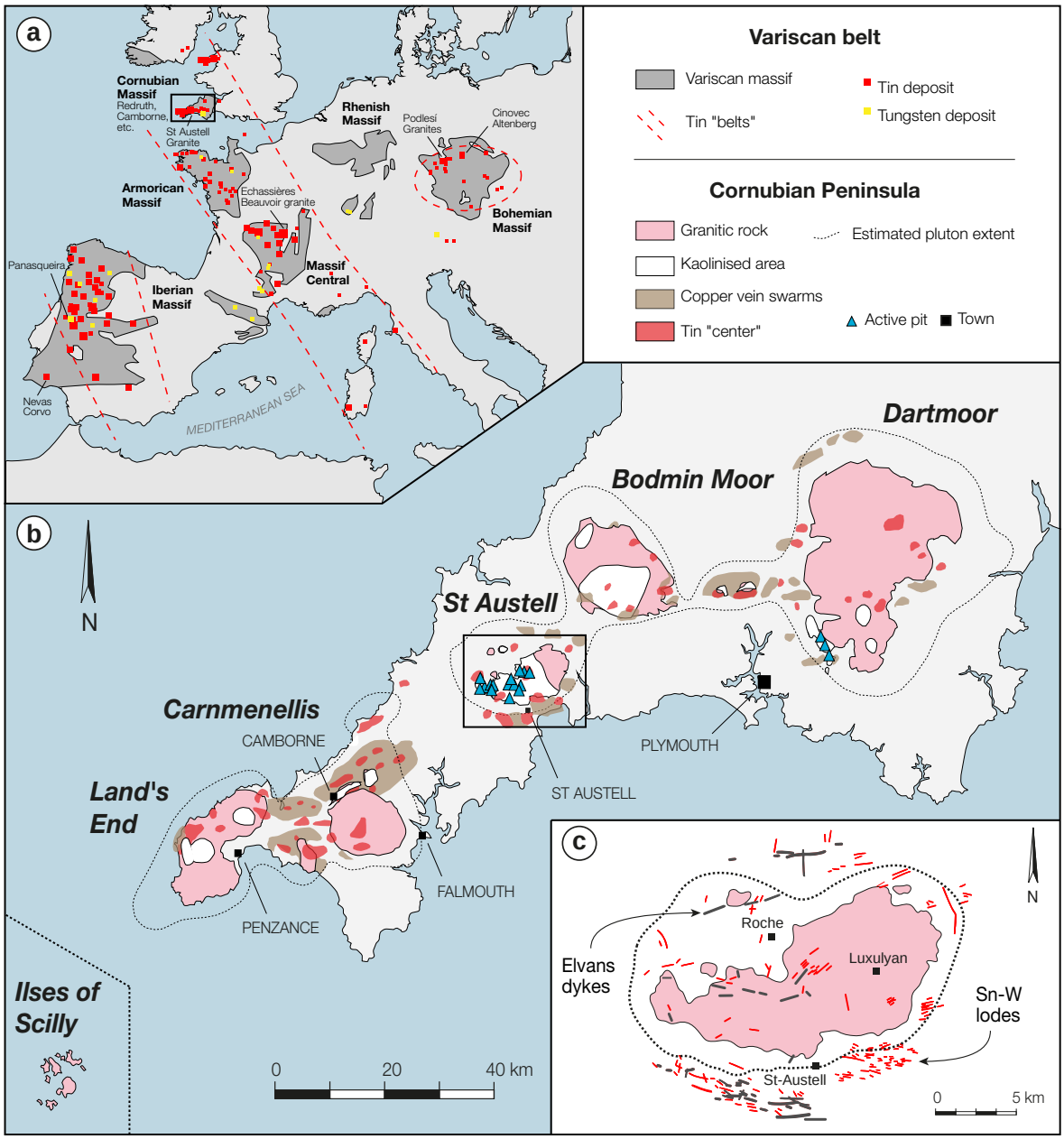


Figure 1.5: Spatial relationship at distinct geological scales between Variscan granites and Sn-W deposits. (a) Tin belts in Europe and their spatial connection to the Variscan belt modified from Schuiling (1967). Main Sn-W deposits are from the PROMINE project (BRGM, 2011). (b) Outline geologic map of south west England peninsula showing the location of the major plutons of the Cornubian batholith, the kaolinised areas and the active kaolin pits, modified from Černý et al. (2005). (c) Distribution of the felsite dykes (elvans) and Sn-W mineral lodes around and within the St Austell rare-metal granite after Bray and Spooner (1983).

The batholith of SW England was formed during late Variscan orogeny in the Late Carboniferous to Early Permian (270-300 Ma) intruding deformed Devonian-Carboniferous terrestrial to marine sediments. The batholith has a 200-km-long extension (Willis-Richards and Jackson, 1989), comprising six major and several minors granite bodies. The major bodies, from east to west, are Dartmoor, Bodmin Moor, St Austell, Carnmenellis, Land's End and the Scilly Isles (Figure 1.5b).

The outcrops are dominated by biotite-bearing monzogranite, with minor intrusions of tourmaline-bearing aplites, pegmatites and local fine-grained facies (Manning et al., 1996). In addition there is some occurrences of other granite types, resulting from multiple intrusive episodes, such as the lithium-mica granites or the topaz-bearing granite in the Tregonning-Godolphin Granite and the St Austell Granite (Manning and Exley, 1984; Manning and Hill, 1990; Manning et al., 1996). The batholith was affected by several episodes of alteration including quartz-tourmaline veining associated with greisening, intrusion of rhyolite dykes, quartz-hematite veining. Kaolinisation is the last alteration event, which is believed to have a meteoric origin (Psyrillos et al., 1998), and was relatively extensive in the western part of the St Austell pluton where the majority of the active kaolin pits are located (Figure 1.5b).

According to Willis-Richards and Jackson (1989) there is a close spatial association between the batholith and the rich Sn, Cu mineralization of the Cornubian Peninsula. Most of the ores of Sn, Cu, W, Zn and As came from vein deposit type mineralisation, along or parallel to the axis of the batholith (Moon, 2010). Within the St Austell granite zones of intense kaolinisation are spatially related to swarms of steeply dipping, quartz-tourmaline±cassiterite±wolframite sheeted veins with greisen (quartz-muscovite-tourmaline±topaz±wolframite) alteration selvages (layered alteration zones), observable at Goonbarrow pit (Bray and Spooner, 1983). These mineral lodes are located South (and North) of the St Austell granite, but some of them actually occurred within the St Austell granite kaolinised area (Figure 1.5b and Figure 1.6). Figure 1.5 illustrate the multi-scale spatial relationship between Variscan granites and Sn-W deposits from the Variscan belt to the St Austell district. This shared relationship is confirmed by the numerous similarities between the St Austell rare-metal granite and several rare-metal granites worldwide, that will be discuss further in Section 1.2.3.

### 1.2.2 The St Austell rare-metal granite

Rare-metal granites are so-called because of their mineralisations being disseminated through the granites rather than concentrated in layers, lodes, etc. The St Austell rare-metal granite share numerous characteristics with other granites of SW England, summarised in many reference papers and textbooks (Floyd et al., 1993; Manning and Hill, 1990; Manning et al., 1996). These granites were originally described by four different granite types, all observed in distinct SW England granites: biotite granite, lithium mica granite, tourmaline granite and topaz granite (Hill and Manning, 1987). Additional granite types were added later based on field and textural observations within the St Austell granite, indicating complex late-stage magmatic and hydrothermal processes (Manning et al., 1996). The St Austell rare-metal granite is composed of six major granite types, each unit being characterised by a specific mineral assemblage and textures (Manning et al., 1996), see Figure 1.6.

The *biotite granite* (BG) is the main lithology, which represent up to 70% of the outcrop of the St Austell granite, exposed in the Western Area, at the eastern part of the pluton and intermittently within the Central Area. It corresponds to the megacrystic biotite granite observed at Land's End and Dartmoor (Manning and Exley, 1984; Manning et al., 1996). It is coarse grained, mainly composed of quartz, K-feldspar and micas with tourmaline and topaz as minor phases. Biotite is the main mica, but muscovite is also present. The main accessory phases are rutile, topaz, apatite, monazite,

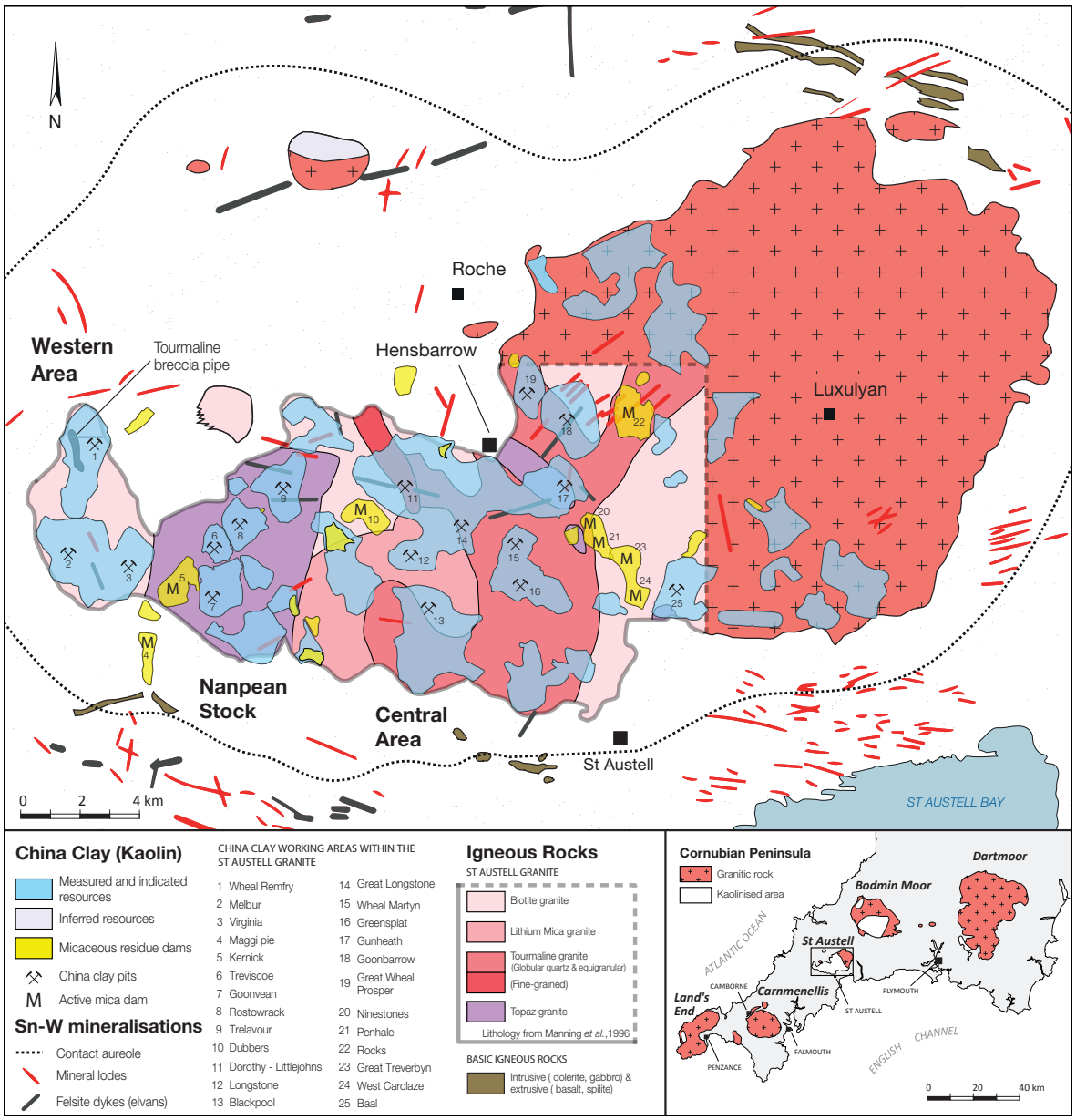


Figure 1.6: Geological map of the St Austell granite showing the distribution of the various granite types from Manning et al. (1996), the major kaolin resources and the micaceous residue dams after British Geological Survey (1997), as well as the main Sn-W mineralisations after Bray and Spooner (1983).

cassiterite, zircon and uraninite (Manning et al., 1996). The main host for the LREE differs depending on the authors. Works of Jefferies (1985) on Carnmenellis biotite granite describe monazite as the main LREE-bearing mineral accounting for approximately 75% of the total LREE content. In contrast microprobe analysis on samples from Cornubian granites by Alderton et al. (1980) show significant concentrations (up to 0.5%) of LREE in other phases, particularly apatite, but also zircon and sphene.

The *lithium mica granite* (LMG) has a similar grain size and texture than the biotite granite (Manning et al., 1996). It is characterized by the presence of lithium mica (zinnwaldite) and plagioclase (albite component). The accessory minerals are present as inclusion in zinnwaldite (apatite, monazite, zircon and rutile) or in plagio-

clase (apatite, fluorite and secondary micas). Additional alteration products include fine-grained topaz aggregates, and replacements of zinnwaldite by tourmaline (Manning et al., 1996).

The tourmaline granites were subdivided Manning et al. (1996) in a *tourmaline granite* (TG), it-self regrouping a globular quartz and medium coarse-grained equigranular facies, and in a *fine-grained tourmaline granite* (FGTG) with fine-grained (<0.5 mm) equigranular facies. The globular quartz facies is characterized by a considerable textural variation. It contains large quartz grains, phenocrysts of K-feldspar, zinnwaldite with a fine grained groundmass of quartz, plagioclase, zinnwaldite, tourmaline and topaz. The accessory phases are limited to apatite and rutile. On the contrary, the fine-grained facies is an equigranular rock with euhedral albite, lithium mica (zinnwaldite). Accessory minerals include monazite, apatite, zircon and rutile with some occurrences of arsenopyrite and cassiterite (Manning et al., 1996).

The *topaz granite* (TZG) is medium grained, characterized by euhedral-subhedral fluorine-rich topaz, interstitial lithium mica, albite, plagioclase feldspar with perthitic orthoclase, and subhedral quartz (Manning and Hill, 1990). It contains a smaller proportion of accessory phase but a wider variety including sub-economic minerals (Manning et al., 1996). The accessory minerals are apatite, amblygonite, zircon, Nb-Ta oxides (columbite-tantalite and ilmenorutile) and uraninite. According to (Manning and Exley, 1984), the field relations indicates a separate origin of the topaz granite. The mineralogy of the six granites is summarized in Table 1.2.

Table 1.2: Mineralogy of the six major granite types of the St Austell rare-metal granite, based on Manning et al. (1996) and Shail et al. (2009).

| Granite Type | Major minerals | Minor minerals | Accessory minerals |
|---|---|---|---|
| **Biotite granite (BG)** | Quartz, K-feldspar, plagioclase, biotite, muscovite | Tourmaline | Rutile, topaz, apatite, monazite, uraninite, zircon, cassiterite |
| **Lithium-mica granite (LMG)** | Quartz, K-feldspar, plagioclase (albite), lithium-mica (zinnwaldite, lepidolite) | Tourmaline, topaz | Apatite, monazite, zircon, rutile, fluorite |
| **Tourmaline granite (TG)** | Quartz, K-feldspar, plagioclase, lithium-mica (zinnwaldite) | Tourmaline, topaz | Apatite, rutile |
| **Fine-grained tourmaline granite (FGTG)** | Quartz, K-feldspar, plagioclase (albite), lithium-mica (zinnwaldite) | Tourmaline, topaz | Monazite, apatite, zircon, rutile, arsenopyrite, cassiterite |
| **Topaz granite (TZG)** | Quartz, K-feldspar (orthoclase), plagioclase, lithium-mica (zinnwaldite, lepidolite), muscovite | Topaz, fluorite, tourmaline | Apatite, amblygonite, zircon, Nb-Ta oxides (columbite-tantalite, ilmenorutile), uraninite |

Apart from these disseminated mineralisations, Sn-W mineralisations associated with quartz-tourmaline sheeted veins previously described, are also present within the

St Austell granite (Bray and Spooner, 1983). Whereas two different types of mineralisations, a Sn breccia-stockwork in the Treliver area, generally unenriched in base metals, and a E-W veins complex enriched in base metals have been identified north of the St Austell pluton (Camm and Dominy, 1999; Camm and Moon, 2001). In addition, Müller and Halls (2005) describe an intrusive tourmaline breccia in biotite granite at Wheal Remfry where zoned rutile is the principal mineral hosting Sn (up to 1.88%) and also includes high W (up to 1.95%) and Nb (up to 2.05%) domains.

### 1.2.3 Similarities with granites-based kaolin deposits worldwide

From all the magmatic units of the St Austell pluton, the topaz granite is the youngest, and the most geochemically different, relatively enriched in Li, Rb and with a much higher Nb/Zr ratio (Manning and Hill, 1990). Nonetheless, there are close similarities between the mineralogical assemblages described above and the accessory minerals assemblage of evolved granite elsewhere described as peraluminous high to intermediate phosphorus granites (Linnen and Cuney, 2005). All the St Austell granite types are felsic and weakly peraluminous (1.16>A/CNK>1) granites. However if $Li_2O$ is included, the molecular ratio A/CNKL is reduced, to less than 1 in the case of topaz granite (Manning et al., 1996). The comparison of the $P_2O_5/SiO_2$ ratio of the St Austell granites with other rare-metal granites shows that the St Austell granites belong to the intermediate phosphorous granite (IHP) type (Figure 1.5a). The relatively low Zr and Th contents of St Austell granites, visible in Figure 1.7b are characteristic of non-peralkaline rare-metal granites.

These granites are formed in a late-orogenic context and associated with orogenic belts (Figure 1.5b) and are usually characterised by highly differentiated leucocratic

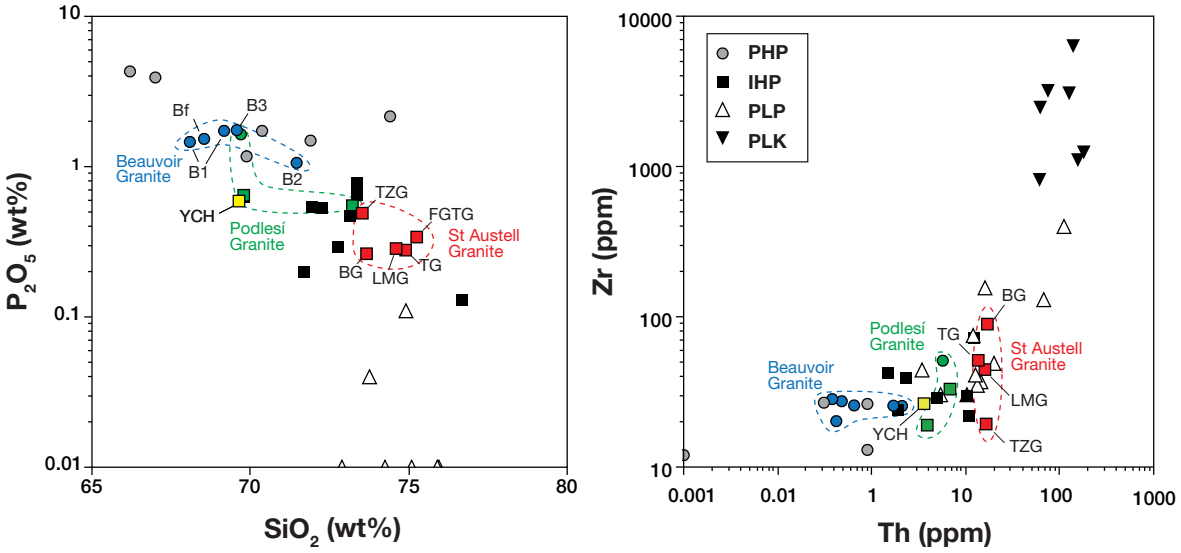


Figure 1.7: Trace-element characteristics of peraluminous high phosphorous (PHP), peraluminous intermediate phosphorous (IHP), peraluminous low phosphorous (PLP) and peralkaline granites (PLK). (a) Silica-phosphorus diagram. (b) Zirconium-thorium diagram. B series: Beauvoir granite, Massif Central; YCH: Yichun granite, Jiangxi, China. Abbreviations for St Austell granites are given in the text. Based on data from Manning et al. (1996) and the review of Raimbault et al. (1995).

two-micas granites, corresponding to the S-type, rich in hydroxylated minerals (muscovite) and enriched in lithophile elements such as Nb, Ta, Li, Be, P , F (Jébrak and Marcoux, 2008). Among these granites some display similarities with the St Austell granite and are associated with Sn, W, and Ta-Nb disseminated mineralisations (Černý et al., 2005). Some of this granites are associated to kaolin deposits which are also known to display similarities with Cornish kaolin deposits (Wilson and Jiranek, 1995; Wilson et al., 1997).

According to Scott et al. (1998), the Yichun granite in China is one of the closest rare-metal granite, in terms of lithology. It comprises also several magmatic units including a biotite granite and a Li-mica (lepidolite) granite such as the St Austell granite. The Li-micas granite is the most evolved magmatic unit (cf. St Austell topaz granite) and display a similar accessory assemblage of amblygonite/montrebasite, apatite, fluorite, Mn-tantalite, microlite, Ta-cassiterite, ilmenite, monazite, zircon, sphalerite and topaz (Belkasmi et al., 2000; Yin et al., 1995). The Beauvoir topaz-lepidolite albite granite (Massif Central, France) is also very similar to the St Austell topaz granite and display a Sn-Li-Ta-Nb-Be disseminated mineralisation with an accessory minerals assemblage composed of topaz, apatite, amblygonite, columbite-tantalite, microlite, zircon, uraninite and sphalerite (Cuney et al., 1992; Raimbault et al., 1995). Further similarities exist with the Podlesí granite in Czech Republic which is composed of three magmatic units, including biotite granite, and two Li-mica granites. All granite types contain disseminated Ta-Nb-Ti-W-Sn minerals including rutile, cassiterite, Fe-columbite, ixiolite and ferberite (Breiter et al., 2007).

All the above-cited deposits are considered as potential source for Nb, Ta, Sn or W and some of them are actually mined for these metals. For instance the Yichun granite is mined for Ta and Li (Schwartz, 1992) and the Beauvoir granite is known to produce cassiterite (800 g/t Sn) and columbite (190 g/t Ta plus 120 g/t Nb) as by-product of the kaolin production (Pohl, 2011).

By analogy with the Beauvoir granite it is possible to estimate the most prospective Nb-Ta-Sn and REE target. Rare-element chemistry of the Beauvoir granite shows that the concentration of most metallic elements including Nb, Ta, Sn and W is very high and increase with the Li contents from the bottom to the upper part of the granite body (Cuney et al., 1992). The outcrop surface dimensions of the Beauvoir Granite (around 14 k $m^2$) are considerably less than even the smallest occurrence of topaz granite, but it correspond to the top of the cupola, which is the most enriched part of the orebody in terms of rare-metals, due to a combination of magmatic process and interaction with meteoric water (Raimbault et al., 1995). It is therefore the upper parts of the topaz granite that should have the greatest potential for disseminated magmatic mineralization. The exact morphology and the intern organisation of the topaz granite is poorly constrained but Manning and Hill (1990) suggested that the individual outcrops of topaz granite may be connected at depth. The field relations indicate that the Nanpean stock represents a position well below the roof of the granite body and that the Hensbarrow stock represents the roof. Thus, from a pure metallogenic perspective, the Hensbarrow stock, which represents the upper part of the St Austell topaz granite, is the most prospective target zone for Ta, Nb and Sn within the topaz granite.

## 1.3 Kaolin from St Austell

China clay, also called kaolin, is a commercial clay material mainly composed of kaolinite ($Al_2Si_2O_5(OH)_4$), an hydrated aluminosilicate clay mineral. Its main use is for coating and filling in paper industry (75% of world's production), but it has a wide variety of uses for plastics, ceramics, ink, paint, rubber, and pharmaceutical industry. The commercial value of a kaolin product is based on its whiteness and its fine particle size. Particle size affects fluidity, strength, plasticity, colour, abrasiveness and ease of dispersion. Other important properties include its flat particle shape, which increases opacity or hiding power, its soft and non-abrasive texture, due to the absence of coarser impurities, and its chemical inertness (Highley et al., 2009).

### 1.3.1 St Austell Kaolin deposits

UK is the world's third largest producer and exporter of kaolin after the USA and Brazil, supplying up to 1.36 million dry tonnes of clay per annum, in 2008 for the paper, ceramics, paints, plastics and rubber industries (Highley et al., 2009). Production is supplied from a large number of open pits scattered throughout the western part of the granite outcrop within a complex landscape of spoil heaps and mica lagoons as shown in Figure 1.6. Kaolinite is a secondary mineral formed by weathering and hydrothermal alteration of the alumina silicates of the host rock, mostly feldspar minerals, by acid aqueous fluids to form an aggregate of kaolinite and secondary micas. The main chemical reaction corresponding to the dissolution of K-feldspar can be summarised as follows:

$$2KAlSi_3O_8 + 2H^+ + H_2O \longrightarrow Al_2Si_2O_5(OH)_4 + 2K^+ + 4SiO_{2\,(aq)}$$

The chemical reaction is exactly the same for Na-feldspars, with Na instead of K. Under acidic conditions, muscovite may also be kaolinised following the chemical reaction:

$$2KAl_3Si_3O_{10}(OH)_2 + 2H^+ + 3H_2O \longrightarrow 3Al_2Si_2O_5(OH)_4 + 2K^+$$

If potassium is not leached, illite is formed instead of kaolinite.

The St Austell kaolin deposits are primary deposits, formed by alteration of the underlying St Austell granite. The genesis of the kaolin deposits have been subject to a debate between those in favour of a weathering origin under sub-tropical conditions as supported by stable isotopes compositions of St Austell's kaolin (Sheppard, 1977) and those in favour of an hydrothermal origin either in association with late magmatic fluids (as an extension of the Sn–W mineralisations and the greisenisation of the host granites), or during the last stages of hydrothermal circulation (Alderton and Rankin, 1983; Bray and Spooner, 1983). However the most recent researches show that it is probably the result of a complex multi-stage process (Scott et al., 2002). After granite deposition, early high temperature hydrothermal alterations, forming the quartz-tourmaline veins (associated with Sn-W mineralisations) have increased the overall permeability of the granites which made them more susceptible to later kaolinisation (Mueller et al., 1999). This stage is followed by the final phase of granitic intrusion represented by the felsitic "elvan" dykes (dated around 270 Ma), notably visible at Goonbarrow and Wheal Remfry pits, see Figure 1.6. The field association between kaolinised zones and quartz-hematite veining suggest that a first stage of argillic alteration associated with

this veining episode and faulting may have occurred. However fluid inclusions studies shows that the solutions had high temperature and moderate-high salinity (Jackson et al., 1989) which are not compatible with kaolinite stability. The main stage of kaolinisation is probably due to the circulation of meteoric water through the high permeability zones, as suggested by geochemical modelling which indicate that appropriate mineral assemblages are obtained from granite rock by reaction with meteoric water at low temperatures (Psyrillos et al., 1998; Scott et al., 2002). The resulting kaolin deposits are usually funnel-shaped extending down to several hundred meters (Figure 1.8).

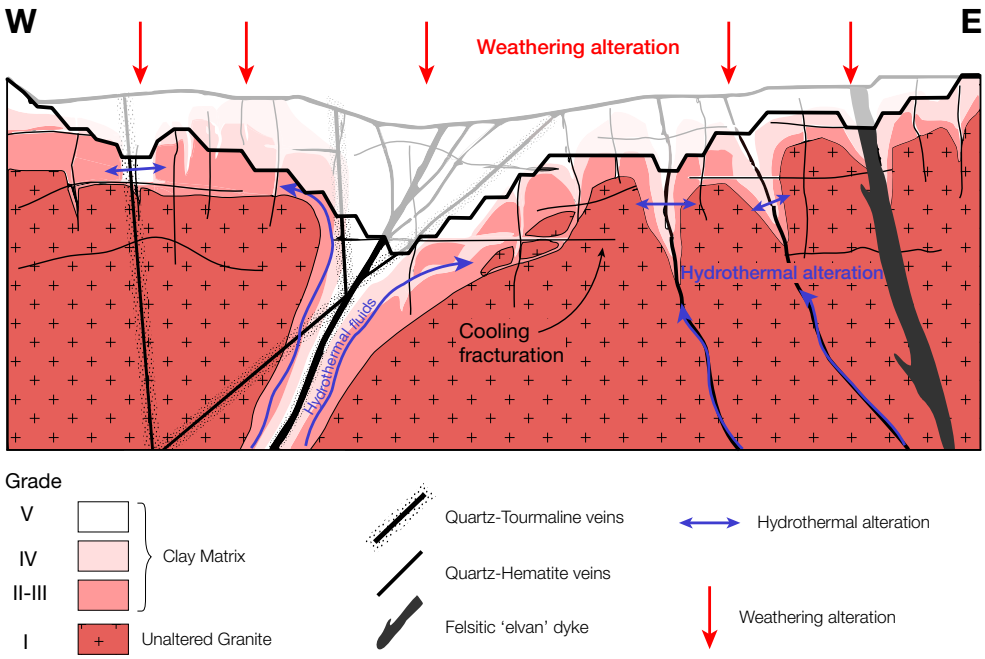


Figure 1.8: Geological E-W cross section through a typical kaolin deposit, with current position of pits surface, showing the combined action of hydrothermal and weathering processes on the formation of the kaolin deposits.

Table 1.3: Classification of the kaolin resources based on original texture preservation and feldspar alteration, ranging from grade I to master grade V (Imerys, personal communication).

| **Grade** | **Geological Grouping** | **Description** | | | |
|---|---|---|---|---|---|
| | | **Alteration** | | **Original Texture** | **Others** |
| | | **Na-Feldspar** | **K-Feldspar** | | |
| **V** | Fully kaolinised granite | Full | Full | None | The matrix can be manually rolled into a ball. |
| **IV** | Nearly fully kaolinised granite | Nearly full | Strong to nearly full | Partial destruction | Matrix can be broken by hand |
| **III** | Partly kaolinised granite | Minor to strong | Minor to Partial | Intact | Matrix is hard and cannot be broken by hand |
| **II** | Nearly fresh granite | None to minor | None | Intact | |
| **I** | Fresh granite | None | None | Intact | |

The composition of the granites has a significant influence on the quality of kaolin ore (Scott et al., 2002). Most of the important kaolin deposits are in the western two-third of the St Austell granite. Kaolin for the paper industry comes mainly from the Central Area whilst those for ceramics generally come from the Western Area, Figure 1.6. For ore mining and processing needs, Imerys use a geological classification to characterise the ore based on the degree of kaolinisation of the granite rock, classifying the potential kaolin resources into 5 grade categories (Table 1.3). Normally only the most altered grades (IV-V) are considered to constitute ore.

### 1.3.2 Kaolin extraction

There are three extraction methods currently used by Imerys to extract china clay, which are hydraulic mining, cut & carry and dry mining.

*Hydraulic mining*

This is the historical kaolin mining extraction methods in Cornwall and Devon. This method uses pressurised water system within the pit to provide high pressure (14-20 bar) water at the nozzle of washing hoses called "monitors" (Figure 1.9a). These can be compared to fire-fighters hoses projecting high volumes of water at high pressure. Clay matrix is either blasted or pushed by bulldozers (depending on rock hardness) from the quarry face towards the monitor to facilitate the hydraulic mining process. High pressure monitor water blasts the kaolin from the clay matrix which is then held in suspension and runs in a clay stream, leaving behind the less well decomposed material in the form of sand and rock, locally called "stent". The resulting "clay stream" flows into the pit sink (Figure 1.9b) and is then pumped to the in-pit processing loop (Figure 1.9c). Pit processing removes finer sand and residue waste before the clay slurry is pumped to settling tanks to increase in density before it is sent to the refiner for further processing. This extraction method is not perfect and raises many problems in terms of selective mining and product traceability. Indeed the material in front of the monitor must either be washed or tipped as waste and contamination may occur while the "clay stream" flows into the pit. Therefore a small amount of stained clay present in the clay matrix can contaminate a large amount of high quality clay. This can cause a problem if a pit is operating a small number of monitors, all of which have poor kaolin quality at one time. In addition there is no traceability or the material pumped into the processing route because of the mixing of the clay streams from different monitors into the pit sink and the above-mentioned contamination issues.

*Cut and carry*

Cut and Carry is a modern variation of the traditional hydraulic method. Cut and carry adds flexibility to the kaolin extraction process as the clay matrix is transported from an excavation site and tipped at a monitor for washing. Thus an area in a quarry can be selectively mined for the desired quality of clay and possible sources of contamination can be removed. The kaolin and stent waste is processed in the same manner as highlighted in hydraulic mining method (Figure 1.9d)

*Dry mining*

Dry mining is the most modern kaolin extraction method used by Imerys. This method offers many advantages as it do not use in pit pressurised water system and removes the need for pumping water and clay slurry over large distances as for the historical hydraulic mining method. A centralised processing plant, localised in the Western Area is fed with clay matrix, which is transported from Wheal Remfry and Melbur-Virginia pits to the processing plant by a dedicated clay matrix team consisting of a wheeled loader and fleet of dump trucks. This is the most interesting kaolin extraction method as it avoids contamination issues and allows traceability of the kaolin ore processed in the dry mining plant. About 45% of Imerys' output is now produced using this methodology (Highley et al., 2009). In addition Western Area kaolin operations, produce in excess of 600 000 t of kaolin per annum, making it one of the largest mining operations within the Imerys group. The present work focused on this kaolin processing plant.


Figure 1.9: Imerys kaolin extraction methods at St Austell. Hydraulic mining use high pressure water to blast the kaolin out of the clay matrix (a). The resulting "clay stream" flows down into the pit sink (b) and is then pumped to the in-pit processing loop (c). (d) Cut and carry operation.

### 1.3.3 Kaolin dry mining processing

Designed to process several million tonnes of matrix a year, the Western Area Dry Mining (WADM) plant operates six days a week and is shut down one day a week for routine maintenance (Imerys Ltd, 2008). This centralised processing plant is fed with clay matrix, which is transported directly from the pit by cut and carry operations without any washing (dry mining). Two static grizzlies within the pits are used for primary segregation of large boulders and the segregated material is then delivered to storage bays at the dry mining plant. A wheeled loader selects the desired grade of material from the designated storage bay, and tips this material into the feed hopper. Because there is no washing the material fed into the plant is much coarser and more classification stages a required to remove the coarsest materials.

The first stages of kaolin ore processing consist in removing the coarsest fractions of the clay matrix which are not valuable for kaolin recovery. Thus the WADM plant can be seen as a classification plant producing different size classified wastes and a fine kaolin product (Figure 1.10). The first sized-classified wastes *i.e.* crushed stones (21-11 cm) travels on the top of the grizzly cassettes and fall into a jaw crusher, then the conveyors transport the material to the crushed stone stockpile. Because the material has not been washed yet, a certain amount of clays is loss with this material as it is visible in Figure 1.10a. The underflow from the grizzly screen is fed into a rotary washing barrel where the majority of the kaolin is released from the matrix. The washed material is then separated onto a screen where +8 mm material is washed on the wash screen to remove traces of clay and sand (Figure 1.10b) before it is conveyed onto the gravel (110-8 mm) stockpile. The underflow flows into a sand separation system consisting of two bucket wheels de-sander (Figure 1.10c) and de-watering screens which remove the sand material which is then conveyed to the sand (8-0.5 mm) stockpile. Sand is the single largest waste stream derived from the original matrix and can be generated at plus 300 t/h (Imerys Ltd, 2008). The last classification stage is realised by series of hydrocyclone loops. The finer (-53 $\mu$m) particles go to the product stream (hydrocyclone overflow, Figure 1.10e) and are pumped to the refiner for further classification and processing whereas the coarser ($\sim$500-53 $\mu$m) particles are reported to the micaceous residue (hydrocyclone underflow, Figure 1.10d) where they are held in suspension and pumped to a tailing dam.

Additional techniques are used to improve the brightness (whiteness) and particle size of specific grades of clay. These include blending, fine grinding, chemical reductive bleaching and/or the removal of iron-bearing impurities using superconducting magnets. Some kaolin products are also calcined at specific temperatures to give different products.

### 1.3.4 Waste management

Kaolin extraction in Cornwall is a moderate waste-generating process which typically produces for each tonne of kaolin product, 9 tonnes of sized-classified wastes including crushed stones and gravels, both accounting for 4 tonnes, sands and micaceous residues accounting for 4 tonnes and 1 tonne respectively (Highley et al., 2009). The annual waste production of the whole industry is about 10 million tonnes (Highley et al., 2009) which are in part sold as construction material locally for the coarsest fractions but the majority is engineered and disposed in large waste piles. However fine

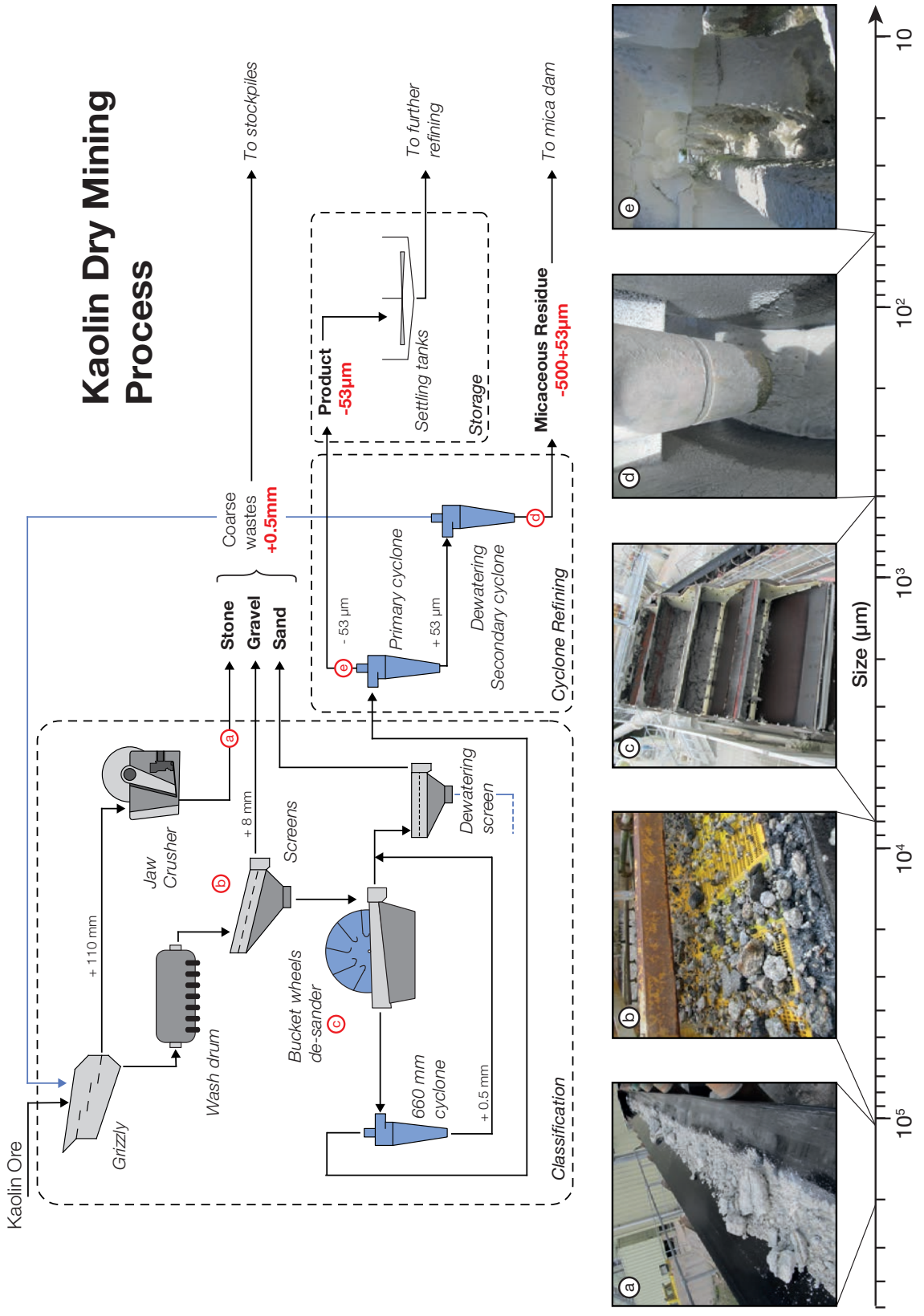


Figure 1.10: Simplified flowsheet of the Western Area Dry Mining (WADM) process. It can be seen as a size-classification process which removes the coarsest fractions of the clay matrix which are not valuable for kaolin recovery. This results in the production of five size-classified wastes which are named, by size, stone (a), gravel (b), sand (c), micaceous residue (d) and a fine product (e) for additional refining.

wastes such as the micaceous residue are not valorized. These wastes are transported via pipelines for storage under water to prevent wind dispersal in mica lagoons or mica dams. The dams are not homogeneous and comprise layers which contribute to the stability of the structure. In a normal circumstance the backfilled areas have layers of micaceous residue, clay and sand. Most of the tailing dams were fed with material from different pits covering distinct granite type. The major tailing dams of the St Austell area are (for location of the tailing dams see Figure 1.6):

- Kernick dam, backfilled by micaceous residue from Western Area biotite granite as well as lithium-micas and tourmaline granite (Scott and Bristow, 2002),
- Dubbers, an active china clay waste disposal currently fed by micaceous residue,
- Maggi Pie dam, an historic dam, now de-watered which was mostly fed by material from Western Area biotite granite,
- Innis Moor and West Carclaze, backfilled by micaceous residue from historic workings of Carclaze, Goonbarrow and Rocks pits,
- Great Treverbyn, a historic tailing dam backfilled by micaceous residue from Western Area biotite granite located adjacent to Carclaze Pit.

## 1.4 Literature review

### 1.4.1 CRMs (LREE, Nb-Ta, W) and Sn as by-products

A by-product is by definition, a secondary or additional product (usually a metal) which is secondarily recovered in an industrial extraction process, in addition to a primary product. This notion is independent of the respective selling prices of the main products and by-products.

*LREE*

REEs are recovered as a co-products/by-products of certain other minerals in many mining operations (Kumari et al., 2015). The only active mine in the western world operated exclusively for the recovery of rare earths is the Mountain Pass (United States) deposit, where bastnäsite is the main REE-mineral (Chen, 2011). However there is a possibility of recovering REE as a primary product in at least three deposits in Australia, especially Mt. Weld and to a lesser extent Yangibana, and John Galt deposits (Chen, 2011; Gupta and Krishnamurthy, 2004; Kingsnorth, 2014a).

Apart from these few examples the commercial mine production of REE is feasible in most cases only as a by-product of some other mineral commodity. For instance in 2009 about 49% of the Total Rare Earths Oxides (TREO) production were ensured by by-products (Table 1.4). This is due to the fact that most of REE occurrences are considered as low grade ores and thus the extraction of REE alone is not economical and cannot support entirely the mining and production costs involved in such an operation (Golev et al., 2014). However, when rare earths are recovered as a by-product, the recovery and sale of rare earths is not a necessary condition for making the recovery

and the sale of the main product economically viable (Gupta and Krishnamurthy, 2004).

For instance in placer deposits or beach sands, REE minerals occurs as a minor phase while the major minerals are ilmenite, rutile, zircon, and quartz. In these deposits, the REE minerals have been invariably recovered as a by-product of ilmenite in most of the cases, cassiterite in southeast Asia, and in some cases as a by-product of placer gold (Gupta and Krishnamurthy, 2004). Other examples are recovery of REE as by-product of uranium extraction at Denison Mines (Canada) or (formerly) as by-product of iron ore mining at Bayan Oba (China) (Gupta and Krishnamurthy, 2004). For other examples of by-product production of REE, see Table 1.4.

Table 1.4: Production of rare earth elements as by-product in 2009. Adapted after Long et al. (2010); US Geological Survey (2010).

| Country | Deposit | TREO Production (metric tons) | | Primary product | By-product |
|---|---|---|---|---|---|
| Brazil | Buena Norte | 650 | | Ilmenite | Monazite |
| China | Bayan Obo | 55 000 | | Iron ore | Bastnäsite |
| India | Heavy mineral sands | 2 700 | | Ilmenite | Monazite |
| Malaysia | Ipoh sand plant | 380 | | Cassiterite | Xenotime |
| Russia | Lovozero | 2 500 | | Loparite | REE chloride |
| Total | | 61 230 | (49%) | | |
| World total | | 124 000 | (100%) | | |
| Difference | | 62 770 | (51%) | | |

*Nb-Ta*

Niobium and tantalum mineral concentrates can be produced as by-products of mining operations worldwide, but the majority of the world's niobium concentrate is produced as primary concentrates by three mines in Araxá and Catalão (Brazil) and Niobec or St. Honoré mine (Canada) whereas the mines in the Congo geographic area (Burundi, Congo, and Rwanda), account for about 53% of world's tantalum production (US Geological Survey, 2015).

However niobium and tantalum can also be extracted as a by-product of tin smelter waste that arises from the smelting of cassiterite ore concentrates, *i.e.* tin slags (Fields and Bally, 1967). More than 56% of the western supply of niobium-tantalum came as a by-products from tin smelting from cassiterite in Thailand and Malaysia (Suri et al., 1992). But more recent data reported by the Tantalum-Niobium International Study Center suggest that this proportion tends to be much lower for tantalum, around 20% of total global production (Tantalum-Niobium International Study Center, 2013), see Table 1.5. Proportion of niobium produced in this way is far less significant as it accounts for less than 2% of total global niobium production (Shaw and Goodenough, 2011). Some tin smelter waste contains 8 to 10% $Ta_2O_5$, although exceptionally this may rise to 30% (Shaw and Goodenough, 2011). Low-grade smelter wastes can be upgraded by electrothermic reduction, yielding a synthetic concentrate with up to 50% tantalum and niobium oxides (Roethe, 1989). Tantalum is also recovered as by-product of cassiterite in the middlings of some placer deposits using shaking tables, and mag-

netic/electrostatic separation methods (Shaw and Goodenough, 2011; Bose and Gupta, 2002).

Table 1.5: Proportions of each sources for the global tantalum supply in 2008 and 2012 (Tantalum-Niobium International Study Center, 2013).

| Source | Percentage of world production (%) | |
|---|---|---|
| | 2008 | 2012 |
| **Primary concentrates** | 60 | 40 |
| **Secondary concentrates** | 10 | 10 |
| **By-product (tin slags)** | 10 | 20 |
| **Recycling, synthetic concentrates** | 20 | 30 |

*Sn-W*

There are many occurrences of Sn-W mineralisations, especially in the Variscan belt (see Figure 1.5) such as the Panasqueira, Borralha and Montesinho Sn-W deposits in Spain or the tin deposits of the Cornubian orefield such as Camborne, Redruth, Saint-Just, deposits (Jébrak and Marcoux, 2008). In these deposits tungsten and tin have often been mined as co-/by-products. For instance, there are many deposits in the Cornubian orefield where tungsten has been extracted as a by-product of tin and copper mining (Scrivener et al., 1997). In some mines tin and tungsten are by-product of other metals, including zinc, silver and tantalum but this only represent a small share of world tin and tungsten production.

However one atypical example where CRMs are produced as a by-product, is the Beauvoir-Echassières kaolin deposit (Massif Central, France) which is known to produce cassiterite (800 g/t Sn) and columbite (190 g/t Ta plus 120 g/t Nb) as by-product of kaolin production (Pohl, 2011). This deposit is of primary importance for this work as it displays similarities with the St Austell mineralisations (see Section 1.2.3) and Sn by-product recovery operations at the Beauvoir-Echassières kaolin deposit will be further discussed in Section 1.4.4.1.

### 1.4.2 CRM-bearing minerals processing overview

The CRM-bearing minerals are numerous for the CRMs of interest, *i.e.* LREE, Nb-Ta, W and Sn. However in the following section focus will be made on the major potential CRM-bearing minerals occurring within the St Austell area. Table 1.6 lists the major potential CRM-bearing minerals within the St Austell rare-metal granite reported in the literature, and their main physico-chemical properties, including chemical formulas, specific gravities (*i.e.* density), magnetic properties and CRM contents (when data is available). As it can be seen, the overall densities of the potential CRM-bearing minerals are relatively high ($>3\ g.cm^{-3}$) in comparison with densities of typical gangue minerals from granitic rocks which are usually around 2.6 $g.cm^{-3}$. This shared property is one of the most fundamental characteristic of the CRM-bearing minerals as it allows their common separation by gravity concentration techniques. However the magnetic properties differ from one mineral to another which gives potential insights to separate these minerals.

Table 1.6: List of potential CRM-bearing minerals of the St Austell granite and their physical properties (Anthony et al., 2001; Long et al., 2010; Rosenblum and Brownfield, 1999). Chemical data for Nb-Ta minerals from (Scott et al., 1998) and for Sn-W rutile from (Müller and Halls, 2005). Most important CRM-bearing minerals are highlighted in bold.

| **Mineral** | **Chemical formula** | **Density** ($g.cm^{-3}$) | **Magnetic properties** | **CRMs content (wt.%)** | | | | |
|---|---|---|---|---|---|---|---|---|
| | | | | REO | $SnO_2$ | $Nb_2O_5$ | $Ta_2O_5$ | $WO_3$ |
| *Rare Earth Elements* | | | | | | | | |
| Apatite | $(Ca,Ce)_5(PO4)_3F$ | 3.10-3.25 | n/a | 0-21 | - | - | - | - |
| **Monazite** | $(Ce,La,Nd,Th)PO_4$ | 4.98-5.43 | Paramagnetic | 35-71 | - | - | - | - |
| Xenotime | $YPO_4$ | 4.40-5.10 | Paramagnetic | 52-67 | - | - | - | - |
| Sphene (titanite) | $(Ca,REE)TiSiO_5$ | 3.48-3.60 | Paramagnetic | <3 | - | - | - | - |
| Zircon | $(Zr,Hf,REE)SiO_4$ | 4.60-4.70 | Diamagnetic | 4.41 | - | - | - | - |
| *Tin* | | | | | | | | |
| **Cassiterite** | $SnO_2$ | 6.80-7.10 | Diamagnetic | - | 99-100 | tr | tr | tr |
| *Niobium-tantalum* | | | | | | | | |
| **Columbite-tantalite** | $(Fe,Mn)(Nb,Ta)_2O_6$ | 5.17-6.65 | Paramagnetic | - | - | 28-71 | 6-60 | - |
| Nb-Ta-rutile | $(Ti,Nb,Ta,Fe)O_2$ | 4.23[1,2] | Dia/Paramagnetic[1] | - | - | 7-24 | 4-19 | - |
| *Tungsten* | | | | | | | | |
| **Wolframite** | $(Fe,Mn)WO_4$ | 7.1-7.5 | Paramagnetic | - | - | - | - | 60.63 |
| *Tin-tungsten-niobium* | | | | | | | | |
| Sn-W-Nb-Rutile | $(Ti,Nb,Sn,W,Fe)O_2$ | n/a | n/a | n/a | 0.6-24 | 10-30 | n/a | 0.6-25 |

[1] Depending on chemistry

[2] Increase with Nb-Ta content

The highlighted minerals in Table 1.6, monazite (LREE), cassiterite (Sn), columbite-tantalite (Nb-Ta) and wolframite (W) correspond to the most important CRM-bearing minerals within the St Austell granite described in the literature (Manning and Hill, 1990; Manning et al., 1996; Scott et al., 1998; Shail et al., 2009) and also to the most commonly extracted CRM-bearing minerals (Angadi et al., 2015; Bulatovic, 2010; Jordens et al., 2013).

#### 1.4.2.1 Monazite processing

The most important deposits for monazite extraction are the beach sands and placer deposits in which monazite occurs as the minor constituent while major minerals are quartz, rutile, ilmenite and zircon. For these deposits, typical processing flowsheets of the REE-bearing minerals like monazite usually start by physical beneficiation techniques which are used to obtain primary concentrates removing up to 90% of the gangue minerals (Kumari et al., 2015). Physical separation is performed by high-capacity gravity separation steps, to take advantage of the high specific gravity of monazite (between 4.98-5.43) while the typical gangue minerals in these deposits have specific gravities less than 3.5 (Jordens et al., 2013). This step is followed by additional gravity, magnetic, electrostatic and occasionally flotation separation steps (Ferron et al., 1991; Houot, 1982). An example of physical beneficiation of REE placer deposits is presented in Figure 1.11. After obtaining a heavy mineral concentrate by multi-stages gravity concentration, the heavy minerals are separated using a combination of magnetic and electrostatic separation. Monazite is non-conductive and can be

separated with zircon by electrostatic separation from the others heavy minerals found in placer deposits, like ilmenite or rutile (Walters and Lusty, 2011). Zircon is then eliminated by electromagnetic or further gravity processing as it as slightly higher magnetic susceptibility and specific gravity than monazite. Separation of monazite from xenotime is more complex as the two minerals have similar magnetic properties and specific gravities. The separation of monazite and xenotime has been investigated by magnetic separation (Ito et al., 1991) or flotation (Cheng et al., 1993; Pavez et al., 1996; Sorensen and Lundgaard, 1966; Pavez and Peres, 1994) and precise gravity methods like air or wet tables may also be used (Walters and Lusty, 2011).

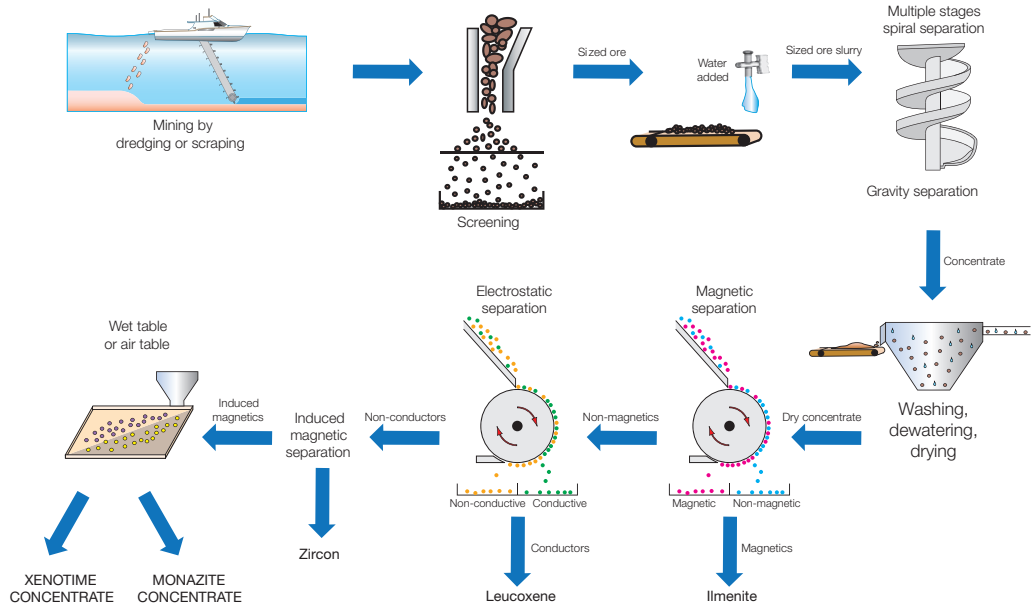


Figure 1.11: Simplified flowsheet for the extraction of monazite and xenotime from placer deposits (Walters and Lusty, 2011).

Chemical beneficiation or chemical processing of the concentrate obtained after physical beneficiation usually involves hydrometallurgical and sometimes pyrometallurgical operations, including leaching, solvent extraction, precipitation etc. (Gupta and Krishnamurthy, 2004; Kumari et al., 2015; Zhu et al., 2015). These chemical beneficiation steps by hydrometallurgy techniques are unavoidable as there is a need for applying hydrometallurgical separation processes for isolating rare earths from one another (Gupta and Krishnamurthy, 2004).

#### 1.4.2.2 Cassiterite processing

Cassiterite is the main tin mineral present in the earth crust followed by stannite, kesterite, mawsonite, and other tin sulphides (Angadi et al., 2015) and is also the major ore-mineral for tin recovery (Wills and Napier-Munn, 2005). The importance of mineralogy, texture and mineralogical associations in the beneficiation of tin ores is well known and have been reported in many reference articles (Angadi et al., 2015; Holl and Bromley, 1988; Veasey et al., 1989). These characteristics often depend on the origin of the cassiterite mineralisation. The two main types of economic deposits of cassiterite are primary deposits of veins/hard-rock mineralisations and secondary placer deposits (Jébrak and Marcoux, 2008). Hence different processing route are employed depending

on the deposit type. In placer deposits cassiterite occurs in a liberated state, thus comminution is not required for the beneficiation whereas deposits veins/hard-rock requires fine grinding to liberate mineral values from the host rock which lead to the formation of ultrafine particles which are difficult to process (Angadi et al., 2015).

Removal of an important proportion of gangue minerals prior to ore beneficiation is often employed in cassiterite beneficiation. Pre-concentration of tin is mainly performed by a combination of ore-cleaning and gravity pre-concentration steps to remove the clay and gangue minerals and to obtain a primary cassiterite concentrate, taking advantage of its high specific gravity (between 6.8-7.1), its chemical stability and resistance to abrasion (Angadi et al., 2015; Falcon, 1982). The obtained primary concentrates have varying tin grades depending on the deposit and the mineralogy of the heavy minerals in the ore but most of the time the primary concentrate grades are around 15 to 30% Sn (De Cuyper and Delwasse, 1999). The up-gradation circuit configuration depends on the type and nature of gangue minerals associated with cassiterite.

For alluvial tin, residual gangue minerals in the primary concentrates are removed by further gravity concentrations using jigs for the coarser fractions and spirals, Reichert cones or shaking tables for the finer fractions. The heavy mineral concentrate is then cleaned by magnetic separation to remove iron oxides, ilmenite, wolframite or columbite-tantalite in the magnetic fraction. The non-magnetic fraction is then treated by electrostatic separation to concentrate the cassiterite in the conductive fraction which could be ultimately processed by high intensity magnetic separation to remove paramagnetic minerals which have not been removed during the previous steps because of the presence of Nb-Ta and Fe inclusions. The resulting cassiterite concentrate can reach grades up to 75% Sn (De Cuyper and Delwasse, 1999).

The beneficiation of veins/hard-rock deposits cassiterite is much more complex as the ore contains also sulphide minerals which have also high specific gravities. Some of these sulphides can be removed by magnetic separation but most of the time sulphide mineral are recovered in the non-magnetic fraction. In this case film flotation of sulphide minerals is used prior to concentration of cassiterite by gravity concentration, hydraulic classification and flotation (Angadi et al., 2015).

One other complex aspect of the beneficiation of such tin ores is the treatment of fine particles. Indeed classical gravity concentrators (spirals, shaking tables) are used to recover cassiterite particles down to 30 $\mu$m, particle size below-which cassiterite cannot be recovered by classical gravity concentration techniques (Angadi et al., 2015). According to Lepetic (1987), these correspond to a considerable loss of about 30 to 40% of cassiterite in the gravity tails. Since then, many developments have allowed to decrease the lower size efficiency or gravity concentration devices using enhanced gravity or more recently centrifugal concentrators (Bo et al., 2011; Burt, 1984a). The fine fractions are then treated by fine-particle gravity separators but in many cases direct flotation of cassiterite is preferred using specific collectors (Angadi et al., 2015; De Cuyper and Delwasse, 1999).

The obtained cassiterite concentrate are then treated by pyrometallurgy using conventional smelting including reduction with coke or coal at between 1150 and 1300 °C to produce metal and slag (Rankin, 1986). A detailed description of tin pyrometallurgical processes and its numerous variations can be find in the reference book by Wright (Wright, 1982).

#### 1.4.2.3 Columbite-tantalite processing

Because niobium and tantalum have similar chemical properties, they often replace each other, and occurs almost exclusively as Nb-Ta oxides (Bose and Gupta, 2002; Rockenbauer, 1984). Niobium and tantalum occurs conjointly in many deposits within two main ore mineral groups which are the columbite-tantalite, occurring in granite pegmatites associated with cassiterite, wolframite, tourmaline, feldspar and quartz, and the pyrochlore group, occurring in pegmatites associated with zircon and apatite (Bulatovic, 2010; Wills and Napier-Munn, 2005).

In actual practice, there are three basic beneficiation methods of niobium-tantalum ores, which are physical pre-concentration, combination of physical pre-concentration and flotation or direct flotation (Bulatovic, 2010). However the two last methods are mainly employed for the beneficiation of pyrochlore group minerals which can be recovered by flotation (Gibson et al., 2015).

Typical beneficiation routes start with crushing, milling and screening operations to liberate the niobium-tantalum minerals (Shaw and Goodenough, 2011). The main method used for beneficiation of columbite-tantalite ores is gravity pre-concentration on the different sized-fractions, to take advantage of the high specific gravity of columbite-tantalite (between 5.17-6.65) while gangue minerals have generally lower specific gravity (Bulatovic, 2010). Figure 1.12 present a typical flowsheet used for gravity pre-concentration of Nb-Ta ores, similar to those used at Greenbushes (Australia) and Bernic Lake (Canada) operations (Bulatovic, 2010; Fetherston, 2004). These gravity pre-concentrations stages are usually performed by spiral concentrators, jigs and shaking tables. However, fine particles are also a significant source of losses for Nb-Ta ore gravity processing. Most of the losses in the gravity tailings, around 36% Ta and 50% Nb, occurred in the fine -200 mesh fraction and cyclone slimes at Greenbushes (Bulatovic, 2010; Fetherston, 2004) while around 32% Ta and 53% Nb are lost in the gravity tailings at Bernic Lake, mainly because of the -30 $\mu$m tantalum (Bulatovic, 2010; Burt et al., 1995). In such cases centrifugal concentrators can be used such as Falcon concentrators at Wodgina (Australia) operations (Fetherston, 2004) or Bartles-Mozley Separators (BMS) and Crossbelt Concentrators at Bernic Lake (Burt et al., 1995) to reduce tantalum and niobium losses. According to Bulatovic (2010), direct flotation of tantalum ores is not a common practice in operating plants. However some plants have successfully tested the use of flotation to recover tantalum from the gravity tailings, including the aforementioned Bernic Lac and Greenbushes operations (Bulatovic, 2010; Fetherston, 2004). The primary concentrate at Greenbushes is upgraded by further wet or dry gravity separation followed by high intensity magnetic separation to recover paramagnetic columbite-tantalite. The magnetic fraction is then concentrated by roasting to reach around 30% $Ta_2O_5$ (Fetherston, 2004).

The extraction and separation of niobium and tantalum is performed by hydrometallurgical and pyrometallurgical processes. The separation of tantalum from niobium formerly performed by fractional crystallization (Rockenbauer, 1984) is now largely performed in chemical and metallurgical industries by solvent extraction from fluoride-containing solutions (Ayanda and Adekola, 2011; Bose and Gupta, 2002). Final reduction of Nb and oxide is performed by aluminothermic reaction to form niobium metal (Ayanda and Adekola, 2011) whereas Ta oxide is reduced by reaction with sodium or by electrolysis in the molten state, to form tantalum metal powder (Bose and Gupta, 2002; Fetherston, 2004).

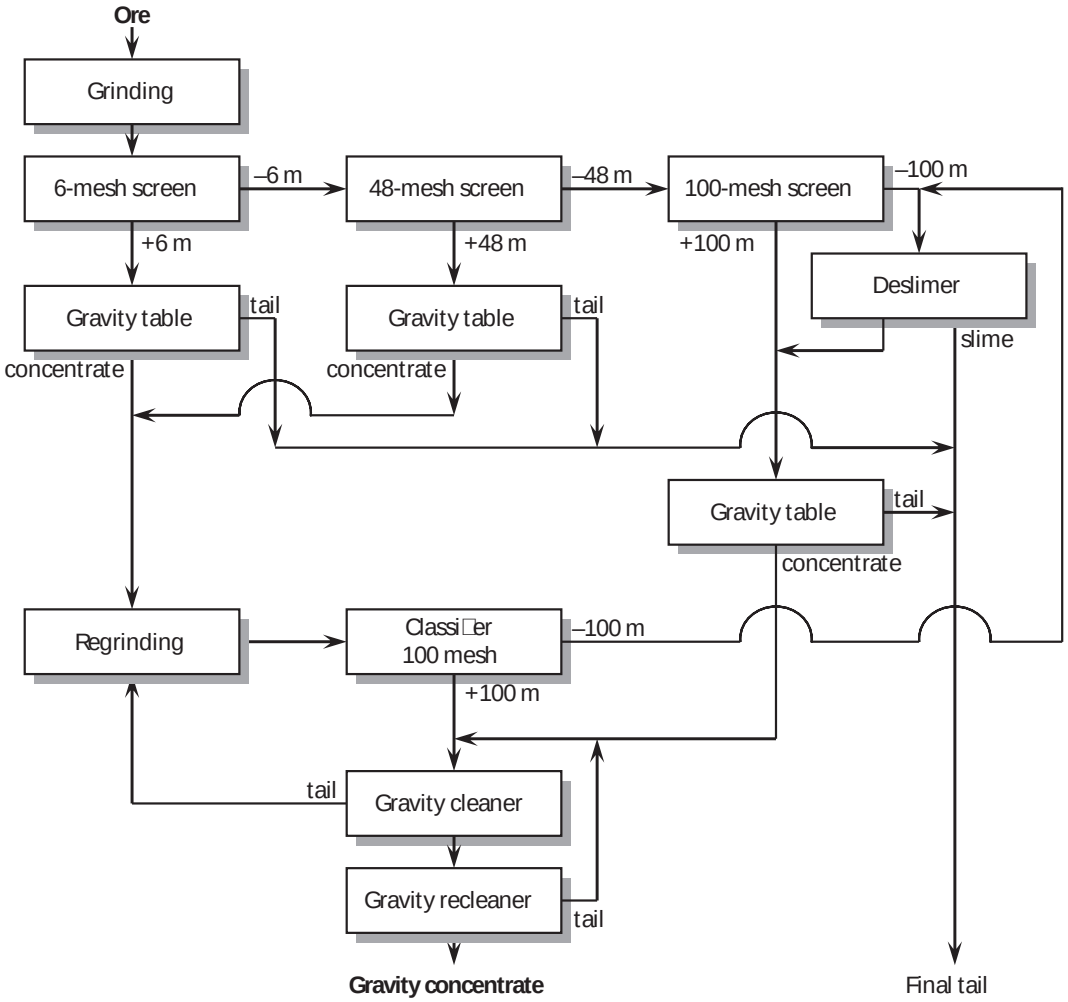


Figure 1.12: Generalised Nb-Ta minerals gravity concentration flowsheet (Bulatovic, 2010).

#### 1.4.2.4 Wolframite processing

Wolframite constitutes, in roughly equal importance with scheelite, the major tungsten mineral that are exploited for tungsten recovery. Beneficiation of tungsten has been limited, until the late 1980s, to classical gravity concentration techniques, followed by cleaning of the concentrates to achieve marketable concentrate grades, usually above 65% $WO_3$ (Burt, 1984c). However with increasing complexity of the exploited tungsten ores, new high capacity gravity concentration devices have been introduced and a variety of processes have been developed for the re-treatment of finer fractions, including flotation (Burt, 1984c).

The tungsten ore processing usually starts by crushing in jaw, cone or impact crushers and milling in rod or ball mills working in closed circuits with vibratory screens and classifiers to liberate the tungsten mineral grains (Pitfield and Brown, 2011). Various pre-concentration processes are then employed with the objective of rejecting the bulk of the low grade wastes. The ore treatment usually starts by sorting techniques usually applied to run-of-mine streams to reduce the amount of material that must be processed. Photometric automated sorting and UV Fluorescence sorting (scheelite only) associated with air blast separation have greatly impact the economics of tungsten processing (Lessard et al., 2014), even if hand sorting is still quite common in devel-

oping countries (Burt, 1984c). Gravity concentration techniques can also be-employed at the pre-concentration steps, such as heavy medium separation and jigging. As for the CRMs, tungsten gravity processing faces the problem of fine particles processing. Literature on tungsten processing in India indicates that more than 40% of tungsten values are being lost during beneficiation as slimes (Jakhu and Ray, 1996; Rao and Satynarayana, 1987). These losses can be reduced by the introduction of fine gravity concentrator or high intensity magnetic separation devices and froth flotation, shear flocculation and spherical agglomeration in the ultrafine size range (Pradip, 1996).

The primary tungsten concentrate is then treated in a concentration process by various large capacity gravity concentration devices including banks of spiral concentrators or Reichert cones followed by lower capacity gravity concentration methods (shaking tables, fine gravity concentrators). Additional treatment can include several other methods such as froth flotation, magnetic and electrostatic separation, depending upon the characteristics of the ore (Pitfield and Brown, 2011). The resulting concentrate containing more than 65% $WO_3$ can then either be used directly for production of ferrotungsten and steel manufacture, converted to a number of intermediate tungsten compounds by hydrometallurgical processes or further refined to pure tungsten using additional pyrometallurgical techniques (Pitfield and Brown, 2011).

A summary of the generic processing steps for the aforementioned CRMs is presented in Figure 1.13. The overall pre-concentration stages of these CRMs are similar and mainly relies on physical separation or physico-chemical separation techniques. The most common separation techniques used in the pre-concentration steps are gravity concentration techniques which are used at the beginning of the beneficiation process for the vast majority of CRMs benefaction routes.

### 1.4.3 Gravity concentration

Gravity concentration is the separation of one or more minerals from others based on their difference in density, by relative movement in response to the force of gravity and other forces (Burt, 2000). Gravity concentration is one of the oldest forms of mineral processing in the industrial history. Until the late $19^{th}$ century, these techniques ruled the world extractive industry but due to the arrival of more selective methods involving chemical or physicochemical properties (*i.e.* flotation and hydrometallurgy), the interest in gravity concentration declined (Burt, 1999). However, the complexity, cost and the difficulties associated with methods involving chemical or physicochemical properties such as pollution or environmental issues, contrasts with the relative simplicity, low processing costs, environmental friendly operation (no reagents) and other benefits (treatment of coarse particles, high capacity units) of gravity concentration (Richards et al., 2000).

Indeed, in the treatment of some metallic minerals, and in particular the ones of interest in this study, like cassiterite, wolframite, columbite-tantalite or monazite, gravity concentration remains as the only, or at least the primary, means of concentration (Burt, 1999). Even when flotation is employed, generally for the treatment of the ultrafine fractions, it is common to combine gravity concentration to flotation to clean-up the concentrate, as for the former Wheal Jane tin plant in Cornwall (Turner and Hallewell, 1993) or the Bernic Lake tantalum operations in Canada (Burt et al., 1995).

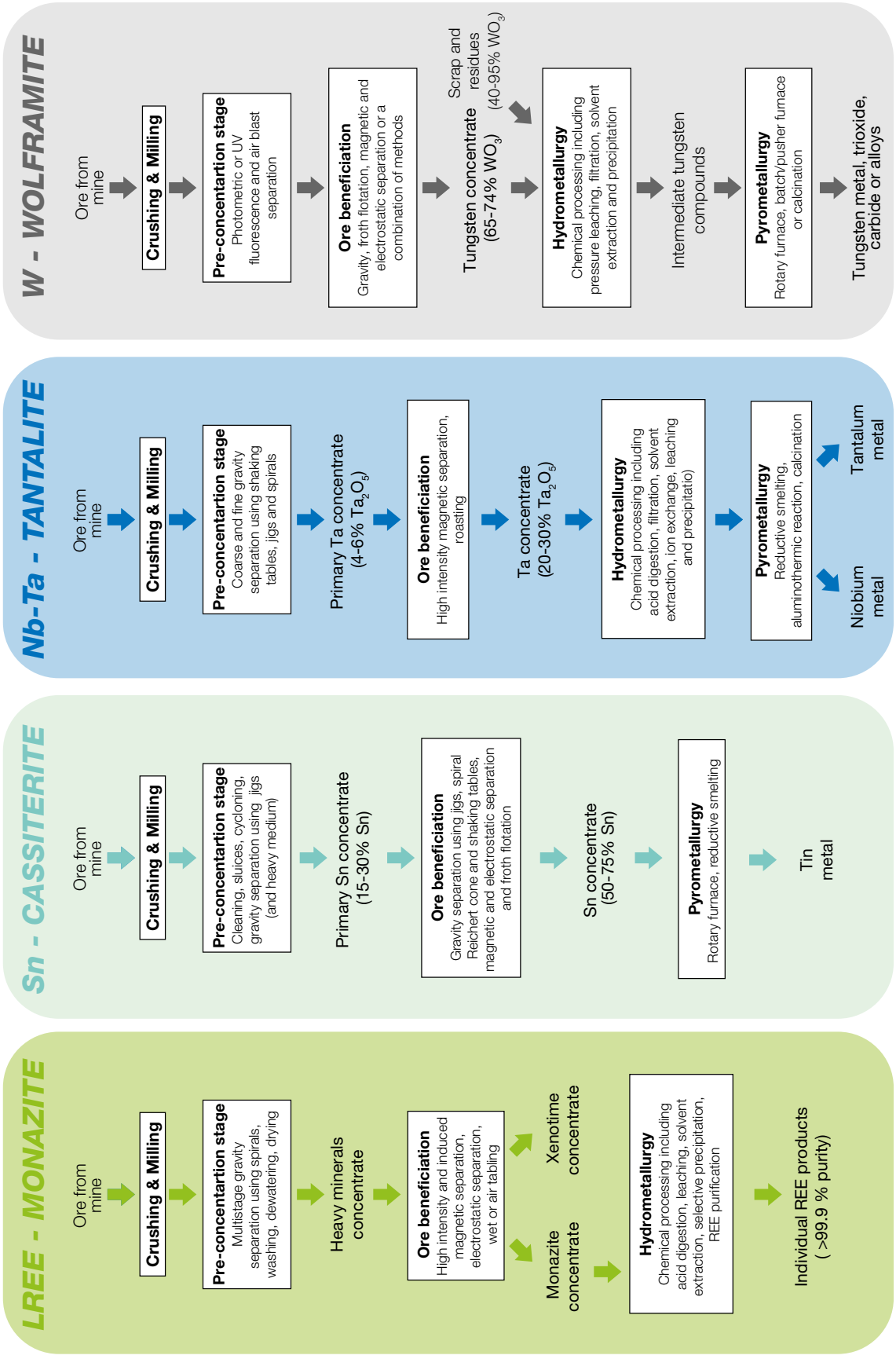


Figure 1.13: Simplified flowsheets illustrating the generic steps of CRMs processing. Adapted from (Walters and Lusty, 2011; De Cuyper and Delwasse, 1999; Pitfield and Brown, 2011; Shaw and Goodenough, 2011).

#### 1.4.3.1 Principle

Gravity concentration is effected by the relative movement of minerals of different density in response to gravity and one or more other forces, which often include the resistance to motion offered by a viscous fluid (Burt, 1984b). Thus the working principle is induced by different force field environment that characterise the gravity concentrators. Burt (1984b) classified gravity concentrators, based on these characteristics, into 4 main categories:

- **Density:** This mechanism uses a viscous fluid with a density, or apparent density, between that of the minerals to be separated. Thus, part of the particles (usually gangue minerals) has a net positive buoyancy and floats, whereas the dense particles (usually the target minerals) have a net negative buoyancy and sinks. This classification includes dense medium separation devices (static and dynamic) and magnetohydrostatic separation.

- **Stratification:** The separation of particles is imparted due to pulsation and suction offered by the fluid in a vertical plane which stratified the various particles constituents. This classification is represented by the jigs family, which include a large range of devices, the more recent being the inline pressure jigs.

- **Flowing film:** The particles constituents are separated by their relative movement through a slurry stream, which flows down a plane by the action of gravity on which a centrifugal force can be superimposed to ad lateral movement. This classification is represented by the sluice, pinched sluice, Reichert cone and spiral, the latter being the most represented in the mineral processing industry.

- **Shaking:** The particles components are separated by superimposing a horizontal shear force on the flowing film. This force can be oscillating, as in a shaking table, or orbital, as in the Bartles-Mozley Separator (BMS) or Crossbelt concentrator.

Centrifugal separators can be seen as a ramification of the flowing film category which employs centrifugal force to enhance the relative settling velocities of particles components. It enhances the intensity of the above mechanisms but it is not a different mechanism in itself (Burt, 1999). This separation method is especially designed for the treatment of fine particles. This classification is mainly represented by the Knelson and Falcon concentrators as well as the Kelsey Jig and Multi Gravity Separator (MGS). The two latter devices actually use one additional separation mechanism, *i.e.* stratification for the Kelsey jig and shaking for the MGS.

A simplified representation of the gravity separation classification is shown in Figure 1.14. In all the aforementioned devices water is used as the separation media but some dry gravity concentration devices also exist, using air as the separating media. A detailed description of separation mechanisms involved in gravity concentration is presented in the reference textbook by Burt (Burt, 1984b).

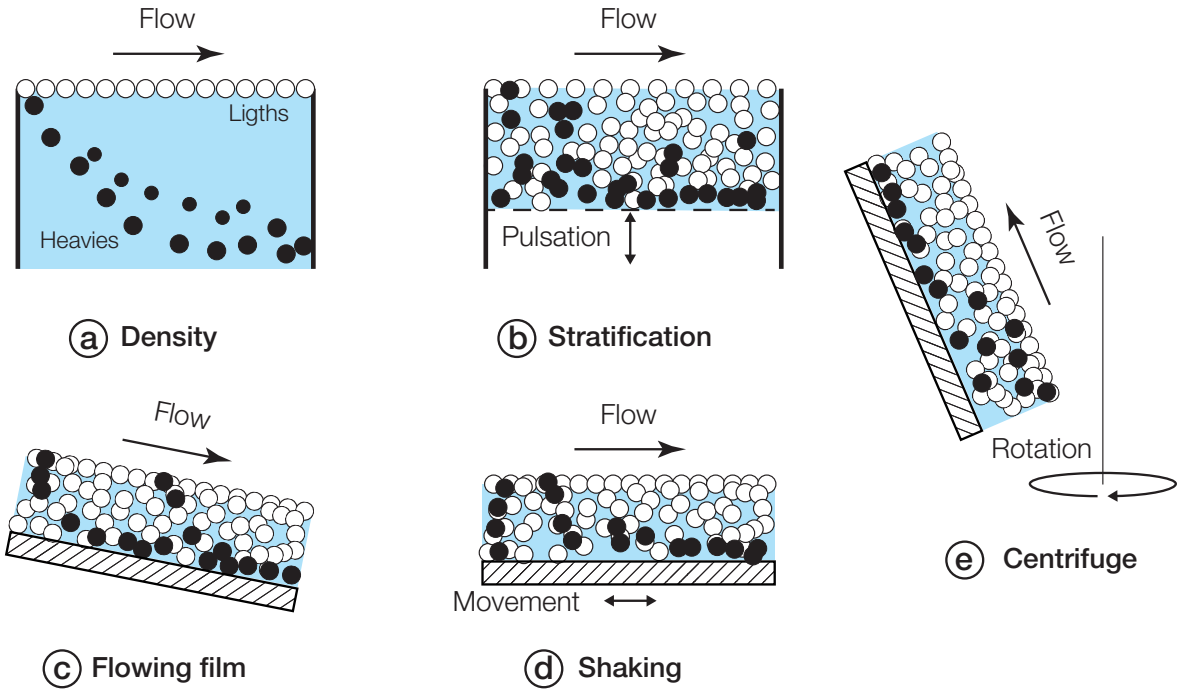


Figure 1.14: The major classifications of gravity concentration methods, adapted after Burt (1984b). (a) Density, (b) Stratification, (c) Flowing film, (d) Shaking and (e) Centrifuge.

#### 1.4.3.2 The unit processes of gravity concentration/choice of equipment

There is a wide variety of gravity concentration equipment available. The choice of the equipment is determined by several factors, including the duty required (roughing, scavenging, cleaning), the desired throughput and efficiency, the unit cost (capital and operating) and the size range of the particles to be separated, the latter being one of the most restrictive (Burt, 2000).

This limitation is illustrated by the overall decreasing efficiency of gravity concentration techniques as the ore particle sizes decrease. However the overall size range handled by gravity concentration is much larger than any other concentration process, ranging from 500 mm to about 6 µm (Burt, 1984b). Nonetheless no gravity concentration equipment can handle the entire size range amenable to gravity concentration. Figure 1.15 presents the working particle size range of common gravity concentration equipments.

The effective gravity equipments range from the heavy media for the coarsest particle sizes to the centrifugal equipments for the ultrafine particles. Most of the gravity concentration devices are effective on the 0.1-1 mm particle size range, the choice then depends on the relative efficiency and other characteristics of these devices for the separation required. Jigs and sluices are capable of treating a fairly wide range of sizes, but some loss of efficiency occurs at the top, bottom, and middle of the size range whereas other equipments (BMS, Crossbelt, MGS, Falcon, Spiral, Table etc.) operate significantly better on sized or classified feed (Burt, 2000). Therefore the design of the treatment circuit will be completely different depending on the type of device. The first ones (jig, sluices) are usually used in series circuit to treat unsized feed whereas the other ones are operated in parallel circuits to treat sized feed.

Other factors are critical for the choice of the gravity equipment. The capacity,

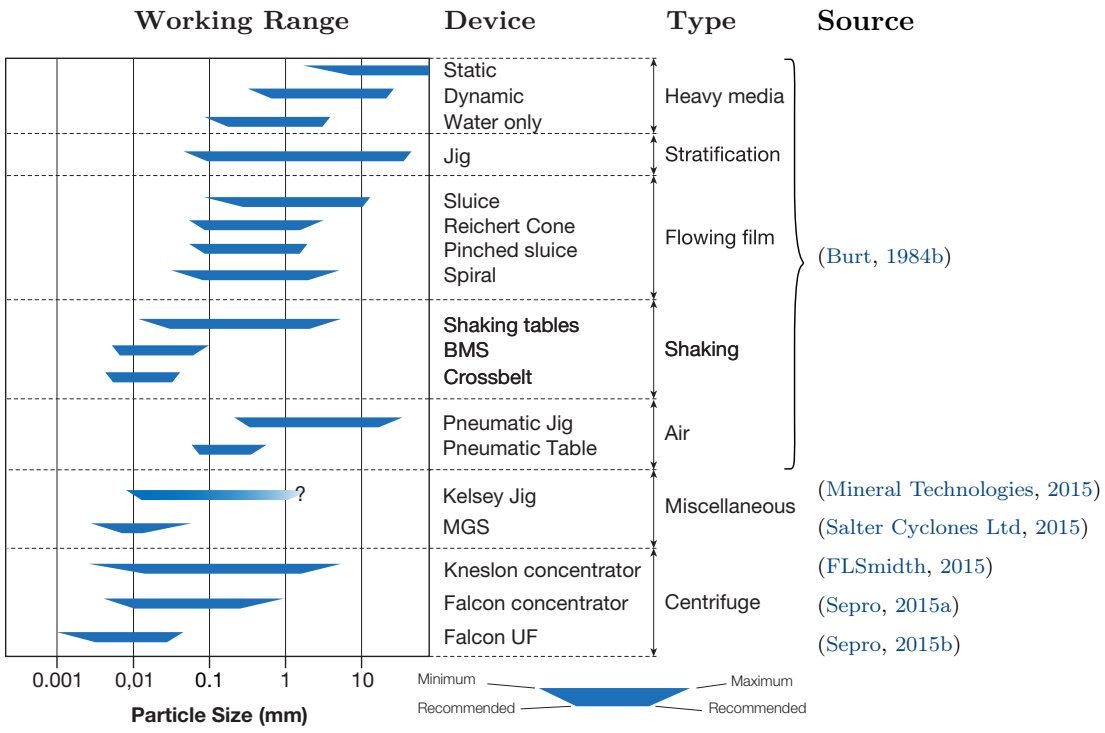


Figure 1.15: Working particle size range of gravity concentration equipments completed after Burt (1984b).

*i.e.* throughput, of gravity equipment is an important factor which will determine the position of the equipment along the treatment circuit. There is also a wide range of capacity for gravity concentration equipment ranging from few kilograms per hour to about 1000 tons per hour (Burt, 2000). The efficiency of a given equipment is case sensitive and thus difficult to predict. Indeed the efficiency of the separation will depend on the material treated, its mineralogy, size distribution, liberation state of the target minerals, and some operating factors which are not directly controllable such as feed flowrate or pulp solid density. Finally, the equipment cost should be taken into account, but due to the varying inflation, exchange rates and other factors that depend on the economic situation, it could only be determined at the time of requirement. However, given the relative small number of manufacturers listed in the Buyer's Guide of the Mining Magazine that produce gravity concentration devices (Mining Magazine, 2014) and the relatively low cost of gravity concentration equipments in comparison with other techniques, the equipment's amenability to treat the material and its relative efficiency are generally more important factors.

Table 1.7 compares the characteristics of various gravity concentration equipments, including the feed size range, the dry and slurry capacity, energy and process water consumption as well as the main uses and current manufacturers when data is available.

Table 1.7: Comparison between operating size range, capacity, energy and water consumption of various gravity concentration devices with current official manufacturers listed in Mining Magazine (2014). Abbreviations: bar: barites, dmd: diamonds, flr: fluorspar, gp: gypsum, grt: garnet, ky: kyanite, mgs: magnesite, scp: scrap recycling, slg: slag, WEEE: Waste Electrical and Electronic Equipment.

| Device | Feed size | | Solid capacity | Slurry capacity | Solid ratio | Power | Water | Main uses | Current Manufactures | Source |
|---|---|---|---|---|---|---|---|---|---|---|
| | ($\mu m$) | ($mm$) | ($t/h$) | ($m^3/h$) | ($wt.\%$) | ($kW$) | ($m^3/h$) | In order of importance | | Literature and manufacturers |
| *Heavy media* | | | | | | | | | | |
| Static | 3000 | 250 | 900 | | | None | | Coal, gp, mgs, flr, Fe, Cr, Pb, Zn, Ag, U | FLSmidth, Parnaby Cyclones, Gekko | (Burt, 1984b, 2000) |
| Dynamic | 500 | 100 | 10-230 | | | | | Coal, dmd, Sn, Pb, Zn, W, Ni, Cr, etc. | Sepro Mineral Systems Corp | (Burt, 1984b, 2000; Sepro, 2015c) |
| Water | 100 | 50 | | | | | | | | (Burt, 1984b, 2000) |
| *Stratification* | | | | | | | | | | |
| Jig | 50-100 | 200 | 5-1000 | | 30-50 | | | Fe, Sn, Mn, Fe slg, bar | FLSmidth, Allmineral GmbH, MBE C&M Tech., Tenova | (Burt, 1984b, 2000) |
| IL Pressure Jig | 60 | 6-25 | 3-100 | 9-200 | 60-75 | 1.5-4 | 0.4-100 | Au, dmd, Ag, Zn-Pb-Cu,W, Sn, Ta, Mn | Gekko Systems | (Gekko, 2015) |
| *Flowing Film* | | | | | | | | | | |
| Sluice | 100 | 10 | 500 | | 0.5-4 | None | | Au, Sn | | (Burt, 1984b, 2000) |
| Reichert Cone | 40 | 2-3 | 70-300 | | 60-70 | None | | Fe, W, Sn, Au, Cu, Zr | | (Burt, 1984b, 2000) |
| Pinched sluice | 70 | 1.5-2 | 3-6 | | 60-65 | None | | Sn, Mineral sands | | (Burt, 1984b, 2000) |
| Spiral | 40 | 1.5-2 | 1-12 | 6 | 35-50 | None | 0-1.5 | Fe, coal, Ti, Zr, Cr, Mn,Sn, Ta, W, Au,Cu, grt, ky | Mineral Tech., Outotec, Multotec, AKW Apparate & Verfahren, Parnaby Cyclones | (Burt, 1984b, 2000) (Multotec, 2015; Outotec, 2015) |
| *Air* | | | | | | | | | | |
| Pneumatic jig | 200 | 50 | 20-100 | - | - | | None | Coal | Allmineral GmbH | (Burt, 1984b; Allminerall, 2015) |
| Pneumatic table | 70 | 0.7 | 6-8 | - | - | | None | Coal, Zr, Sn, Scp | Eriez Manufacturing Co. | (Burt, 1984b; Eriez, 2012) |
| *Shaking* | | | | | | | | | | |
| Shaking table | 40 | 2 | 0.45-5 (x2-3) | | 25 | 0.4-2.2 (x2) | 0.5-3.6 | Au, Sn, W, Cu, Cr, WEEE | Holman Wilfley Ltd., Deister Concentrator LLC, Mineral Technologies | (Deister, 2015) (Holman Wilfley Ltd., 2014) |
| BMS | 7 | 0.1 | 2-4 | | | | 0.35 | Sn, Ta, W | | (Sivamohan and Forssberg, 1985c) |
| Crossbelt | 5 | 0.07 | 0.3-0.5 | | 20 | | | Sn, Ta, Cr | | (Sivamohan and Forssberg, 1985c) |
| *Centrifuge* | | | | | | | | | | |
| Kelsey Jig | 10 | | 50 | | | | | Zr, Ti, Ta, W, Au, | Mineral Technologies | (Mineral Technologies, 2015) |
| MGS | 5 | 0.01 | 0.2-8 | | | 1-3.3 | | Sn, Cr, Cu, Zn, coal | Salter Cyclones Ltd. | (Salter Cyclones Ltd, 2015) |
| Knelson | 20 | 2-6 | 2-1000 | 4-1360 | 50-75 | 2-345 | | Au, Ag | FLSmidth | (FLSmidth, 2015) |
| Falcon | 10 | 1-2 | 1-400 | 30-450 | 40-70 | 3.7-75 | 3-35 | Au, Ag, Pt, Sn, coal | Sepro Mineral Systems Corp. | (Sepro, 2015a) |
| Falcon UF | <5 | 0.038 | 0.5-2 | 6-20 | 5-15 | 4.5-45 | None | Coal, Sn, Ta, W | Sepro Mineral Systems Corp. | (Sepro, 2015b) |

#### 1.4.3.3 Gravity processing of fine particles

Processing of fine particles by gravity concentration methods is one of the challenging problem of mineral processing (Singh et al., 1997; Sivamohan, 1990). In addition to the inherent difficulty of separating fine particles by gravity, fine particles also exhibit a large surface area which increases the pulp viscosity resulting in a decline of separation efficiency.

One of the most successful slimes gravity concentrators introduce in the early 70s were the Bartles Mozley Separator (BMS) and Bartles Crossbelt which superimpose, an orbital shear motion on a slightly inclined surface, and are capable of recoveries as fine as 6 µm (Burt, 2000). In the recent past, many new types of equipments have been designed with the intension to enhance gravitational force by integrating centrifugal action, the more popular of which are the MGS, Kelsey jig, Knelson, Falcon and Falcon UF concentrators. The efficiency of these gravity concentration devices have been compared in several studies (Burt, 1984b; Burt et al., 1995). Figure 1.16a shows the size-recovery relationship of various fine gravity concentrators treating fine liberated tin or tungsten ores. It can be observed that the continuous shear units and especially the orbital shear equipments (BMS and Crossbelt) recover finer material that the other units. However most of the particles recovered are in the 40-5 µm range and no equipment is able to recover particle finer than 5 µm. Figure 1.16b shows the size-enrichment ratio relationship of fine gravity concentrators treating tantalum ore slimes. The results suggest that Knelson and Kelsey Jig are inefficient to recover fine tantalum and that MGS and Falcon centrifugal concentrators out-performed the existing BMS. However a single pass MGS test is superior to two pass Falcon test, suggesting the MGS as the most adapted device (Burt et al., 1995).

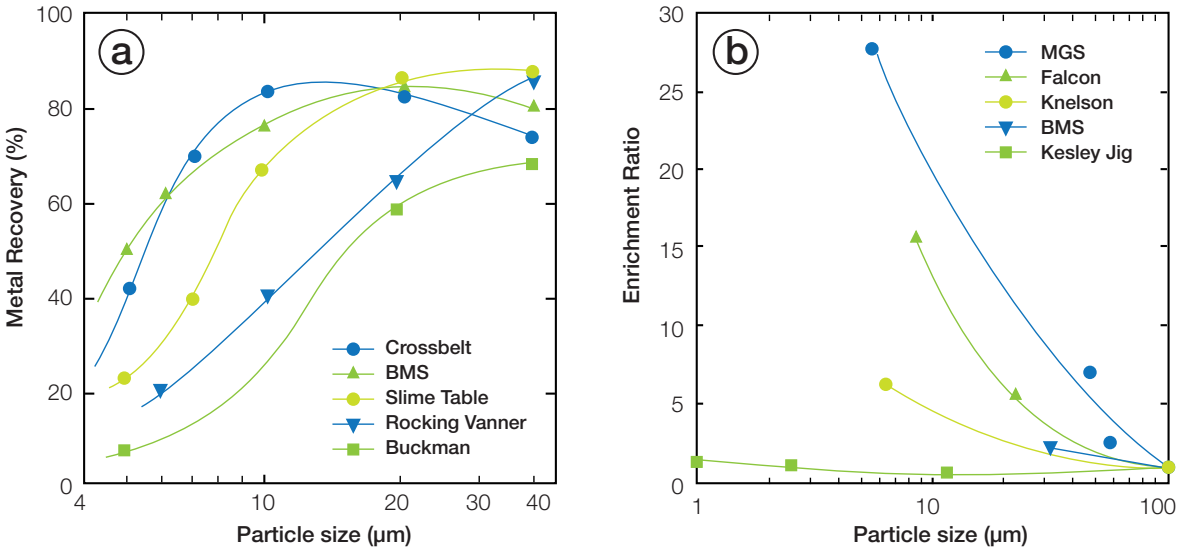


Figure 1.16: Comparison of the performance of various fine gravity concentrators. (a) Size-recovery relationship of fine gravity concentrators treating liberated tin or tungsten ores, after Burt (1984b). (b) Size-enrichment ratio relationship of fine gravity concentrators treating tantalum ore slimes, after Burt et al. (1995).

The use of fine gravity concentrators have been investigated and sometimes successfully applied to most of the CRMs of interest in this study. Burt and Ottley (1974)

present results from pilot scale and industrial scale tests that shows the benefit of the introduction of a BMS in the treatment flowsheet of tungsten and tin ores. The processing of ultrafine plant slimes containing wolframite (mostly distributed in the -25 µm fraction) from Panasqueira mine (Portugal) by MGS have been investigated by Clemente et al. (1993). Results show that, in combination with a sulphide flotation step, a three-stage MGS separation produce a wolframite concentrate of 50% $WO_3$ at around 60% recovery. The use of MGS for the treatment of slimes has also been investigated on a Turkish LREE ore which shows that a leachable concentrate can be obtained with a concentrate grade around 30% LREE (Özbayoğlu and Ümit Atalay, 2000). At the former Wheal Jane tin processing plant the flotation circuit has been improved through many modifications in the circuit including the addition of MGS instead of the flotation column, achieving a concentrate grade of 55.42% Sn and 65.41% Sn recovery (Chan et al., 1991; Turner and Hallewell, 1993). In Renison tin mine, the replacement of Mozley gravity separator by a Falcon UF 1500 device have resulted in an enrichment of the flotation concentrate from 15% to 40% Sn (Angadi et al., 2015).

### 1.4.4 By-product recovery of CRMs and Sn from kaolin production

#### 1.4.4.1 Beneficiation of Sn as by product of Beauvoir kaolins

The Beauvoir-Echassières kaolin deposit (Massif Central, France) is known to produce cassiterite (800 g/t Sn) and columbite (190 g/t Ta plus 120 g/t Nb) as by-product of the kaolin production (Pohl, 2011).

The kaolin ore is extracted using a dry mining process by quarry excavator, transported by truck and stored by quality on a platform located at the entrance of the plant. The kaolin ore is then fed to a kaolin beneficiation process which starts by grinding and washing of the ore (Figure 1.17, left). The kaolin ore is then screened successively to remove the coarse sands (5-40 mm) and fine sands (1-5 mm) by rotary screen and rake classifier respectively, and the very fin sands (0.04-1 mm) are removed by hydrocyclones (Negroni, 2015). The clay matrix is then screened to remove the remaining fine micas and the resulting kaolin pulp is then refined via settling and filtration (Meyer-Joly, 1988).

The heavy mineral concentrate is obtained from treatment of the fine sand residues of the kaolin processing route. According to Meyer-Joly (1988), two sand fractions are treated separately, the 0.2-1 mm and the 40-200 µm fractions. These fine sands are first treated by gravity concentration using spiral concentrators followed by shaking tables to obtain a primary pre-concentrate (Figure 1.17, right). This concentrate contains cassiterite, columbo-tantalite, microlite, topaz, titanium and iron oxides as well as some remaining micas. The characterisation of the primary concentrate shows that cassiterite is either free or associated or included in Li-micas (lepidolite), microlite and tantalo-columbite display no association with cassiterite which facilitate their separation whereas significant amounts of Nb (up to 10% Nb) are found in rutile (Meyer-Joly, 1988).

The obtained primary concentrates are then treated on two separate routes (one for each size fraction) following the same procedure. The primary concentrates are dried and then treated by medium intensity magnetic separation to obtain a tantalo-columbite concentrate in the magnetic fraction. The non-magnetic fraction is treated

by electrostatic separation producing a middling concentrate (containing microlite, topaz and cassiterite) and marketable cassiterite concentrate (Figure 1.17, right).

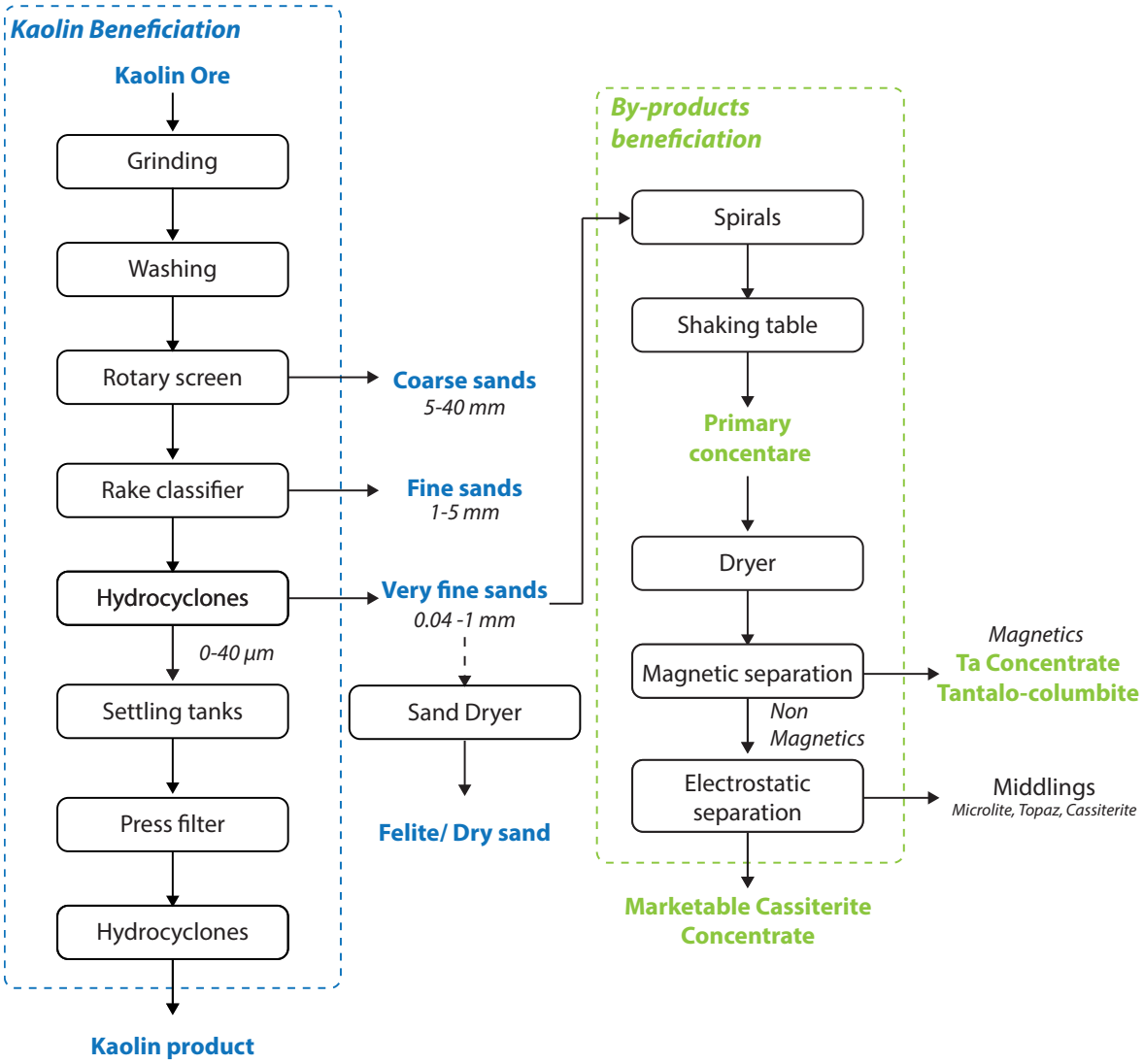


Figure 1.17: Flowsheet of the Beauvoir kaolin beneficiation process as well as the by-product concentration process to produces a Ta concentrate and a marketable cassiterite (Sn) concentrate, modified after Meyer-Joly (1988). The current by-product route may be limited to primary concentrate production.

Comparison of the distinct product or residues in terms of particle size between the kaolins of St Austell and Beauvoir shows that they produces similar waste materials like gravels, sands and a fine residue (Figure 1.18). The micaceous residue from St Austell (∼500-53 µm) is the closest waste material, in terms of particle size, to the Beauvoir fine sands (0.1-1 mm) which are treated for heavy mineral recovery. Moreover these waste streams consist both in hydrocyclone underflows obtained after a similar processing route. However, even if the St Austell micaceous residue can be considered as an equivalent to the Beauvoir fine sands, it is a much fine grained material that the Beauvoir fine sands, which could change drastically the way of processing this material. Indeed the particle size ranges of the Beauvoir fine sands falls into the

range of application of most gravity concentration techniques. However the micaceous residue is much fine-grained with particles as fine as 53 µm, and possibly lower since hydrocyclone separation is not perfect, which is outside the recommended size-range of most of the gravity concentration devices apart from the enhanced gravity and centrifugal separators (see Figure 1.15).

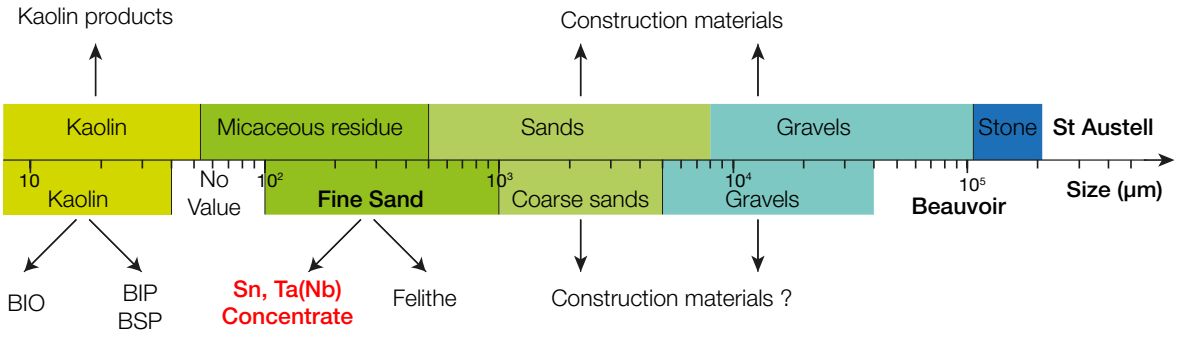


Figure 1.18: Comparison of distinct size-classified products/residues from the St Austell and Beauvoir kaolin deposits. Data for the Beauvoir kaolins are from Negroni (2015).

#### 1.4.4.2 Previous work at St Austell

The kaolinised granite of the Goonbarrow pit is spatially related to quartz-tourmaline, cassiterite, and wolframite sheeted veins edged by greisen alteration. It's one of the only china clay pits where a tin recovery plant operated and treated hydrocyclone underflows. The recovery of tin has been achieved using a combination of hydrosizer, spiral classifier and shaking tables with a feed grade around 900 ppm $SnO_2$, a recovery around 35% and a concentrate grade of 10% $SnO_2$ (Shail et al., 2009). The low recovery of tin is attributed to tin losses in the fine fraction, as 49.25% of the tin was contained in the -63 µm fraction.

Recovery of columbite-tantalite, rutile, cassiterite and other accessory minerals from hydrocyclone underflows has also been investigated by Scott et al. (1998). It is the only study that used samples from Goonvean Pit and Rostowrack pit located in areas covering the topaz granite (see map on Figure 1.6). They separated a fine grained (-100 µm) accessory minerals concentrate using a simple two-stage gravity concentration using a laboratory shaking table and a BMS. The mineralogy of heavy mineral concentrates was dominated by topaz (23 to 61%), rutile (8 to 33%) and columbite-tantalite (16 to 34%). The other minerals occurred in smaller proportion, cassiterite (1 to 8%), apatite (2 to 14%), zircon (1 to 5%) and monazite (<1%).

Heavy mineral concentration has also been performed on six hydrocyclone underflow samples from Imerys production sites (Melbur, Littlejohn and Wheal Martyn) located in the Western Area following the same two-step gravity concentration method for the purpose of a scoping study (Shail et al., 2009). The average tin grade of the micaceous residue samples varies between 5-150 ppm $SnO_2$. The obtained accessory minerals concentrates have yields ranging from 0.2 to 0.3 wt.%. The mineralogy of the heavy mineral concentrates was dominated by tourmaline (27-45%), topaz (5 to 38%), quartz (7-14%), rutile (3 to 34%), cassiterite (0.4 to 1.3%), zircon (0.5-6.5%) and monazite (0.4-6.4%). The remaining 10% contain biotite, muscovite, kaolinite,

and apatite. Small amounts of columbite-tantalite and wolframite were also detected which is the first recorded occurrence of Nb-Ta oxides from non-topaz granite. Since some the concentration Sn, LREE and other CRMs was below detection limits for some products, the metallurgical balance was calculated for $TiO_2$ and Zr only. The recoveries for both $TiO_2$ (in part because $TiO_2$ is also likely to be hosted by mica) and Zr were very low ranging from 3.73% to 11.52% for $TiO_2$ and from 1.78% to 28.48% for Zr. However high enrichment ratios are obtained, for $TiO_2$ (19-67x), Zr (3400-17100x), Nb (2500-8300x), Sn (3400-6900x) and monazite-hosted REE such as Ce, La, Nd, Pr (Shail et al., 2009).

Textural analysis using QEMSCAN fieldscan mode (10 µm analysis spacing) indicate that the concentrates are globally fine-grained (mean grainsize between 58 µm and 82 µm) with very fine grainsizes for cassiterite (40-68 µm), monazite (37-55 µm) and wolframite (15-51 µm). Analysis by QEMSCAN in TMS (Trace Mineral Search) mode, more robust (2 µm analysis spacing), even indicate that the majority of cassiterite grains are under 50 µm and the vast majority under 10 µm (Shail et al., 2009).

Previous studies (Scott et al., 1998; Shail et al., 2009) show that it was possible to recover accessory minerals from hydrocyclone underflows and to obtain a heavy mineral concentrate with topaz, rutile, cassiterite, columbite-tantalite, zircon, and monazite with varying proportions and recovery effectiveness depending on the sampling site. Apart from the historical tin recovery at Goonbarrow pit and columbite-tantalite-rutile concentration study from Scott et al. (1998) which display the best results, the grades of the heavy minerals concentrate from hydrocyclone underflows appear to be insufficient to have a commercial potential (Shail et al., 2009). In terms of recovery, the only results suggest that only minor proportion of CRM-bearing minerals is recovered in the gravity concentrates with significant losses in the table tailings (Shail et al., 2009).

Although these previous works give insight on the feasibility of CRMs recovery from kaolin residues, they cannot be considered as representative of the overall potentiality of CRMs as by-product of kaolin production. First, the historical tin recovery at Goonbarrow pit was associated with cassiterite vein type mineralisations which are not representative of the disseminated mineralisation typical of the rare-metal granite which makes up the majority of the exploited areas. Next, although the investigation of Scott et al. (1998) and Shail et al. (2009) deals only with disseminated mineralisation, the size of the samples used in each study, around 3 kg and 10 kg respectively, are far too small for the low grades and fine grainsizes of the CRM-bearing minerals in the micaceous residue to be considered as truly representative.

However, given the low recoveries obtained with all the gravity concentration tests, it is legitimate to wonder if the recovery from the hydrocyclone underflows can be improved. The grainsize of the CRM-bearing minerals is not optimal for gravity concentration as it tends to the finer fractions end of the hydrocyclone underflow. This is likely to be one of the most critical factors for CRMs concentration. Another critical point highlighted by Shail et al. (2009), in the light of the difference of the tin content between hydrocyclone underflow bulk samples (100-150 ppm) and the tin content of blast drillhole cuttings (∼1200 ppm), is that a significant proportion of the cassiterite, and the other heavy minerals, could have been previously removed in the sand fraction, and thus never enter the hydrocyclone banks. Therefore it is of primary importance to assess the metallurgical balance of the CRMs of interest between the various streams of the kaolin processing plant in order to locate potential losses in other waste streams.

## 1.5 Study objectives

This work aims to address two types of objectives. The first ones are the scientific objectives which are linked to the unconventional ore that represent the material used in this work as it falls in the category of low grade and fine grained ores. The scientific objectives are (1) to develop an effective beneficiation process for the recovery of CRMs from kaolin residues, (2) to develop a new method to assess the representativeness of process samples in view of metallurgical assessment tests and (3) to combine geological information and metallurgical results to develop tools for the geometallurgical modelling of the deposit. The second type of objective is obviously the industrial challenge which is to assess the by-product potential for CRMs of kaolin production.

### 1.5.1 Scientific objectives

#### 1.5.1.1 Process development for CRMs recovery from kaolin residue

Because they are considered as low-grade ore, most rare-metal granite-related deposits are not considered to have significant economic value. For instance, tantalum/columbite granites are of economic interest when the columbite content of the ore ranges from 0.001% to 0.01% and the tantalite up to 0.2% (Bulatovic, 2010). As targeted metals are originated from a weathered rare-metal granite, this work lies within the scope of low-grade ores processing as one of the main scientific objectives will be to develop a pre-concentration process that will allow the recovery of CRMs from low-grade kaolin residue.

*Low grade ores*

Despite the increasing developments and efforts in metal recycling, some metals like REE and other CRMs still have low recycling rates and very few effective substitutes. According to Laznicka (2006) the future supplies for the strategic metals will likely be dependant, in addition to classical ore deposits, to numerous unconventional resources (Figure 1.19a). This general trend is likely to change depending on the commodity, especially for the CRMs for which recycling is not a significant source, which reduce the future supply sources for these metals to giant or large deposits and unconventional resources. Among these unconventional resources, low grade ores represent the next logical step for the mining industry as illustrated by the overall decrease of the metallic ores grade as the higher grade reserves are exploited first and are progressively depleted. This is illustrated by the overall decline of ore grades in Australia for various base metals, precious metals and other commodities over time highlighted by the work of Mudd (2009), see Figure 1.19b.

As grades fall and increasing orebody complexity is expected in the future, the consequences in terms of energy consumption and associated greenhouse gas emission for primary metal production will be significant. Indeed, Norgate and Jahanshahi (2006) show that, at grades below about 1%, the additional energy consumed and greenhouse gases emitted in the mining and mineral processing stages to move and treat the additional gangue (waste) material increase drastically. Life cycle assessment studies show that, except for the cases where fine grinding is required, conventional concentration and smelting is the preferred route to direct smelting (Norgate and Jahanshahi, 2010).

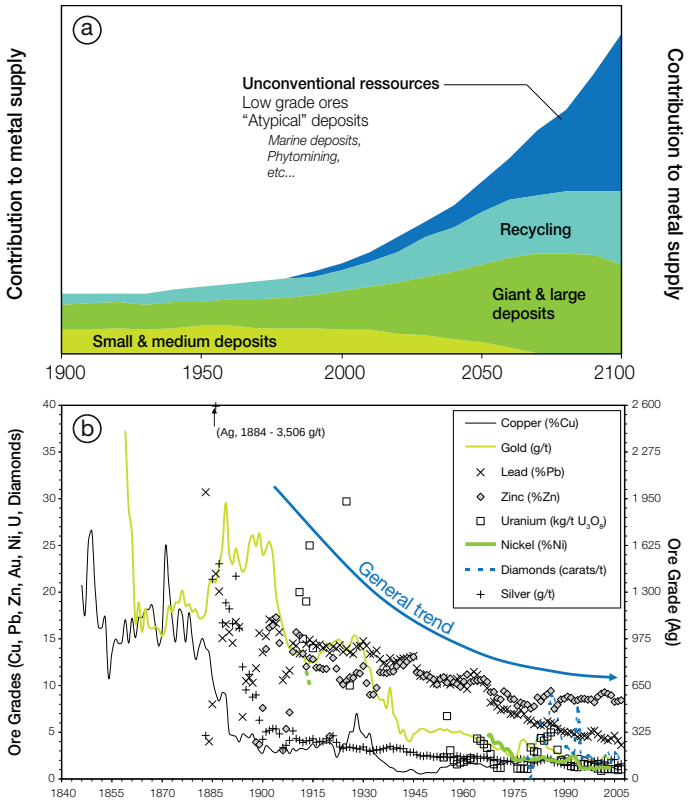


Figure 1.19: The increasing importance of low grade ores for metal supplies. (a) Projected future metal supplies, modified after Laznicka (2006). (b) Decline in Australian ore grade over time, after Mudd (2009).

A low grade ore might be defined as one ore which cannot be exploited economically using an existing processing route and which would not, under the present economic situation, support the implementation of a new plant. Thus, there is no economic value in low grade ore bodies and industrial residues until new economic methods are provided to extract them. For these complex low grade ores, mineralogical examination is essential for the selection of the best processing route. This is critical for low-grade ores where cost margin are small and high recoveries are essential (Zhou, 1976). Thus it is necessary to enhance the effectiveness of existing mineral processing techniques or developing new ones. When treating a low-grade ore, it is often advantageous to use pre-concentration steps to reduce or eliminate costly beneficiation processes.

*Fine particle processing*

Processing of fine grained ores by gravity concentration is a complex task and a significant source of losses in the industry for all the CRMs of interest in this work (Burt, 1988; Sivamohan and Forssberg, 1985c; Sivamohan, 1990; Somasundaran, 1986). According to Shail et al. (2009), the majority of cassiterite grains in the micaceous residue are under 50 µm which is below the working particle size range of the majority of gravity concentration techniques (Figure 1.15).

Recovering fine particles is an inherent problem in mineral processing for distinct reasons depending on the mineral processing methods *i.e.*, physical (gravity, magnetic,

electrostatic) or surface-based (froth flotation, etc.). The main causes are small masses, high surface area, colloidal coating, low momentum, heteroaggreagation, increased surface energy and pulp viscosity of fine particles (Sivamohan, 1990). In every gravity separation method, particles are separated by differential spatial displacement which will depend on their density, size and shape. In particular, the critical effect of decreasing particle size on gravity concentration efficiency could be illustrated by the expression of the terminal velocity $V_t$ of Stokes for free settling of spherical particles in a fluid:

$$V_t = \frac{(\rho_p - \rho_s)\, d^2}{18\eta} G \tag{1.1}$$

In this equation $\rho_p$ and $d$ are the particle properties (particle density and diameter), $\rho_f$ and $\eta$ are the fluid properties (fluid density and dynamic viscosity) and $G$ the gravitational field. It can be seen that the terminal velocity is only proportional to the linear effect of density difference with the fluid whereas it is proportional to the squared particle diameter. Hence with decreasing particle size, the terminal velocity decreases rapidly until a critical value is reached for which the contrast in particle displacement during the residence time became comparable with the limit of detection of the separator. Many mineral processing techniques have been developed to decrease this limitation (see Section 1.4.3.3) either by increasing the residence time (BMS, Crossbelt) or by combining several forces (Kelsey jig, MGS). In particular enhanced gravity concentrators impart acceleration up to 300 times that of Earth's gravity by centrifugation, in order to enhance the separation. This is illustrated by the change in terminal velocities of particles of distinct specific gravity derived from Equation (1.1) at 1 or 200 G (Figure 1.20).

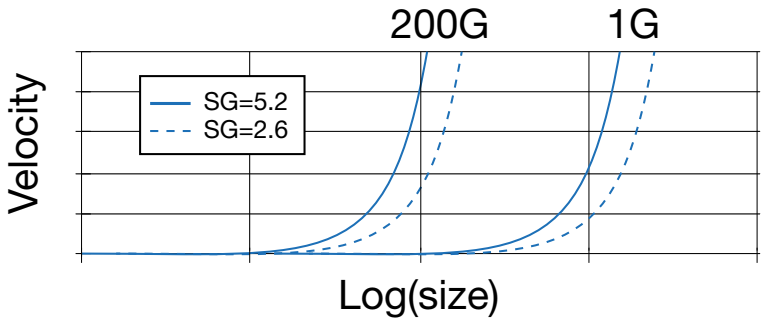


Figure 1.20: Illustration of the relative change of terminal velocity with enhanced gravity (McAlister and Armstrong, 1998).

Thus, the concentration of CRMs by these techniques is a real challenge that will involve the use of non-conventional techniques such as the Falcon concentrator, which is dedicated to the recovery of ultrafine particles (*e.g.* Falcon UF).

*Unconventional resources*

Even if the St Austell kaolin deposits display similarities with other kaolin deposits which manage to produce CRMs as a by-product, the success of such an initiative is very case sensitive and deserves a proper study. Apart from the Beauvoir kaolin operations, there is no record in the literature of kaolin residue beneficiation for CRMs

recovery. Previous works on kaolin residue from St Austell are of significant interest but, given the small-size samples used and the limited number of tests performed in each study, they cannot be taken as definite answers to CRMs' by-product potentiality. Processing such an unconventional material, with low CRM grades potentially distributed in the finer particle sizes is a real challenge that requires a full metallurgical assessment. This include the determination of the most adapted techniques through series of beneficiation tests at laboratory and pilot scales and the determination of best achievable performances through Design Of Experiments (DOE) methodology and, when appropriate, modelling of the effect of the operating parameters to predict the performance of the separation.

#### 1.5.1.2 Evaluate representativeness of process samples

In every mining project, economic improvements pass through metallurgical assessment based on series of metallurgical tests performed on the so-called process samples. Process samples are typically extracted from flowing streams of ore, concentrate or residue, at regular intervals to obtain representative samples regarding a given chemical analyte, a mineralogical or physical property. Metallurgical tests explore the best operating parameters to reach the desired recovery objectives and grade contents, therefore improving the process. The effectiveness of these improvements will depend directly on the representativeness of samples initially collected for the tests (Abzalov, 2013).

Although it may appear as a simple task, the sample collection process must be carefully carried out to avoid the introduction of systematic errors and to maximize the reproducibility. The various sources of errors associated with sampling of heterogeneous particulate material have been identified in Theory of Sampling (TOS) and described in many reference textbooks (Gy, 1971; Pitard, 1993; Gy, 1998). Process streams such as sand on a conveyor or flowing slurry in a pipe can be seen as 1D elongated objects (Gy, 2004b). The preferred method for sampling 1D lots is composite sampling (Minkkinen and Esbensen, 2009), which involves taking increments of the entire stream for a fraction of the time and then aggregating the increments together to make the final sample (Gy, 2004c). This method is based on the mathematical model that is used to integrate a curve $a(t)$ by means of sample points, with $a$ being the analytical results of a component A. In order to study the process variability over time, TOS introduced the concept of heterogeneity, by opposition to the concept of homogeneity (*i.e.* the fact of being constituted of strictly identical objects). The relative heterogeneity $h_i$ that is associated with the analytical results, $a$, in a single unit of mass $M_i$ of a lot comprising $N$ increments, which is expressed in the concentration $a_i$, is defined as follows:

$$h_i = \frac{a_i - a_L}{a_L} \frac{M_i}{\overline{M}_i}, \quad i = 1, \ldots, N \tag{1.2}$$

where $\overline{M}_i$ is the average mass increment and $a_L$ is the lot mean. This relative heterogeneity is dimensionless, so the component A can describe any intensive property that characterises the material (chemical or physical property, *e.g.*, density, humidity or particle size). This definition is univariate and its application is often limited in practice to grade estimation of valuable metal in a lot.

This is potentially problematic when samples are collected for metallurgical testing as results from metallurgical tests often depend on several properties (chemical analytes

or physical properties). Hence, the process samples need to be representative not only for one property but for a certain range of properties. In these situations the practical approach is to identify the property with the highest heterogeneity contribution and to take only this property into account. The main difficulty of this approach lies in the fact that it doesn't account for the multivariate nature of heterogeneity, which can lead to an underestimation of significant heterogeneity between close neighbours (Bourgault et al., 1992). The importance of considering the multivariate nature of heterogeneity is well-known in geostatistics and particularly for spatial data analysis but has only been addressed to TOS in a limited number of studies (Kardanpour et al., 2014; Minkkinen and Esbensen, 2014). One of the scientific objectives of this work will be to introduce new tool(s) for process sampling and to compare it with the classical and other existing approaches in order to define a mean of assessing the multivariate representativeness of process samples for metallurgical testing.

#### 1.5.1.3 Geometallurgy and by-product resource estimation

Geometallurgy combines geological and metallurgical information to generate a spatially-based predictive model for mineral processing plants in order to reduce technical risk (Lamberg, 2011). This implies to document variability within the orebody and quantify the impact of some geological and mineralogical factors on metallurgical processes (grinding, recovery). The database thus generated can be readily integrated into a 3D model (Williams and Richardson, 2004).

Such an approach is fundamental for the unconventional 'resource' investigated in this work, not only because of its nature but also because the target metals must be considered as by-products. However applying a geometallurgical approach to this case study may be challenging for several reasons:

- First, there are no a priori certainties, neither on the technical nor on the economic feasibility of CRMs by-product recovery. This causes an important lack of information for the establishment of a hypothetical geometallurgical model when most of geometallurgical program are applied to more conventional deposits already in operation for which a significant amount of data is available. In addition, most of the data available only concerns the main commodity,

- In this work only a limited amount of data and samples will be accessible and no historical production data is available to support this approach. Given the complexity of the investigated deposit, this means that this approach could not consider the whole deposit but will have to focus on specific facies, ore-type or locations and that the representativeness of the results that will be obtained is a key feature for a potential application,

- Next, since the CRMs are considered as potential by-product, the resource must be primarily valuable for the main commodity, *i.e.* kaolin, which means that both kaolin and CRMs must be taken into account in the geometallurgical model,

- Finally, the development of performance prediction models for a hypothetical CRMs recovery process to assess the by-product potentiality is critical as no data is available on the required CRMs grade or recovery.

Nevertheless one objective of this work will be to propose a by-product resource estimation model that will integrate all the results generated from ore characterisation and metallurgical testing to allow a more holistic evaluation of the by-product potentiality of CRMs.

### 1.5.2 Industrial challenge

The industrial challenges of this study are highlighted by the objectives of the STOICISM project and more particularly those of the task 2.6 "CRM Recovery" (see Section 1.1.3.3).

*CRM Recovery*

First, it is necessary to define which material stream of the kaolin mineral processing route (raw materials/waste streams) has the highest potential for CRMs recovery. Next a proper characterisation of the selected material is necessary to identify the CRM-bearing minerals and the degree of dissemination in the selected stream to evaluate the way of processing. The next logical step is to develop a pre-concentration process, starting by physical methods such as gravity (*i.e.*, centrifuge) and advanced flotation technique. The developed process should be tested at laboratory and pilot scale in order to assess the potential for scale-up of the technologies developed.

*Sustainability*

The specific objective of the STOICISM project is to develop cleaner, more energy efficient extraction and processing technologies reducing the carbon footprint, thereby looking at the whole supply chain from the extraction, waste valorization and optimisation of the functionality for the end users. In this idea, one of the objectives will be to evaluate the potential for treatment of waste material streams rather than raw material, and to assess the potential for historic waste valorization. In addition, the developed process must be as environmentally friendly as possible. Therefore, effort will be made to reduce the environmental footprint of the developed techniques by reducing energy consumption, chemical product consumption or potential waste production (when applicable).

*By/co-product resource evaluation*

When a commodity is extracted as a by-product, the market value of the main product supports the cost of extraction of this commodity, and the recovery of this commodity in turn makes the recovery of the main product economically more attractive. There is a sharing of mining and production costs between a co-product and a main product, the latter carrying a major share of the overall cost burden (Gupta and Krishnamurthy, 2004). This must be taken into account for the evaluation of the CRMs by/co-product potentiality.

# Chapter 2

# Materials and methods

## Contents

## 2.1 Materials sampling and sample preparation

Materials treated in this study correspond to the output streams of the Western Area plant described in Section 1.3.3 and two other in-pit processes linked with a hydraulic extraction method (Figure 2.1). Three mining areas were considered (see Figure 1.6 for the locations):

- Western Area Dry Mining (WADM) plant treating master grade (grade V) kaolin ore from Melbur and Virginia pit located on biotite granite,
- Treviscoe Hydraulic Mining (THM) process treating grade III-IV kaolin ore from Treviscoe pit located on topaz granite,
- Wheal Martyn Hydraulic Mining (WMHM) process treating grade III-IV kaolin ore from Wheal Martyn pit located on tourmaline granite,

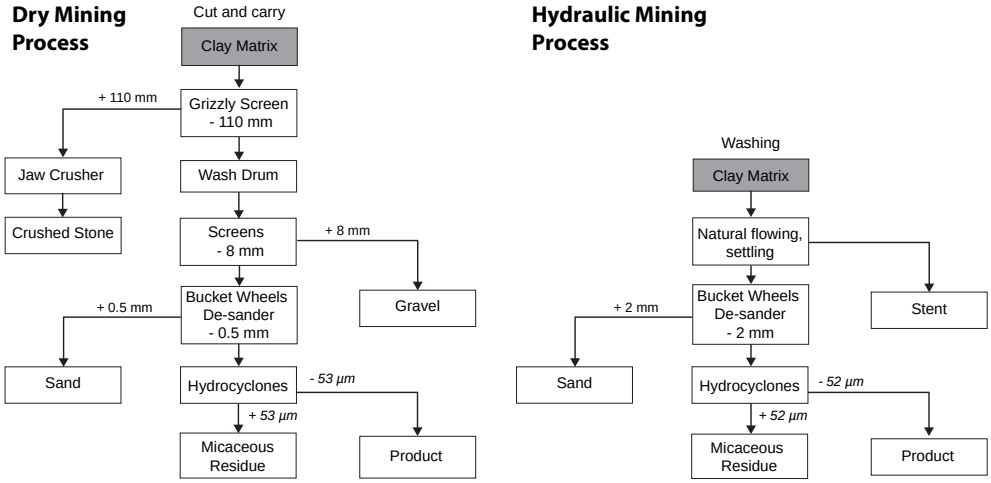


Figure 2.1: Simplified flowsheets of the dry and hydraulic mining processes.

### 2.1.1 Waste streams sampling for waste selection and characterisation

#### 2.1.1.1 Sampling of waste streams

The Theory Of Sampling (TOS) introduced by Pierre Gy has been widely described in many reference books (Gy, 1998, 1992, 1971; Pitard, 1993). It gives a simple set of rules for good sampling practice in order to eliminate sampling biases and to minimise the sampling errors. Process samples are usually collected from conveyor belts, stockpiled, blast holes or during ships loading. The fundamental principle of correct process sampling is that all parts of the material/stream sampled must have an equal probability of being collected to make the final samples (Gy, 1992; Pitard, 1993). In this regard, some common sampling practice such as grab sampling from the side of a stockpile or taking a "dip" sample from a slurry tank must be excluded (Holmes, 2004). The considered process streams are represented in TOS by one-dimensional (1D) model according to their projection on the flowing direction (Gy, 2004b). The preferred method

for sampling 1D lots is composite sampling (Minkkinen and Esbensen, 2009), which consists basically in taking increments of the whole stream for a fraction of the time and then aggregate the increments together to make the final sample (Gy, 2004c).

Waste streams of the 3 locations were sampled with the double objective of performing a metallurgical balance and characterising the CRM-bearing minerals (on micaceous residue sample only). For each location, the batch of samples were composed of waste samples from every outputs of the plants, *i.e.* 5 to 6 representative samples each, depending of the mining technique (dry or hydraulic mining). Each stream sample have been aggregated from daily increment sampling over a one week period (10/05/13 – 17/05/13) for WADM samples and a 7 days sampling distributed over a fortnight for THM samples (04/06/13 – 20/06/13). These samples have been collected in accordance with a protocol developed and implemented by Imerys and are taken to represent a typical material from both kaolinised biotite and topaz granite. Samples for WMHM were collected later and during one day only (15/05/2014). Thus they can only be taken to represent the average products of one day production.

Representative sampling of plant streams is a difficult exercise which deserves a proper attention. The design of automatic sampling tools and to study the CRMs content variability of each waste stream is required to design an adapted sampling protocol, which is far beyond the scope of this study. However, a prudent rule of thumb for correct cross-stream sampling is that when collecting samples from moving streams or slurries, a full cross section of the flow must be sampled for a fraction of the time. Hence, in the case of Wheal Martyn samples, efforts have been made to respect this rule and favour sampling points where the whole stream could be correctly collected. An example of some of the sampling points used to sample the WMHM process is shown in Figure 2.2.

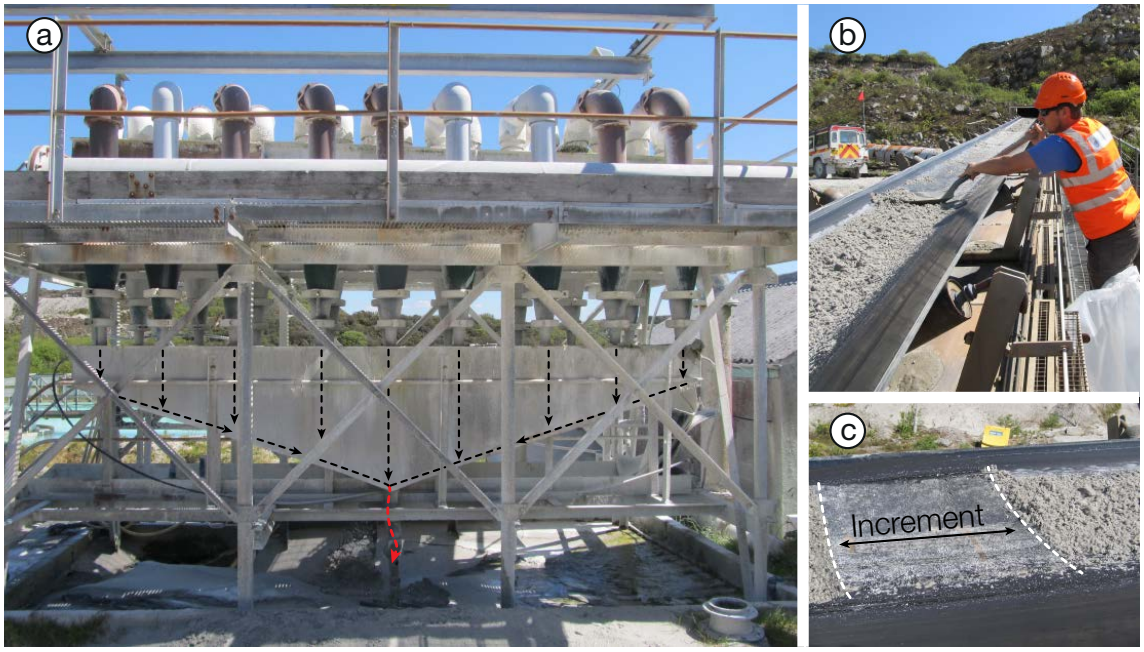


Figure 2.2: Weal Martyn sampling exercise. (a) Hydrocyclone banks with micaceous residue sampling point highlighted in red. (b) Increment sampling of sand material from a conveyor belt. (c) Delimitation of an increment sample from the sand conveyor.

For instance, the WMHM micaceous residue increments were collected from the underflow tank of the hydrocyclones banks (Figure 2.2a). For the sand stream, sample collection has been performed at the conveyor belt close to the discharge to the stockpile instead of collecting at the output of the screens (Figure 2.2b). The conveyor was stopped and increment collected manually from the belt (Figure 2.2c). The conveyor starts again until the material accumulated during the time the conveyor was stopped is conveyed to the stockpile (equilibrium) and then stops again to proceed to the sampling of the next increment. The procedure is repeated until the required amount of sample is accumulated.

#### 2.1.1.2 Sub-sampling and sample preparation

Table 2.1 lists the samples collected for each location with their corresponding weight. Since the micaceous residue samples were also collected for characterisation purpose, they were collected in larger amounts and divided in two sub-samples.

Table 2.1: List of samples and sample weights for the 3 considered locations.

| Sample type | | Sample weight (kg) | | |
|---|---|---|---|---|
| | | WADM | TWM | WMHM |
| Crushed stone | Stent | 20 | 40 | 250 |
| Gravel | | 24 | | |
| Sand | | 24 | 30 | 200 |
| Micaceous residue | | 60 | 60 | 300 |
| Hydrocyclone product | | 8 | 0.5 | 10 |

Samples sizes need to be reduced from several kilograms to approximately 10 grams representative sub-samples for subsequent analyses. To do so, the samples must be crushed and riffled alternatively in agreement with the TOS to obtain representative subsamples for chemical analysis (Petersen et al., 2004). Figure 2.3 shows a general sample preparation protocol for kaolin waste streams using laboratory jaw crushers, rotary crusher or roll crusher to decrease the particle size. The last particle size reduction stage is performed by a swinging mill which allows recovering powdered samples ready for analysis. Riffling or dividing the sample to reduce sample sizes were carried out with adapted riffle splitters with chutes wider than three to four times the maximum particle size to prevent blocking (large particles) or bridging (powders) during riffling (Petersen et al., 2004). When samples were too large to be riffled by manual laboratory riffle splitters, the samples were divided using a rotational sampler divider fed using a vibrating conveyor (Appendix B.1).

### 2.1.2 Micaceous residue sampling for metallurgical testing and variographic analysis

The WADM micaceous residue is a kaolin waste stream with the highest potential for CRM recovery (see Chapter 3). Hence, an additional sampling exercise has been performed for this waste stream. This sampling exercise has a double objective: (1) perform a variographic study to assess the variability of the micaceous residue for some critical properties (grades, particle size, etc.) and develop a method to assess the

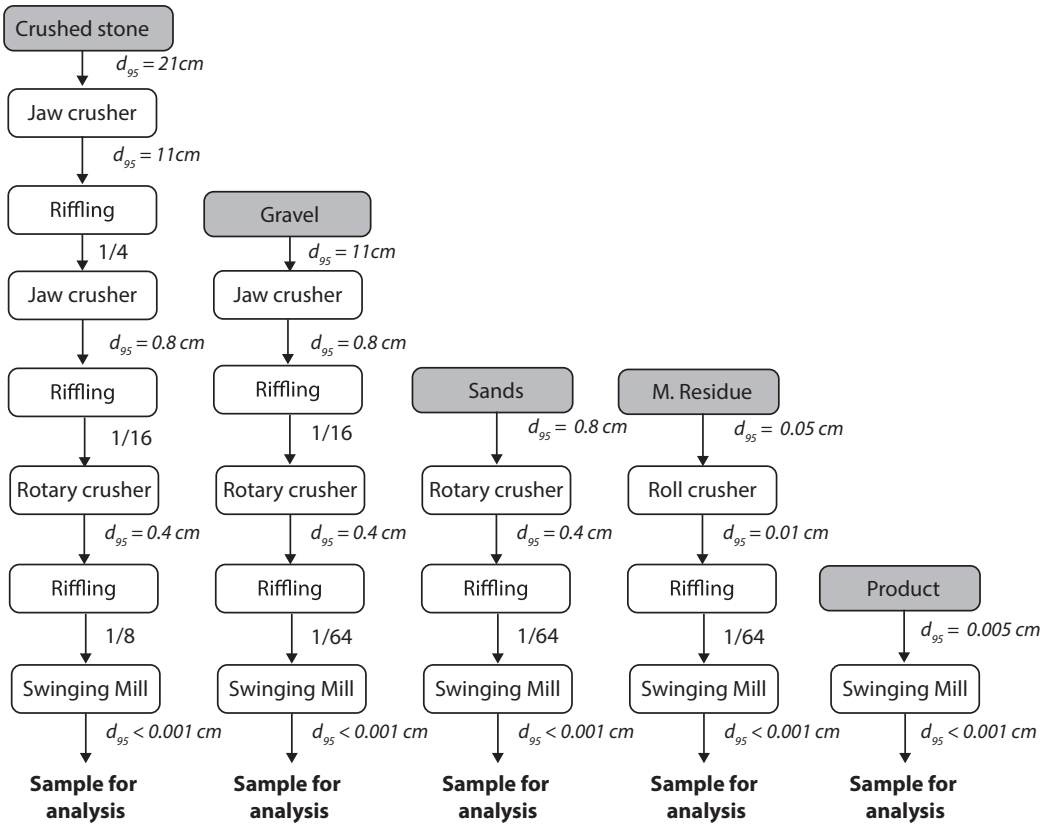


Figure 2.3: Sample preparation protocol for chemical analysis for each kaolin waste streams which were crushed and riffled alternatively. The riffling ratios may vary depending on the sample batch.

representativeness of the process sample for gravity processing, and (2) collect a large micaceous residue sample for metallurgical testing.

This residue corresponds to the secondary hydrocyclones underflow stream of the WADM plant operating at an approximate flow rate of 15 tons/hours. The objective was to collect only micaceous residue similar to the one used for characterisation, *i.e.* micaceous residue obtained by processing master grade kaolin ore from Melbur and Virginia pits located on biotite granite. This limits the room for large scale sampling campaign because the choice of which ore type to process is governed by the demand which cannot be predicted. Hence, during the week planned for the sampling exercise master grade ore was only processed once, during an approximately 2-3 hrs shift. A total of 50 samples (of approximately 25 kg) were collected from this stream, 30 min after the beginning of the shift to ensure that circuit was at the equilibrium and to limit contamination by material previously processed. The increments were manually extracted every 2 minutes systematically using a by-pass (Figure 2.4a) which collects the whole stream into the sample collector (Figure 2.4b). The by-pass is opened using a removable stopper which is then used to close the regular output. This may lead to an Increment Extraction Error (IEE) which is difficult to assess as the material flows both onto the regular and by-pass outputs in a split second when changing positions of the stopper. To limit this error, the by-pass was open and closed few seconds before and after the sample collection. However this error was technically unavoidable with the means at our disposal. Fortunately, given the large mass of the individual increments,

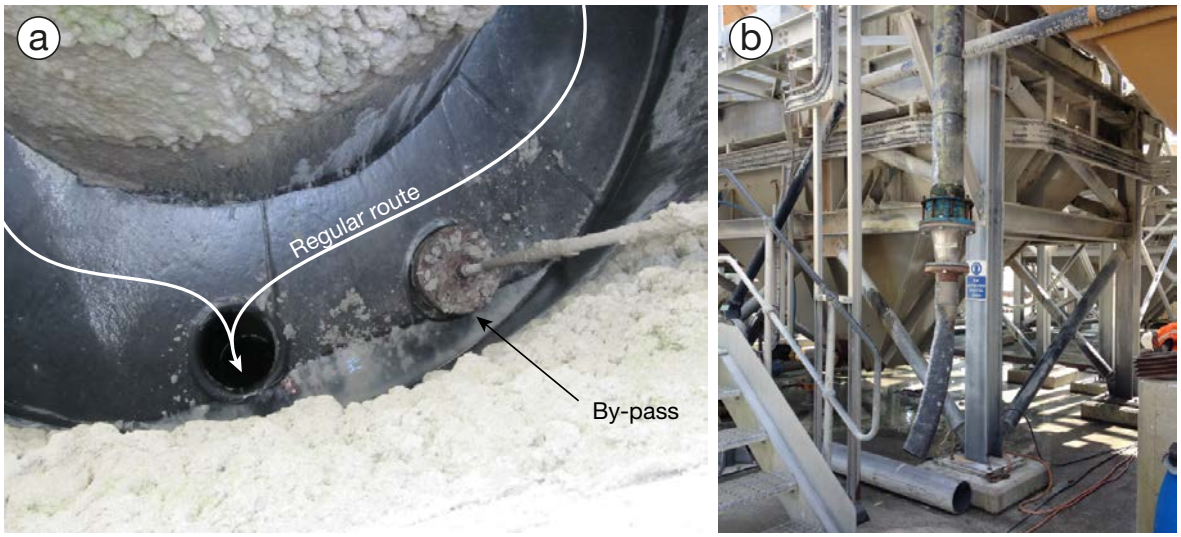


Figure 2.4: Sampling of micaceous residue. (a) Removable stopper used to by-pass the whole micaceous residue from hydrocyclones underflow tank to the sample collector pipe (b).

this loss of material could be neglected.

Since the number of increments required for a representative aggregated sample could only be known *a posteriori*, 9 large samples, of approximately 250 kg each, were collected for metallurgical testing before the end of the shift.

The accurate estimation of the pulp density and wet mass is a critical point, because moisture content of samples can change rapidly after sampling, due to evaporation. Thus all the samples were stored in sealed containers. Even though condensation may occur inside the container, which is difficult to mix back into the sample (Holmes, 2004). To avoid this issue the raw weight (containers + wet sample) have been measured and the container has been weighted afterwards. The samples were then dried directly without dewatering to avoid fine particles losses. Once dried, the samples were weighted to estimate their initial pulp density and then riffled to obtain subsamples for particle size analyses.

The 50 increments collected during the sampling exercise were used in the multivariate variographic study presented in Chapter 4. The large micaceous residue samples were screened into 3 size fractions, *i.e.* +180 µm, 53-180 µm and -53 µm to be processed separately, see Chapters 5 and 6.

## 2.2 Chemical analysis

For all chemical analyses, samples were crushed and riffled alternatively in accordance with the theory of sampling to obtain representative subsamples.

### 2.2.1 Inductively Coupled Plasma (ICP) analysis

Powdered samples (300 mg) are fused in Pt crucibles along with ultra-pure $LiBO_2$ at 980 °C and dissolved in nitric acid. The chemical analysis of the obtained solutions were carried out by Inductively Coupled Plasma Optical-Emission Spectrometry (ICP-OES, Thermo Fischer ICap 6500) for major elements (Si, Al, Fe, Mn, Mg, Na,

Ca, K, Ti, P) and Mass Spectrometry (ICP-MS, Thermo Elemental X7) for 42 trace elements following the routine procedure of liquid chromatography ICP-MS described in Carignan et al. (2001). Calibration was performed using international geostandards undergoing the same treatment. The measured concentrations for major elements are expressed as oxide percentages by weight taken at 110 °C. The loss on ignition (LOI) was gravimetrically determined by burning the sample in a furnace at 1000 °C. The relative uncertainties and limits of detection for major and trace elements are given in Appendix B.2. All ICP analyses were performed at the *Service d'Analyses des Roches et des Minéraux* (SARM-CNRS, Nancy, France).

In addition, some tailing samples were analysed using Laser Ablation (LA)-ICP-MS at the GeoRessources laboratory (Vandoeuvre-lès-Nancy, France) composed of a 193 nm MicroLas Pro ArF Excimer coupled with an Agilent 7500c quadrupole ICP-MS. The measurements followed the procedure described in Lach et al. (2013), using the NIST 612 glass as external standard and known compositions in Si (ICP, SARM) for internal calibration. Samples were dried and pressed into pellets before being analysed. Each sample were ablated 6 times with 120 µm spots in order to ensure a representative number of data that would account for a satisfactory 'bulk' sample analysis. The results were treated following the procedure described in Longerich et al. (1996), using the Iolite software (Paton et al., 2011). For most elements the limits of detection were below the ppm level.

### 2.2.2 X-Ray Fluorescence (XRF) analysis

*Equipment and sample preparation*

A set of 20 elements/oxides were analysed by X-Ray Fluorescence (XRF), among which major elements (Si, Al, Fe, Mn, Mg, Na, Ca, K, Ti, P) and trace elements LREE (La, Ce, Nd), Sn, Nb, Zr and W. Representative 10 g powdered aliquots were mixed with Cereox wax (Fluxana® GmbH & Co. KG) in a vortex mixer with mixing balls and then pressed into pellets at 20 t.

Chemical analyses were carried out by Energy Dispersive XRF spectroscopy (ED-XRF) using a S2 RANGER (Bruker Corporation) at the GeoRessources laboratory (Vandoeuvre-lès-Nancy, France). The S2 RANGER is equipped with a Pd X-ray tube and a 9-positions automatic filter changer. During the analysis several filters are used to remove undesired parts of the spectrum (low energies), decrease the continuous background, reduce the count rate and eliminating diffraction peaks (Bruker, 2015).

Two filters are used to cover the desired range of elements:

- An Aluminium 500 µm filter is used to analyse K, Ca, Ti, Mn, Ta, W, Ce, Pr, Nd, Sm, and LREE,
- A Copper 250 µm filter is used to analyse Y, Zr, Nb, Sn, La and Th.

However, in practice some elements can be analysed with either Al or Cu filters whereas some elements like Na, Mg, Al, Si and P don't require filters to be analysed (Table 2.2). Typical XRF spectra of a sample used for calibration are presented in Figure 2.5.

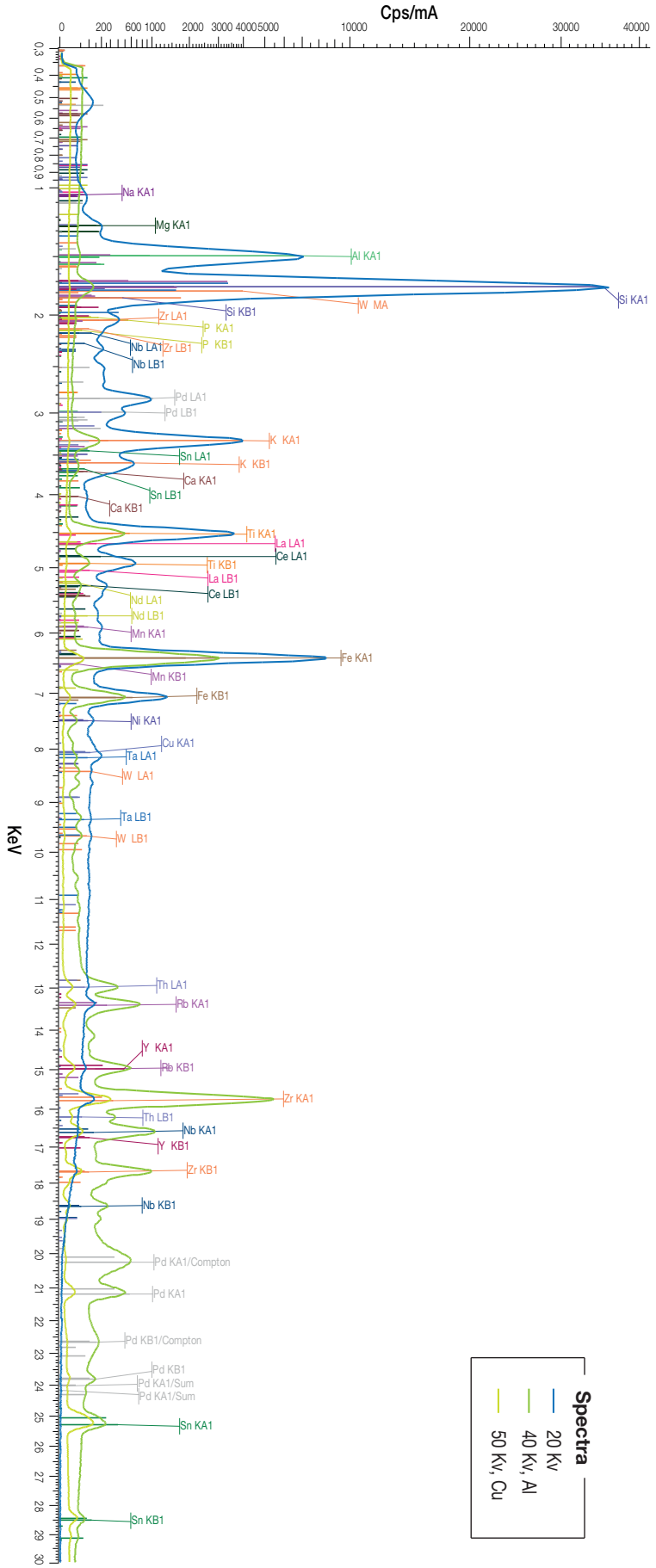


Figure 2.5: Typical XRF spectra of a rough concentrate sample showing peaks and abundance of each line determined for all elements.

Table 2.2: XRF analysis measurement method information.

| Energy (kV) | Filter | Time (s) | Current (µA) | Limit (kV) | Can be used to analyse |
|---|---|---|---|---|---|
| 50 | Cu | 100 | 250 | 100 | Al, Si, K, Ca, Ti, Mn, FeZr, Nb, Sn, La, Ce, Nd, W |
| 40 | Al | 100 | 250 | 100 | Na, Mg, Al, Si, P, K, Ca, Ti, Mn, Fe, Zr, Nb, Sn, La, Ce, Nd, W |
| 20 | None | 100 | 250 | 100 | Na, Mg, Al, Si, P, K, Ca, Ti, Mn, Fe, Zr, Nb Sn, La, Ce, Nd, W |

*Comparison with ICP analysis*

A major disadvantage of conventional XRF is the poor elemental sensitivity which is mainly due to instrumental geometries and sample matrix effects resulting in high background noise levels (Mukhtar et al., 1991). When testing the accuracy of XRF analysis, it is insufficient to assess an individual instrument parameter, but rather the performance of the complete analytical procedure, from sample preparation to analytical result (Towett et al., 2013). Hence, the accuracy of the XRF analysis was tested by means of multi-element standards with known concentrations from ICP-OES for major elements and ICP-MS for the trace elements analyses. A total of 27 samples were used in the testing of the applicability, accuracy and recalibration of XRF method. These samples are raw materials (kaolin residues), micaceous residues size fractions, and gravity concentration products (concentrate, middling, tailings) obtained during the characterisation stage of this work (Chapter 3) offering a wide range of elemental concentrations to calibrate the S2 RANGER for major and trace elements analysed.

Comparison between the estimated concentrations for major elements obtained by XRF analysis against the measured concentration obtained by ICP-OES suggests that XRF analysis accurately determined the concentration of most major elements (Appendix B.3). Indeed, most of the major elements display high R squared ($R^2$) above 0.8 and low root mean squared error (RMSE). Other elements are estimated with an acceptable accuracy ($0.7<R^2<0.8$) such as $SiO_2$ which display a $R^2$ of 0.77 and large confidence intervals suggesting a less accurate estimation by XRF analysis for this major elements. Although $MnO$ and $MgO$ display $R^2>0.8$, the small number of data points for $MnO$ and the large confidence intervals for both major elements indicate only an acceptable accuracy for these elements.

For the metals, comparison between the estimated concentrations obtained by XRF analysis against the measured concentration obtained by ICP-MS suggests that XRF analysis accurately determined the concentration of most trace elements (Appendix B.4). However, even if La and Ce display reasonable $R^2$ (0.62 and 0.89 respectively) the corresponding RMSE are large as illustrated by the very large confidence intervals (Appendix B.4ef). The difficulty of quantifying La and Ce in rock or soil samples (and LREE in general) by XRF analysis is well known and is attributed to line interferences with Ba, Sm and especially Ti (Towett et al., 2013). This difficulty is more pronounced for the gravity concentrate samples with high Fe, Ti and low Si contents but also for fine-grained samples which also display low Si contents. In order to overcome this issue internal calibration have been applied to take into accounts overlaps and interferences between peaks and a proper calibration have been implemented

for these samples. The comparison of the La and Ce concentrations obtained by XRF analysis against the measured concentration obtained by ICP-MS with this dedicated method is shown in Appendix B.4gh. Results are far more accurate with this dedicated method as illustrated by the high $R^2$ (>0.98), lower RMSE and trend line slope close to 1.

*External calibration*

In order to improve the accuracy of the XRF analyses, external calibration can be applied to XRF results using the above-mentioned reference samples by validation of the regression models. Among these samples, an independent validation set of 11 samples was randomly selected and the remaining 16 samples were used as a training set to test the accuracy of the XRF analysis and build regression models. Hence, the regression models obtained by comparing XRF analyses to ICP analyses for the training set, similar to those obtained with the full dataset (Appendices B.3 and B.4), were tested on the validation set (Table 2.3). This methodology requires a significant number of data points and cannot be applied to the dedicated analytical method which only has 10 data points. Single-element recalibration improved significantly the XRF analyses accuracy. Subsequent analysis revealed that XRF determined total element concentrations of Al, Fe, Mn, Mg, Ca, Na, K, Ti, P, Sn, Nb, W and Nd accurately (model efficacy/slope close to 1, and $R^2$>0.80) over a wide range of samples. Si could be estimated with an acceptable precision ($R^2$=0.77) compared with ICP-MS, although this could be improved by multivariate calibration as Si estimation errors are known to be correlated with Al. La and Ce could also be estimated with an acceptable precision ($R^2 \geq 0.70$) but only for low to moderately concentrated samples such as raw residues or gravity concentration tailings.

Table 2.3: Evaluation of the efficiency of the external calibration for the classical XRF analysis method using the validation set.

| Oxide (%)/Element (ppm) | $R^2$ | RMSE | Slope | Application |
|---|---|---|---|---|
| Classical method | | | | |
| $SiO_2$ | 0.77 | 2.99 | 0.98 | Raw residue, Gravity tailings and concentrate |
| $Al_2O_3$ | 0.99 | 0.30 | 1.00 | Raw residue, Gravity tailings and concentrate |
| $Fe_2O_3$ | 0.98 | 0.16 | 1.02 | Raw residue, Gravity tailings and concentrate |
| MnO | 0.85 | >0.01 | 1.02 | Raw residue, Gravity tailings and concentrate |
| MgO | 0.95 | 0.04 | 0.98 | Raw residue, Gravity tailings and concentrate |
| CaO | 0.81 | 0.04 | 1.03 | Raw residue, Gravity tailings and concentrate |
| $Na_2O$ | 0.89 | 0.06 | 0.98 | Raw residue, Gravity tailings and concentrate |
| $K_2O$ | 0.99 | 0.14 | 1.00 | Raw residue, Gravity tailings and concentrate |
| $TiO_2$ | >0.99 | 0.02 | 1.00 | Raw residue, Gravity tailings and concentrate |
| $P_2O_5$ | 0.98 | 0.02 | 0.98 | Raw residue, Gravity tailings and concentrate |
| Sn | >0.99 | 32.57 | 0.98 | Raw residue, Gravity tailings and concentrate |
| Nb | >0.99 | 3.70 | 1.00 | Raw residue, Gravity tailings and concentrate |
| Zr | >0.99 | 66.39 | 0.96 | Raw residue, Gravity tailings and concentrate |
| W | 0.88 | 41.13 | 0.94 | Raw residue, Gravity tailings and concentrate |
| Ce | 0.80 | 15.73 | 0.94 | Raw residue, Gravity tailings |
| La | 0.70 | 8.48 | 0.89 | Raw residue, Gravity tailings |
| Nd | 0.99 | 30.30 | 1.12 | Raw residue, Gravity tailings and concentrate |

## 2.3 Material Characterisation

### 2.3.1 Particle size analysis

Particle size analyses have been performed following two distinct techniques depending on material coarseness and the required resolution. However both techniques yield similar results, see Appendix B.5.

For coarse material, when a limited number of size fractions are required or when the size fraction must be analysed, particle size analysis was performed using a Rotap apparatus and a standard laboratory wet and dry sieving procedure (ISO 2591-1:1988).

Alternatively, when the fine size fraction analysis was required, particle size analysis has been performed by laser light scattering.

The obtained particle size distributions are the mean of 5 duplicate particle size analyses. Particle size analysis has been performed using a Helium-Neon Laser Optical System Mastersizer 3000 (Malvern instruments Ltd.) coupled with a Hydro Extended Volume (EV) sample dispersion unit. Sample was introduced in a beaker coupled with a sample dispersion unit, equipped with a dip-in centrifugal pump and a stirrer, until the desired obscuration level (up to 20%) is reached. The dispersed sample passes though the measurement area of the optical bench, where a laser beam illuminates the particles. A series of detectors then measure the intensity of light scattered by the particles within the sample for both red and blue light wavelengths providing superior sensitivity in the size range of 10-1000 nm. The specifications of the instrument are reported in Table 2.4.

Table 2.4: Specifications of the Malvern Mastersizer 3000.

| Specificity | | Range |
|---|---|---|
| Size range | | 0.01-3500 µm |
| Detection systems | | |
| | *Red light* | Forward, side and back scattering |
| | *Blue light* | Wide angle forward and back scattering |
| Light Source | | |
| | *Red light* | Max 4mW He-Ne, 682.8 nm |
| | *Blue light* | Max 10mW LED, 470 nm |
| Effective focal length | | 300 mm |
| Detector angles | | 0.015-144° |

### 2.3.2 Heavy medium separation

Heavy or dense medium separation has a wide use in the laboratory for the appraisal of gravity-separation techniques on ores (Wills and Napier-Munn, 2005). This technique has been used in this work for various purposes including material characterisation, washability (*i.e.* size-density distribution) determination or assessing the efficiency of gravity concentration operations.

The aim of this technique is to separate the material samples into a series of fractions, according to their density relatively to the separation medium. The samples were treated by dense medium separation using bromoform (SG=2.89), which may be diluted with ethanol to lower its specific gravity, combined with centrifugation (up to

1500 rpm). To avoid contamination between the float and sink fraction during the recovery of each product, the base of the sample tubes, containing the sink fraction, was frozen using liquid nitrogen. This operation allows obtaining a clean sink product containing all the heavy particles whereas the float product only contains the light particles.

## 2.4 Mineral Characterisation

### 2.4.1 X-Ray diffraction (XRD) analysis

*Principle*

X-Ray diffraction (XRD) is a characterisation technique used for the semi- to full-quantitative assessment of the minerals present in a given sample and in what relative proportions they occur.

Every mineral is characterised by the specific distribution of its atoms forming equidistant parallel planes, *i.e.* lattice planes, described by the Miller indices $\{h, k, l\}$. When a monochromatic beam of X-ray photons, with a given wavelength, hits the crystal surface, three basic phenomena may result, namely scattering, absorption and fluorescence. The coherently scattered photons may undergo subsequent interference leading in turn to the generation of diffraction maxima. The angle $\theta$ at which the diffraction maxima occur can be related to the interplanar spacing $d$ of the crystal lattice using Bragg's law, which describes the condition on $\theta$ for the constructive interference to be at its strongest:

$$n\lambda = 2dsin\theta \tag{2.1}$$

where $n$ is a positive integer and $\lambda$ is the wavelength of the X-Ray beam. The diffracted rays are detected by a scintillation detector or counter which measures their intensity in certain directions. Counter and specimen are mechanically coupled such that a rotation of the specimen through $\theta$ is accompanied by a $2\theta$ rotation of the counter. Addition of a knife-edge diaphragm eliminates the parasitic effect of the incident beam at small angles ($2\theta < 10°$).

The obtained X-ray pattern is characteristic of the material from which it was derived as each mineral is made up of a similar unique combination and arrangement of atoms. Thus X-ray diffraction patterns can be used to identify the mineral species in the sample.

*Equipment*

Qualitative mineralogical analysis of the major phases was performed by X-ray diffraction on a Brucker's D8 Advance (Bruker Corporation), operating with a cobalt $K_{\alpha 1}$ ray (1.789 Å), a tension of 35 kV and an intensity of 45 mA. The obtained diffractograms were initially interpreted with the EVA software to perform an accurate qualitative analysis. The assignment of peaks to different mineral species is carried out by comparison with reference diffractograms of pure species from the Crystallography Open Database (COD) or Powder Diffraction File (PDF).

*Mineral quantification*

Quantitative mineralogical analysis was undertaken by Rietveld analysis using the TOPAS software and data from chemical analysis, following the method of (Johnson et al., 1985). The method involved back-calculating the chemical composition of the samples by using the estimated mineral grades obtained by XRD analysis and the chemical composition of minerals and comparing it with that obtained by chemical analysis. New estimates are calculated by an iterative process following a least squares regression method.

### 2.4.2 Zeta potential

During the immersion of a mineral into an aqueous solution containing ions, an electrical double layer is formed at the mineral/solution interface. This double layer balance the apparent excess of charge of the mineral surface by a diffuse region of equal but opposite charges (called counter ions). The first layer, the closest to the mineral surface, is the Stern layer where adsorbed ions are located whereas the external layer is the diffuse layer (Gouy-Chapman) in which the arrangement of the ions is controlled by electric and mechanical forces. When an electric field is applied inside the liquid, the particles move and shearing forces occur at the location of the so-called slipping plane. The electrical compensation is no more fully ensured, which generates a potential difference called electrokinetic potential or zeta potential ($\zeta$). The zeta potential measurement provides the overall surface charge of a solid particle in suspension. This overall surface charge determines the specificity of adsorption of certain collectors and the choice of the most suitable reagents for a given pH.

Electrophoretic mobility measurements were carried out by timed image analysis with a Zetaphoremeter IV (CAD Instrumentation, France). The $\zeta$-potentials were evaluated after the Helmholtz–Smoluchowski and Hückel equations modified by Henry (Hiemenz and Rajagopalan, 1997). The experiments were performed on 30 µg of pure minerals samples grounded to -5 µm in an agate mortar and suspended in 300 mL KCl solution ($10^{-3}$ M). The pH of the solution was adjusted with drops of NaOH or HCl solutions to vary between 2 and 12 pH units. The specifications of the Zetaphoremeter IV are reported in Table 2.5.

Table 2.5: Specifications of Zetaphoremeter IV.

| **Specificity** | | **Range** |
|---|---|---|
| **Zeta potential** | | -150 to +150 mV |
| **Conductivity** | | 100 µS.cm$^{-1}$ - 100 mS/cm$^{-1}$ |
| **Applied electric field** | | |
| | *Voltage* | 0 - 255 V |
| | *Current intesnity* | 0 - 9.99 mA |
| **Particle size** | | 0.1-50 µm |
| **Concentration** | | 1-10 000 ppm |
| **pH** | | 2-12 |

### 2.4.3 Scanning electron microscopy

Investigation of samples by scanning electron microscopy (SEM) allows detailed identification of CRM-bearing minerals, their associations and their semi-quantitative chemical analysis, either *in situ* within a polished thin-section prepared from a rock sample, or a sample mount prepared from a concentrate (or other processing products). All microscopic analysis have been realised at the *Service Commun de Microscopie Electronique et Microanalyses X* (SCMEM-UL, GeoRessources, Nancy).

*Principle*

The surface of a specimen is submitted to an electron beam emitted by an electron gun. Numerous emissions are generated from the electron-mater interaction such as secondary electrons, back-scattered electrons, Auger electrons, X-rays and photons.

Secondary electron imaging allows the visualisation of 3D objects (grains, powders) and the characterisation of morphological attributes and mineral fabrics.

Back-scattered electron imaging allows the qualitative analysis and mapping of the spatial distribution of various elements and the localisation of minor or trace phases of interest, which are otherwise difficult to recognise using conventional microscopic procedures.

Auger electrons and X-rays are analysed for semi-quantitative microanalysis using an energy dispersive system (EDS) as an add-on to the SEM. This analysis can be used to solve questions on the natures of mineral phases and mineralogical distribution patterns and to achieve full mineralogical characterisation of a given sample.

*Equipment*

All textural observations and local X-ray microanalysis have been realized on a Hitachi FEG S4800 scanning electron microscope with an imaging voltage of 20 kV and equipped with an energy-dispersive X-ray spectrometer (Si-Li Thermo-Noran) for local semi-quantitative analysis of a wide range of elements with a maximum spatial resolution of 3 $\mu m^3$. Sample mounts were coated with carbon by vacuum evaporation in order to ensure the superficial conduction of electrons and to prevent the accumulation of electrostatic charge at the surface.

### 2.4.4 Electron microprobe analysis

Electron microprobe (EMP) analysis is used to characterise the chemical composition of minerals making up the sample and to assess potential atomic substitutions in mineral lattice. It relies on measuring the intensity of X-rays emitted by a given atomic element in special excitation conditions.

*Principle*

The working principle of electron microprobe is the same as the scanning electron microscope. The X-ray spectrum emitted by the specimen impacted by the electron beam comes from the whole inelastic collisions of the incident electrons with electrons in the inner shells of atoms in the sample. When an incident electron communicates

enough energy to a "stable" atom, it may result in the ejection of an inner-shell electron of this atom from its orbit, leaving a vacancy. Hence, when an electron from higher energy level drops to fill the vacancy in a lower energy level, it must shed some energy as an X-Ray quantum with a characteristic energy.

*Equipment*

The electron microprobe used in this work is a CAMECA SX100 with 5 WDS spectrometers equipped with classic monochromatic crystals (TAO, LiF, PET) and large crystals (LLiF, LPET). The measurements are performed with a primary current of 10 nA and an acceleration voltage of 15 kV, for a beam diameter of about 1.5 microns. The electron microprobe provides quantitative data for sufficiently concentrated elements (several hundreds of ppm). The chemical compositions are given in percentage of components (% oxides, % weight or atomic %).

## 2.5 Mineral processing

All the gravity concentration tests described in this work have been realised at the *Station Expérimentale de Valorisation des matières premières et des substances résiduaires* (STEVAL) pilot plant of the GeoRessources laboratory (Nancy, France).

### 2.5.1 Sample pre-treatment

The large micaceous residue samples collected in Section 2.1.2 have been pre-treated by screening and hydrocycloning in order to be further processed by distinct mineral processing techniques. Pulp samples were screened into 3 size fractions namely +180 µm, 53-180 µm and –53 µm to follow distinct processing routes (Figure 2.6).

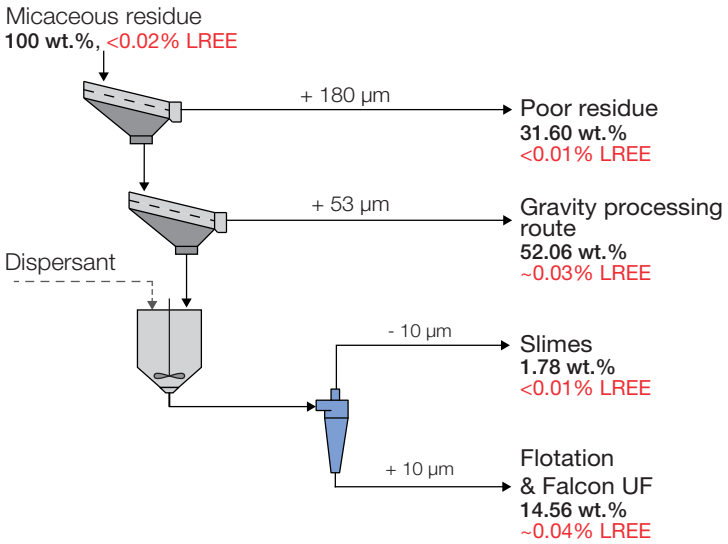


Figure 2.6: Sample pre-treatment flowsheet for the micaceous residue with material balance and average LREE grades.

The sieves opening have been selected based on the washability of the materials (see Chapter 5), in order to improve the efficiency of the gravity concentration, but also

with the objective of establishing process performance prediction models to be applied to core sample data (see Chapter 7).

The two first screening operations were performed with a vibrating Roto-Sieve apparatus model RS60 (Chauvin SA, France). Figure 2.7 shows the partition curve of these two screening operations. The efficiency of the separation, as indicated by the steepness of the curve, is acceptable and the cut-points ($d_{50}$) observed, 48 µm and 175 µm respectively, are close to the desired separation sizes. The 53-180 µm fraction was treated following a gravity processing route (see Chapter 5) whereas the low grade +180 µm fraction was not considered for metal recovery in this work.

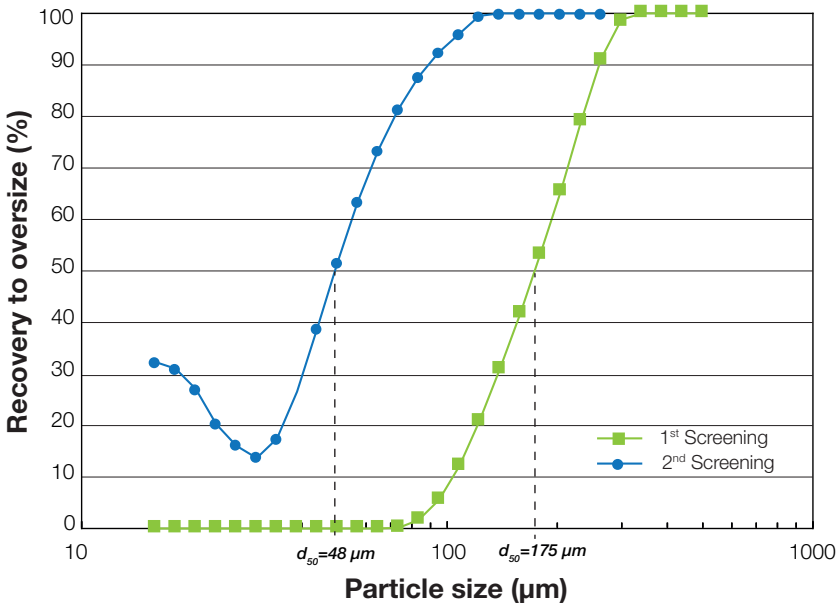


Figure 2.7: Partition curves for the 1st and 2nd screening operations indicating a correct efficiency of separation with cut points of 48 µm and 175 µm respectively.

The -53 µm fraction has been deslimed using a 2 inch Mozley C124 hydrocyclone (Mozley, UK) equipped with a 14 mm-diameter vortex finder and a 5 mm-diameter spigot cap. The pulp was agitated in a feed tank prior to desliming with and without dispersant to test the influence of dispersion on flotation performance and then fed to the hydrocyclone test rig. The deslimed -53 µm fractions were then divided into representative subsamples using rotational pulp sample divider (Appendix B.1b), to constitute the feed material for the flotation and Falcon tests presented in Chapter 6.

## 2.5.2 Gravity processing

### 2.5.2.1 Spiral concentrator

Spiral concentrators are high capacity, low cost units used for the recovery of heavy minerals from sands and ores with minimum operating costs as there is no energy consumption (Burt, 1984b; Wills and Napier-Munn, 2005). Spirals are the major equipment of the flowing film classification. The principle of separation is based on gravity and centrifugal forces that act together to separate light and heavy minerals based on their specific gravity, size and shape. For more details on the separation mechanism, the interested reader is invited to refer to the literature (Atasoy and Spottiswood, 1995;

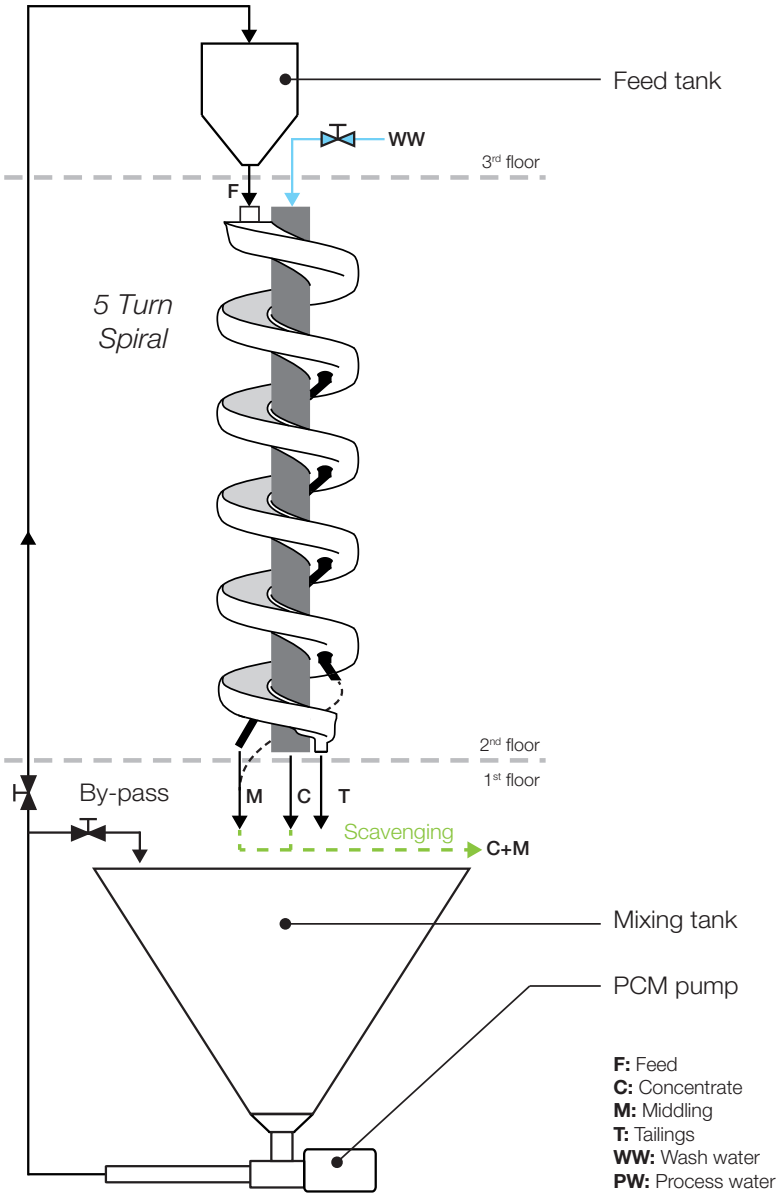


Figure 2.8: Pilot scale experimental set-up for closed-circuit MKIIA Reichert spiral testing.

Burt, 1984b; Sivamohan and Forssberg, 1985a). Despite the large variety of spirals and manufacturers, the operating parameters are the same, *i.e.* feed rate, feed pulp density (solid wt.%), splitter position and wash water flow rate. Generally speaking, increasing feed rate usually results in lower performance as for feed pulp density but the latter tend also to have a positive effect on fine particles recovery (Falconer, 2003). Wash water has also a significant effect as it clean the concentrate stream of the entrapped light particles.

The spiral concentrator tested in this work is a 5 turn MKIIA Reichert spiral (Mineral Deposit Limited, Australia), with a 387 mm pitch, 2370 mm overall height and a 590 mm trough diameter.

The dry sample is mixed with water in the mixing tank, forming pulp. The pulp is then pumped to the feed tank using a Progressing Cavity Moineau (PCM) pump (Figure 2.8). Concentrate (C), middling (M) and tailings (T) discharge into the mixing

tank via flexible pipes, which allow sample collection while operating in closed-circuit. Due to wash water (WW) addition the feed (F) pulp density decreases during the operation. This dilution can be easily controlled since the initial pulp density and wash water flowrates are known. Hence, samples can be collected at specific times during the operation to represent a given feed pulp density. The steady state is achieved when sampling is carried out. Because this stage is a roughing stage, the two middling offtakes were considered a single group. Wash water is supplied at each spiral turn via a wash water trough wrapped around the central column. The amount of wash water supplied to each wash water point on the spiral turns was adjusted by rotating the end of the wash water quill inserted in the polyurethane trough to ensure an even distribution of wash water to each turn. Scavenging tests were also performed with a similar set-up by recovering continuously concentrate and middlings during time, simulating successive passes in spirals separator. Again, the pulp density is known, so by measuring the feed flowrate it is possible to assess the time of one pass, which is the time beyond which all the sample have passed through the spiral, and hence the number of passes. When spiral were operated to study the effect of pulp density and wash water addition, the concentrate splitters position were set at the beginning of the tests at a 3/4 aperture and remained fixed during the whole experiment.

#### 2.5.2.2 Shaking table

Shaking tables are one of the most efficient devices in mineral processing (Burt, 1984b). However it is a relatively low capacity device in comparison to spiral concentrator and is usually employed in second steps of concentration. The principle of separation is based on the thin film concentration process across an inclined table having an asymmetric periodic motion to allow selective stratification of the particles according to their specific gravity, size and shape (Sivamohan and Forssberg, 1985b). This motion causes the fine high specific gravity particles to migrate closest to the deck surface along the riffles to discharge at the opposite (concentrate) edge of the table, while the low specific gravity coarser particles move or remain closer to the surface of the slurry and ride over the riffles, discharging over the side (tailing) edge of the table (Falconer, 2003). The main operating parameter is undoubtedly the deck angle which impacts directly the grade and recovery of the concentrates. Others operating variables are feed rate, pulp density, wash water flowrate and motion frequency. For a comprehensive understanding of the influence of the operating parameters, the interesting reader is directed to the work of Manser et al. (1991).

The shaking table used for concentration is a Wilfley laboratory shaking table (Wilfley N°13). Based on feasibility tests results, among the 8 outputs of the discharge launder, the two first outputs at the front of the deck were considered as concentrate (C), the third to fifth, located at the table corner, as middling (M) and the other outputs were combined to one tailing (T), see Figure 2.9.

Shaking table feed (F) corresponds to spiral concentrates aggregated from additional spiral tests performed with the optimal operating parameters for the heavy minerals recovery given by the design of experiments to get the necessary amount of material. Operating in closed circuit is much more complicated with the laboratory shaking table. Indeed the feed flowrate is much lower than for spiral which is not suitable for slurry pumping and hence the table could only be fed with dry material via a screw feeder. As the amount of material required for one test is relatively large (minimum 20 kg), due

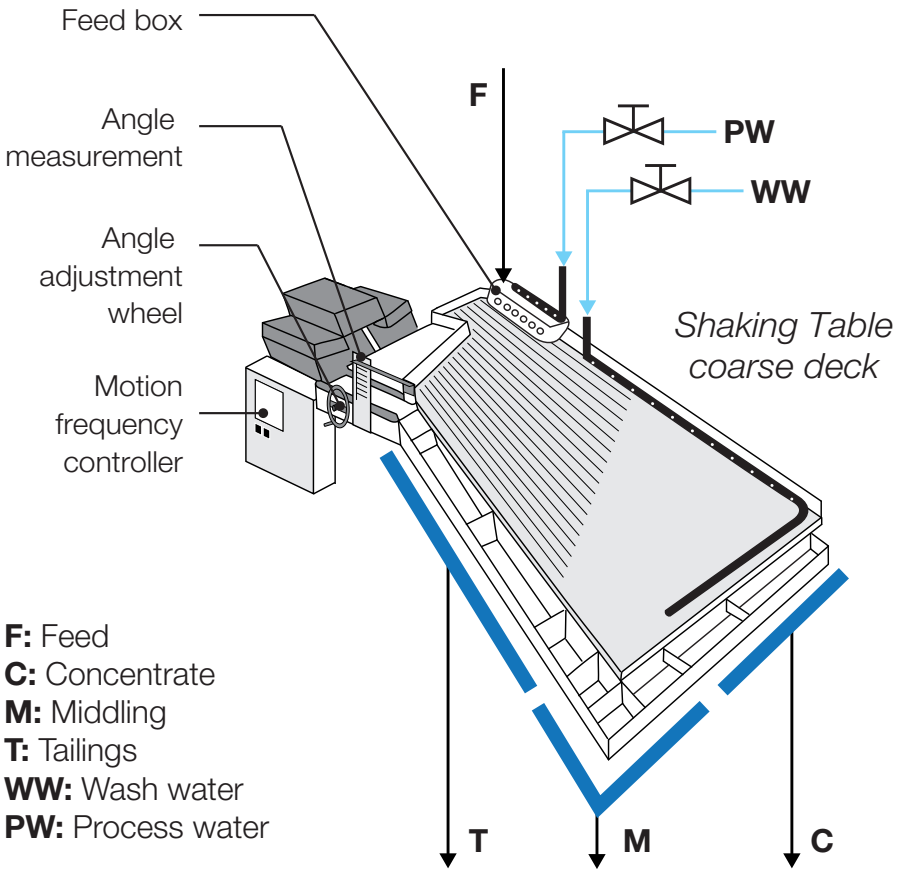


Figure 2.9: Experimental set-up for Wilfley shaking table testing.

to the time required to reach the steady state, every output were recovered and mixed back together after each test and then were dried to serve as feed of the following tests. This procedure may lead to fluctuations of feed properties due to the drying process.

#### 2.5.2.3 Falcon concentrator

The Falcon concentrators are part of the flowing film category of gravity concentrators which use centrifugal forces to enhance the efficiency of the separation. They can be described as a centrifuge capable of operating at high rotation speed (up to 600 G) to enable fine particles of different specific gravity to be separated (Falconer, 2003). The feed slurry enter the Flacon bowl at its bottom center and flows upwards along the bowl wall due to the combined effect of bowl opening angle and centrifugal force (Kroll-Rabotin et al., 2010). A slight reduction in diameter at the outlet retains the heavy particles inside the bowl while the light particles are flushed over the top of the separator with the process water.

*Equipment*

The Falcon experiments presented in this work were carried out on the -53 µm residue with a Falcon L40 laboratory semi-batch (SB) model (Sepro Mineral Systems, Canada) able to operate at up to 300 G. The Falcon L40 is a small capacity device with a solid capacity below 300 kg/h producing a concentrate of 80-100 g (Falcon

Concentrators Inc., 2007). The Falcon L40 can be equipped with two types of (4" diameter) bowls, *i.e.* the classic SB fluidised bowls (Figure 2.10a) and the ultrafine (UF) bowl dedicated to ultrafine particles recovery (Figure 2.10b). The two bowl series differ by the way they trap particles once particles have been classified by differential settling in the flowing film. Falcon SB series uses fluidized annular grooves upstream of the bowl outlet. High pressure fluidisation water is introduced through drilled holes within the retention zones modifying the retention capacity and concentrate grade by adjusting the counter-pressure flow rate (Kroll-Rabotin et al., 2013). Falcon UF lacks fluidisation water; instead the smooth bowls are designed with a slight reduction in diameter at the outlet which creates a non-flowing region.

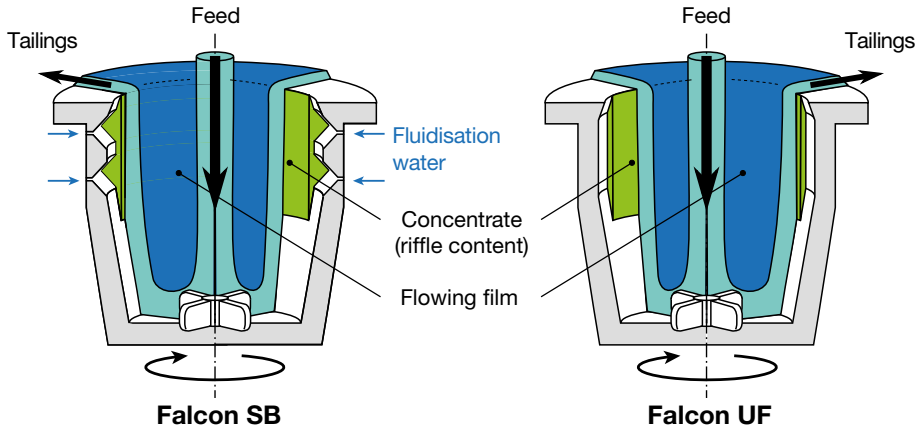


Figure 2.10: Falcon L40 SB (left) and UF (right) bowl schematics modified after Kroll-Rabotin et al. (2010).

The main operating parameters of the Falcon L40 are the rotation speed, fluidisation pressure (SB bowl only), slurry solid density and feed flowrate. The experimental setup used in this work, inspired by the work of Kroll-Rabotin (2010), allow controlling all those parameters to operate at the desired operating conditions (Figure 2.11).

*Experimental setup*

The Falcon is fed via two agitated tanks. The mixing tank (∼60 L capacity) is used to introduce the sample into the water which is agitated to prevent particles settling and provide a homogeneous slurry. The feed tank (∼10 L capacity), used to feed the Falcon concentrator, is a constant-head tank which always maintains a constant water level so that the feed flowrate depends only on the pressure drop imposed by a valve placed at the tank output which reduces flowrate fluctuations. The slurry is pumped from the mixing tank to the feed tank by a peristaltic pump (PCM Delasco) with a higher capacity than the feed flowrate to maintain the overflow and ensure a constant water level in the feed tank. The overflow from the feed tank goes back to the mixing tank through the level control bleed pipe.

In addition a by-pass is placed at the output of the feed tank to allow operating in closed circuit. This allows a better feed preparation as desired water amount can be introduced into the closed circuit prior to sample introduction. Thus when dry sample is introduced into the mixing tank the whole circuit is already wet and the obtained slurry is at the desired pulp density. The closed circuit is then maintained

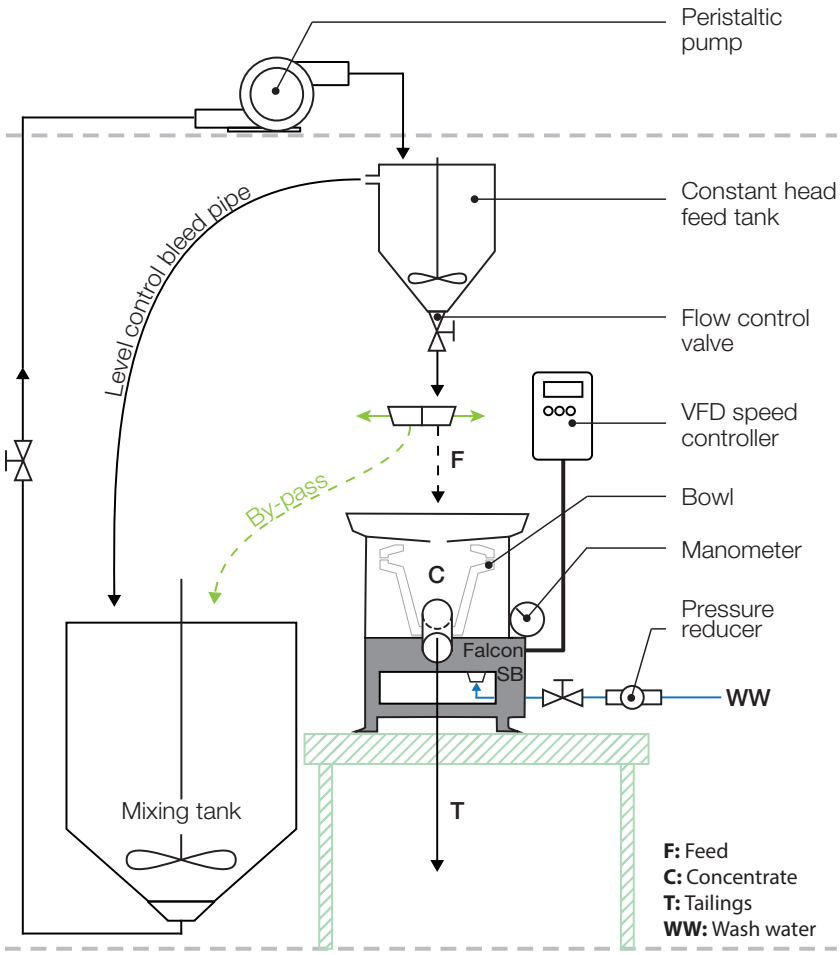


Figure 2.11: Laboratory scale experimental set-up for Falcon L40 testing.

until the slurry is well homogenised. Another advantage of the by-pass is the possibility of measuring the feed flowrate directly without interrupting the operation. Hence the feed flowrate can be set at the desired value prior to operation while the system is still in closed circuit.

A Variable-Frequency Drive (VFD) speed controller allow to set the bowl velocity in Hertz and the corresponding effective velocity in G is given by a conversion table in the Falcon manual (Falcon Concentrators Inc., 2007). The fluidisation water flowrate is controlled by a valve below the device and the corresponding fluidisation pressure can be read on a manometer. In order to prevent drops in pressure during operation a pressure reducer is used to limit the fluctuations in water pressure from the public water supply.

### 2.5.3 Jar-tests

The effect of dispersant type and dosage on slime dispersion has been tested using the jar test methodology. The tests were performed on 170 g wet samples (∼110 g dry solid) of -53 µm micaceous residue samples prior to desliming. The samples were introduced in 1L beakers and water was added to reach a pulp solid density of 10 wt.%. The pulp was agitated during 3 mins at 220 rpm followed by 5 mins conditioning at 200 rpm after dispersant addition. Three dispersant dosages have been tested, *i.e.* 10,

20 and 30 mg/L corresponding to a dosage of 90, 180 and 270 g/t of solid respectively. For each test a beaker containing only pulp with demineralized water was used as a reference. After agitation was stopped, interface height was recorded every 5 mins during the first hour and then at random for the most dispersed solutions until 22 h after the beginning of the recording.

Three types of dispersant have been tested in these experiments including sodium silicate ($Na_2SiO_3$), also used as depressant during flotation tests and polymeric dispersants. The latter comprise sodium polyacrylate solutions such as Antiprex® D (BASF, France) and 42%-purity Coatex GX TP supplied by Coatex (Arkema group, France) but also sodium acrylate/acrylamide copolymer such as Cyquest® dispersants (CQ4000, CQ3223) supplied by Cytec (Solvay group, France). The structure of these polymers is presented in Table 2.6.

Table 2.6: Structure of water-soluble polymers used in this study after Klimpel (1999), where x and y are the monomer molar ratios.

| Polymer type | Structure | Product |
|---|---|---|
| Polyacrylic acid | 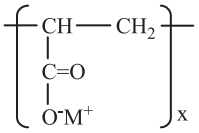 | Antiprex, CoaTex |
| Copolymer of Acrylamide and Acrylic acid | 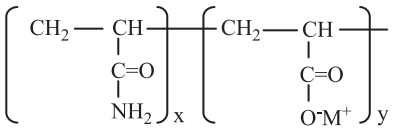 | CQ3223, CQ4000 |

## 2.5.4 Froth flotation

Principle of froth flotation is based on the modification of the surface properties of minerals. Floatability of minerals is determined by their ability to adsorb selectively or not, on their surface, collectors present in solution, making the surface of minerals hydrophobic. The conditioning step is essential since it allows the selective adsorption of heteropolar reagent on the surface of the mineral to be recovered. This step is followed by a flotation step during which the air in the form of fine bubbles, having a maximum diameter of 1 mm, is injected into the conditioned pulp (Nguyen, 2007). Under the constraint of a collision probability and attachment between particle and air, the bubbles adhere to the hydrophobic solid particles. As a result, air-solid aggregates are carried to the surface, forming a froth layer.

*Equipment*

Figure 2.12 presents the flotation flowsheet investigated in this paper comprising one roughing stage followed by cleaning of the floated product and scavenging of the non-floated product. The flotation tests were carried out using a conventional Agitair LA-500 flotation cell (1.5 L), see Figure 2.13a. Agitair rotor/stator flotation cells are externally-aerated "supercharged" as air is introduced via an external blower (Wills and

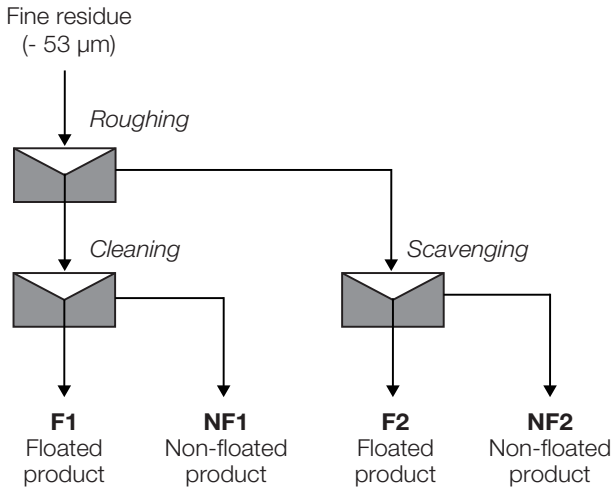


Figure 2.12: Flowsheet of the flotation experiments applied to the fine micaceous residue.

Napier-Munn, 2005). The Agitair cell is equipped with a separate impeller consisting of a horizontal disk with cylindrical fingers extending toward the bottom and rotating in a stationary baffle system (Fuerstenau and Somasundaran, 2003), see Figure 2.13b. Air is blown into the pulp through a hollow standpipe surrounding the impeller shaft, and sheared into fine bubbles of 1 mm or less at the manufacturer's recommended impeller speed (Gorain et al., 1995). The main characteristics of Agitair flotation cells are froth crowding action with single side discharge, the use of large-diameter impellers allowing lower peripheral speeds, the use of junction boxes for breaking pulp flow, reagent stage addition, and pulp level control (Dreyer, 1976).

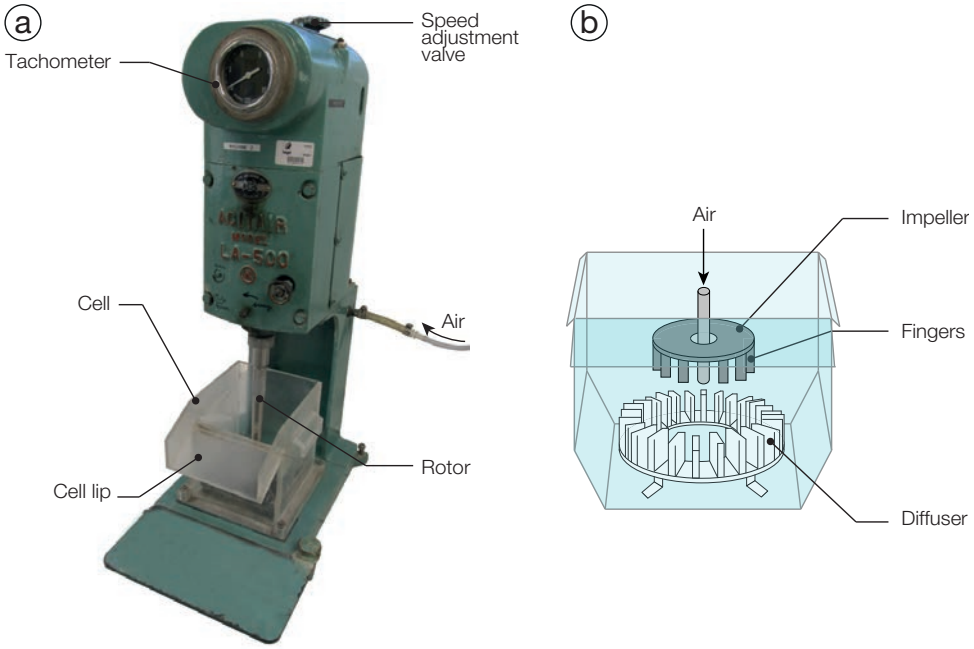


Figure 2.13: Agitair flotation machine. (a) Agitair LA-500. (b) Schematic representation of an Agitair flotation cell modified after Barbery (1983).

*Flotation tests*

The flotation tests were carried out on the -53 µm fraction of micaceous residue samples, the results of which are presented in Chapter 6. For each experiment, a pulp sample containing ∼500 g dry sample was mixed into the cell with water at 1100 rpm for 10 min to obtain a 10 wt.% solid density. Sodium hydroxide (NaOH) was added to adjust the pH of the slurry to 9.8-10 during the conditioning step, followed by frother, collector and depressant addition. The pulp was aerated with an air flowrate of 50 L/h and the froth product was collected for a total time of 7 to 13 mins. Non-floated products are recovered into the cell and dewatered. All flotation products are then dried at 30°C.

*Reagents*

Aliphatic alcohol (MIBC) was used as a frother and sodium silicate (VWR BDH Prolabo, 3.33 $Na_2O/SiO_2$ ratio) was used as depressant of silicate minerals. The frother dosage was 5 g/t in all experiments and sodium silicate dosage was around 1000 g/t and 100 g/t for the roughing and cleaning stage respectively. Several collectors have been investigated in this work, including 98%-purity sodium oleate (Arcos Organics, France), hydroxamate (AC-3) purchased from Cytec (Solvay group, Belgium), and non-ionic reagent iso-tridecanol (PX4826) supplied by CECA (Arkema group, France). A detailed description of operating conditions for each flotation experiments is presented in Appendix B.6.

# Chapter 3

# Selection and characterisation of the most valuable stream

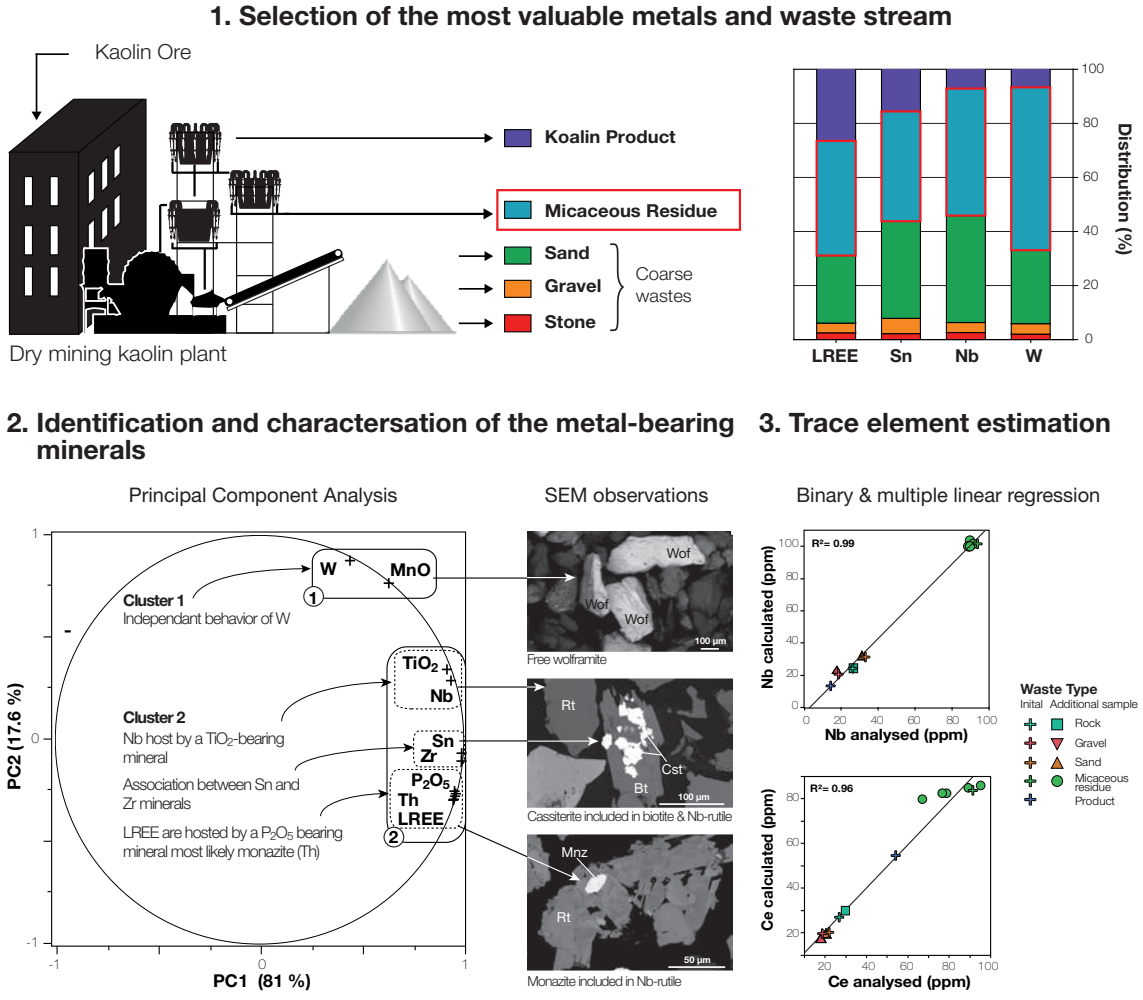

## Contents



# 3.1 Introduction

Among the 3 locations selected to assess the potential of kaolin waste streams as a source of CRMs to be recovered as by-product, the Western Area Dry Mining (WADM) plant is of great interest as it treats material from two of Imerys' largest kaolin pits located on biotite granite. In addition, it is also associated with more reliable extraction and processing method which allows to have a greater control of variable costs and reduce the impact of energy price increases (Imerys Ltd, 2008). As a consequence, first characterisation works focused on this location.

The objective of this preliminary work is to analyse every output stream of the selected plants in order to select the most valuable waste stream for CRMs recovery. This implies to assess the mean CRMs grades in each streams and to perform a metallurgical balance in order to estimate the level of pre-concentration and the distribution of each CRM of interest in the output streams. The selected wastes will be used for metallurgical assessment of CRMs recovery.

The main results for samples from the WADM plant are presented in the following article. A comparison with results obtained with samples from the two other locations, *i.e.* Treviscoe and Wheal Martyn, in terms of CRM grades and mass balance is presented after the article.

# 3.2 Selection and characterisation of the valuable stream from WADM plant

The following article analyses output streams of the WADM plant to select the most valuable waste stream for CRMs recovery. The results indicate that CRMs are pre-concentrated in the micaceous residue which contains a relatively high LREE concentration of around 170 ppm. This residue has been characterised using a two-stage gravity pre-concentration process involving a Falcon SB concentrator and a shaking table to obtain concentrates suitable for mineralogical study. A statistical analysis, combined with qualitative mineralogy, highlights the main mineralogical associations and identifies monazite, cassiterite, Nb-rutile and wolframite as the main metal-bearing minerals. Estimation formulas for Nb and LREE using only the $TiO_2$ and $SiO_2$ content of the wastes, obtained by binary and multiple linear regression, show very accurate results suggesting a possible on-line application. The selected residue will be used for metallurgical test works to assess the potential for by-product recovery of these metals.

Minerals Engineering 76 (2015) 141–153

Contents lists available at ScienceDirect

Minerals Engineering

journal homepage: www.elsevier.com/locate/mineng

# Rare earth (La, Ce, Nd) and rare metals (Sn, Nb, W) as by-product of kaolin production, Cornwall: Part1: Selection and characterisation of the valuable stream

Q. Dehaine, L.O. Filippov *

*GeoRessources, Université de Lorraine, CNRS, UMR 7359, 2 rue du Doyen Marcel Roubault, TSA 70605, F54518 Vandœuvre-lès-Nancy, France*

ARTICLE INFO

*Article history:*
Received 28 July 2014
Revised 2 October 2014
Accepted 6 October 2014
Available online 27 November 2014

*Keywords:*
Kaolin waste
Light Rare Earths
Rare metals
Gravity concentration
Statistical analysis

ABSTRACT

This paper analyses output streams of a kaolin plant to select the most valuable waste stream for metal recovery. The results indicate that rare metals (Sn, Nb, W) and Light Rare Earth Elements (LREEs) are pre-concentrated in the micaceous residue which contains a relatively high LREE (La, Ce, Nd) concentration of around 170 ppm. This residue have been characterised using a two-stage gravity pre-concentration process involving a Falcon concentrator and a shaking table to obtain concentrates suitable for mineralogical study. A statistical analysis, combined with qualitative mineralogy, highlights the main mineralogical associations and identifies monazite, cassiterite, Nb-rutile and wolframite as the main metal-bearing minerals. Estimation formulas for Nb and LREE using only the $TiO_2$ and $SiO_2$ content of the wastes, obtained by binary and multiple linear regression, show very accurate results suggesting a possible on-line application. This will provide tools to select the most valuable waste streams or the associated tailing dams (using historical data) for metals recovery. These selected wastes will be used for metallurgical test works to assess the potential for by-product recovery of these metals.



## 1. Introduction

### 1.1. Economic background

During the last few years the supply of some strategic raw materials such as the Rare Earth Elements (REEs) became a concern. No less than 97% of the REE world production is provided by China, which has recently reduced its exports in order to protect its environment (Massari and Ruberti, 2013). As a result, the REE prices increased significantly, causing tension and uncertainty in the high-technology manufacturing industry. In the light of this economic situation, the European Commission published in 2010 a list of 14 economically important Critical Raw Materials (CRMs), recently extended to 20 (European Commission, 2014). These materials, including the elements Niobium (Nb), Tungsten (W) and the Light Rare Earth Elements (LREEs), are considered to be subject to a relatively high supply risk. While LREE prices have since dropped due to re-opening of large mining projects outside China, such Mountain Pass (United States) and Mount Weld (Australia), demand for Neodymium (Nd) and Cerium (Ce) is expected to grow due to their use in permanent magnets (Kingsnorth, 2014) and some forecast see demand exceeding supply for these elements.

Rare metals granites have always been considered of poor economic value due to their low metal grades but, when altered, they are often exploited for their industrial minerals. The potential to recover the metals as by-products of industrial mineral production is therefore of significant interest. The Cornubian China clay deposits in the UK could prove a valuable resource of rare metals as the area is also well known for its historically deposits of tin and base metals and its disseminated rare metal mineralisations (Jackson et al., 1989; Manning and Hill, 1990; Manning et al., 1996; Willis-Richards and Jackson, 1989).

Kaolin extraction in Cornwall and its associated generation of size-classified waste, including crushed stones, gravels, sands and a micaceous residue, are described in Highley et al. (2009). These wastes are the coarsest fractions of the clay matrix which are not valuable for kaolin recovery and consist mainly of more or less altered host granite. The annual waste production of the whole industry is about 10 million tonnes (Highley et al., 2009) which are, in part, sold as construction material locally but the majority is engineered and disposed in large waste piles.

* Corresponding author. Tel.: +33 (0) 383596358; fax: +33 (0) 383596339.
*E-mail addresses:* quentin.dehaine@univ-lorraine.fr (Q. Dehaine), lev.filippov@univ-lorraine.fr (L.O. Filippov).

http://dx.doi.org/10.1016/j.mineng.2014.10.006
0892-6875/

### 1.2. Geological background

The China clay deposits of SW England lay on the so-called Cornubian batholith which has a 200-km-long extension, comprising six major and several minors granite bodies (Willis-Richards and Jackson, 1989). The batholith has been affected by several episodes of alteration including quartz-tourmaline veining associated with greisening and Sn–W–Cu mineralisation, intrusion of rhyolite dykes, and quartz-hematite veining. Kaolinisation is the last alteration event and was relatively extensive in the St. Austell area where the majority of the active kaolin pits are located (Fig. 1a).

The St. Austell granite is composed of six major granite types (Manning et al., 1996). The main lithology of the pluton, which represents 70% of the outcrop, is the biotite granite, exposed in the Western Area, at the eastern part of the granite and intermittently within the Central Area (Fig. 1b).

As a consequence of multiple intrusive episodes, the other granite units are mostly exposed in the Central Area such as the lithium-mica granite, the coarse and fine-grained tourmaline granite or in the Nanpean Stock for the topaz granite (Manning and Exley, 1984; Manning et al., 1996). The biotite granite, shown in Fig. 1b, is coarse grained, mainly composed of quartz, K-feldspar and micas with tourmaline as minor phase. Biotite is the main mica, but muscovite is also present. The main accessory phases are reported as rutile, topaz, apatite, monazite, cassiterite, zircon and uraninite (Manning et al., 1996). The main host for the LREE differs depending on the authors. Works of Jefferies (1985) on Carnmenellis biotite granite describe monazite as the main LREE-bearing mineral accounting for approximately 75% of the total LREE content. In contrast microprobe analysis on samples from Cornubian granites by Alderton et al. (1980) show significant concentrations (up to 0.5%) of La, Ce, Nd and Sm in other phases, particularly apatite, but also zircon and sphene.

Apart from these disseminated mineralisations, cassiterite and wolframite associated with quartz-tourmaline sheeted veins have been identified in Goonbarrow pit (Bray and Spooner, 1983). Whereas two different types of mineralisations, a Sn breccia-stockwork in the Treliver area, and a E–W veins complex enriched in base metals have been identified north of the St. Austell pluton (Camm and Dominy, 1999; Camm and Moon, 2001). In addition, Müller and Halls (2005) describe an intrusive tourmaline breccia at Wheal Remfry where zoned rutile is the principal mineral hosting Sn (up to 1.88%) and also includes high W (up to 1.95%) and Nb (up to 2.05%) domains.

Geological kaolinisation process consists in the hydrolysis of the feldspar minerals of the host rock by acid aqueous fluids to form an aggregate of kaolinite and secondary mica. As a consequence the accessory minerals of the host granite are partially liberated from the gangue with respect to the degree of kaolinisation, which allows their separation through the classification stages of the kaolin production route (Scott et al., 1998).

### 1.3. Methodology

In this study we investigate the potential of the wastes from kaolin production for metals recovery. The methodology used in this work is separated in two steps corresponding to the two main objectives of this study (Fig. 2). The first step is to analyse the typical chemical composition of the waste streams and to identify the most valuable metals present. The second step focusses on the characterisation of the selected waste stream in terms of mineralogical observations on accessory minerals, combined with analysis of the correlations between elements and oxides contents. Finally, binary and multiple linear regressions provide insight into estimating the Nb and LREE content of the waste streams.

## 2. Materials and methods

### 2.1. Material sampling

All the samples used in this work were supplied by Imerys Ltd., UK. The samples were collected and aggregated from daily sampling over one week from every output stream of the initial classification stages of the kaolin dry mining plant. The first stages of kaolin extraction consist in removing the coarsest fractions of the clay matrix which are not valuable for kaolin recovery (Fig. 3). The first sized-classified wastes *i.e.* crushed stones (21–11 cm), gravels (110–8 mm) and sands (8–0.5 mm), are removed by screening and sent to stockpiles. The last classification stage is realised by series of hydrocyclone loops. The finer (−53 μm) particles go to the product stream (hydrocyclone overflow) for further refining whereas the coarser (~500–53 μm) particles are reported to the micaceous residue (hydrocyclone underflow) where they are held in suspension and pumped to a tailing dam.

The degree of alteration varies within the deposits and is usually classified by kaolin decomposition grades, ranging from high grade, when full alteration of feldspars is observed, to low grade (nearly fresh granite) when only minor indications of alteration are observed (Mueller et al., 1999). During the sampling period, only master grade (highest kaolinisation grade) was processed with a clay matrix obtained from Virginia and Melbur pits located on biotite granite. These samples are considered to be typical material from the biotite granite.

### 2.2. Chemical analysis

Samples were crushed and riffled alternatively in accordance with the theory of sampling (Gy, 1998) to obtain representative subsamples suitable for whole rock analysis. Chemical analyses were carried out by Inductively Coupled Plasma Atom-Emission analysis (ICP-AES) for major elements and mass spectral analysis (ICP-MS) for the trace elements following the routine procedure described in Carignan et al. (2001) at the Service d'Analyses des Roches et des Minéraux (SARM-CNRS, Nancy, France). In addition, tailing samples were analysed using Laser Ablation (LA)-ICP-MS at the GeoRessources laboratory (Vandoeuvre-lès-Nancy, France) composed of a 193 nm MicroLas Pro ArF Excimer coupled with an Agilent 7500c quadrupole ICP-MS. The measurements followed the procedure described in Lach et al. (2013), using the NIST 612 glass as external standard and known compositions in Si (ICP-MS, SARM) for internal calibration. Samples were dried and pressed into pellets before being analysed. Each sample were ablated 6 times with 120 μm spots in order to ensure a representative number of data that would account for a satisfactory 'bulk' sample analysis. The results were treated following the procedure described in Longerich et al. (1996), using the Iolite software (Paton et al., 2011). For most elements the limits of detection were below the ppm level.

### 2.3. Material balance

Chemical analysis on the collected samples combined with on-line measurement data during sampling (flow rates, pulp density) was used for metallurgical accounting over a one week period. Since all output streams were sampled it was also possible to assess mean feed material composition during the sampling period. Data reconciliation was done with the BILCO software dedicated to data reconciliation by material balance. Estimation errors were computed taking into account analytical errors and errors on stream distribution estimation (set at 10%).

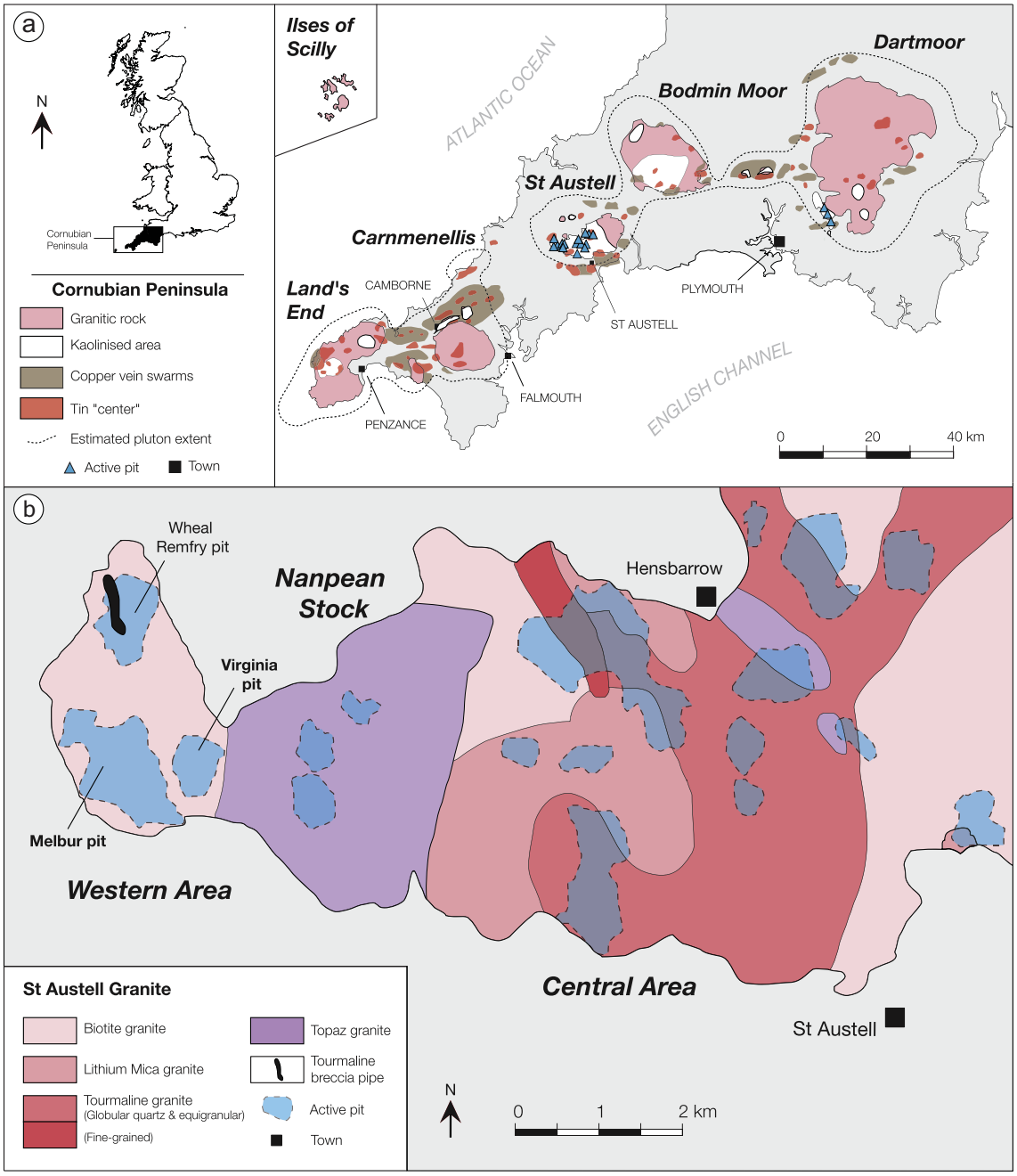


**Fig. 1.** (a) Location map of the major plutons of the Cornubian batholith showing the kaolinised areas and the active kaolin pits, (modified from Černý et al. (2005)). (b) Geological map of the St. Austell granite showing the distribution of the various granite types and the major kaolin pits including the Melbur and Virginia pits where the material for this study was collected (modified from Manning et al. (1996)).

### 2.4. Mineralogical analysis

The particle size distribution of the micaceous residue for chemical analysis was obtained from a Rotap apparatus and a standard laboratory wet and dry sieving procedure (ISO 2591-1:1988).

Qualitative mineralogical analysis of the major phases has been realised by X-ray diffraction on a Brucker's D8 Advance, operating with a cobalt Kα ray (1.789 Å), a tension of 35 kV and an intensity of 45 mA. Quantitative mineralogical analysis was undertaken by Rietveld analysis using the TOPAS software and data from chemical analysis, following the method of Johnson et al. (1985).

All textural observations and local X-ray microanalysis have been realised on a Hitachi S4800 scanning electron microscope with an imaging voltage of 20 kV and equipped for Energy-Dispersive X-ray Spectroscopy (EDS) for local semi-quantitative analysis of a wide range of elements.

### 2.5. Gravity concentration process

Characterisation of the accessory minerals assemblage of the wastes samples requires pre-concentration due to the relatively low rare metals and LREE contents. Characterisation results, especially the distribution of metals by particle size, give important information to select the most appropriate concentration technique for the recovery of these metals. Gravity separation is widely used in mineral processing for pre-concentration of high

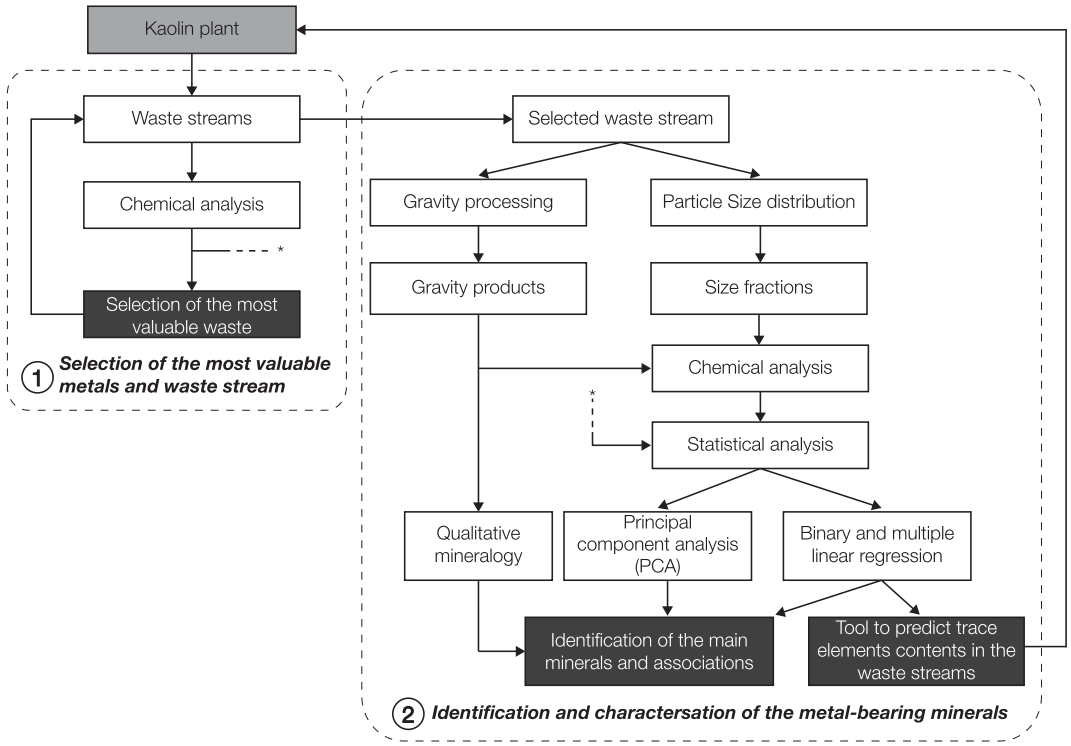


**Fig. 2.** Outline of the methodology used in this study.

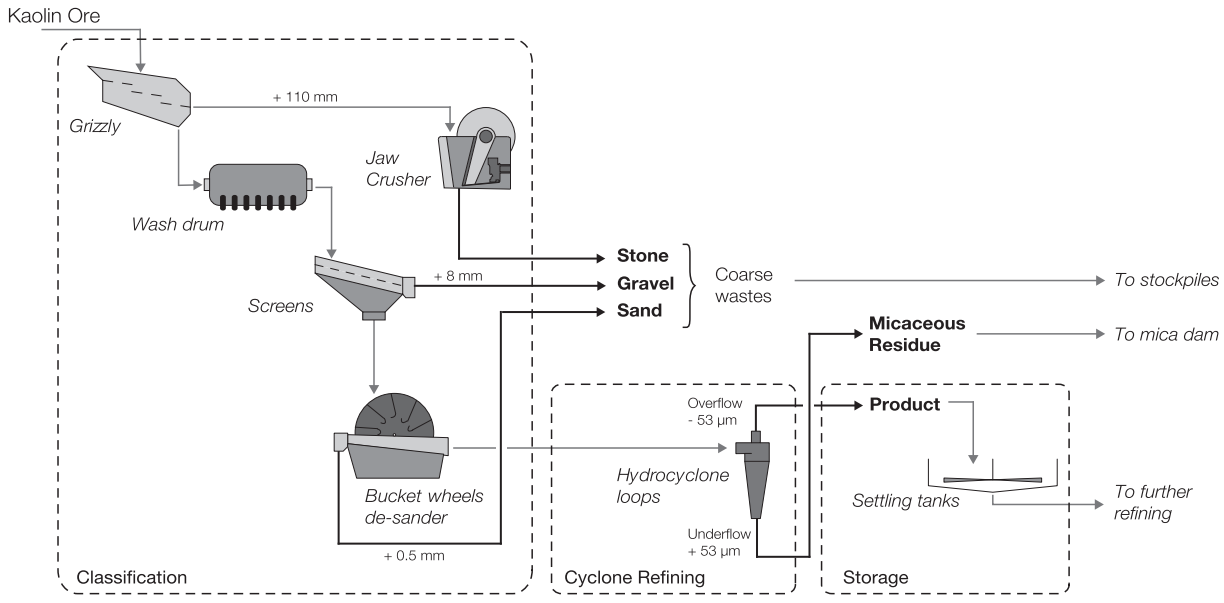


**Fig. 3.** Simplified flow sheet of the dry mining process showing the sampling points (bold lines).

specific gravity REE-bearing minerals (Jordens et al., 2013). In particular, centrifugal separators such as Falcon and Knelson concentrators are the most common gravity separators used for the recovery of fine particles (Falconer, 2003) and have proven to be effective for REE mineral recovery (Jordens et al., 2014). A 20 kg sample of micaceous residue was riffled in two sub-samples, to match the sample mass requirements of the Falcon concentrator, and introduced in a gravity concentration process (Fig. 4). The concentrates were subsequently separated to heavy and light fraction by heavy medium separation with bromoform (SG = 2.89).

The Falcon separator used in this work was a Falcon L40 laboratory model (Sepro Mineral Systems, Canada) operated with a pulp density of 30% solid and a pulp flow rate of 6.7 L/min. The operating fluidisation water pressure varied between 1.5 and 2 psi and the centrifugal field was set at 200 G's.

The shaking table used for concentration was a Wilfley laboratory shaking table. The shaking table was run at dry feed rate of 0.23 kg/min and a water throughput of 5 L/min. The operating frequency was set at 35 Hz and the deck angle at 7°. Among the 8 outputs of the discharge launder, the first output at the front of

Q. Dehaine, L.O. Filippov / Minerals Engineering 76 (2015) 141–153 

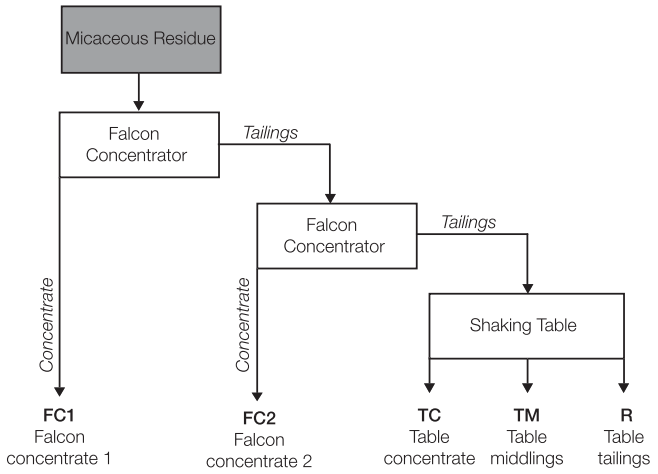


**Fig. 4.** Flowsheet of the gravity concentration experiments applied to the micaceous residue.

the deck was considered as concentrate, the second as middling and the other outputs were combined to one tailing.

## 3. Results

### 3.1. Identification of the valuable metals and waste streams

Trace element composition of the streams analysed by ICP-MS are shown in Fig. 5. The results show that the highest concentrations of metals are found in the micaceous residue obtained from the underflow of the hydrocyclones, with 168.8 ± 8.4 ppm LREE (including 40 ± 2 ppm La, 91.4 ± 4.6 ppm Ce, 37.3 ± 1.9 ppm Nd), 139.4 ± 7 ppm Sn, 93.7 ± 4.7 ppm Nb and 69.2 ± 3.5 ppm W. Since all output streams have been analysed it is possible to estimate the mean feed content of the plant during the sampling period by back-calculation (Fig. 5) and assess the distribution of the metals in the plant (Fig. 6). Comparison of the feed composition with the LREE and rare metal contents of the waste streams shows that the metals are indeed pre-concentrated into the micaceous residue and depleted in other waste streams. However, it is important to note that the LREE are also concentrated in the product stream (103.7 ± 5.2 ppm).

The distributions of the metals in the plant are less contrasted but the micaceous residue clearly accounts for a major proportion of the mass of metal entering the plant, closely followed by the sand stream and the "product" stream for the LREE only (Fig. 6). The fact that metals tend to be present, in significant amounts (especially for Sn and Nb), in the sand fraction is largely due to the size of the sand stream, which represents almost half of the total mass which is processed in the plant. Preferred separation of valuable metals is possible only if the metal-bearing minerals are liberated from the other minerals. Otherwise they would have been removed from the main stream by the bucket wheels and never enter the hydrocyclones. This implies that variations in the intensity of kaolinisation within the deposit, which results in variation in the liberation degree of the accessory minerals, have consequences on metals distribution. However, the material balance and liberation state of the minerals are linked because a less-kaolinised feed (and thus, less liberated accessory minerals) means larger proportions of coarse wastes. Therefore, the distribution of metals within the outputs of the plant reflects the liberation degree of metal-bearing minerals. Since the material fed into the plant during the sampling period corresponds to the most kaolinised material mined for kaolin, the distribution observed in (Fig. 6) could be close to the most favourable for metals enrichment for the biotite granite.

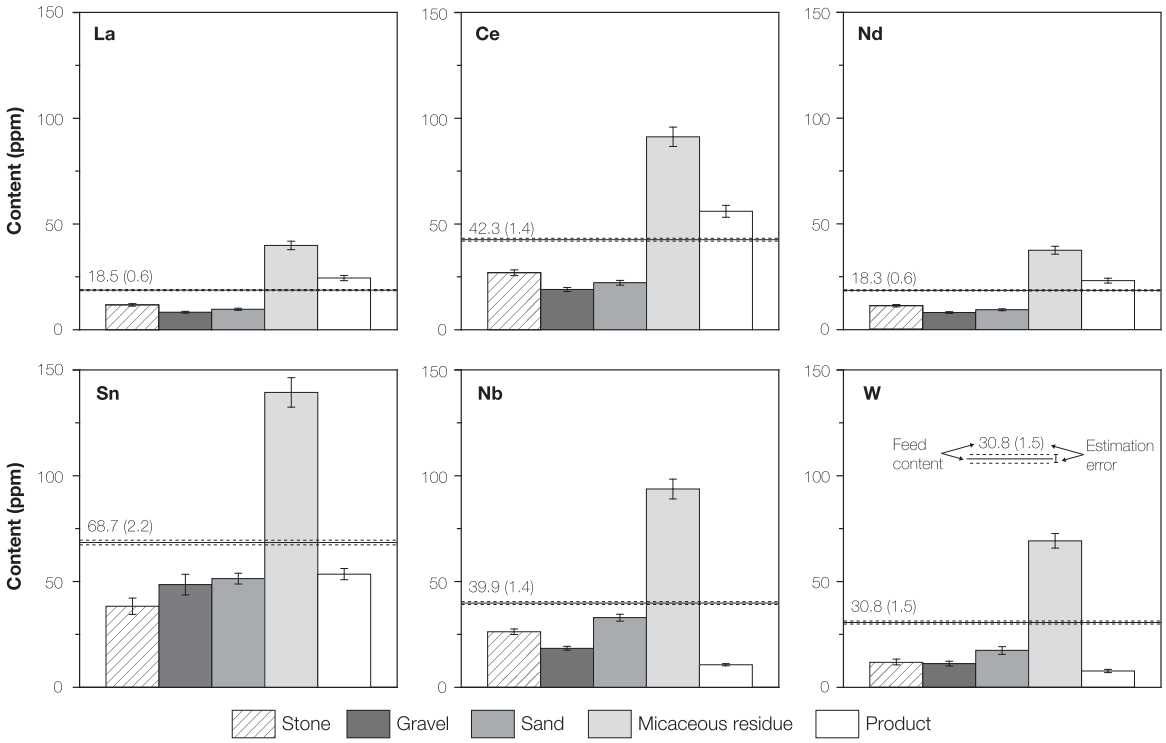


**Fig. 5.** LREE and rare metals contents in the output streams of the kaolin plant (1σ standard error bars) and the estimated feed content obtained by metallurgical accounting (with 1σ estimation error). Reported elements are concentrated in the micaceous residue. In other streams the grades are even or very similar with the exception of the LREE which are also concentrated in the product stream.

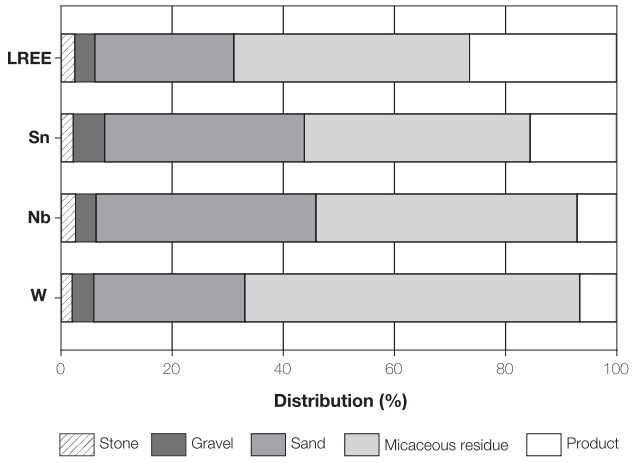


**Fig. 6.** Metallurgical balance showing the distribution of the LREE (La, Ce, Nd) and rare metals within the output streams of the kaolin dry mining plant.

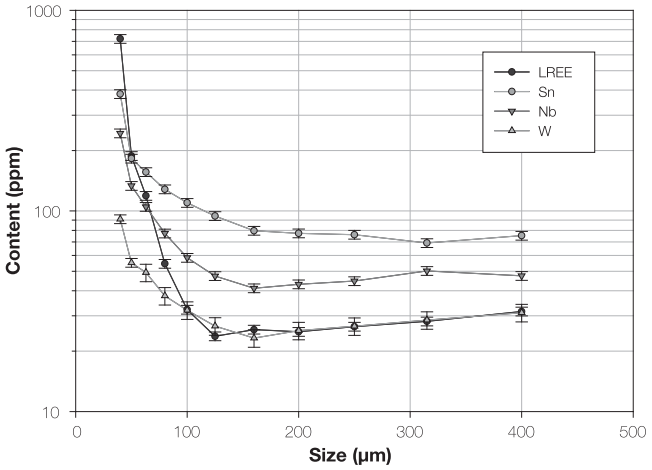


**Fig. 7.** LREE (La, Ce, Nd) and rare metals contents of the micaceous residue as a function of the particle size (upper sieve opening) and the associated uncertainty (1σ standard error bars).

### 3.2. Characterisation procedure of the selected stream

#### 3.2.1. Distribution of the metals within the micaceous residue

The mineralogy of the micaceous residue, determined by XRD analysis, is dominated by quartz, unaltered K-feldspar, mostly orthoclase, and micas. Two types of micas are present: biotite (siderophyllite-annite), and muscovite which is less abundant, confirming the observation of Manning et al. (1996). Tourmaline (schorl-dravite) is the main accessory mineral with rutile and some remaining kaolinite is also present. However, the content of the possible metals and REE minerals is too low to be detected by XRD. The mineralogical composition of the micaceous residue is given in Table 1.

Each size fraction of the micaceous residue has been analysed by ICP-MS to assess the distribution of metals in the sample. All rare metals display a similar trend, with the metal content increasing with decreasing particle size (Fig. 7). The increase in the LREE content is more pronounced towards the finest fractions.

Overall, 95% of LREE, 84% of Sn, 87% of Nb, and 83% of W are present in the size fraction below 100 μm (Table 2). This distribution of the metals in the fine fractions could explain why they are preferentially concentrated in the micaceous residue which corresponds to a hydrocyclone underflow (~500–53 μm). With 61% of the LREE content present in the −40 μm fraction, this explains why a non-negligible proportion of LREE goes in the final product, *i.e.* hydrocyclone overflow (−53 μm).

Finally it is interesting to note that a significant proportion of the metals are distributed in the −50 μm size fraction, which should have reported to the hydrocyclone overflow. Thus, it can be suggested that these metals are likely to be hosted by heavy accessory minerals.

**Table 1**
Estimated mineralogical composition of the micaceous residue samples from hydrocyclone underflow.

| Mineral | Formula | Phase (wt.%) |
|---|---|---|
| Quartz | $SiO_2$ | 36 |
| Biotite (siderophyllite-annite) | $K(Fe, Mg)_3(AlSi_3)O_{10}(F,OH)_2$ | 16 |
| Muscovite | $KAl_2(Al\ Si_3)O_{10}(F,OH)_2$ | 15 |
| K-feldspar (orthoclase, microcline) | $KAlSi_3O_8$ | 14 |
| Tourmaline (schorl-dravite) | $NaMg_{3-z}Fe^{2+}{}_zAl_6(BO_3)_3Si_6O_{18}(OH)_4$ | 10 |
| Kaolinite | $Al_2Si_2O_5(OH)_4$ | 8 |
| Rutile | $TiO_2$ | 1 |
| Total | | 100 |

**Table 2**
Distribution of mass, LREE (La, Ce, Nd) and rare metals by size-fractions in the micaceous residue.

| Size fraction (μm) | Wt.% | LREE (%) | Sn (%) | Nb (%) | W (%) |
|---|---|---|---|---|---|
| +315 | 0.3 | 0.1 | 0.1 | 0.1 | 0.2 |
| 315–250 | 0.5 | 0.1 | 0.2 | 0.3 | 0.3 |
| 250–200 | 1.5 | 0.3 | 0.8 | 0.7 | 1.0 |
| 200–160 | 2.9 | 0.5 | 1.4 | 1.3 | 1.7 |
| 160–125 | 10.3 | 1.8 | 5.4 | 4.5 | 5.6 |
| 125–100 | 12.7 | 2.1 | 7.8 | 6.4 | 7.9 |
| 100–80 | 18.0 | 4.0 | 12.9 | 11.2 | 13.4 |
| 80–63 | 17.2 | 6.5 | 14.4 | 14.1 | 15.1 |
| 63–50 | 16.0 | 13.1 | 16.3 | 17.8 | 18.3 |
| 50–40 | 8.3 | 10.7 | 9.8 | 11.7 | 10.6 |
| −40 | 12.3 | 61.0 | 30.7 | 31.8 | 26.0 |
| Total | 100 | 100 | 100 | 100 | 100 |

#### 3.2.2. Relationship between elements and oxides

Given the metals contents and distribution in the micaceous residue, it is necessary to make a pre-concentration of the accessory minerals in order to obtain a concentrate suitable for characterisation. The results of two concentration tests using a Falcon concentrator and a shaking-table are presented in Table 3.

A first screening of the chemical data, before further investigation by principal component analysis, allows assessing the relationship between some elements according to their well-known geochemical behaviour. Fig. 8 shows the strong correlation between each LREE ($R^2 > 0.99$) and between $TiO_2$ and Nb ($R^2 = 0.99$). The strong correlation between LREE involves a proportional relationship between these elements which mean constant relative proportions of (Ce/Nd) = 2.35 and (Ce/La) = 2.30 in all samples (Fig. 8a). The same observation can be made for the correlation between $TiO_2$ and Nb which suggest a proportional relationship and a constant ratio ($TiO_2$/Nb) = 55.32 in all samples (Fig. 8b). These proportional relationships, verified for all samples, suggest that LREE are likely to be located in a single phase, while the Nb is most likely associated with a $TiO_2$-bearing mineral.

#### 3.2.3. Principal component analysis on major/trace elements data

Principal Component Analysis (PCA) proved to be a powerful tool in the field of mineral processing to show relationship

**Table 3**
Chemical analysis of the gravity concentration products from the two tests on the micaceous residue from dry mining plant and the associated maximum uncertainty (SE: 1σ standard error).

| Product | Mass | Concentrations | | | | | | | |
|---|---|---|---|---|---|---|---|---|---|
| | | LREE | | Sn | | Nb | | W | |
| | (wt.%) | (wt.%) | (SE) | (wt.%) | (SE) | (ppm wt.) | (SE) | (ppm wt.) | (SE) |
| *Test 1* | | | | | | | | | |
| F | 100 | 0.011 | 0.001 | 0.017 | 0.001 | 66.4 | 0.33 | 153.5 | 0.77 |
| FC1 | 0.50 | 0.404 | 0.020 | 0.246 | 0.012 | 549.4 | 2.75 | 772.7 | 3.86 |
| FC2 | 0.50 | 0.376 | 0.019 | 0.187 | 0.009 | 577.9 | 2.89 | 313.5 | 1.57 |
| TC | 2.15 | 0.125 | 0.006 | 0.140 | 0.007 | 567.8 | 2.84 | 3736.0 | 18.68 |
| TM | 11.18 | 0.027 | 0.001 | 0.032 | 0.002 | 198.9 | 0.99 | 442.1 | 2.21 |
| R | 85.65 | 0.002[a] | <0.001[b] | 0.010[a] | <0.001[b] | 30.8[a] | 3.83[b] | 21.3[a] | 3.17[b] |
| *Test 2* | | | | | | | | | |
| F | 100 | 0.011 | 0.001 | 0.014 | 0.001 | 60.5 | 0.30 | 45.5 | 0.23 |
| FC1 | 0.44 | 0.598 | 0.030 | 0.345 | 0.017 | 736.3 | 3.68 | 646.2 | 3.23 |
| FC2 | 0.45 | 0.337 | 0.017 | 0.212 | 0.011 | 517.8 | 2.59 | 276.2 | 1.38 |
| TC | 0.27 | 0.183 | 0.009 | 0.197 | 0.010 | 923.4 | 4.62 | 2833.0 | 14.17 |
| TM | 5.75 | 0.066 | 0.003 | 0.045 | 0.002 | 344.9 | 1.72 | 201.8 | 1.01 |
| R | 92.19 | 0.003[a] | <0.001[b] | 0.009[a] | <0.001[b] | 35.5[a] | 3.59[b] | 24.2[a] | 2.69[b] |

For product's names refer to Fig. 4, F: feed calculated by mass balance, FC: Falcon concentrate, TC: table concentrate, TM: table middling and R: residue.
[a] Value calculated using mass balance and the mean value of 6 LA-ICP-MS analyses on the table tailings.
[b] Value calculated using mass balance and the calculated standard error of 6 LA-ICP-MS analyses on the table tailings.

between the chemical components and subsequently infer their mineralogy (Benzaazoua et al., 2002). PCA, applied to all chemical data, allows characterisation of the relationship between trace and major elements, with the two first principal components explaining 98.6% of the variability (Fig. 9).

Projection of elements on the PC1–PC2 plane shows two independent cluster of elements (Fig. 9, right): A group containing MnO and W (loading PC2) and another group composed of major elements $TiO_2$ and $P_2O_5$ and trace elements Nb, Sn, Zr and LREE (loading PC1). The latter can be divided into (Nb, $TiO_2$), (Sn, Zr) and (LREE, $P_2O_5$) sub-groups corresponding to stronger correlations. The layout of the individuals on the factorial plane PC1–PC2 (Fig. 9, left) indicates that these two main components are related to the concentration techniques. Thus, PC2 (loaded by MnO and W) is correlated with the points corresponding to shaking table concentrates while PC1 (loaded by $TiO_2$, $P_2O_5$ and other metals) is correlated with Falcon concentrates. This indicates a tendency to concentrate preferentially W with the shaking table and the LREE, Sn and Nb with the Falcon concentrator.

From a mineralogical point of view, the PCA suggest that W (loading PC2) is likely to be hosted by a MnO-bearing mineral that should have no mineralogical association with the minerals hosting the other metals (loading PC1). Likewise, the grouping of Nb, Sn and LREE on the PCA suggest their mineralogical association. The strong correlations of this cluster of elements, divided into three sub-groups, allow identification of the possible metal-bearing minerals. Indeed, the strong correlation between $TiO_2$ and Nb, previously observed (Fig. 8b), suggests that the host mineral for Nb should be a $TiO_2$-bearing mineral, most likely rutile as it accounts for most of the $TiO_2$ content in the samples. Similarly, the strong correlation between $P_2O_5$ and LREE suggests that these elements are hosted by a $P_2O_5$-bearing mineral such as apatite or monazite, but the correlation between LREE and Th suggest that monazite is the most likely the host mineral for the LREE. Finally,

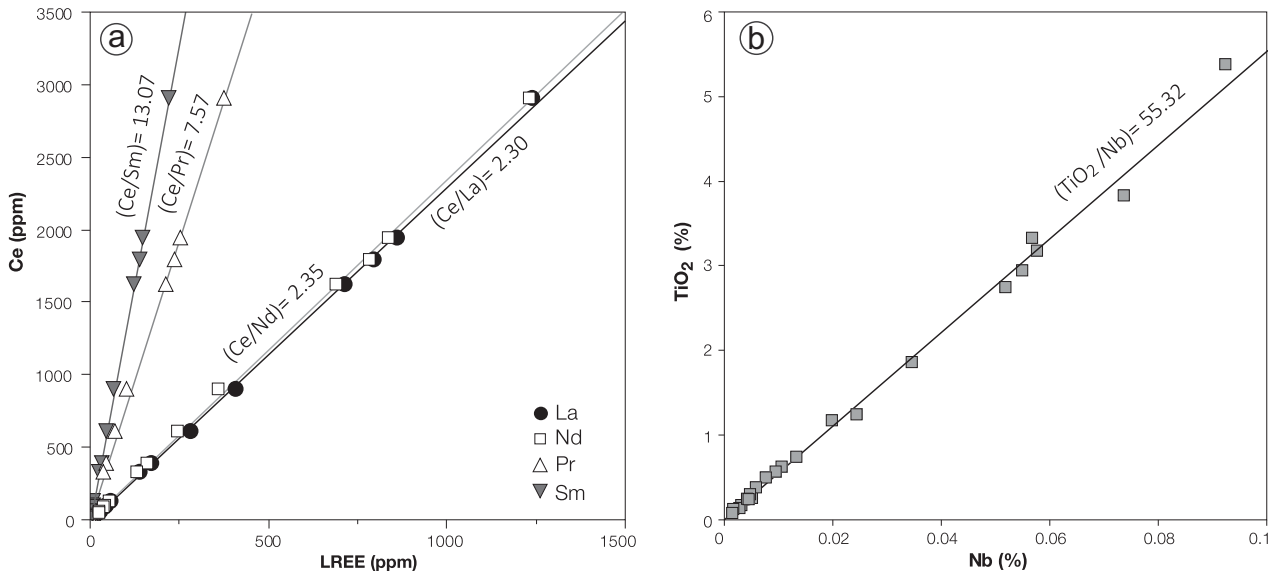


**Fig. 8.** Binary linear correlation plots and trend lines between elements using all chemical data set. (a) Strong correlations ($R^2 > 0.99$) suggesting a proportional relationship between each LREE. (b) Strong correlation ($R^2 = 0.99$) suggesting a proportional relationship between $TiO_2$ and Nb.

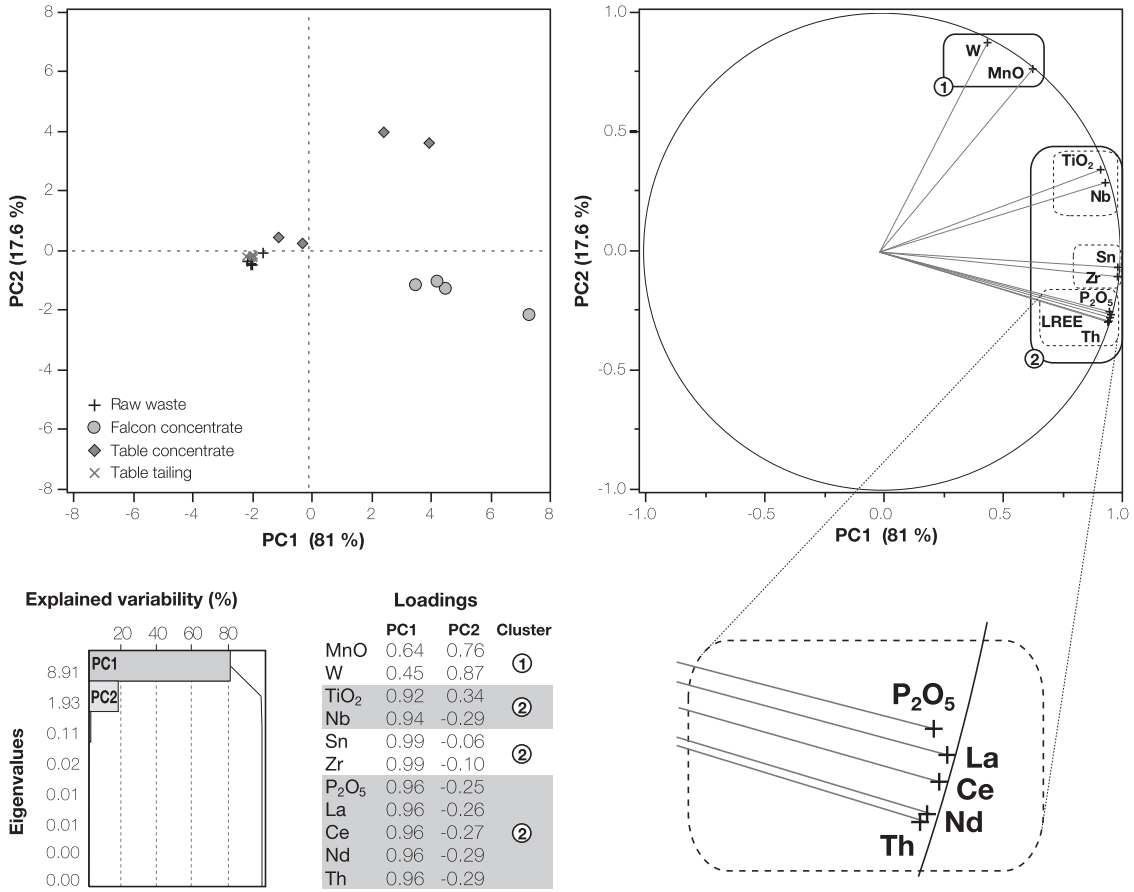


| | PC1 | PC2 | Cluster |
|---|---|---|---|
| MnO | 0.64 | 0.76 | ① |
| W | 0.45 | 0.87 | |
| $TiO_2$ | 0.92 | 0.34 | ② |
| Nb | 0.94 | -0.29 | |
| Sn | 0.99 | -0.06 | ② |
| Zr | 0.99 | -0.10 | |
| $P_2O_5$ | 0.96 | -0.25 | ② |
| La | 0.96 | -0.26 | |
| Ce | 0.96 | -0.27 | |
| Nd | 0.96 | -0.29 | |
| Th | 0.96 | -0.29 | |

**Fig. 9.** PCA applied to all chemical data set (raw wastes, gravity products). Upper left frame: projection of the individuals on the factorial plane PC1 vs. PC2, explaining 98.6% of contents variability. Upper right frame: projection of the elements/oxides (*i.e.*, variables) in the same plane and detail of one sub-cluster. Bottom left frame: eigenvalues and loadings of the principal components. This PCA allows the identification of two opposed cluster of points: Cluster 1, contain the correlated elements/oxides (W, MnO) which are enriched in shaking table concentrates whereas cluster 2 contain the correlated elements/oxides ($P_2O_5$, LREE, Th), (Sn, Zr), and (Nb, $TiO_2$), which are enriched in Falcon concentrates.

even if the correlation between the occurrence of Zr and Sn cannot be interpreted in terms of host mineral, it suggests a possible mineralogical association between their host minerals.

However, this approach has its limitations because it cannot identify some complex mineralogical associations that might occur in the sample such as one element hosted by several minerals that are also correlated because of a mineralogical association or similar physical properties. Thus, to conclude on the identity of the host minerals, all results need to be confirmed by mineralogical observation.

### 3.2.4. Confirming the results through mineralogical observations

No significant content of LREE was detected by EDS analysis although zircon is present in large amounts while apatite is less abundant. Monazite is the only LREE-bearing mineral observed as free grains (Fig. 10a), which is sometimes hosted in biotite (Fig. 10b), but most frequently in rutile (Fig. 10c). EDS analyses of monazite grains highlight a strong correlation ($R^2 = 0.92$) between Ce and La (Fig. 11a) and a relatively moderate correlation ($R^2 = 0.53$) between Ce and Nd (Fig. 11b). This low correlation between Ce and Nd can be attributed to low accuracy of the EDS analysis for Nd quantification due to peaks overlaps with Ce, La and also Sm and Pr on the EDS spectrum. Nevertheless the ratios (Ce/La) = 2.13 and (Ce/Nd) = 2.20 obtained on monazite grains are relatively close to those previously described for ICP-MS on various samples (Fig. 8a). This correspondence between the microscopic and macroscopic LREE ratios is a strong evidence, suggesting monazite as the only LREE-bearing mineral.

EDS analyses confirm the proportional relationship observed at the macroscopic scale between $TiO_2$ and Nb as all the rutile analysed contains Nb but the amount of Nb varies from one crystal to the other (2200–6900 ppm). This high Nb content variability in rutile could be again attributed to the accuracy of the EDS analysis but some observation of zoned Nb–Sn–W–Ta rutile (Fig. 10c) could also be an important factor. This zoned rutile corresponds to the specimens described in Wheal Remfry tourmaline breccia (Müller and Halls, 2005) which indicates the presence of two rutile generations.

Cassiterite was identified as the main host mineral for Sn and is often observed free (Fig. 10e), associated with rutile (Fig. 10a) or included in biotite (Fig. 10d). The latter, quite frequent, could explain the covariance between Sn and Zr highlighted by PCA, since zircon have been reported to be also included in biotite (Manning et al., 1996).

Tungsten (W) is mainly observed in free wolframite (Fig. 10f) which is consistent with PCA results and confirms that wolframite should have a hydrothermal origin rather than magmatic origin like the other metal-bearing minerals.

## 3.3. Simple and multiple linear regressions

One of the major issues in evaluating the potentiality of industrial mineral production wastes for metal recovery is to assess trace element contents in these materials. Indeed industrial mineral industry usually requires limited chemical analysis by classical techniques, mostly XRF analysis, for on-line measurement or

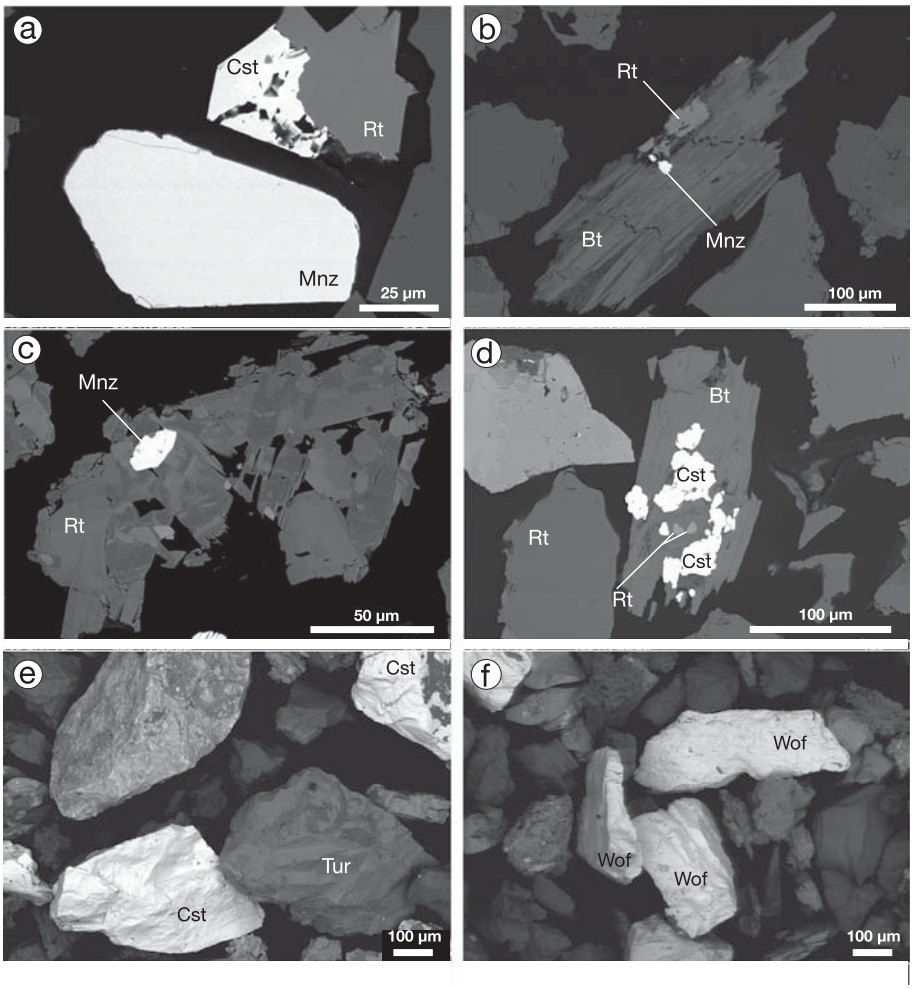


**Fig. 10.** Scanning electron micrographs in back-scattered electron mode of grains from the heavy mineral concentrates. (a) Polished sections showing free monazite (Mnz) and cassiterite (Cst) associated with Nb-rutile (Rt). (b) Polished sections showing biotite (Bt) with inclusions of Nb-rutile and monazite. (c) Polished sections showing zoned Nb–(Sn, W, Ta)-rutile with an inclusion of monazite. (d) Polished sections showing biotite with major inclusions of cassiterite and smaller inclusions of Nb-rutile. (e) and (f) Grains from the shaking table concentrates with free cassiterite, wolframite (Wof) and tourmaline (Tur).

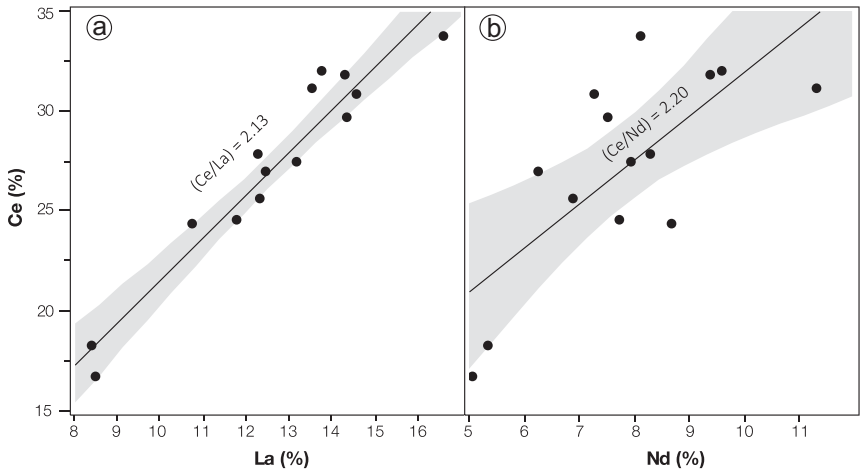


**Fig. 11.** Binary linear correlation plots, 95% confidence intervals and trend lines between LREE contents in monazites obtained by EDS analysis. (a) Strong correlation ($R^2$ = 0.92) between Ce and La suggesting a constant ratio (Ce/La) = 2.13 close to the one determined by ICP-MS analyses on raw samples. (b) Moderate correlation ($R^2$ = 0.53) between Ce and Nd, due to the low accuracy of the EDS analysis for LREE. However it is noticeable that the mean ratio (Ce/Nd) = 2.20 is close to the one determined by ICP-MS analyses on raw samples.

resource evaluation. The LREE and rare metal grades in the studied materials are close or below the limits of detection of such techniques and cannot be estimated correctly. Although the use of more accurate techniques such as ICP-MS may be possible on-line (Beeston et al., 2007), they are more expansive and difficult to implement due to practical reasons. Thus, it is interesting to

develop tools to assess trace elements contents using available data (*i.e.* major elements content).

*3.3.1. Simple linear regression to assess Nb content in waste streams*

One of the most obvious relationships to use to assess Nb content in waste streams is the strong correlation ($R^2$ = 0.99) between $TiO_2$ and Nb (Fig. 8b). This correlation suggests that it is possible to assess the Nb content in all waste streams using the following expression:

$$\text{Nb (ppm)} = 179.87 \cdot \text{TiO}_2\ (\%) \quad (1)$$

In order to assess the accuracy of this estimation tool, some additional samples from the kaolin production plant, using the same feed material, were analysed for trace element content. The relationship between Nb analysed by ICP-MS and Nb calculated using Eq. (1) is presented in Fig. 12a. Estimated values are very close to the calculated ones ($R^2$ = 0.99) with a trend line slope close to 1. The comparison between calculated and estimated values show that the difference between both values vary from 0 to 13.8 ppm for the materials with the highest Nb contents (*i.e.* micaceous residue) which is far below the typical estimation error of XRF analysis.

*3.3.2. Multiple linear regression to assess LREE content in waste streams*

Results from PCA and mineralogical observations suggest that the same method can be used to estimate the LREE content in the waste streams using the $P_2O_5$ content. Although the plot of the relationship between $P_2O_5$ and Ce shows that if there is a good correlation between these two variables, it is only valid for the gravity concentration product (Fig. 13). Indeed, the $P_2O_5$ content corresponding to monazite is diluted in the raw waste streams by the presence of other $P_2O_5$-bearing minerals such as apatite which leads to the absence of a clear relationship between the $P_2O_5$ and the LREE. On the contrary, these other phosphate minerals have been removed during the concentration process in favour of monazite, which is the main $P_2O_5$-bearing mineral in the concentrates.

However the established correlation between LREE and major elements, highlighted by the PCA analysis and mineralogical observations, suggest that a multiple linear regression is most appropriate to assess the LREE contents in waste streams. The total number of major elements in typical chemical analysis rising to 11 (LOI included), at least the same number of samples are required to initialize the multiple linear regression.

Thus, it is necessary to use, in addition to the 5 initial waste samples, the 8 additional samples to initialize the regression and increase the accuracy of the prediction formula. A multiple linear regression has been repeated successively removing one by one insignificant oxide terms (using the Student's *T*-test). The following expressions were obtained:

$$\text{Ce (ppm)} = 105.87 - 1.26 \cdot \text{SiO}_2\ (\%) + 111.93 \cdot \text{TiO}_2\ (\%)\ \text{(all waste streams)} \quad (2)$$

$$\text{Ce (ppm)} = -25.61 - 4.72 \cdot \text{SiO}_2\ (\%) + 758.32 \cdot \text{TiO}_2\ (\%)\ \text{(micaceous residue)} \quad (3)$$

The role of $TiO_2$ in these polynomials can be interpreted as a consequence of the mineralogical association between monazite and rutile, more significant than the nature of their host mineral at the waste streams level. The role of $SiO_2$ cannot be interpreted as the result of any mineralogical association, but rather as a dilution effect of $SiO_2$. Fig. 12b shows that the Ce contents estimated by Eq. (2) are highly correlated ($R^2$ = 0.96) to the analysed Ce contents, with a regression slope close to 1. However, Ce estimations for the micaceous residue seem to have a slightly different behaviour. Indeed the points corresponding to the micaceous residue are aligned following a different trend line, indicating a correlation with different regression coefficients expressed in the polynomial (3). In this polynomial, the weight of the $TiO_2$ term is more important which remains consistent because rutile is separated preferably in the micaceous residue. Ce contents estimated with Eq. (3) are much closer to the analysed content as shown in Fig. 12c. Thus, it is possible to estimate accurately, the Ce content from $TiO_2$ and $SiO_2$ content in the wastes, and therefore all the other LREE through the coefficients presented in Fig. 8.

## 4. Discussion

Every year around 145,000 tonnes of micaceous residue are produced by the kaolin plant using material extracted from Melbur and Virginia pit. Considering the biotite granite as a quite homogeneous source for the LREE and rare metals, as it has been suggested for other granite types in the St. Austell area (Scott et al., 1998), chemical data from Fig. 5 suggest that around 13 t Ce, 6 t La, 5 t Nd and 20 t Sn is lost every year in the micaceous residue going to waste. This rough estimation indicates that this waste stream and the associated tailing dams, fed by material from biotite granite, could be a potential source for these metals. However the dams are not homogenous and comprise layers which contribute to the stability of the structure. In a normal circumstance, the backfilled areas have layers of micaceous residue, clay and sand. Thus, the pre-concentration of the micaceous residue is diluted by the other materials. In addition some tailing dams were fed with material from different granite which could also contribute to the dilution. However, the other granite types also display interesting accessory minerals, for instance, the micaceous from Li-mica granite can be treated for lithium recovery (Siame and Pascoe, 2011).

Numerous rare metal granites worldwide associated with Sn, W, and Ta–Nb disseminated mineralisations display similarities with the St. Austell granite (Černý et al., 2005). Some of this granites are associated to kaolin deposits which are also known to display similarities with Cornwall deposits (Wilson and Jiranek, 1995; Wilson et al., 1997). The Yichun granite (China) is one of the closest geologically, also composed of several units including biotite granite and a most evolved Li-mica granite with a similar accessory assemblage including, topaz, monazite, zircon with columbite group minerals, microlite, rutile and cassiterite as the main Nb, Ta, Sn-bearing minerals (Belkasmi et al., 2000; Yin et al., 1995). The Beauvoir granite (Massif Central, France) is also very similar to the St. Austell granite and display a Sn–Li–Ta–Nb–Be disseminated mineralisation and accessory minerals such as topaz, apatite, amblygonite, columbite–tantalite, microlite, zircon, uraninite and sphalerite (Cuney et al., 1992; Raimbault et al., 1995). Further similarities exist with the Podlesí granite (Czech Republic), which is composed of three magmatic units, including biotite granite, and two Li-mica granites which all contain disseminated Ta–Nb–Ti–W–Sn minerals including rutile, cassiterite, Fe-columbite, ixiolite and ferberite (Breiter et al., 2007). All the above-cited deposits are considered as potential source for Nb, Ta, Sn or W and some of them are actually mined for these metals. For instance the Yichun granite is mined for Ta and Li (Schwartz, 1992) and the Beauvoir granite is known to produce cassiterite (800 g/t Sn) and columbite (190 g/t Ta plus 120 g/t Nb) as by-product of the kaolin production (Pohl, 2011).

These industrial examples, combined with the previously cited annual tonnages, highlight the potential for LREE and rare metal recovery from the St. Austell biotite granite. However, characterisation results presented in this study also bring out the relative complexity of this potential "poly-metallic ore". Indeed, even if

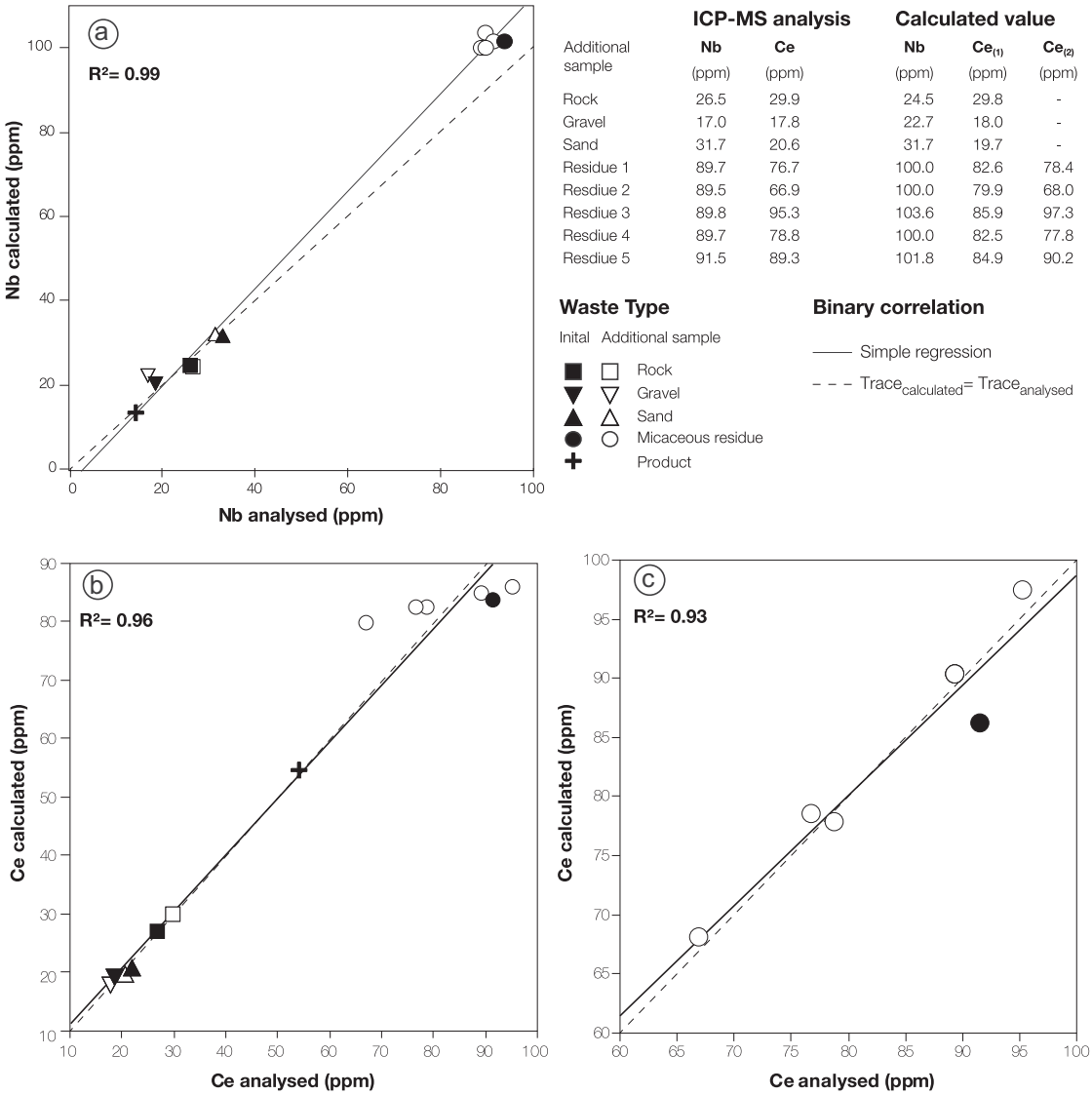


| Additional sample | ICP-MS analysis Nb (ppm) | ICP-MS analysis Ce (ppm) | Calculated value Nb (ppm) | Calculated value $Ce_{(1)}$ (ppm) | Calculated value $Ce_{(2)}$ (ppm) |
|---|---|---|---|---|---|
| Rock | 26.5 | 29.9 | 24.5 | 29.8 | - |
| Gravel | 17.0 | 17.8 | 22.7 | 18.0 | - |
| Sand | 31.7 | 20.6 | 31.7 | 19.7 | - |
| Residue 1 | 89.7 | 76.7 | 100.0 | 82.6 | 78.4 |
| Resdiue 2 | 89.5 | 66.9 | 100.0 | 79.9 | 68.0 |
| Resdiue 3 | 89.8 | 95.3 | 103.6 | 85.9 | 97.3 |
| Resdiue 4 | 89.7 | 78.8 | 100.0 | 82.5 | 77.8 |
| Resdiue 5 | 91.5 | 89.3 | 101.8 | 84.9 | 90.2 |

**Fig. 12.** Comparison between trace element contents analysed by ICP-MS and calculated using linear regression models on initial and additional waste samples. (a) Strong correlation ($R^2$ = 0.99) between Nb calculated using binary correlation formula (1) and Nb analysed. (b) Strong correlation ($R^2$ = 0.96) between Ce calculated using polynomial (2), obtained by multiple linear regression, and Ce analysed with however a different behaviour of the micaceous residue plots. (c) Strong correlation ($R^2$ = 0.93) between Ce calculated using polynomial (3), obtained by multiple linear regression, and Ce analysed for the micaceous residue only.

the objectives of this work were not to develop a concentration process, it is worthwhile to observe that concentrate grades remain low. This could be explained by the fact that most of the metals lies in the fine (<100 μm) or ultrafine (<40 μm) fractions while the micaceous residue has a wide size distribution. Moreover even if the metal-bearing minerals are liberated from the gangue, some of them remains associated or included in minerals with intermediate densities, sometimes difficult to concentrate by gravity concentration. Thus, the concentration of these metals by these techniques is a real challenge that will involve the use of non-conventional techniques such as centrifugal separators like the Falcon concentrator, which is dedicated to the recovery of ultrafine particles (*e.g.* Falcon UF).

## 5. Conclusions

This study shows that when treating high grade kaolin ore, the LREE and rare metals are pre-concentrated in the micaceous residue as a consequence of the pre-concentration of the accessory minerals from the host granite in the hydrocyclone underflow. This preferred separation of the rare metals and LREE can be explained by the high proportion of medium and high specific gravity minerals in the fine fraction of the clay matrix.

A statistical analysis combined with mineralogical observations have allowed to identify monazite as the only LREE-bearing mineral and rutile as the only host for Nb while cassiterite and wolframite are the main Sn and W bearing minerals respectively. Monazite and cassiterite are either free or associated with rutile and biotite. PCA analysis reveals that W is independent of other metals and no mineralogical association have been observed for wolframite which is believed to have a hydrothermal origin.

Finally, the use of single or multiple linear regressions has suggested tools to predict Nb and LREE contents in the waste streams using $TiO_2$ (and $SiO_2$) contents. For instance, rutile being the only host for Nb, the $\%TiO_2$ content of a waste stream, affected by an adequate coefficient (179.87) is sufficient to estimate its Nb content (in ppm) accurately. The analysis of these oxides is routinely performed in the kaolin industry because $TiO_2$ is considered as a pollutant of the kaolin product and $SiO_2$ enters in the composition

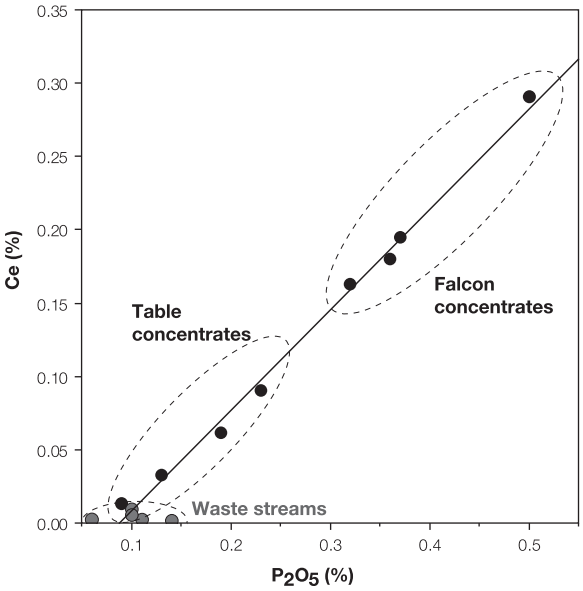


**Fig. 13.** Relationship between Ce and $P_2O_5$ analysed by ICP-MS displaying a good correlation for gravity concentration product and no correlation for the raw waste streams.

of kaolinite. This will provide tools to select the most valuable waste streams or the associated tailing dams (using historical data) for metals recovery. These selected wastes will be therefore used for metallurgical test works to conclude on the by-product potentiality of these metals.

## Acknowledgments

The authors wish to thank the Imerys Ltd., UK, and especially S. Moradi for his support and the access to the samples. This work has been financially supported by the European FP7 project "Sustainable Technologies for Calcined Industrial Minerals in Europe" (STOICIM), Grant NMP2-LA-2012-310645.

## References

Alderton, D.H.M., Pearce, J.A., Potts, P.J., 1980. Rare earth element mobility during granite alteration: evidence from southwest England. Earth Planet. Sci. Lett. 49, 149–165. http://dx.doi.org/10.1016/0012-821X(80)90157-0.

Beeston, M.P., Glass, H.J., van Elteren, J.T., Slejkovec, Z., 2007. Assessment of elemental mobility in soil using a fluidised bed approach with on-line ICP-MS analysis. Anal. Chim. Acta 599, 264–270. http://dx.doi.org/10.1016/j.aca.2007.08.022.

Belkasmi, M., Cuney, M., Pollard, P.J., Bastoul, A., 2000. Chemistry of the Ta–Nb–Sn–W oxide minerals from the Yichun rare metal granite (SE China): genetic implications and comparison with Moroccan and French Hercynian examples. Mineral. Mag. 64, 507–523. http://dx.doi.org/10.1180/002646100549391.

Benzaazoua, M., Marion, P., Liouville-Bourgeois, L., Joussemet, R., Houot, R., Franco, A., Pinto, A., 2002. Mineralogical distribution of some minor and trace elements during a laboratory flotation processing of Neves-Corvo ore (Portugal). Int. J. Miner. Process. 66, 163–181. http://dx.doi.org/10.1016/S0301-7516(02)00015-7.

Bray, C.J., Spooner, E.T.C., 1983. Sheeted vein Sn–W mineralization and greisenization associated with economic kaolinization, Goonbarrow China clay pit, St. Austell, Cornwall, England: geologic relationships and geochronology. Econ. Geol. 78, 1064–1089. http://dx.doi.org/10.2113/gsecongeo.78.6.1064.

Breiter, K., Škoda, R., Uher, P., 2007. Nb–Ta–Ti–W–Sn-oxide minerals as indicators of a peraluminous P- and F-rich granitic system evolution: Podlesí, Czech Republic. Mineral. Petrol. 91, 225–248. http://dx.doi.org/10.1007/s00710-007-0197-1.

Camm, G., Dominy, S., 1999. Tin mineralization and structure at Treliver, St. Austell, mid-Cornwall. Geosci. South West England 9, 370–373.

Camm, G., Moon, C., 2001. Surficial geochemical signatures of tin and tungsten deposits north of the St. Austell Granite. Geosci. South West England 10, 215–220.

Carignan, J., Hild, P., Mevelle, G., Morel, J., Yeghicheyan, D., 2001. Routine analyses of trace elements in geological samples using flow injection and low pressure on-line liquid chromatography coupled to ICP-MS: a study of geochemical reference materials BR, DR-N, UB-N, AN-G and GH. Geostand. Geoanal. Res. 25, 187–198. http://dx.doi.org/10.1111/j.1751-908X.2001.tb00595.x.

Černý, P., Blevin, P.L., Cuney, M., London, D., 2005. Granite-related ore deposits. In: Hedenquist, J.W., Thompson, J.F.H., Goldfarb, R.J., Richards, J.P. (Eds.), Economic Geology 100th Anniversary Volume. Littleton, Colorado, pp. 337–370.

Cuney, M., Marignac, C., Weisbrod, A., 1992. The Beauvoir topaz-lepidolite albite granite (Massif Central, France): the disseminated magmatic Sn–Li–Ta–Nb–Be mineralization. Econ. Geol. 87, 1766–1794. http://dx.doi.org/10.2113/gsecongeo.87.7.1766.

European Commission, 2014. Report on Critical Raw Materials for the EU, Report of the Ad hoc Working Group on Defining Critical Raw Materials. Brussels.

Falconer, A., 2003. Gravity separation: old technique/new methods. Phys. Separat. Sci. Eng. 12, 31–48. http://dx.doi.org/10.1080/1478647031000104293.

Gy, P., 1998. Sampling for Analytical Purposes, first ed. John Wiley & Sons, Chichester.

Highley, D.E., Brown, T.J., Harrison, D.J., Lusty, P.A.J., Cameron, D.G., Cowley, J., 2009. In: Highley, D.E., Brown, T.J., Harrison, D.J., Lusty, P.A.J., Cameron, D.G., Cowley (Eds.), Mineral Planning Factsheet: Kaolin. British Geological Survey, Nottingham.

Jackson, N.J., Willis-Richards, J., Manning, D.a.C., Sams, M.S., 1989. Evolution of the Cornubian ore field, Southwest England; Part II, Mineral deposits and ore-forming processes. Econ. Geol. 84, 1101–1133. http://dx.doi.org/10.2113/gsecongeo.84.5.1101.

Jefferies, N., 1985. The distribution of the rare earth elements within the Carnmenellis Pluton, Cornwall. Mineral. Mag. 49, 495–504. http://dx.doi.org/10.1180/minmag.1985.049.353.02.

Johnson, L.J., Chu, C.H., Hussey, G.A., 1985. Quantitative clay mineral analysis using simultaneous linear equations. Clays Clay Miner. 33, 107–117. http://dx.doi.org/10.1346/CCMN.1985.0330204.

Jordens, A., Cheng, Y.P., Waters, K.E., 2013. A review of the beneficiation of rare earth element bearing minerals. Miner. Eng. 41, 97–114. http://dx.doi.org/10.1016/j.mineng.2012.10.017.

Jordens, A., Sheridan, R.S., Rowson, N.A., Waters, K.E., 2014. Processing a rare earth mineral deposit using gravity and magnetic separation. Miner. Eng. 62, 9–18. http://dx.doi.org/10.1016/j.mineng.2013.09.011.

Kingsnorth, D.J., 2014. Personal Communication.

Lach, P., Mercadier, J., Dubessy, J., Boiron, M.-C., Cuney, M., 2013. In situ quantitative measurement of rare earth elements in uranium oxides by laser ablation-inductively coupled plasma-mass spectrometry. Geostand. Geoanal. Res. 37, 277–296. http://dx.doi.org/10.1111/j.1751-908X.2012.00161.x.

Longerich, H., Jackson, S., Günther, D., 1996. Inter-laboratory note. Laser ablation inductively coupled plasma mass spectrometric transient signal data acquisition and analyte concentration calculation. J. Anal. At. Spectrom. 11. http://dx.doi.org/10.1039/JA9961100899.

Manning, D.A.C., Exley, C.S., 1984. The origins of late-stage rocks in the St Austell granite – a re-interpretation. J. Geol. Soc. 141, 581–591. http://dx.doi.org/10.1144/gsjgs.141.3.0581.

Manning, D.A.C., Hill, P.I., 1990. The petrogenetic and metallogenetic significance of topaz granite from the southwest England orefield. Geol. Soc. Am. Spec. Pap. 246, 51–70. http://dx.doi.org/10.1130/SPE246-p51.

Manning, D.A.C., Hill, P.I., Howe, J.H., 1996. Primary lithological variation in the kaolinized St Austell Granite, Cornwall, England. J. Geol. Soc. 153, 827–838. http://dx.doi.org/10.1144/gsjgs.153.6.0827.

Massari, S., Ruberti, M., 2013. Rare earth elements as critical raw materials: focus on international markets and future strategies. Resour. Pol. 38, 36–43. http://dx.doi.org/10.1016/j.resourpol.2012.07.001.

Mueller, S., Scott, P.W., Evans, M.J., 1999. Kaolinisation, mineralisation and structures in biotite granite at Bodelva, St. Austell, Cornwall. Proc. Ussher Soc. 9, 310–317.

Müller, A., Halls, C., 2005. Rutile—the tin–tungsten host in the intrusive tourmaline breccia at Wheal Remfry, SW England. In: Mao, J., Bierlein, F. (Eds.), Mineral Deposit Research: Meeting the Global Challenge SE – 115. Springer, Berlin, pp. 441–444, http://dx.doi.org/10.1007/3-540-27946-6_115.

Paton, C., Hellstrom, J., Paul, B., Woodhead, J., Hergt, J., 2011. Iolite: freeware for the visualisation and processing of mass spectrometric data. J. Anal. At. Spectrom. 26, 2508. http://dx.doi.org/10.1039/c1ja10172b.

Pohl, W.L., 2011. Economic geology of metals. In: Wiley-Blackwell (Ed.), Economic Geology Principles and Practice: Metals, Minerals, Coal and Hydrocarbons – Introduction to Formation and Sustainable Exploitation of Mineral Deposits. Oxford, UK, pp. 149–284. http://dx.doi.org/10.1002/9781444394870.ch2.

Raimbault, L., Cuney, M., Azencott, C., Duthou, J.-L., Joron, J.L., 1995. Geochemical evidence for a multistage magmatic genesis of Ta–Sn–Li mineralization in the granite at Beauvoir, French Massif Central. Econ. Geol. 90, 548–576. http://dx.doi.org/10.2113/gsecongeo.90.3.548.

Schwartz, M.O., 1992. Geochemical criteria for distinguishing magmatic and metasomatic albite-enrichment in granitoids: examples from the Ta–Li granite Yichun (China) and the Sn–W deposit Tikus (Indonesia). Miner. Deposita 27, 101–108. http://dx.doi.org/10.1007/BF00197092.

Scott, P., Pascoe, R., Hart, F., 1998. Columbite–tantalite, rutlie and other accessory minerals from the St Austell topaz granite, Cornwall. Geosci. South-West England 9, 165–170.

Siame, E., Pascoe, R.D., 2011. Extraction of lithium from micaceous waste from China clay production. Miner. Eng. 24, 1595–1602. http://dx.doi.org/10.1016/j.mineng.2011.08.013.

Willis-Richards, J., Jackson, N., 1989. Evolution of the Cornubian ore field, Southwest England; Part I, Batholith modeling and ore distribution. Econ. Geol. 84, 1078–1100.

Wilson, I., Jiranek, J., 1995. Kaolin deposits of the Czech Republic and some comparisons with south-west England. Proc. Usher Soc. 8, 357–362.

Wilson, I.R., Halls, C., Spiro, B., 1997. A comparison between the China clay deposits of China and Cornwall. Proc. Usher Soc. 9, 195–200.

Yin, L., Pollard, P.J., Shouxi, H., Taylor, R.G., 1995. Geologic and geochemical characteristics of the Yichun Ta–Nb–Li deposit, Jiangxi Province, South China. Econ. Geol. 90, 577–585. http://dx.doi.org/10.2113/gsecongeo.90.3.577.

## 3.3 Comparison with other locations

Results for WADM samples show that CRMs and Sn are pre-concentrated in the micaceous residue, as a consequence of the preferred separation of the heavy minerals in the hydrocyclone underflow. Comparison of the metal concentration patterns in the output streams of the 3 investigated locations is presented in Figure 3.1. Most of the metals, with the exception of LREE, display a similar trend than observed for the WADM samples, with an increasing grade from the coarsest waste to the micaceous residue which display the highest overall grades. The pattern is slightly different for LREE grade which continues to increase in the product stream displaying the highest LREE grade for Treviscoe (TWM) and Wheal Martyn (WMHM) samples which means that LREE are more concentrated in the finer fractions of the clay matrix. It can be noted that most CRMs are also slightly more concentrated in the first stream (stone or stent) than in the following stream. This could be a consequence of the extraction method for THM and WMHM as the stent fraction also contains fine material which sticks to the boulders or gravels. Similarly the stone fraction for WADM plant is removed prior to washing and it is known that certain amounts of fine material is also lost in this residue stream (Section 1.3.2).

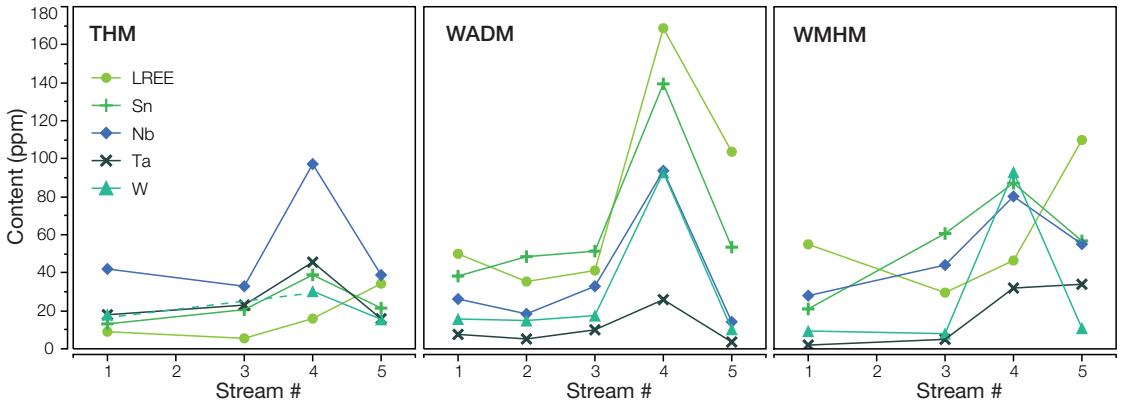


Figure 3.1: CRMs concentration patterns in the output streams of the 3 investigated locations. Streams are numbered as (1) rock/stent, (2) gravel, (3) sands, (4) micaceous residue and (5) product. W grade in stream 3 of THM is not shown because the sample was contaminated.

There is no flowrate recording or systematic weighting for THM and WMHM primary classification processes. Thus, an estimation of the mass balance for these locations was assessed using average production data (Table 3.1). An estimation of the average mass balance of THM and WMHM could be obtained by combining the mass balance for grade III and IV into a grade III-IV (Imerys, personal communication).

Table 3.1: Average distributions (in wt.%) by ore grade. Average grade III-IV is obtained with combining gravel and stone in stent (Imerys, personal communication).

| Stream | Stones | Gravel | Sand | Micaceous | Product |
|---|---|---|---|---|---|
| Grade | Stent | | | residue | |
| V | 4.0 | 8.0 | 48.0 | 20.0 | 20.0 |
| IV | 9.0 | 18.0 | 45.0 | 18.0 | 10.0 |
| III | 18.0 | 27.0 | 36.0 | 9.0 | 10.0 |
| III-IV (THM, WMHM) | 36.0 | | 40.5 | 13.5 | 10.0 |

The material balances allow assessing the distribution of the CRMs within the outputs streams (Figure 3.2). Distribution of metals in TWM and WMHM are sensibly different from WADM as most of the metals are distributed in the coarsest streams (stent and sand), with the exception of Ta and W for WMHM which are mostly distributed in the micaceous residue. Apart from W in WMHM, the CRMs display a less contrasted distribution for the hydraulic mining processes. Indeed Sn, Nb and Ta are slightly more distributed in the sands then equally distributed between stent and the micaceous residue whereas the LREE show a more important proportion in the stent and product stream. The product stream accounts in all plants for a non-negligible proportion of the LREE initially within the clay matrix. This could be explained by the presence of ultrafine monazite either free or hosted in micas aggregates as observed by Manning et al. (1996) on fresh granite.

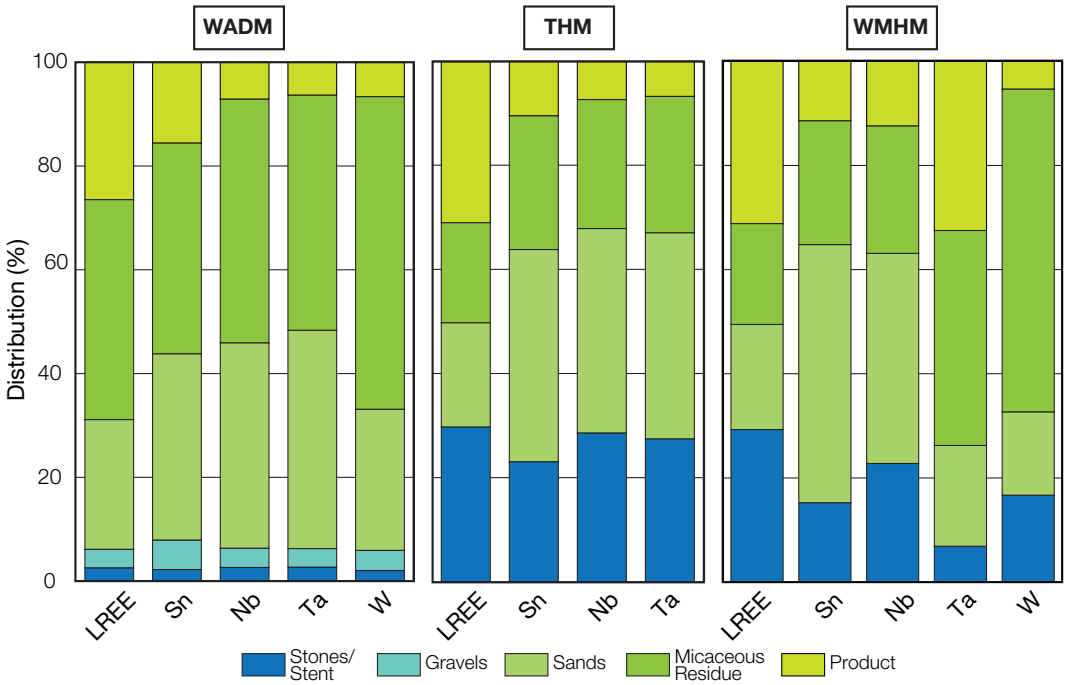


Figure 3.2: Metallurgical balances showing the distribution of the LREE (La, Ce, Nd) and rare metals (Sn, Nb, Ta, W) within the output streams of the Western Area, Treviscoe and Wheal Martyn processes.

The fact that the CRMs tend to go, in a non-negligible proportion in the sands, is largely affected by the material balances which tip the scale in favour of the coarsest waste streams especially for the hydraulic mining process as they represent around 77% of the total mass of the material processed. Moreover the separation of the CRM-bearing minerals in the hydrocyclone underflow is favoured if they are liberated from the gangue. Otherwise they could be removed from the main stream by the sand screens and never enter the hydrocyclones.

Hence, the importance of the sand waste stream in terms of metal distribution also reflects that the CRM-bearing minerals are not fully liberated. This could be explained by the variations in the intensity of kaolinisation within the deposits which results in variation in the liberation state of the accessory minerals. However, these two explanations are linked because a less kaolinised feed (and thus less liberated CRM-

bearing minerals) means lower yields and larger proportions of coarse wastes.

The material mined in Treviscoe pit during sampling was low grade (grade III-IV). Therefore CRMs-bearing minerals are less liberated which could explain the lower grades in the micaceous residue but not the overall depleted grades compared to WADM. Indeed the overall LREE and Sn grades obtained by ICP-MS are significantly higher for WADM than for THM and WHMH. Nb and Ta grade in the micaceous residue are of the same order of magnitude for the 3 locations, whereas the W grade is 3 times lower in THM. This highlights strong differences in CRMs content of the ore processed during the sampling exercises which can largely be attributed to the different origin of the feed materials. This is confirmed by the recalculated feed (matrix) grades for the 3 locations which clearly shows higher LREE, Sn and W grades in the WADM matrix while Nb-Ta grades are slightly higher for THM matrix (Table 3.2).

This is somehow surprising as the St Austell topaz granite, covered by the Treviscoe kaolin operations, was considered as one of the most prospective source for CRMs recovery from a metallogenic point of view because of its strong similarity with other rare-metal granites considered for CRMs recovery (see Section 1.2.3). In addition, the high Nb-Ta grades obtained after a two-stage gravity concentration on hydrocyclone underflow samples presented in Scott et al. (1998), suggested that micaceous residue from these areas may have a potential interest for CRMs recovery. Even if the metal content in the residue samples treated in this paper is not known, it is likely to be significantly higher than the one observed in this work with micaceous residue from THM. However, because of the hydraulic extraction used for THM, samples cannot be located precisely.

Table 3.2: CRM content of the output streams of the 3 investigated sites (ICP-MS analyses).

| Waste Stream/Product | wt.% | LREE ppm | Sn ppm | Nb ppm | Ta ppm | W ppm |
|---|---|---|---|---|---|---|
| *WADM-Melbur-Virginia* | | | | | | |
| Matrix | 100.0 | 79.1 | 68.7 | 39.9 | 11.4 | 30.8 |
| Stone | 4.0 | 50.0 | 38.3 | 26.2 | 7.6 | 15.7 |
| Gravel | 8.0 | 35.4 | 48.5 | 18.4 | 5.2 | 14.9 |
| Sand | 48.0 | 41.2 | 51.4 | 32.9 | 10.0 | 17.5 |
| Micaceous Residue | 20.0 | 168.7 | 139.4 | 93.7 | 25.9 | 92.9 |
| Product | 20.0 | 103.7 | 53.5 | 14.2 | 3.6 | 10.3 |
| *THM-Treviscoe* | | | | | | |
| Matrix | 100.0 | 11.1 | 20.6 | 53.1 | 23.6 | - |
| Stent | 36.0 | 9.0 | 13.1 | 42.0 | 17.9 | 18.0 |
| Sand | 40.5 | 5.5 | 20.6 | 32.9 | 23.0 | - |
| Micaceous Residue | 13.5 | 15.9 | 38.9 | 97.21 | 45.6 | 30.3 |
| Product | 10.0 | 34.3 | 21.4 | 38.84 | 15.8 | 15.5 |
| *WMHM-Wheal Martyn* | | | | | | |
| Matrix | 100.0 | 49.0 | 49.6 | 42.3 | 10.5 | 20.27 |
| Stent | 36.0 | 55.0 | 21.0 | 28.0 | 2.0 | 9.4 |
| Sand | 40.5 | 29.6 | 60.7 | 44.1 | 5.0 | 8.0 |
| Micaceous Residue | 13.5 | 46.5 | 87.2 | 80.2 | 32.0 | 93.0 |
| Product | 10.0 | 109.9 | 56.8 | 55.1 | 34.0 | 10.9 |

It appears that, among the investigated waste streams, the micaceous residue from the WADM plant, treating material from areas covering biotite granite, is the most prospective stream both in terms of CRMs content and distribution. In addition the corresponding kaolin pits are among the largest pits located in the area associated with the more reliable extraction and processing method. In comparison, the CRMs grades are much lowers and CRMs distributions less contrasted in waste streams from Treviscoe and Wheal Martyn pit. Therefore, the potential of CRMs recovery from hydrocyclone underflows at these two sites appears to be limited.

## 3.4 Conclusion

The CRMs content and distribution in the output streams of the kaolin extraction processes are mainly dependent of the source granite and are also likely to be influenced by the degree of kaolinisation of the feed material. CRMs appeared to be pre-concentrated into the micaceous residue streams with the exception of LREE for THM and WMHM which are pre-concentrated in the product stream. The pre-concentration into the micaceous residue is explained by the fine size distribution of CRMs combined to the effect of high specific gravity of the accessory minerals. It appears that the micaceous residue from the WADM plant is the most prospective stream in terms of CRMs content and distribution. Hence, this residue has been selected for further metallurgical testing.

Anyway these results also highlights three critical points: (1) kaolinised topaz granite, and perhaps other granites too, are probably not as homogeneous source area for CRMs as previously stated, (2) hence, a high variability of the CRMs content in the residue streams is expected and (3) as a result, representative sampling a low grade kaolin residue in view of gravity processing is not an easy task and deserves proper attention.

# Chapter 4

# Sampling representativeness for metallurgical testing

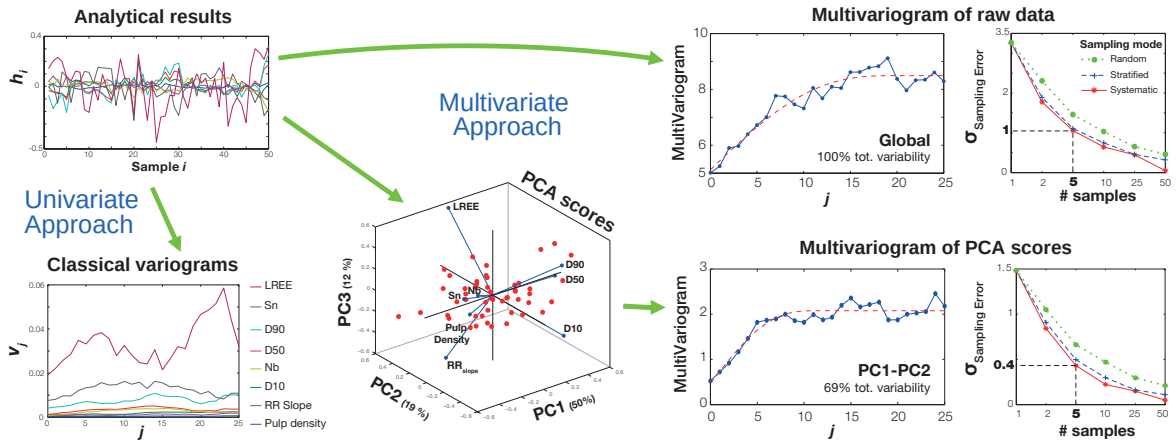


*Forewords*

*The classical application of Theory of Sampling (TOS) is univariate. However, most practical situations in mineral processing address multi-properties (i.e. variables) issues (grades, particle size, pulp density), in which the common belief is that one should focus a variographic study on the property with the most heterogeneous distribution. The purpose of this chapter is to introduce a multivariate approach to process sampling and compares it with the classical univariate and other multivariate approaches of variogram as applied to principal component analysis (PCA) scores.*

## Contents



# 4.1 Introduction

In every mining project, economic improvements pass through metallurgical assessment based on series of metallurgical tests that are performed on so-called process samples. Process samples are typically extracted from flowing streams of ore, concentrate or residue at regular intervals to obtain representative samples of a given chemical analyte, a mineralogical or physical property. Metallurgical tests explore the best operating parameters to reach the desired recovery objectives, therefore improving the process. The effectiveness of these improvements will depend directly on the representativeness of the samples that are initially collected for the tests (Abzalov, 2013).

## 4.1.1 Theory of Sampling

Theory Of Sampling (TOS), which was introduced by Pierre Gy, has been widely described in many reference books (Gy, 1998, 1992, 1971; Pitard, 1993). This theory provides a simple set of rules for good sampling practice to eliminate sampling biases and to minimise sampling errors. Process streams such as particulate material on a conveyor or flowing slurry in a pipe can be seen as elongated objects, with a very long length compared to its two dimensional cross section. These objects are represented in TOS by one-dimensional (1D) models according to their projection in the flow direction (Gy, 2004c). The preferred method for sampling 1D lots is composite sampling (Minkkinen and Esbensen, 2009), which involves taking increments of the entire stream

for a fraction of the time and then aggregating the increments together to make the final sample (Gy, 2004b). This method is based on the mathematical model that is used to integrate a curve *a(t)* by means of sample points, with *a* being the analytical results of a component A, during the sampling period between t=$T_0$ and t=$T_L$. This operation can be performed by following three principal sampling modes (Figure 4.1):

- Random sampling: the samples are collected randomly during the sampling period,
- Stratified sampling: the sampling period is divided into uniform intervals and one sample is collected randomly in each interval,
- Systematic sampling: samples are collected at equal distances (lags) along the time axes.

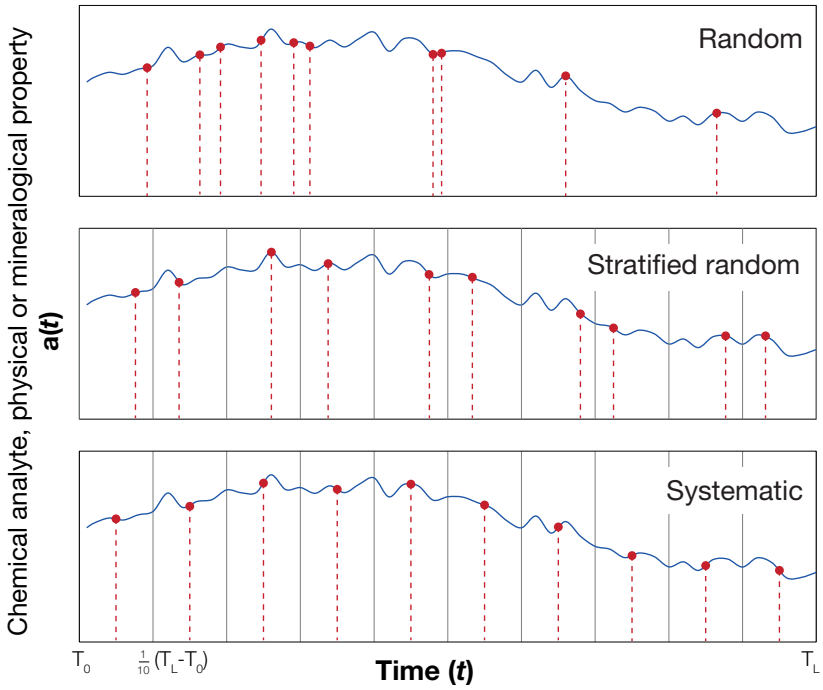


Figure 4.1: Schematic representation of the 3 distinct sampling modes for the 10-increment sampling of a 1D process.

The choice of the sampling mode is very important because it changes the variance of the lot' mean. In most cases, systematic sampling will lead to the lowest sampling variance (Gy, 2004a; Saunders et al., 1989), but stratified sampling may be preferable when periodic phenomena occur or when values are randomly missing (Paakkunainen et al., 2007; Saunders and Robinson, 1989). In the case of sampling for variographic study, samples are usually collected by following a systematic mode for the reasons presented above, and each increment is treated individually as a single sample.

### 4.1.2 Classical variographic approach

TOS introduced semi-variograms (referred to as *variograms* in the present text) as a tool to characterise the autocorrelation between the units of a process and the

heterogeneity of a 1D lot. Variograms provide critical information on the following (Esbensen et al., 2012; Gy, 2004a; Petersen and Esbensen, 2005):

- the process variability over time and the magnitude of the different variability components,
- the lot's mean and the uncertainty of a single measurement with respect to the autocorrelation phenomenon,
- the optimal design and mode (*i.e.*, random, stratified or systematic) for the sampling protocol.

In a typical variographic experiment, a set of $N$ discrete units (*i.e.*, increments) that represents the 1D lot is collected from a one-dimensional flowing stream throughout a time period. The relative heterogeneity $h_i$ that is associated with the analytical results, $a$, in a single unit of mass $M_i$, which is expressed in the concentration $a_i$, is defined as follows:

$$h_i = \frac{a_i - a_L}{a_L} \frac{M_i}{\overline{M}_i}, \quad i = 1, \ldots, N \tag{4.1}$$

where $\overline{M}_i$ is the average mass increment and $a_L$ is the lot mean[1]. This relative heterogeneity is dimensionless, so the component A can describe any intensive property that characterises the material (chemical or physical property, *e.g.*, density, humidity or particle size). The variogram $v_j$ is calculated for a sufficient number of units (up to a maximum of $N/2$) as follows:

$$v_j = \frac{1}{2(N-j)} \sum_{i=1}^{N-j} (h_i - h_{i+j})^2, \quad j = 1, \ldots, N/2 \tag{4.2}$$

where $j$ is a dimensionless lag-parameter that defines the distance between two time increments. The variogram describes the variation from the analyte between units as a function of the distance between them. This value can be seen as twice the statistical variance (or variability) of the studied analyte over a time interval of length $j$. An extensive description of the variographic technique and its practical applications can be found in reference papers (Esbensen et al., 2012; Gy, 2004a; Petersen and Esbensen, 2005).

The shape of the variogram is an important source of information to characterise a process variation (Figure 4.2). The intercept of the variogram with the Y-axis is known as the nugget effect, which is called $V_0$. This variable reflects the short-scale process variability and includes all of the sampling and sample preparation variances (François-Bongarçon, 2004). If only one time series is available, this value is estimated by backward extrapolation towards the zero sampling interval (Heikka and Minkkinen, 1997). The range of the variogram, which is represented by the increasing part of the theoretical variogram model, is the inter-increment distance beyond which no further autocorrelation is observable. Lastly, the sill, which is represented by the flat part of the theoretical model, is the variance of inter-increment pairs beyond the range, *i.e.*,

[1]Univariate functions are noted in lowercase, whereas the multivariate equivalents are noted in uppercase

the long-range variance. This value corresponds to the variance of all the individual heterogeneity contributions in the set of $N$ units and to the constitutional heterogeneity ($ch_L$) of the lot, which is defined as follows (Gy, 1998, 1992; Pitard, 1993):

$$ch_L = s^2(h_i) = \frac{1}{N}\sum_{i=1}^{N}(h_i)^2 \tag{4.3}$$

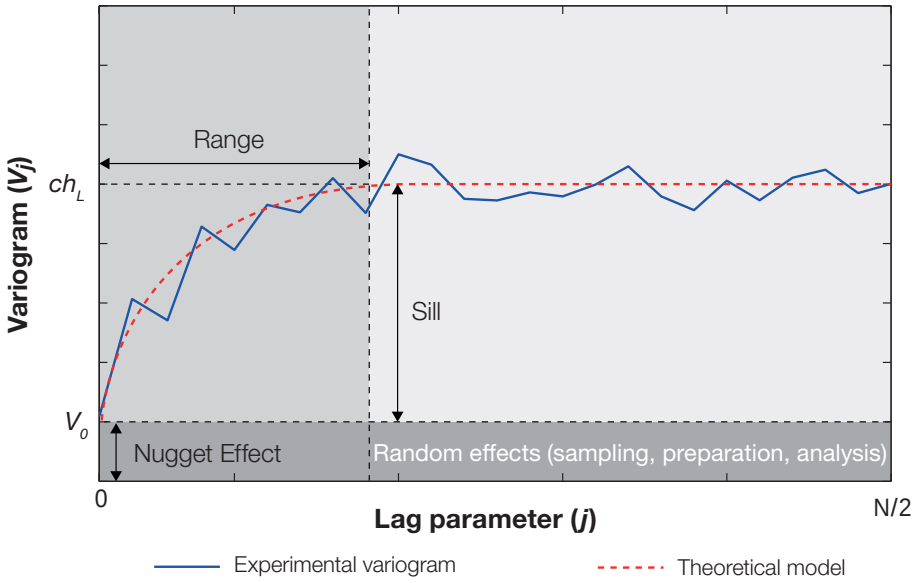


Figure 4.2: Scheme that illustrates the information that can be exploited from the variogram plot. The variogram is a positively increasing function of the distance $j$. The nugget effect is estimated by backward extrapolation of the variogram towards the origin, which provides an estimate of $V_0$. The range is the lag distance beyond which no further autocorrelation occurs, and the total sill, which is denoted as process variance $ch_L$, is the flat part of the variogram.

### 4.1.3 On the multivariate aspects of heterogeneity

The results from metallurgical tests often depend on several properties (chemical analytes or physical properties). Hence, the process samples must be representative not only for one property but for a certain range of properties. In these situations, the practical approach is to identify the property with the highest heterogeneity contribution and to consider only this property. The main difficulty of this approach is that it does not account for the multivariate nature of heterogeneity. In the case of a typical increasing variogram with finite range, heterogeneities of samples spaced in time (or space) of a distance equal or greater than the range are no longer autocorrelated. On the contrary, the closer samples are (spatially) to each other, the more their difference in heterogeneity decline. As a result, reducing the problem to one variogram model, which is a univariate (spatial) function, to represent the (spatial) structure of heterogeneity, which is generally a multivariate measure, can lead to an underestimation of the large difference in heterogeneity that occur between close neighbors (Bourgault et al., 1992). This underestimation could be more or less significant depending on the degree of correlation between the individual properties that characterize the multivariate heterogeneity.

The importance of considering the multivariate nature of heterogeneity is well-known in geostatistics and particularly for spatial data analysis but has not been frequently addressed to TOS. An initial solution to this issue in the field of spatial data analysis was proposed by Oliver and Webster (1989), who suggested to perform a Principal Component Analysis (PCA) on the data and to study the variogram of the first few principal components. However, only a limited number of case studies have recently applied this approach to chemometrics and TOS. Minkkinen and Esbensen (2014) have illustrated the advantages of variographic analysis on PCA scores as a way to perform a combined multivariate chemometric-variogram that explains analyte covariance and the distinct spatial patterns of 1D lots.

A reverse approach that involves applying a PCA analysis on the individual variograms is also worth mentioning (Kardanpour et al., 2014). This method is presented as a more suitable alternative when knowing the characteristics of all of the individual analytes is necessary.

### 4.1.4 Application of multivariate variograms to process sampling

The heterogeneity contribution is now assumed to be a multivariate measurement. If a material is characterised by a number $p$ of properties (chemical analytes or physical properties), the heterogeneity could therefore be represented as a vector of $p$ individual heterogeneity contributions:

$$H_i = [h_1, \ldots, h_k, \ldots, h_p]_i^t, \quad i = 1, \ldots, N \tag{4.4}$$

where $^t$ is the transpose operator and $h_k$ is the heterogeneity vector that is associated with the $k^{th}$ property. The univariate definition of the variogram is thus no longer adapted and must be improved. Bourgault and Marcotte (1991) were the first to formalise the principle of a multivariate variogram for spatial data analysis, which is defined in a similar way to that of a traditional variogram but in a $p$-multidimensional space. This multivariable variogram (referred to as *multivariogram* in the text below) has been mainly used for spatial data analysis and mapping (Bourgault et al., 1992; Kerry and Oliver, 2003) but has never been applied to TOS. For every metric $M$, one can calculate the multivariogram $V_j$ by analogy to the univariate definition:

$$V_j = \frac{1}{2(N-j)} \sum_{i=1}^{N-j} (H_i - H_{i+j}) M (H_i - H_{i+j})^t, \quad j = 1, \ldots, N/2 \tag{4.5}$$

where $M$ is a positive definite $p \times p$ matrix, which defines the metric for calculating the "distances" between the units. This metric defines the relationship between the variables and can be chosen depending on the nature of the variables. The most common metrics that are used to measure distances are the Euclidian distance (ED), in which $M$ is the identity matrix, and the Mahalanobis distance (MD), in which $M$ is defined as the inverse of the variance-covariance matrix. When using ED, the multivariogram is simply the sum of the univariate variograms (Bourgault and Marcotte, 1991), so one should avoid this metric and use MD, which considers the correlation in the data. More information regarding MD can be found in De Maesschalck et al. (2000).

Contrary to the previously mentioned multivariate approaches, this approach captures the variability of all of the variables in a single variogram. Thus, calculating the auxiliary functions and, consequently, the error-generating functions for each sampling mode is still possible by using classical point-by-point calculations (Petersen et al., 2005), except for the random selection mode. Indeed, the error-generating function that is associated with this sampling mode is equal to the constitutional (multivariate) heterogeneity of the lot ($CH_L$), which is defined as the variance of the (multivariate) heterogeneity contribution of all of the units that comprise the lot $L$:

$$CH_L = s^2(h_i) = \frac{1}{N}\sum_{i=1}^{N-j} H_i M H_i^t \tag{4.6}$$

The purpose of this section is to introduce multivariograms as a tool for process sampling and to compare them with the classical univariate approach and multivariate approach of variograms as applied to PCA scores.

## 4.2 Materials and methods

### 4.2.1 Material sampling

The samples that were used in this work were collected with the help of Imerys Minerals Ltd, UK. The primary objective of this sampling exercise was to design a protocol to collect a representative sample from a residue stream of a kaolin plant that operates at an approximate flow rate of 15 t/h. A total of 50 samples (of approximately 25 kg) were collected from this stream during an approximately 2 h shift. The increments were manually extracted every 2 min by systematically using a by-pass that diverted the entire stream into the sample collector.

### 4.2.2 Sample preparation

Accurately estimating the pulp density and wet mass is critical because the moisture content of samples can change rapidly after sampling from evaporation. Thus, all of the samples were stored in sealed containers. However, condensation may occur inside the container, which is difficult to mix back into the sample (Holmes, 2004). To avoid this issue, the raw weight (containers + wet sample) was measured and the container was weighted afterwards. The samples were then dried directly without dewatering to avoid fine particle loss. Once dried, the samples were weighted to estimate their initial pulp density and then riffled to obtain subsamples for particle size analyses. The remaining samples were then crushed and riffled alternatively in agreement with the Theory of Sampling to obtain representative subsamples for chemical analysis (Petersen et al., 2004).

The studied material was sampled for metallurgical testing by gravity concentration. Thus, the analytical methods that are chosen for the variographic study must be adapted to this objective. In addition to classical chemical analysis, the size distribution was measured because it is a critical characteristic of a material for gravity concentration (Burt, 1984b).

### 4.2.3 Chemical analysis

A set of 18 elements/oxides were analysed, including LREEs (La, Ce, Nd), Nb and Sn. Representative 10 g aliquots were mixed with Cereox wax (Fluxana® GmbH & Co. KG) and pressed into pellets. Chemical analyses were performed with Energy Dispersive X-Ray Fluorescence spectroscopy (ED-XRF) by using an S2 Ranger (Bruker Corporation) at the GeoRessources laboratory (Vandoeuvre-lès-Nancy, France). The XRF calibration used results from Inductively Coupled Plasma Mass Spectrometry (ICP-MS) analysis for trace element analyses, which were performed at the *Service d'Analyses des Roches et des Minéraux* (SARM-CNRS, Nancy, France) following the procedure in Carignan et al. (2001).

### 4.2.4 Particle size analysis

Four properties were retained to describe the particle size distribution of the material: D10, D50, D90 and the Rosin Rammler (RR) slope; the first three represent particle sizes below which 10%, 50% and 90% of the particles are distributed, respectively, and the last represents the slope of the size distribution with the Rosin Rammler model (Wills and Napier-Munn, 2005). Particle size analysis was performed by laser light scattering with a Helium-Neon Laser Optical System Mastersizer 3000 (Malvern instruments Ltd.) coupled with a Hydro Extended Volume (EV) sample dispersion unit.

## 4.3 Results

### 4.3.1 Experimental individual variograms

The analytical results of the 8 selected properties (*pulp density*, *D10*, *D50*, *D90*, $RR_{slope}$, *Nb*, *Sn* and *LREEs*) for 50 micaceous residue samples are presented in Figure 4.3. The variation illustrates the stream material's heterogeneity with time. The variability that is expressed by the entire profile for the pulp density, *D10*, *Nb*, *Sn*, and *LREEs* equals the global variation interval that is represented by the mean $\pm\ 2\sigma$ interval, whereas the variability for *D50*, *D90*, and $RR_{slope}$ seems to be associated with slight trends. However, no significant outliers exist in the profiles outside of the mean $\pm\ 3\sigma$, which is often taken as the outlier threshold (Kardanpour et al., 2014). Thus, the analytical results can be used directly without any treatment.

Figure 4.4 present the individual heterogeneity contributions of each parameter, which were calculated by using Equation (4.1). The profiles are similar to the analytical results because the increment masses are practically identical, but this figure shows that the LREE content is the parameter with the highest variability.

The individual variograms and the auxiliary functions $w_j$ and $w'_j$ were calculated from these individual heterogeneity contributions, and the nugget effect $V_0$ was estimated by backward extrapolation (Figure 4.5). The individual variograms allow one to distinguish two main groups: a high-sill variable group (*LREEs*, *D90* and *Sn*) and a low-sill variable group (*pulp density*, *D10*, *D50*, $RR_{slope}$ and *Nb*). The overall range is difficult to directly estimate with the variograms, but the auxiliary functions suggest a range that varies between 5 and 7 lags.

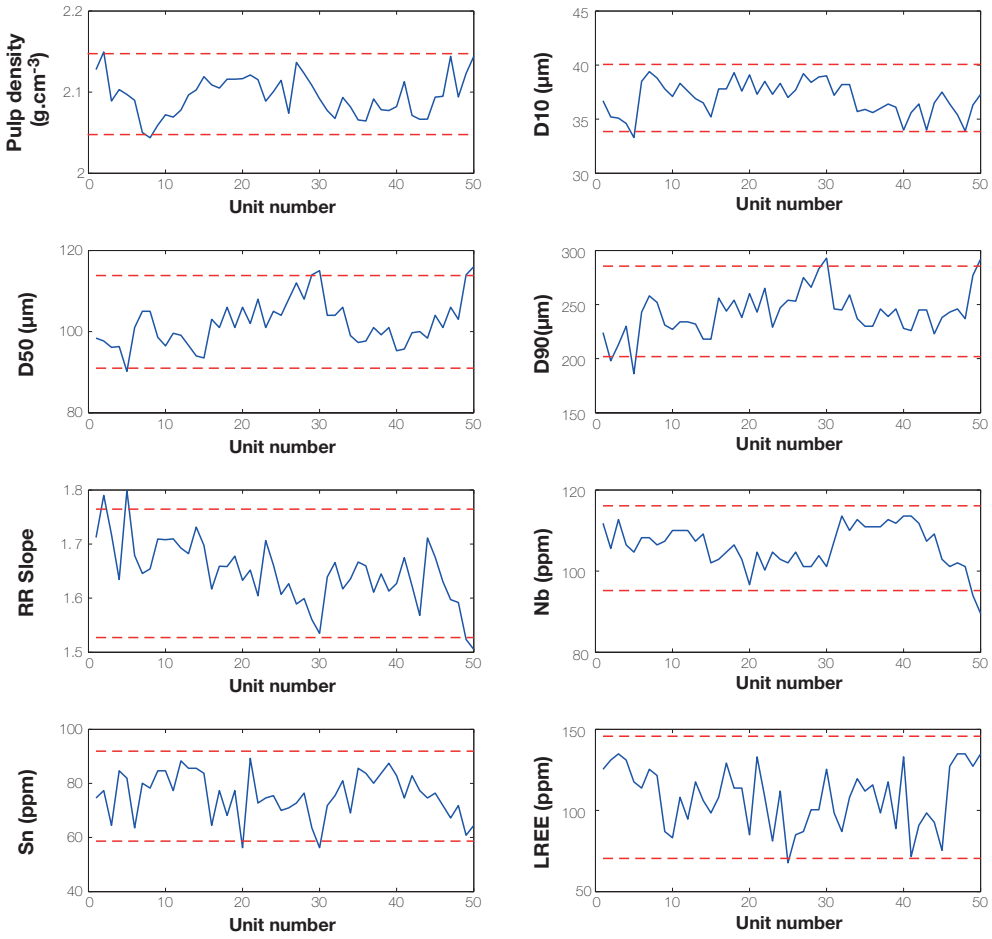


Figure 4.3: Analytical results that show the variations in the pulp density, size distributions (*D10*, *D50*, *D90*, and $RR_{slope}$) and chemical compositions (*Nb*, *Sn*, and *LREEs*) *vs.* unit number, with each unit extracted at 2 min intervals from the micaceous residue stream. The dashed lines represent the mean $\pm$ $2\sigma$ of the analytical results.

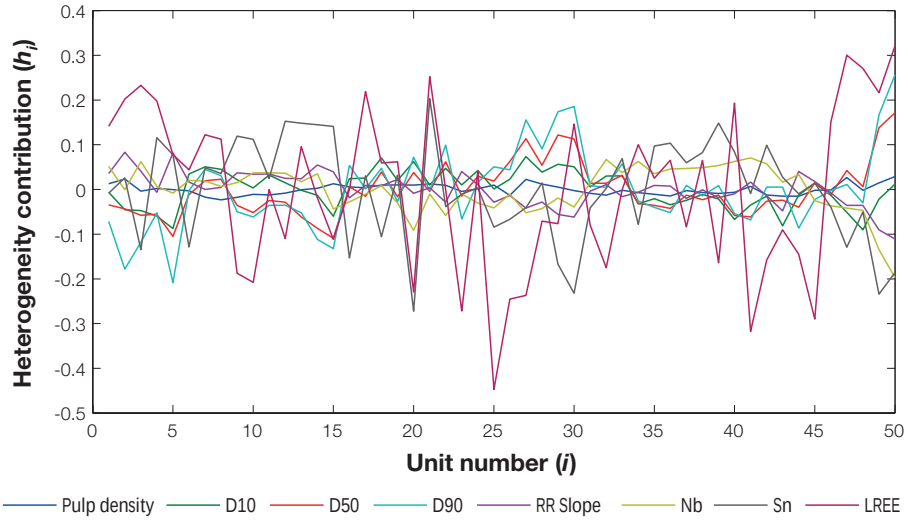


Figure 4.4: Individual heterogeneity contributions $h_i$ of the 8 selected properties for the 50 units of the micaceous residue stream.

The variograms of *pulp density* and *Nb* display a classic increasing variogram shape. A minimum can be observed in the *LREE* and *Sn* variograms at $j = 15$ and $j = 23$, respectively, which indicates that the existence of possible cyclic fluctuations over an excessively long period (*i.e.*, $j = 15 = 30$ min and $j = 23 = 46$ min, respectively) may create another minimum in the variogram plot. Similar observations can be made for the variograms of the size distribution properties. For each of these properties, a local minimum is observed at $j = 7 - 9$ and a tentative repetition occurs at $j = 20$, which suggests correlations between these properties and the existence of some periodic phenomenon that affects the size distribution and exhibits a rather short period of approximately 9 lags (*i.e.*, $j = 9 = 18$ min).

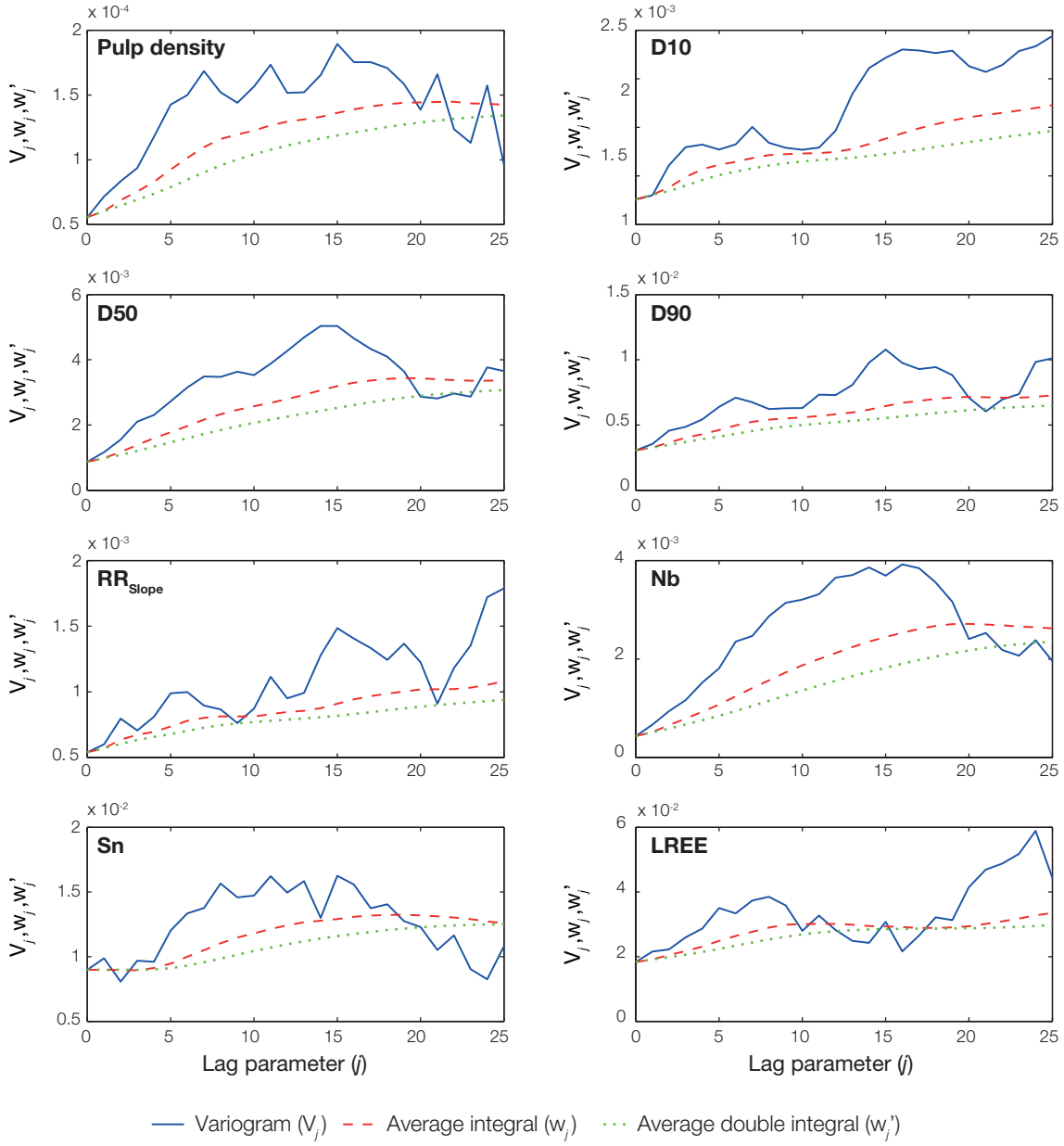


Figure 4.5: Experimental variograms $V_j$, average first order integral $w'_j$ and average second order integral $w'_j$ of the 8 selected properties of the micaceous residue stream. A common range of approximately 5-7 lags (10-14 min) is observed.

The classical conclusion at this point would be to focus the sampling protocol on the property with the highest sill, *i.e.*, the LREE content. Figure 4.6 shows the standard deviation of the sampling error for the LREE content according to the sampling mode. The 3 sampling modes are quite close, but systematic sampling remains the sampling mode with the lowest variance.

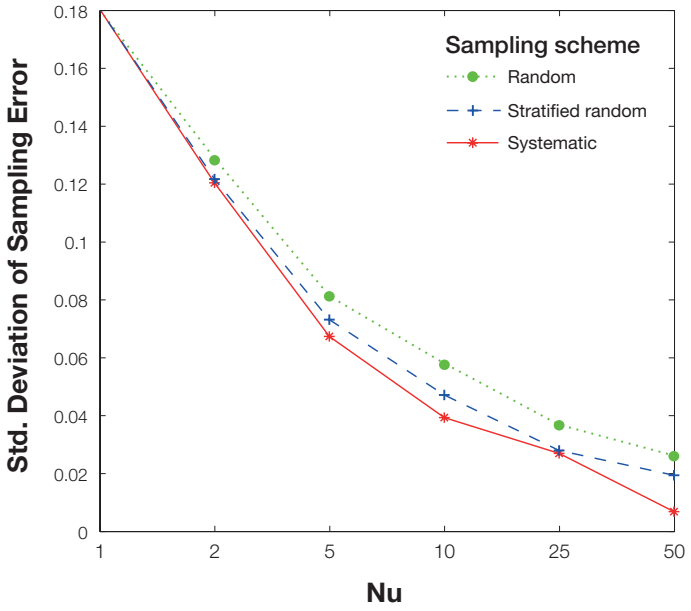


Figure 4.6: Standard deviation of the (continuous) sampling error of the LREE content for the 3 sampling modes as a function of the number of units that are collected (Nu) to make the final micaceous residue process sample.

Even with this simplification, the recommended sampling protocol is hard to define because of the different periodic phenomena. Using stratified random sampling or systematic sampling with at least 5 or 10 increments and a sampling frequency that is higher than two per period of 18 min and 30 min may be recommended (Petersen and Esbensen, 2005). However, even if this sampling protocol is the best for the LREE content, it will certainly not be for the other properties, notably because of the trends and periodic phenomena that these factors display. This observation illustrates why this approach does not account for the multivariate nature of heterogeneity and can lead to a misunderstanding of the spatial structure of the variability and to an underestimation of the global sampling variance.

### 4.3.2 Variograms on PCA scores

Principal Component Analysis (PCA) is a well-known variable reduction procedure in chemometrics that simplifies data by summarising them into a smaller number of more relevant or more interesting components (Jolliffe, 2002; Wold et al., 1987; Esbensen et al., 2002). This multivariable statistical analysis technique is designed to find $k$ new variables, named scores, as linear combinations from the $p$ initial variables in such a way that the system will lose the least possible information. The coefficients of these linear combinations, or loadings, are computed from the eigenvectors of the correlation matrix among the $p$ initial variables of the $N$ observations. These values

can be used to perform a variographic study not to all of the individual variables but to projected scores instead, which is a considerable economy in terms of data modelling and interpretation (Minkkinen and Esbensen, 2014). The results of a PCA analysis that was applied to the autoscaled St Austell micaceous residue process data are shown in Figure 4.7, where both the process samples' characteristics (*i.e.*, properties) and analytical results are projected in the PC1 *vs.* PC2 *vs.* PC3 space, which accounts for 80% of the total variability. PC1, which explains 50% of the total variance, is mostly loaded by the properties that characterize the size distribution of the micaceous residue (*D50*, *D90* and $RR_{slope}$) and to a lesser extent by the low-variance chemical contents (*Nb*, *Sn*). PC2, which explains 19% of the total variance, is loaded by pulp density, LREEs and to a lesser extent by D10. PC3, which explains 11% of the total variance, is mostly loaded by LREEs, pulp density and $RR_{slope}$. Most of the data points in the score plot are clustered around the origin and elongated along the PC1 axis, which reflects the variation in the particle sizes.

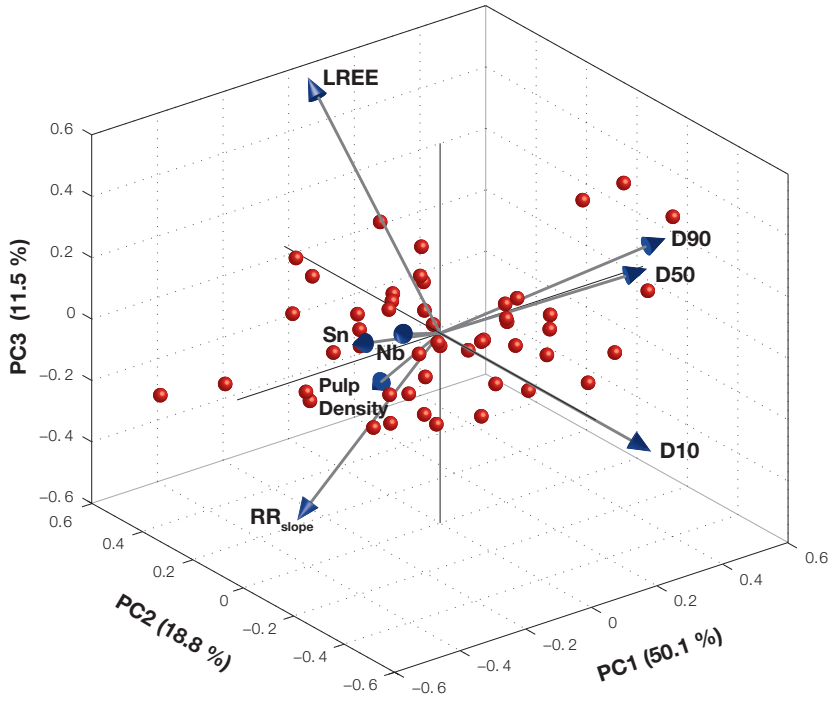


Figure 4.7: 3D biplot of scores and variable loadings for the 3 first principal components, with their explained variability, for the micaceous residue process data.

The eigenvalues correspond to the explained variability that is carried by each component (Table 4.1). By keeping only the eigenvectors with the highest eigenvalues, the PCA reduces the numerous variables into set of a few meaningful factors. The choice of which variograms of the PCA scores should be kept is based on the explained variance of each principal component. Additionally, a randomness test, developed by Minkkinen (2013) for the variograms can be used. This test, which is similar to Fisher's $F$-test, is based on the ratio of the sill and the first value of the experimental variogram, which can be expressed for the $i^{th}$ component as follows:

$$F_i = \frac{s_i^2}{(V_1)_i} = \frac{(CH_L)_i}{(V_1)_i} \tag{4.7}$$

The critical values of this test depend on the number $N$ of data points in the variographic experiments. A table of these critical values, which were obtained after $N \times 10000$ simulations, can be found in Minkkinen (2013). Variograms and auxiliary functions of the four first principal components are presented in Figure 4.8, which account for 88.5 % of the total variability that is displayed by the dataset (Table 4.1). The first four PCs represent most of the relevant information because they are also significant in terms of the $F$-test. PC5 has a clearly non-significant $F$-value, which can be attributed to random variation. Thus, only the PCs up to PC4, which explains 8% of the total variability but 40.5% of the remaining variability after PC3, are considered to be significant. Even if some later PCs such as PC6 or PC8 have higher $F$-test values, the fractions of the total variability that is explained by these PCs, which are 6.6% and 0.05%, respectively, show that no further information can be extracted from these PCs that would have not already been extracted from the previous PCs. In practice, one would not consider components that explain less than 12.5% of the total variability, which is the explained variability ratio when all of the components are equivalent.

Table 4.1: Eigenvalues, explained variability and significance of the score variograms of each PC.

| PC # | Eigenvalue | Explained variability (%) | Cumulated explained variability (%) | Eigenvalue Spectrum 20 40 60 80 | F-test* |
|---|---|---|---|---|---|
| **1** | 3.995 | 50.13 | 50.13 | PC1 | 2.63 |
| **2** | 1.483 | 18.82 | 68.94 | PC2 | 2.81 |
| **3** | 0.948 | 11.47 | 80.41 | PC3 | 1.35 |
| **4** | 0.633 | 7.94 | 88.35 | PC4 | 1.69 |
| **5** | 0.527 | 6.61 | 94.96 | | 0.89 |
| **6** | 0.336 | 4.08 | 99.04 | | 1.53 |
| **7** | 0.073 | 0.92 | 99.96 | | 1.24 |
| **8** | 0.004 | 0.05 | 100.00 | | 1.42 |

*Critical values for the F-test are P(F=0.90)=1.22, P(F=0.95)=1.30 and P(F=0.99)=1.47 (Minkkinen, 2013)

PC1 variogram can be interpreted to reflect the particle size variability of the micaceous residue stream with time. Its variogram displays a slightly increasing trend that reaches a sill for the last lags, which reflects a long range variation. The auxiliary function shows the nested structure of PC1, with two distinct ranges at $j \approx 6$ and $j \approx 17$. This long range nested structure that was captured by PC1 can thus be attributed to the particle size distribution by the loading relationships of PC1 (loaded by D50, D90 and $RR_{slope}$), with all of the loading properties having a similar nested structure.

On the contrary, the variogram of PC2 displays a clear short range structure with an increasing trend at short lags and a sill that was reached quickly at $j \approx 6$. This observation is clearly in line with the short range variation that is displayed by the individual pulp density and LREE content variograms, which both load PC2.

PC3 is obviously related to a cyclic variation with a rather short period of approximately 5 lags. Even if PC3 is loaded by LREEs, the pulp density and $RR_{slope}$, this cyclic pattern is not discernible on the individual variograms, probably because of the low amplitude of the fluctuation and the relatively small proportion of the total variability that is explained by this component. Interpreting later components starting from PC4 is a delicate operation. Even if PC4 is significant in terms of the $F$-test, its variogram is relatively flat compared to those of the first PCs.

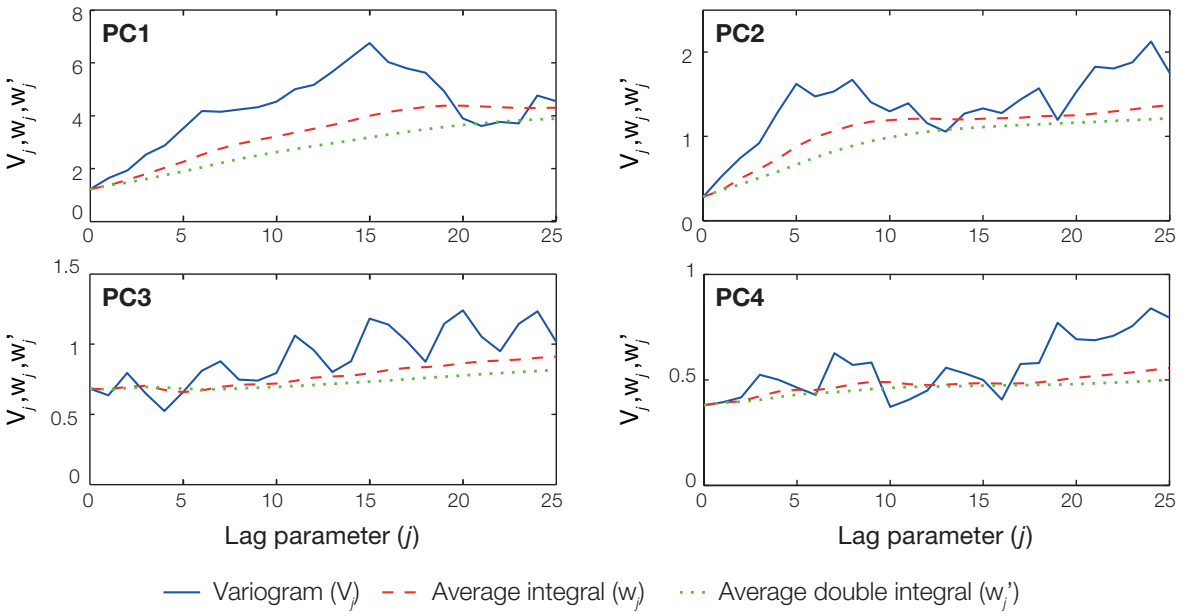


Figure 4.8: Experimental variograms $V_j$ , average first order integral $w_j$ and average second order integral $w'_j$ of the 4 first PCs of the micaceous residue process data.

### 4.3.3 Multivariogram

#### 4.3.3.1 Multivariogram applied to heterogeneity contributions

The 8 selected properties can be divided into 3 distinct classes, namely, the size distribution (D10, D50, D90 and $RR_{slope}$), the metal content (Nb, Sn and LREEs) and the pulp density. The variograms of each class can be modelled by the multivariogram of the corresponding properties. Figure 4.9 shows the multivariograms (or variogram for pulp density) of each of these classes and the global multivariogram shape. The multivariograms are computed by using MD, and the general shapes of the multivariograms are approximated by a smoothed curve that corresponds to the best-fitted theoretical model. The models are obtained by the least-squares method to fit each model to the experimental data and by comparing the models together. The model with the highest $R^2$ value and lowest Root Mean Squared Error (RMSE) is selected (Appendix C.1). The variogram models were fitted to the experimental variograms with the 'variogramfit' algorithm in MATLAB® by using only bounded models (Schwanghart, 2009). Variogram modelling is a complex task (Webster and Oliver, 2007; Singh et al., 1993); the model hereafter only provides a general shape to illustrate the influence of each class on the global multivariogram. For a detailed description of variogram modelling and the different theoretical models, the reader is directed to geostatistics textbooks (Webster and Oliver, 2007).

Each class have a multivariogram that is best modelled by a bounded linear model (blinear) with a clear delimited range. The size distribution and metal content multivariograms both display high sills, which is a consequence of the individual variabilities of the properties that are used for the calculation, compared to the pulp density univariate variogram. However, the ranges are completely different: the size distribution multivariogram clearly displays long range variation, whereas the metal content and pulp density (multi)variograms display medium to small ranges (Appendix C.1).

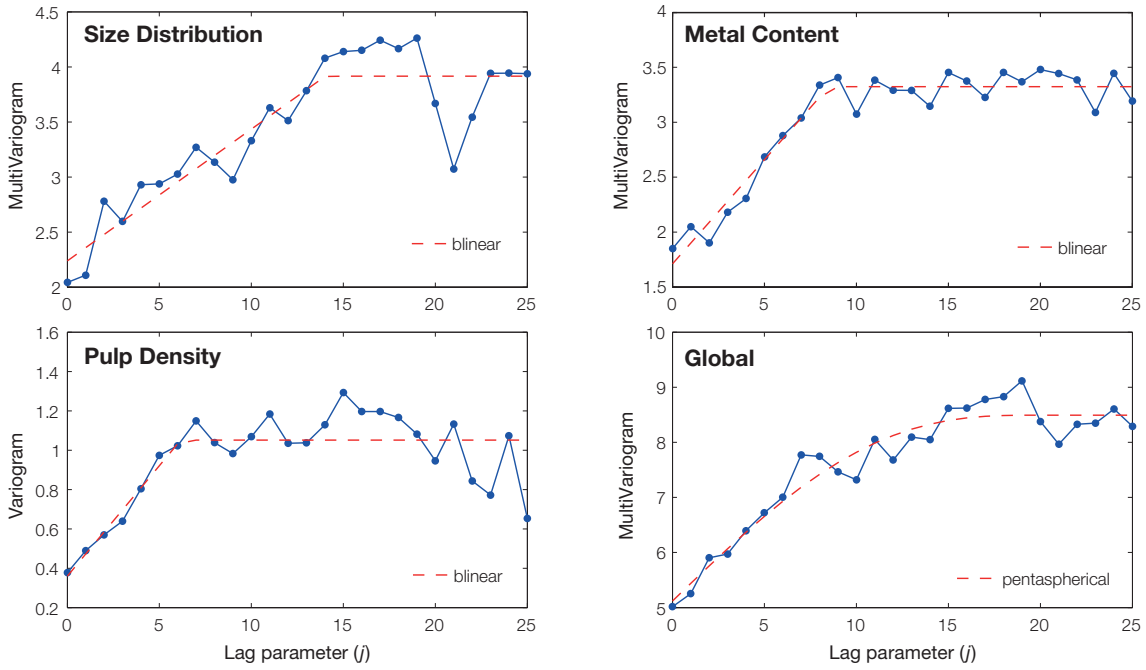


Figure 4.9: Multivariograms that were computed with MD and the associated theoretical model, which illustrate the influence of each property's class, including the size distribution properties (D10, D50, D90 and $RR_{slope}$), metal content (Nb, Sn and LREE) and pulp density, on the global multivariogram.

The influence of each class on the global multivariogram cannot be easily interpreted. Because the MD metric was used instead of the ED metric, the global multivariogram is neither the sum of the univariate variograms nor the sum of the aforementioned class-multivariograms. Indeed MD metric allows taking into account the hidden data structure, linked to an unknown hidden phenomenon, by taking into account the covariance between variables regardless to the class to which these variables belong. However, the shape of the global multivariogram is best fitted by a gradual curve of a pentaspherical model (Webster and Oliver, 2007):

$$V_j = \begin{cases} s\left[\frac{15}{18}\frac{j}{r} - \frac{5}{4}\left(\frac{j}{r}\right)^3 + \frac{3}{8}\left(\frac{j}{r}\right)^5\right] & , \quad j \leq r \\ 0 & , \quad j > r \end{cases} \tag{4.8}$$

where $s$ represent the sill of the variogram and $r$ the range. The fact that the global multivariogram is best fitted by a pentaspherical model with a high range of $j$=20, which has a gradual curve for the increasing sections of the variogram, instead of a linear model is clearly a consequence of the small, medium and long ranges that are displayed by the multivariogram of each class.

The global multivariogram displays a relatively high sill, which is a consequence of the metric that was used for the computation. Hence, the sampling variance is much more important compared to the univariate case. However the results suggest a low frequency phenomenon with a period of approximately 23-25 lags whereas the data only contains 50 lags. Hence the estimation of the sill values and length of periods is uncertain. To confirm this phenomenon, the length of the variographic experiment

should be extended over 3 work shifts (6-9 h). Figure 4.7 shows the global relative standard deviation of the sampling error for all of the properties according to the sampling mode. Random sampling clearly displays the highest sampling variation, whereas systematic sampling appears to be the most adapted sampling mode and has the lowest sampling variation. Taking only two samples instead of one reduces the standard deviation of the sampling error by 37% for systematic sampling, 33% for stratified sampling and 29% for random sampling. However, the standard deviation remains very high even for a high number of increments that are collected to make the final sample; the standard deviation falls below 10% only when 50 increments are collected by systematic sampling. Therefore, the sampling variance seems to be overestimated and finding an approach to reduce it is necessary.

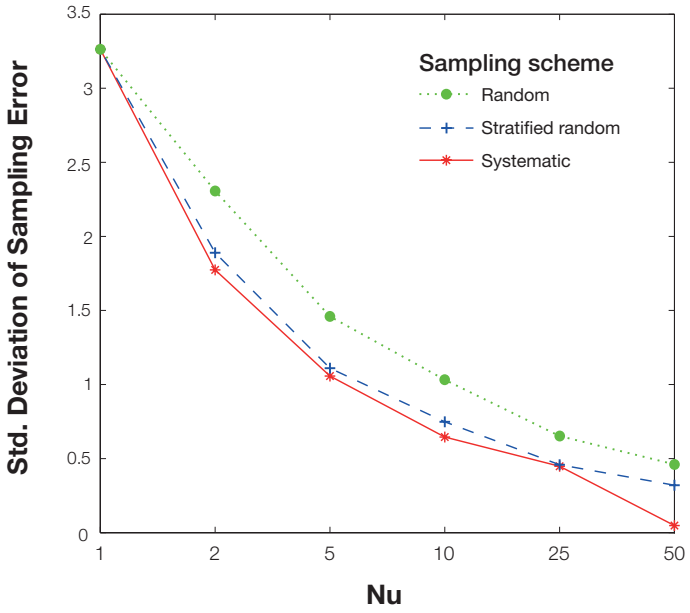


Figure 4.10: Global relative standard deviation of the sampling error for the 3 sampling modes as a function of the number of units that are collected (Nu) to make the micaceous residue process sample.

#### 4.3.3.2 Multivariogram applied to PCA scores

An alternative approach to summarise data variability is to use the PCA scores instead of the raw analytical results, as suggested in the univariate case (Minkkinen and Esbensen, 2014). Figure 4.11 shows the influence of the number of principal components that are retained for calculation on the multivariogram's shape and the standard deviation of the sampling error. The more components are added to the multivariogram, the more important the standard deviation of the sampling error becomes. However, even when the first four PCs are used to compute the multivariogram, its sill and thus the associated standard deviation are still less important than the global multivariogram of the raw data because only the significant PCs were retained to compute the last multivariograms from PC1 to PC4. Thus, all non-significant, noise-generating components that do not provide any relevant information are not integrated into the last multivariogram. PCA acted as a noise-filter on the raw data to retain only relevant information on the global variability of the dataset. Hence, the multivariogram that is

applied to the four first PCs provides a more representative, *i.e.* noiseless, summary of the structure of variability than multivariogram applied to raw data.

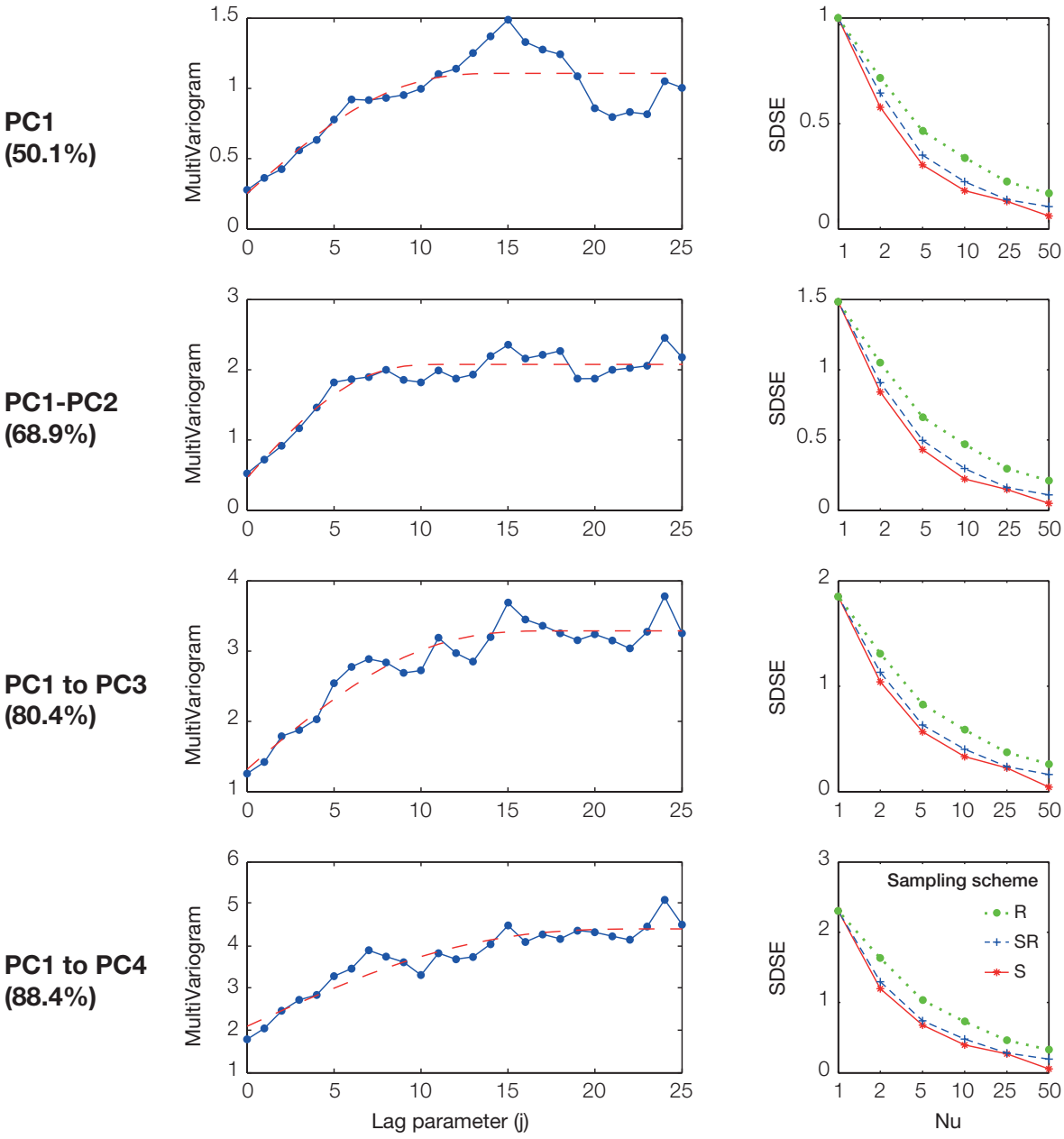


Figure 4.11: Influence of the number of principal components (and the corresponding explained variability) on the multivariogram shape and standard deviation of the sampling error (SDSE) *vs.* the number of collected units (Nu) as a function of the sampling mode, *i.e.*, random (R), stratified random (SR) or systematic (S). The multivariograms were computed with MD and fitted with a pentaspherical model. The PC1 'multivariogram' is different from the variogram of PC1 in Figure 4.8 because of the metric that was used for the computation.

The global shape of the multivariogram is already achieved by using only the two first PCs; additional PCs beyond PC3 do not contribute much more information aside from noise, which increases the nugget effect. By keeping only the first two PCs, the resulting standard deviation of the sampling error remains less important than if all

of the initial data were kept. One could use this PC1-PC2 multivariogram to assess the necessary number of increments to reach the representativeness objective for a composite sample. For instance, the standard deviation with 10 increments sampled is already approximately 20%.

## 4.4 Discussion

Table 4.2 compares the various aforementioned approaches, including the classic univariate variogram, PCA variograms and multivariograms for a multivariate problem with a dataset of $n$ increments with $p$ variables. Summarising the main objectives of each approach suggests that the univariate approach is fundamental for those who are interested in studying the singular variability of each parameter and the associated sampling error. However, this approach requests $p$ variograms, the interpretation of which could be laborious, and the overall sampling error will remain underestimated.

PCA variograms offer the advantage of combining a variable reduction procedure that describes the correlation between variables and a procedure that characterizes autocorrelations within an ordered dataset. This approach first highlights the property groups by using PCA and distinct spatial patterns by using variograms. Nevertheless, even if this process significantly reduces the number of variables for the variographic study, the same number of variograms is available to study because no significant PCs are present. Thus, assessing the true sampling error and choosing which variogram will be based on the sampling protocol are still an issue. Furthermore, this approach requires a large dataset with a number of observations $n$ (*i.e.*, increments) that is larger than the number of variables $p$ (*i.e.*, properties), which can be an issue for some process sampling cases where $n < p$, especially if $n \ll p$ as with some types of chemicals or spectral data. In these cases, one cannot obtain more than $n$ PCs (Koch, 2013).

Multivariograms summarize the overall spatial variability of a set of properties by one structural function and thus highlight the spatial structures that are *common* to these properties. The resulting multivariograms can be used to assess the true global variance of the sampling error and thus design the optimal sampling protocol. However, the estimated global variance with this approach is very high and implies that a large number of increments must be sampled to obtain a reasonable sampling variation. Indeed, the more properties that are considered, the more important the sampling error will become; thus, the properties that are used for multivariogram computation must be chosen carefully.

One can combine the two previously mentioned multivariate approaches to avoid this issue by computing the multivariogram of the first PCs' scores, which reduces the influence of noisy data and thus reduces the sampling variance. However, in some cases that deal with a high number of properties, the same issues that are linked to the PCA technique may arise and limit this approach. These problems could be avoided by applying the multivariogram to the linear coregionalization model, which was proposed by Bourgault and Marcotte (1991), to find the elementary variograms that characterise the different spatial scales, thus recovering the advantages of PCA on variograms without constraining the size of the data set.

Importantly, the variographic experiment on the St Austell micaceous residue sampling case study was performed on a shift-scale sample, which is a small scale for process sampling, especially because variograms of a given process can change with time as a

function of ore variability (Marques and Costa, 2014). Thus, performing a larger scale sampling campaign should determine if the sampling protocol must be adjusted.

Table 4.2: Comparison summary that lists the advantages (+) and disadvantages (-) of the 3 variographic approaches in this study for a multivariate case that deals with a dataset of $n$ samples and $p$ variables.

| **Univariate variogram** | **Variograms of PCA** | **Multivariogram** |
|---|---|---|
| | *Number of variograms* | |
| $p$ | $\leq min(n\text{-}1, p)$ | 1 |
| | *Sampling error(s) estimation* | |
| − p sampling errors<br>+ Estimation of the singular sampling errors | ± As many sampling errors as the significant PC that is selected | + One sampling error only<br>+ Estimation of the overall sampling error<br>− Sampling error can be very large |
| | *Representativeness* | |
| + Representative of the singular variability contribution<br>− Underestimation of the global variability | + Representative of (part of) the overall multivariate variability<br>− Depends on the variability as explained by the selected PCs | + Representative of the overall multivariate variability |
| | *Sampling protocol design* | |
| − Choosing the variable with the highest sampling error leads to an underestimation of the real (global) sampling variance | + Allows one to design the optimal sampling protocol regarding all of the spatial patterns within the multivariate data | + Allows one to design the optimal sampling protocol in terms of the global sampling variance for all of the variables<br>− The number of required increments can be very large |

## 4.5 Conclusion

The multivariate approach that was presented in this paper is a powerful tool when the overall time-variability of process streams must be summarized in terms of a large set of properties. However, this approach is not meant to replace the previously introduced conventional approaches but instead to complement them because they can all be applied to distinct objectives (Table 4.3). The multivariate approach of process variograms can describe the multivariate aspect of heterogeneity by considering all of the properties of interest. This approach provides an opportunity to choose all of the material properties that are critical for given objectives and to use multivariograms as a summarising tool to simultaneously handle $p$ simultaneous properties.

Most of the variability of the St Austell micaceous residue process stream is due to the LREE concentration on an individual scale, whereas the multivariate scale indicates that size distribution is the most important contribution. If the process samples from this stream were to be used for metallurgical testing, for instance, by gravity concentration, a minimum of 10 increments should be collected by systematic sampling to ensure an acceptable overall representativeness.

This paper has introduced effective multivariate approaches to describe the overall variability of a material and design an optimal process sampling protocol. However, this case study could also be applied to environmental, feed & food, pharmaceutical or any other fields that address multi-analyte sampling issues.

Table 4.3: Summary of the distinct objectives behind all the approaches presented in this study.

| **Data/Method** | **PCA** | **Variograms** | **Multivariogram** |
|---|---|---|---|
| **Raw data** | *PCA on raw data*<br>• Perform variable reduction,<br>• Filter noise from the data. | *Variograms on Raw data*<br>• Study the spatial characteristics of all individual parameters,<br>• Design the optimal sampling protocol for one property. | *Multivariogram on Raw data*<br>• Summarize the overall variability in one variogram,<br>• Assess the global sampling's representativeness. |
| **PCA scores** | | *Variograms on PCA scores*<br>• Highlight distinct spatial patterns through variable grouping in a reduced number of variograms (Minkkinen and Esbensen, 2014),<br>• Design the optimal sampling protocol. | |
| **Variogram** | *PCA on variograms*<br>• Study and then summarize the spatial characteristics of all individual analytes (Kardanpour et al., 2014). | | |

# Chapter 5

# Gravity processing of the selected residue

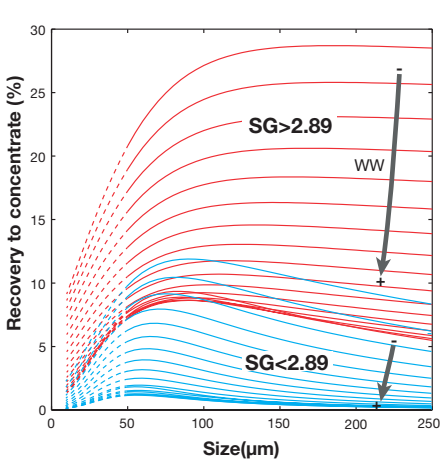


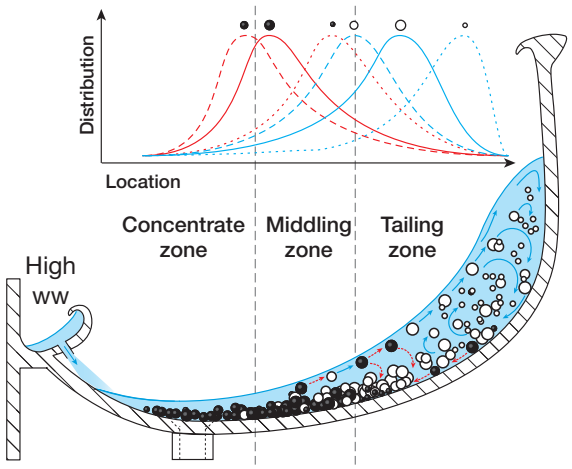


*Forewords*

*This chapter presents the main results of the gravity concentration testworks undertaken on the 53-180 µm fraction of the micaceous residue. It is organised in two main sections corresponding to two independent articles that can be addressed separately. The first article presents the results of spiral and shaking table concentration using the design of experiments (DOE) methodology to set the best operating parameters for heavy minerals recovery. The second article addresses and models the effect of wash water and pulp density on size recovery curves in spiral concentration of heavy minerals using the DOE methodology.*

## Contents



# 5.1 Gravity processing of the micaceous residue

## 5.1.1 Introduction

Despite the increasing developments and efforts in metal recycling, some metals like Rare Earth metals still have low recycling rates and very few effective substitutes. For these strategic metals the future metal supplies will likely be dependent, in addition to classical ore deposits, upon numerous unconventional resources. Among these unconventional resources, low grade ores represent the next logical step for the mining industry as illustrated by the decrease of the minimum cut-off grades of all metals with time (Laznicka, 2006; Norgate and Jahanshahi, 2010). Industrial process residues often contain low rare-earth concentrations, but volumes are large (Binnemans et al., 2015). In the case of St Austell kaolin dry mining plant, Light Rare-Earth Elements (LREE) and rare metals (Sn, Nb and W) are pre-concentrated in the micaceous residue from hydrocyclones underflow (Chapter 3). The main LREE in terms of grades are in decreasing order: Ce, La, Nd, (Pr, Sm). The overall grades obtained from daily sampling over one week are around 170 ppm LREE, 140 ppm Sn, 94 ppm Nb and 70 ppm W. These values are indicative and give an idea of the order of magnitude of metal grades within the micaceous residue. Indeed core samples data show non negligible large scale variability of metal grades and batch-scale sampling of the micaceous also show that short-scale variability is observed (Chapter 4).

Despite this grade variability the host minerals for LREE and rare-metals seems to be the same within the deposit. Conservation of the LREE ratio from macroscopic to microscopic scale indicates that monazite is the only LREE-bearing mineral within St Austell biotite granite. The main host mineral for Sn is cassiterite whereas W is mainly hosted in wolframite. Rutile seems to be the main host for Nb but two species of rutile have been observed, a Nb-rutile and a less common zoned Nb–Sn–W–Ta rutile corresponding to the specimens described in Wheal Remfry tourmaline breccia

pipe (Müller and Halls, 2005). Mineralogical observations suggest that most of the metal-bearing minerals are free, sometimes associated with rutile (monazite) or micas (cassiterite, monazite, rutile) with the exception of wolframite which is always observed as free grains (Chapter 3).

Low grade ores processing usually lead to increasing energy consumption and greenhouse gas emission. Thus concentration of metals of interest (when no necessary grinding is required) prior to pyro/hydrometallurgy is necessary to reduce energy consumption and environmental impacts (Norgate and Jahanshahi, 2010).

#### 5.1.1.1 Gravity processing of low grade ores

The complexity, the cost and the difficulties associated with methods involving chemical or physicochemical properties (*i.e* hydrometallurgy) such as pollution or environmental issues, contrasts with the relative simplicity, low cost and other benefits such as treatment of coarse particles or larger tonnages unit of some gravity concentration methods (Burt, 1999). It is the most common technique used for pre-concentration of high specific gravity REE-minerals (Jordens et al., 2013; Kumari et al., 2015). Typical processing flowsheets of REE-bearing minerals like monazite usually start by gravity concentration followed by additional gravity, magnetic, electrostatic and occasionally flotation separation steps (Ferron et al., 1991; Houot, 1982). For the monazite rich ores, concentrates are usually treated by various pyro/hydrometallurgical processes including leaching, solvent extraction or precipitation (Gupta and Krishnamurthy, 2004; Zhu et al., 2015). Cassiterite concentration is mainly performed by a combination of gravity pre-concentration followed by flotation of the fine fraction to upgrade the concentrate (Angadi et al., 2015).

Spiral concentrators are high capacity, low cost units used for the recovery of heavy minerals from sands and ores with minimum operating costs as there is no energy consumption (Burt, 1984b; Wills and Napier-Munn, 2005). The principle of separation is based on gravity and centrifugal forces that act together to separate light and heavy minerals. For more details on the separation mechanism, the interested reader is invited to refer to the literature (Atasoy and Spottiswood, 1995; Burt, 1984b; Sivamohan and Forssberg, 1985a). Despite the large variety of spirals and manufacturers the operating parameters are the same, *i.e.* feed rate, feed pulp density (solid wt. %), splitter position and wash water flow rate. Generally speaking, increasing feed rate usually results in lower performance as for feed pulp density but the latter tends also to have a positive effect on fine particles recovery (Falconer, 2003). Wash water has also a significant effect as it clean the concentrate stream of the entrapped light particles.

Shaking tables are one of the most efficient devices in mineral processing (Burt, 1984b). However it is a relatively low capacity device in comparison to spiral concentrator and is usually employed in second steps of concentration. The principle of separation is based on the thin film concentration process across an inclined table having an asymmetric periodic motion to allow selective stratification of the particles according to their SG, size and shape (Sivamohan and Forssberg, 1985c). The main operating parameter is undoubtedly the deck angle which impacts directly the grade and recovery of the concentrates. Others operating variables are feed rate, pulp density, wash water flow rate and motion frequency. For a comprehensive understanding of the influence of the operating parameters, the interested reader is directed to the work of Manser et al. (1991).

#### 5.1.1.2 Response surface method (RSM)

Design of experiments are characterised by the number $k$ of factors which are investigated and the number $l$ of levels taken by each factor with the notation $l^k$. When there is a need for good, possibly non-linear, model of the studied phenomenon the number of levels required must be equal or above 3 (Goupy and Creighton, 2007). In this case ($l \geq 3$) the response surface method (RSM) can be applied to model and optimise the response surface influences by the $k$ factors. When there is no information about the relation between a response $y$ and the $k$ factors, the response surface can be expressed in its general form (Myers et al., 2009):

$$y = f(x_1, x_2, \ldots, x_k) + \varepsilon \tag{5.1}$$

where $x_i$ are the measurable variables (factors) and $\varepsilon$ a residual grouping the lack of fit (difference between the model chosen before the trials from the true model) and random experimental error (or pure error). This function is too general; typically a more functional relationship between the response and the independent variable is used through a limited Taylor development of Equation (5.1) :

$$y = a_0 + \sum_{i=1}^{k} a_i x_i + \sum_{i=1}^{k} a_{ii} x_i^2 + \sum_{i=1}^{k-1} \sum_{j=1}^{k} a_{ij} x_i x_j + \ldots + \varepsilon \tag{5.2}$$

where $a_0, a_i, a_{ii}, a_{ij}$ are the model coefficients, called constant, linear, quadratic and interaction terms respectively, that are estimated using experimental results. This corresponds to a system of $n$ equations ($n$ trials) with $p$ unknowns ($k$ factors) in the matrix notation:

$$Y = X.A + \varepsilon' \tag{5.3}$$

where $Y$ is the response vector, $A$ is the coefficients vector, $X$ is the design matrix of variables values fixed by the chosen experimental points and $\varepsilon'$ a residual vector grouping the previous residual $\varepsilon$ and $a_0$. The least squares estimate $\hat{A}$ of the vector $A$, which minimizes the sum of square errors, is expressed as (Goupy and Creighton, 2007):

$$\hat{A} = (X^T X)^{-1} X^T Y \tag{5.4}$$

where $X^T$ is the transpose of the matrix $X$ and $(X^T X)^{-1}$ the inverse of the matrix $X^T X$. The resolution methodology, based on the least square method can be found in many reference textbooks, *e.g.* (Goupy and Creighton, 2007; Montgomery, 2008; Myers et al., 2009).

This study investigates the use of two gravity concentration techniques, *i.e.* spiral concentrator and shaking table, using $3^2$ factorial designs, with the main objective of producing a heavy minerals pre-concentrate from the micaceous residue.

## 5.1.2 Materials and methods

### 5.1.2.1 Material

All samples used in this work were collected with the support of Imerys Minerals Ltd, UK. The material treated in this paper corresponds to the kaolin micaceous residue described in Chapter 3. A 4 tons daily pulp sample were collected and aggregated from the secondary hydrocyclones underflow operating at an approximate flow rate of 15 tons/hour, during the processing of master grade (highly kaolinised ore) extracted from Melbur and Virginia pits. The samples were extracted by systematic sampling using a by-pass that diverted the entire stream into the sample collector and then aggregated into large samples for metallurgical testing (see Section 2.1.2). The average concentrations in LREE (∼110 ppm) and rare-metals (∼75 ppm Sn and 105 ppm Nb) in this daily micaceous residue sample are considerably lower than the average grades presented in Chapter 3, suggesting long-term grade variability.

### 5.1.2.2 Chemical analysis

Samples were grinded and riffled alternatively in accordance with theory of sampling to obtain representative subsamples suitable for whole rock analysis. Chemical analyses were carried out by Energy Dispersive X-Ray Fluorescence spectroscopy (ED-XRF) using a S2 Ranger (Bruker Corporation). Calibration of the XRF used results from Inductively Coupled Plasma Mass Spectrometry (ICP-MS) for the trace elements analyses performed at the *Service d'Analyses des Roches et des Minéraux* (SARM-CNRS, Nancy, France).

### 5.1.2.3 X-Ray Diffraction (XRD)

Characterisation of the crystalline phases has been performed by X-ray diffraction using a D8 Advance X-ray diffractometer (Bruker Corporation), equipped with a cobalt $K_{\alpha 1}$ ray (1.789 Å) on disoriented powdered samples. The diffraction patterns were processed using DIFFRAC.EVA software (Bruker Corporation) for peaks identification with PDF database.

### 5.1.2.4 Gravity concentration set-ups

The gravity concentration tests were realised at the STEVAL pilot plant at the GeoRessources laboratory (Nancy, France). In order to improve the efficiency of the gravity separation process, the material needs to be screened into several size fractions. The size fractions have been selected on the basis of the washability of the material, *i.e.* its size-density distribution. The washability of the material was obtained by dense medium separation combined with centrifugation using pure and diluted bromoform (SG=2.89 and 2.79 respectively) on the different size fractions. The Figure 5.1 presents a typical washability of a micaceous residue sample.

The size distribution of the heavy particles is clearly shifted to the fine fractions, especially bellow 90 µm. However in order to correspond to standard sieve sizes used in practice, the samples were screened at 180 µm and 53 µm following the general flowsheet presented in Figure 2.6 (see Chapter 2).

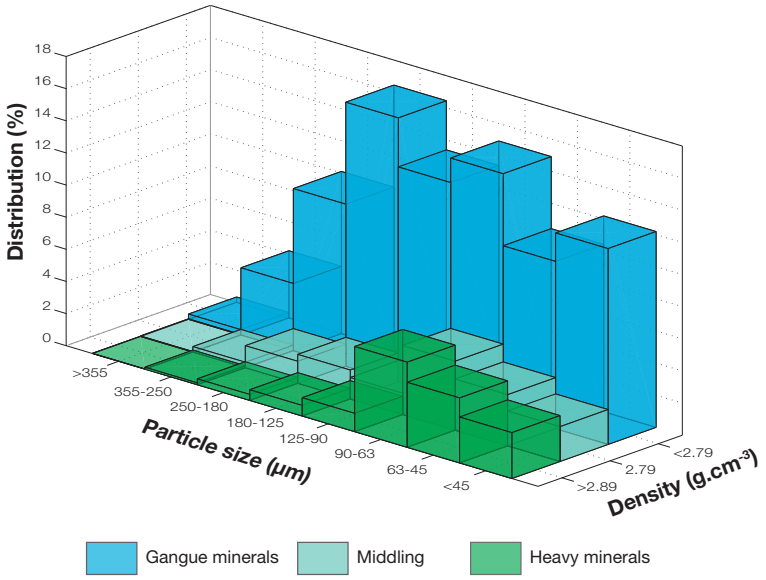


Figure 5.1: Typical washability of the micaceous residue sample.

The spiral separator tested in this research paper is a 5 turn MKIIA Reichert spiral (Mineral Deposit Limited, Australia). Since the objective of this stage is to improve the recovery, the two middling offtakes were grouped to one. The dry sample was mixed with water in the mixing tank into pulp which was then pumped to the feed tank (see Figure 2.8 in Chapter 2). Concentrate, middling and tailings were discharged into the mixing tank by flexible pipes to allow sample collection while operating in closed-circuit. Due to wash water addition the feed pulp density decreases during the operation. This dilution can be easily controlled from the initial pulp density as wash water flow rates are known. Hence samples can be collected at specific times during the operation to represent a given feed pulp density. The steady state is achieved when sampling is carried out. Scavenging tests were also performed with a similar set-up by recovering continuously concentrate and middlings during time, simulating successive passes in spirals separator. Again the pulp density is known so, by measuring the feed flow rate, it is possible to assess the time of one pass, *i.e.* the time beyond which all the sample have passed through the spiral, and hence the number of passes. The concentrate splitters position were set at the beginning of the tests and remained fixed during the whole experiment.

The shaking table used for concentration is a Wilfley laboratory shaking table. Based on feasibility tests results, among the 8 outputs of the discharge launder, the two first outputs at the front of the deck were considered as concentrate, the third to fifth, located at the table corner, as middling and the other outputs were combined to one tailing (see Figure 2.9 in Chapter 2). Shaking table feed corresponds to spiral concentrate aggregated from additional spiral tests performed with the optimal operating parameters for the heavy minerals recovery given by the design of experiments to get the necessary amount of material. Operating in closed circuit is much more complicated with the laboratory shaking table. Indeed the feed flow rate is much lower than for spiral which is not suitable for slurry pumping and hence the table could only be fed with dry material via a screw feeder. As the amount of material required for one test is relatively large (minimum 20 kg), due to the time required to reach the

steady state, every output were recovered and mixed back together after each test and then were dried to serve as feed of the following tests. This procedure may lead to fluctuations of feed properties due to the drying process.

#### 5.1.2.5 Experimental designs

For both devices, $3^2$ full factorial designs were used to investigate the relationship between the independent variables and the responses, with wash water flow rate and feed pulp density for the spiral tests and deck angle and motion frequency for the shaking table. Heavy mineral grade (G) in the concentrate and heavy minerals recovery (R) were used as response variables to qualify the efficiency of gravity concentration and avoid multiple responses modelling for each metal. This approach allows assessing the true effectiveness of the investigated concentration techniques as heavy minerals concentrators disregarding the fact that the treated samples are depleted in metals. Randomly selected duplicate tests under the same experimental conditions were performed to characterise the repeatability of the tests and an estimate of the experimental errors (Montgomery, 2008). For each device the levels were chosen in accordance with preliminary results and the operating range recommended by the manufacturers (Table 5.1). An Analysis of Variance (ANOVA) was used to provide useful statistical measurements to help in evaluating the models used in the analysis. It allows assessing the significance of the regression coefficients and the associated regression models by using the Fischer's $F$-test to calculate $F$-ratios and p-values. The $F$-ratio allows the calculation of the probability that the two mean squares are not equal. Hence the higher the $F$-ratio is, the smaller is the probability that the model is only due to the effect of the mean (Goupy and Creighton, 2007). The critical $F$-ratios choosing 95% confidence level can be found in the related $F$-statistics table and the regression model is considered significant if the $p$-value is less than 0.05. Similarly the Student's $t$-test is used to assess the significance of the regression coefficients. The experimental designs were generated using the D-optimal design tool of JMP® statistical software (SAS institute). The data processing and statistical analysis were performed using the same tool (Goupy and Creighton, 2007).

Table 5.1: Independent factors and corresponding levels for the experimental designs.

| **Factors** | **Symbol** | **Levels** | | |
|---|---|---|---|---|
| | | **Low** (-1) | **Centre** (0) | **High** (+1) |
| *Spiral* | | | | |
| **Wash water flow rate (Lpm)** | WFR | 2 | 6 | 10 |
| **Pulp density (wt.%)** | %S | 15 | 20 | 25 |
| *Shaking table* | | | | |
| **Deck angle (°)** | A | 1 | 1.5 | 2 |
| **Motion frequency (Hz)** | F | 39 | 42 | 45 |

### 5.1.3 Results

Where spirals are employed for roughing low grade feeds, or as scavenging units, recovery is more important than grade (Burt, 1984b). The objective of this first preconcentration step is thus to maximize heavy minerals recovery and then to refine concentration using the shaking table.

#### 5.1.3.1 Spiral pre-concentration

The effects of operating parameters are analysed first by classical grade-recovery based approach in order to set the best operating parameters for heavy minerals recovery. Based on these results scavenging tests were performed to analyse the influence of the number of passes, again using a grade-recovery based approach for heavy minerals.

##### 5.1.3.1.1 Design of experiments results and critical validation

Spiral separation performance results from the 11 tests are summarized by combining both concentrate and middling into a rough concentrate (Table 5.2). In order to minimize random errors, test order was randomly generated. A first screening of the results, prior to regression models clearly shows that variations of wash water flow rate strongly influence the concentrate grade as well as the recovery. The highest grades are reached for the highest wash water flow rates but these also correspond to the lower recoveries. From Table 5.2, the effects of pulp density and parameters interaction is less straightforward and further statistical analysis have been applied.

Table 5.2: $3^2$ factorial design used for the spiral tests and experimental results, *i.e.* heavy minerals grade ($G$) and recovery ($R$). The number in the brackets present the level according to design of experiment set.

| **Test #** | **$x_1$ (WFR)** | **$x_2$ (%S)** | **Yield** | **G** | **R** |
|---|---|---|---|---|---|
| Units | Lpm | wt.% | % | % | % |
| **1** | 10 (+ 1) | 15 (– 1) | 5.5 | 70.1 | 14.8 |
| **2** | 10 (+ 1) | 20 (0) | 3.2 | 71.4 | 8.3 |
| **3** | 10 (+ 1) | 25 (+ 1) | 2.7 | 68.7 | 6.2 |
| **4** | 6 (0) | 15 (– 1) | 6.8 | 64.5 | 15.7 |
| **5** | 6 (0) | 20 (0) | 5.4 | 66.2 | 12.3 |
| **6** | 6 (0) | 15 (– 1) | 6.8 | 64.5 | 15.7 |
| **7** | 2 (– 1) | 15 (– 1) | 19.6 | 44.7 | 35.7 |
| **8** | 2 (– 1) | 20 (0) | 14.7 | 49.1 | 24.5 |
| **9** | 2 (– 1) | 25 (+ 1) | 12.3 | 48.3 | 20.2 |
| **10** | 2 (– 1) | 25 (+ 1) | 12.9 | 48.5 | 21.0 |
| **11** | 10 (+ 1) | 25 (+ 1) | 2.6 | 69.2 | 6.1 |

The obtained models for heavy minerals grade ($G$) and recovery ($R$) to the spiral concentrate as a function of wash water flow rate ($x_1$) and pulp density ($x_2$) are:

$$G = 66.45 + 11.39x_1 + 0.49x_2 - 1.21x_1x_2 - 6.39x_1^2 - 2.01x_2^2 \tag{5.5}$$

$$R = 11.05 - 8.64x_1 - 5.20x_2(+1.55x_1x_2) + 5.98x_1^2(+1.83x_2^2) \tag{5.6}$$

The models significance was assessed through an analysis of variance (ANOVA) that includes tests on the effects and lack of fit (Table 5.3). According to the degrees of freedom (DF) of models and residuals, which both have a DF of 5, the critical $F$-value for the 0.05 significance level is much lower ($F_{(5,5)} = 5.05$), than the $F$-values ($F$) for the grade and recovery models which are around 1635.01 and 59.74 respectively. This indicates that the observed variations of grade and recovery are likely due to variation in the factors. Accordingly $p$-values ($P$) are very low, $<0.0001$ for the grade and 0.0002 for the recovery regression models, which indicates that there is a small probability that the obtained model is only due to the effect of the mean.

Table 5.3: Analysis of variance (ANOVA) for spiral heavy minerals grade and recovery models with degrees of freedom (DF), sum of squares (SS), $F$-ratios (F) and $p$-values (P).

| Source of variation | DF | Grade | | | Recovery | | |
|---|---|---|---|---|---|---|---|
| | | SS | F | P | SS | F | P |
| Model | 5 | 1090.15 | 1635.01* | <.0001 | 809.31 | 59.74* | 0.0002 |
| $x_1$ (WFR) | 1 | 950.00 | 7124.00 | <.0001 | 546.97 | 201.86 | <.0001 |
| $x_2$ (%S) | 1 | 1.78 | 13.36 | 0.0147 | 199.84 | 73.75 | 0.0004 |
| $x_1$* $x_2$ (WFR*%S) | 1 | 8.02 | 60.11 | 0.0006 | 13.14 | 4.85 | 0.0789** |
| $x_1^2$ (WFR²) | 1 | 87.21 | 653.99 | <.0001 | 76.32 | 28.17 | 0.0032 |
| $x_2^2$ (%S²) | 1 | 8.61 | 64.55 | 0.0005 | 7.15 | 2.64 | 0.1651** |
| Residuals | 5 | 0.67 | | | 13.55 | | |
| Total | 10 | 1090.82 | | | 822.57 | | |
| Lack of fit | 3 | 0.61 | 7.71 | <.0001 | 13.22 | 27.12 | 0.0358 |
| Pure error | 2 | 0.05 | | | 0.33 | | |
| Total error | 5 | 0.67 | | | 13.55 | | |

*Critical F-value for the 0.05 significance level is $F_{(5,5)}$=5.05.

**Non-significant parameter.

The accuracy of the models is illustrated by the relationship between the observed experimental results and the predicted results using regression models (Equations (5.5) and (5.6)) and the corresponding summary of fit (Figure 5.2). There is a strong correlation between predicted and observed results for both grade and recovery models with $R^2$ >0.99 and 0.98 respectively, far above the recommended $R^2$ values (Montgomery, 2008). The predicted values are in agreement with the predictions with a trend line slope around 1 for grade and very close to 1 (slope = 0.98) for recovery. The root mean square errors (RMSE) are quite low for both grade and recovery models, 0.27 and 1.22 respectively, and of the same order of magnitude as the experimental error.

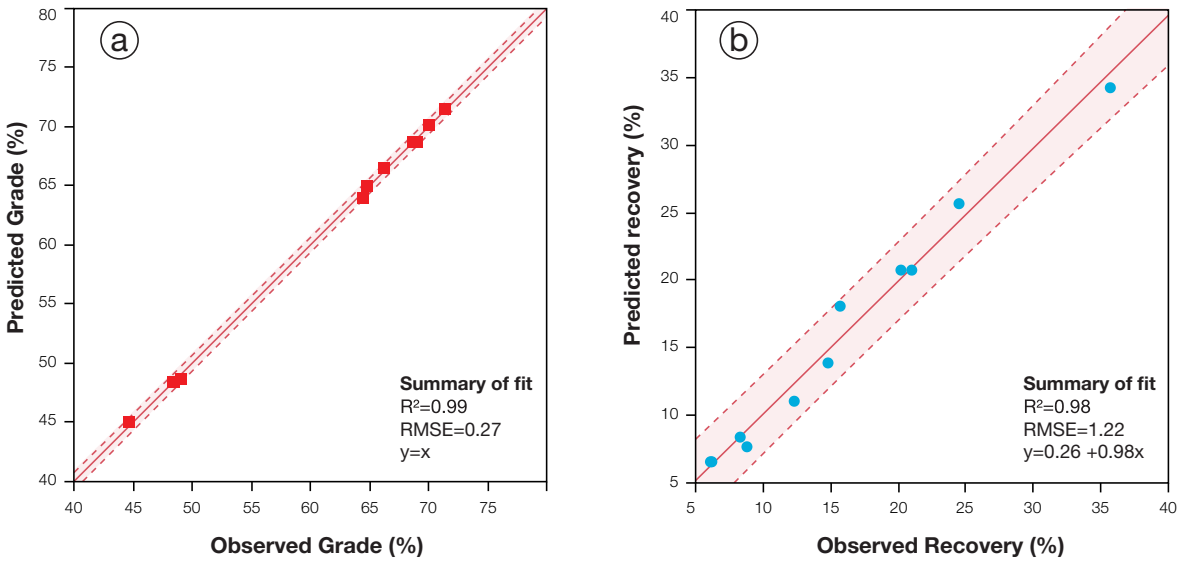


Figure 5.2: Comparison between observed and predicted results using regression models with trend lines, 95% confidence intervals and summary of fit. (a) Strong correlation ($R^2$>0.99) between observed and predicted grades. (b) Strong correlation ($R^2$=0.98) between observed and predicted recoveries.

It is also important to analyse the residuals to make sure that there is no structural information in the results (Goupy and Creighton, 2007). Residuals are plotted as a function of the predicted responses in Figure 5.3. There is no latent pattern observable in the residuals plot but a random dispersion of the residuals, suggesting a normal distribution of errors and an adequate prediction model.

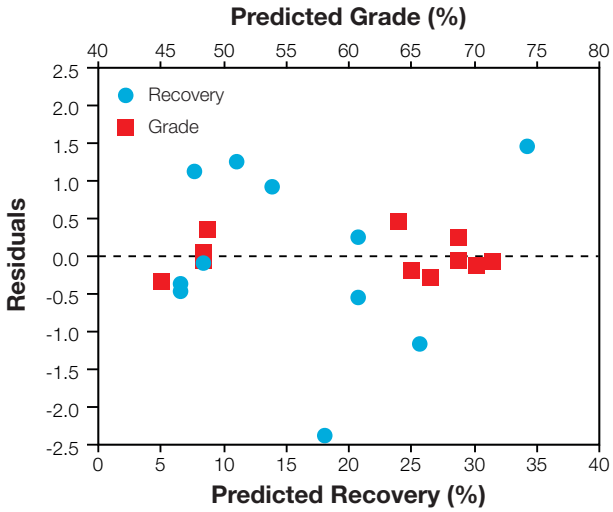


Figure 5.3: Residual plot for predicted recovery and grade. The residuals are well uniformly distributed for the grade and recovery, indicating a normal distribution of errors.

#### 5.1.3.1.2 Interpretation of the regression models

Table 5.4 shows the parameter estimates, the associated standard errors and their significances according to the Student's $t$-test. To determine if a factor influence significantly the results, a commonly chosen limit is two or three times the standard error (Goupy and Creighton, 2007). It must also differ significantly from zero and having a $p$-value below 0.05.

For heavy minerals grade model, all factors are significant according to both their standard deviation and the $t$-test. Even if the $t$-value ($T$) for pulp density ($x_2$) is quite low (3.66), its $p$-value is less than 0.05, so this factor can be considered to be influential. The $t$-value for wash water flow rate ($x_1$) is the highest for the grade, indicating a positive linear effect of this factor. The grade is also affected by a positive linear effect of pulp density ($x_2$), due to the positive but low coefficient (0.49). On the contrary, quadratic effects for these factors seem to impact negatively the heavy minerals grade with negative coefficient for wash water flow rate and pulp density of -6.39 and -2.01 respectively. Interestingly, the interactional effect between these two factors is significant, with a positive effect on heavy minerals grade. These opposite effects of linear terms in comparison with quadratic terms indicate that a local extremum, even if not reached during the experiments, is located within the experimental domain. In this case, since the quadratic coefficients are negative, this extremum is a maximum for heavy minerals grade.

The linear effect of both wash water flow rate ($x_1$) and pulp density ($x_2$) on heavy minerals recovery is negative, with coefficients of -8.64 and -5.20 respectively. However, the recovery is positively affected by the quadratic effect of wash water flow rate ($x_1$)

due to its positive coefficient of 5.98. The quadratic effects of pulp density as well as the interaction effect, with $p$-values of 0.1651 and 0.0789, are not significant for the recovery as suggested by the ANOVA results in Table 5.4.

Table 5.4: Parameter estimates for the concentrate heavy minerals grade and recovery as a function of the standardized parameters with standard errors (STD), $t$-ratios (T) and corresponding $p$-value (P).

| Term | Estimate | STD Error | T | P |
|---|---|---|---|---|
| *Heavy minerals grade* | | | | |
| Constant | 66.45 | 0.27 | 247.40 | <.0001 |
| $x_1$ (WFR) | 11.38 | 0.14 | 84.40 | <.0001 |
| $x_2$ (%S) | 0.49 | 0.13 | 3.66 | 0.0147 |
| $x_1$* $x_2$(WFR*%S) | -1.21 | 0.16 | -7.75 | 0.0006 |
| $x_1^2$ (WFR$^2$) | -6.39 | 0.25 | -25.57 | <.0001 |
| $x_2^2$ (%S$^2$) | -2.01 | 0.25 | -8.03 | 0.0005 |
| *Heavy minerals recovery* | | | | |
| Constant | 11.05 | 1.21 | 9.12 | 0.0003 |
| $x_1$ (WFR) | -8.64 | 0.61 | -14.21 | <.0001 |
| $x_2$ (%S) | -5.20 | 0.61 | -8.59 | 0.0004 |
| $x_1$* $x_2$(WFR*%S) | 1.55 | 0.70 | 2.20 | 0.0789* |
| $x_1^2$ (WFR$^2$) | 5.98 | 1.13 | 5.31 | 0.0032 |
| $x_2^2$ (%S$^2$) | 1.83 | 1.13 | 1.62 | 0.1651* |

* Non-significant parameter.

The global effect of each factor on heavy minerals grade and recovery can be better understood from the response surfaces fitted to experimental data (Figure 5.4). It can be seen that wash water flow rate is clearly the most significant factor both for the grade and recovery. Indeed the grade is only affected by a minor effect of pulp density whereas the recovery is slightly more affected. However, it is observed that the grade response surface reaches a local maximum for the high water flow rate and an average pulp density. The recovery response surface seems monotonous and no local maximum is reached for this response. The opposite effect of wash water on grade and recovery is illustrated by the increasing grade while recovery falls with increasing wash water flow rate. This corresponds to the well-known opposite behaviour of grade and recovery which is clearly observable in Figure 5.4. For optimisation purposes, the models are plotted on iso-response plots, to see the influence of the two factors on both responses on the same plot (Figure 5.5). This corresponds to the projection of the response surface with a 5% increment. It can be observed that the high grade domains logically correspond to the low recovery domains. The minor influence of pulp density ($x_2$) on grade appears clearly with iso-response curves sub-parallel to the $x_2$-axis for low wash water flow rate values. However, for high wash water flow rates, above 8 Lpm, the influence of pulp density is more important and defines a high recovery domain for average pulp densities around 20 wt.%. Even if this domain is at the edge of the experimental domain, it indicates that increasing the wash water flow rate too much will have a negative effect on heavy minerals grade. The maximum heavy minerals grade that could be achieved according to model is 71.6% of heavy minerals for a wash water flow rate of 9.6 Lpm and a pulp density of 19.2 wt.% which is close to the 71.4

% grade obtained for test n°2 (Table 5.2).

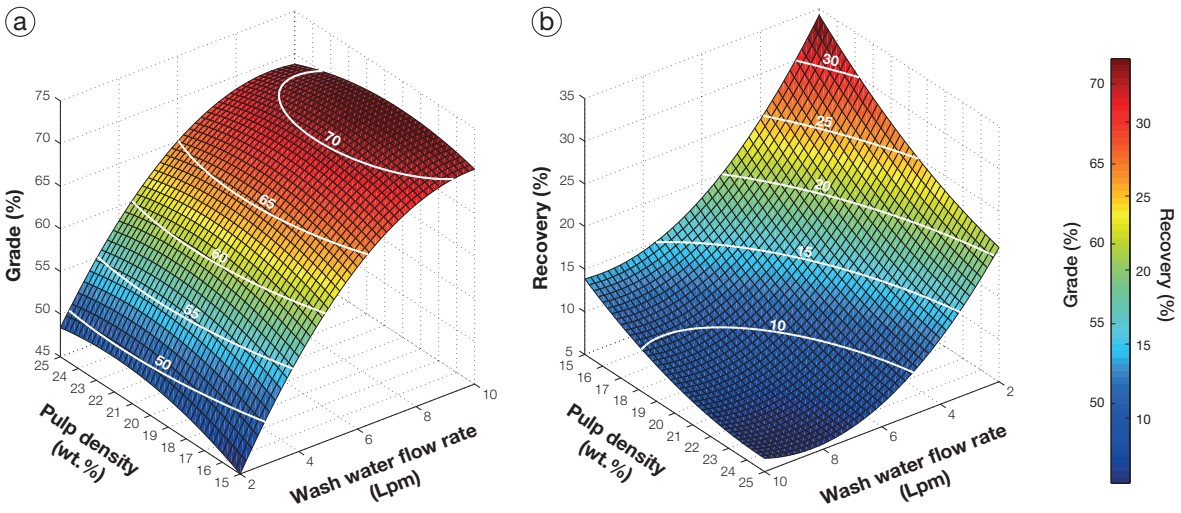


Figure 5.4: Response surface plots showing the influence of wash water flow rate and pulp density on heavy minerals grade (a) and recovery of heavy minerals (b) in the concentrate.

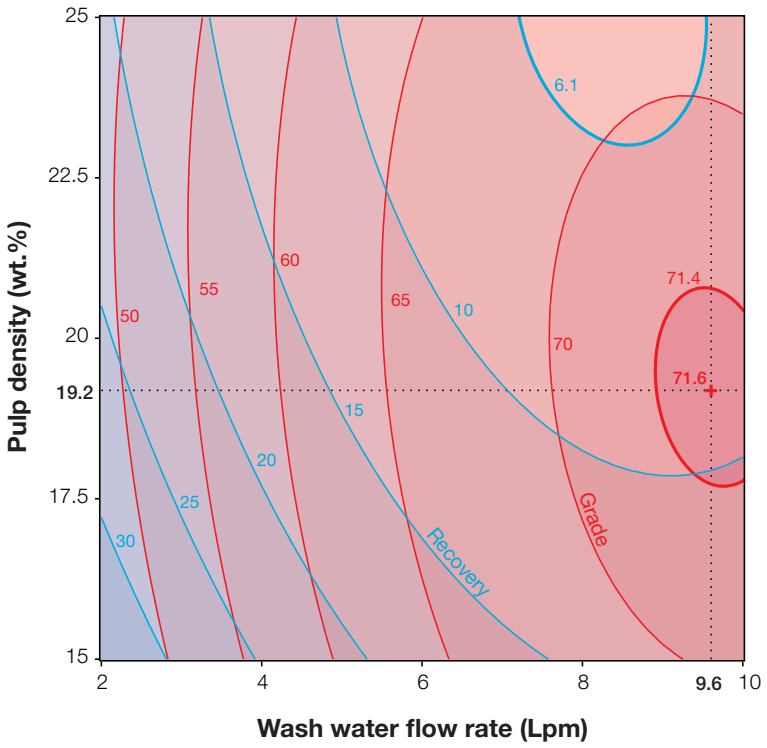


Figure 5.5: Iso-response surface of heavy minerals grade and recovery in spiral concentrate as a function of wash water flow rate and feed pulp density. A local maximum of 71.6% is reached for heavy minerals grade whereas the recovery displays no maximum inside the domain.

Unfortunately no maximum for heavy minerals recovery is observed within the experimental domain. Since recovery increase with decreasing wash water flow rate and pulp density, it could be interesting to expanse the experimental domain and add

lower levels for each factor. Nonetheless the value chosen for the low level of each factor are already quite outside the recommended operating range. Indeed decreasing further the wash water flow rate is practically feasible but wash water supplied will not be equally distributed down the spiral and no wash water will enter the last turns.

#### 5.1.3.1.3 Scavenging

Scavenging tests were performed in order to assess how many passes are necessary to recover the majority of the heavy minerals. Thus scavenging tests have been performed using the lowest values for both wash water flow rate and pulp density in order to favour recovery. The scavenging tests were performed by recovering continuously the heavy minerals concentrate and middling together while the tailings were pumped back to the spiral feed tank. Samples were collected systematically in order to follow the cumulated heavy minerals recovery and grade (Figure 5.6). The cumulated recovery increases almost linearly with the number of passes, with up to 80 % recovery for 4 passes while the mean grade of the resulting concentrate decreases from 47% down to 33% heavy minerals. Even if it seems that continuing the scavenging up to few more passes could increase recovery further, the corresponding yield will increase too. Indeed, after 4 passes, the yield is already very high with almost 50% of the feed material recovered in the concentrate. Thus it is of primary importance to know when to stop the scavenging and the number of passes required.

In order to answer that question, the sink fraction (SG>2.89) of the spiral concentrates have been analysed by XRD analysis in order to observe the eventual changes in mineralogy with the number of passes. The XRD patterns for some selected concentrates corresponding to the timing of the first 4 passes as well as the final tailing are shown in Figure 5.7. It appears that the mineralogy of the heavy minerals fraction in the first concentrate is clearly dominated by tourmaline (mainly schorl) and to a lesser extent by micas. Topaz and Nb-rutile are also present but in minor amounts. The main difficulty with XRD analysis is that it only detects the major phases. In

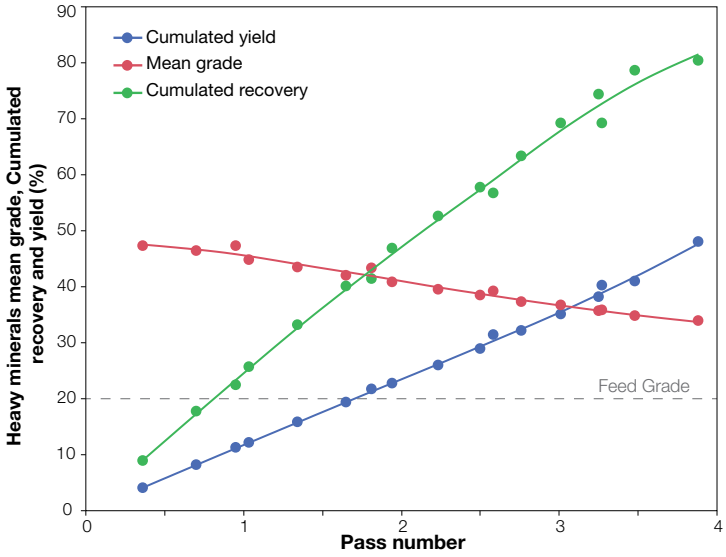


Figure 5.6: Cumulated yield, recovery and heavy minerals mean grade of the spiral concentrates as a function of the number of passes.

this case monazite is not enough concentrated to be detected clearly and thus no variations in monazite grades can be observed on the basis of XRD analysis. Another key difficulty is that cassiterite has its most intense diffraction peak (at d=3.35 Å) very close to the one of quartz (at d=3.34 Å), which results in serious difficulties to discern evolution in cassiterite concentration. However it seems that the peak at d=3.35 Å is due to cassiterite that is concentrated in the first concentrate as the secondary peak of quartz (at d=4.26 Å) is not observed. As the number of passes increases, the intensity of schorl, topaz and rutile diffraction peaks decreases, whereas the ones of micas increase. After 3 passes (270-300 s), the cassiterite peak is no longer discernible and is overlapped by quartz main peak. The fact that quartz peaks are present in the heavy minerals fraction suggest that after 3 passes, quartz middlings start to be recovered in the concentrate. The mineralogy of the heavy fraction of the final tailings is clearly dominated by micas, schorl and to a lesser extent by quartz. However no diffraction peaks of rutile or cassiterite were detected indicating that the majority of metal-bearing minerals have been recovered.

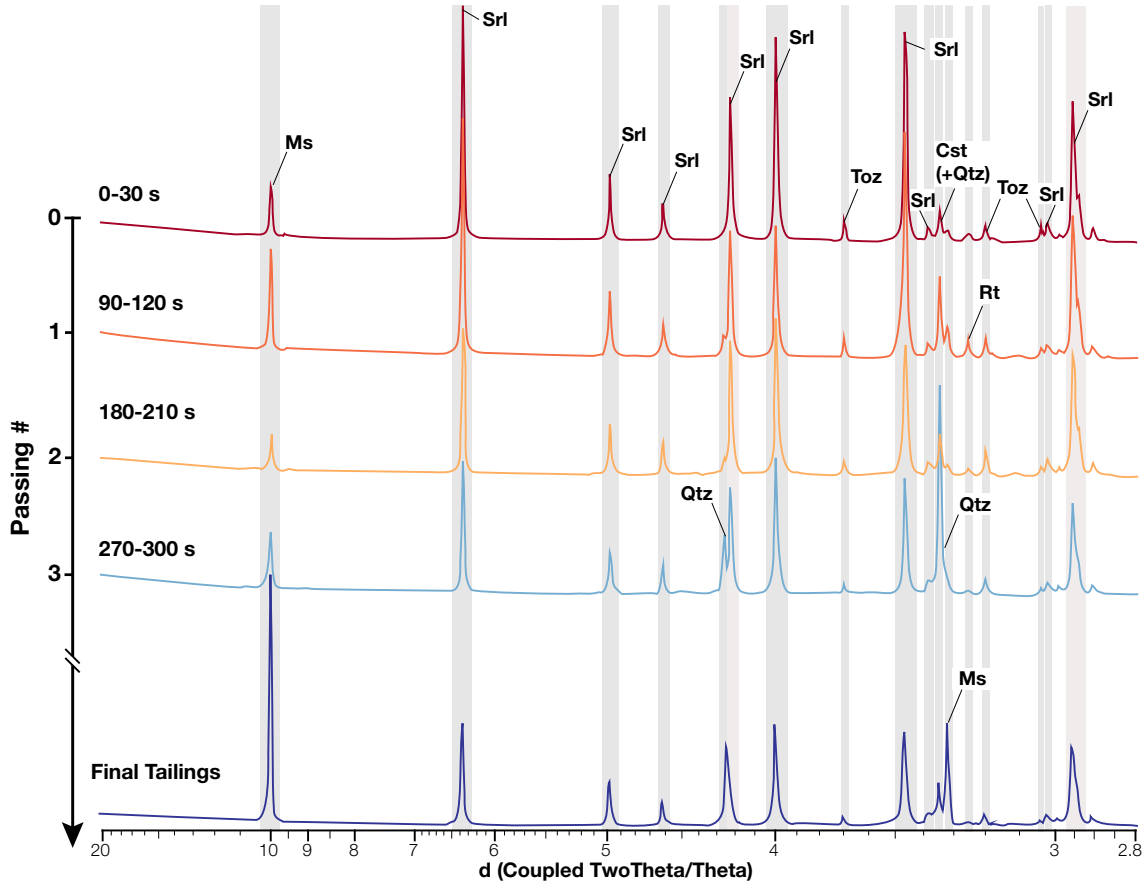


Figure 5.7: Evolution of the XRD pattern of the heavy minerals fraction in spiral concentrates as a function of the number of passes. Most of the heavy minerals recovered are schorl (Srl) but peaks of micas (Ms), cassiterite (Cst), topaz (Toz) and rutile (Rt) are also discernible in the first concentrates. At 3 passes, quartz (Qtz) peaks indicate that middling are being recovered in the concentrate. The final tailings XRD pattern only displays peaks of micas, schorl and quartz middlings.

#### 5.1.3.2 Table testing

The effects of operating parameters are analysed by classical grade-recovery based approach for heavy minerals in order to set the best operating parameters for heavy minerals recovery. Based on previous results, a pre-concentrate from a spiral operating at 2 Lpm wash water flow rate and with a 15 wt.% pulp density, were used as feed material for the shaking table.

##### 5.1.3.2.1 Design of experiments results and critical validation

The experimental results along with the operating conditions of the 9 shaking table tests of the $3^2$ factorial designs are presented in Table 5.5. The results obtained prior to regression models clearly show that the variations of deck angle strongly influence the heavy minerals recovery and to a lesser extent the grade. The highest grades are reached for the highest deck angles but these also correspond to the lower recoveries.

Table 5.5: $3^2$ factorial design used for the shaking table tests and experimental results. The number in brackets present the level according to design of experiment set.

| **Test #** | **$x_1$ (A)** | **$x_2$ (F)** | **Yield** | **Grade** | **Recovery** |
|---|---|---|---|---|---|
| Units | ° | Hz | % | % | % |
| **1** | 1 (– 1) | 39 (– 1) | 36.62 | 91.81 | 63.07 |
| **2** | 1.5 (0) | 39 (– 1) | 25.99 | 91.93 | 41.39 |
| **3** | 2 (+ 1) | 39 (– 1) | 23.30 | 96.77 | 36.79 |
| **4** | 1 (– 1) | 42 (0) | 35.88 | 91.73 | 78.28 |
| **5** | 1.5 (0) | 42 (0) | 31.45 | 86.67 | 53.80 |
| **6** | 2 (+ 1) | 42 (0) | 23.35 | 95.04 | 33.29 |
| **7** | 1 (– 1) | 45 (+ 1) | 38.21 | 89.95 | 71.95 |
| **8** | 1.5 (0) | 45 (+ 1) | 24.07 | 87.10 | 54.71 |
| **9** | 2 (+ 1) | 45 (+ 1) | 23.69 | 98.48 | 39.54 |

The ANOVA results describing models significance for heavy minerals grade and recovery are presented in Table 5.6. As there are no replicate experiments in this case, the ANOVA only includes tests on the effects but no lack of fit. According to the Degrees of Freedom (DF) of models and residuals, the critical $F$-value for the 0.05 significance level is $F_{(9,3)} = 9.01$ which is greater that the $F$-value ($F$) of the grade model and slightly below the $F$-value of the recovery model which are around 5.32 and 11.35 respectively. This means that the model for heavy minerals grade is not significant and that there is a high probability that the obtained model is only due to the effect of the mean. Searching the effects of the grade model, it can be seen that only linear and quadratic effect of the deck angle are actually significant with $p$-values slightly below the 0.05 limit. The recovery model is significant regarding the $F$-test but has only one truly significant effect. Indeed, apart for the linear effect of deck angles, which has a $p$-value of 0.0055, all the other effects are insignificant regarding their $p$-values. The accuracy of the recovery model is illustrated by the relationship between the predicted recovery and the observed experimental results (Figure 5.8). The predicted values are in agreement with a correlation between predicted and observed results with a $R^2$ =0.95 and a trend line slope of 0.95. However, given the low significance of all the factors, except the linear effect of the deck angle, no response surface model can be reasonably extracted from these experimental results.

Table 5.6: Analyses of variance (ANOVA) for shaking table heavy minerals grade and recovery models with degrees of freedom (DF), sum of squares ($SS$), $F$-ratios ($F$) and $p$-values ($P$).

| Source of variation | DF | Grade | | | Recovery | | |
|---|---|---|---|---|---|---|---|
| | | *SS* | *F* | *P* | *SS* | *F* | *P* |
| **Model** | 5 | 117.27 | 5.32* | 0.0996** | 1964.57 | 11.35* | 0.0365 |
| $x_1$ (A) | 1 | 47.04 | 10.68 | 0.0468 | 1791.59 | 51.75 | 0.0055 |
| $x_2$ (F) | 1 | 4.13 | 0.94 | 0.4040** | 103.75 | 2.99 | 0.1818** |
| $x_1$* $x_2$ (A*F) | 1 | 3.18 | 0.72 | 0.4574** | 29.69 | 0.88 | 0.6384** |
| $x_1^2$ ($A^2$) | 1 | 58.25 | 13.23 | 0.0358 | 9.39 | 0.27 | 0.6384** |
| $x_2^2$ ($F^2$) | 1 | 4.66 | 1.06 | 0.3792** | 30.13 | 0.87 | 0.4196** |
| **Residuals** | 3 | 13.21 | | | 103.85 | | |
| **Total** | 8 | 130.48 | | | 2068.42 | | |

* *Critical F-value for the 0.05 significance level is $F_{(5,3)}$=9.01.*

***Non-significant parameter.*

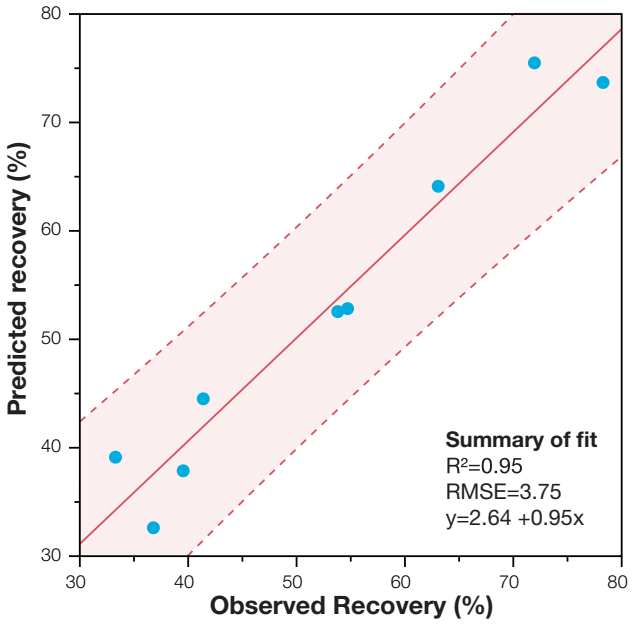


Figure 5.8: Comparison between observed and predicted recovery using empirical models with trend lines and 95% confidence intervals and summary of fit.

#### 5.1.3.2.2 Influence of deck angle and motion frequency

Figure 5.9 illustrates the influence of deck angle and motion frequency on heavy minerals grade and recovery for each output according to the experimental results. It is clear that deck angle is the most important factor with a strong negative effect on heavy minerals recovery given the small variation in deck angle. Indeed recovery to concentrate is reduced by half only by changing deck angle from 1° to 2°, which is still a low angle value as in practice deck angle could vary until 7°.

It could be observed that no clear effect of deck angle on the concentrate grade is observable. However, even if the heavy minerals grade in the concentrate remains roughly constant while deck angle increase, it increases drastically in the middlings output. This illustrates the displacement of the concentrate/middlings limit when the deck angle is changed. Indeed as the angle increase the concentrate band width increase

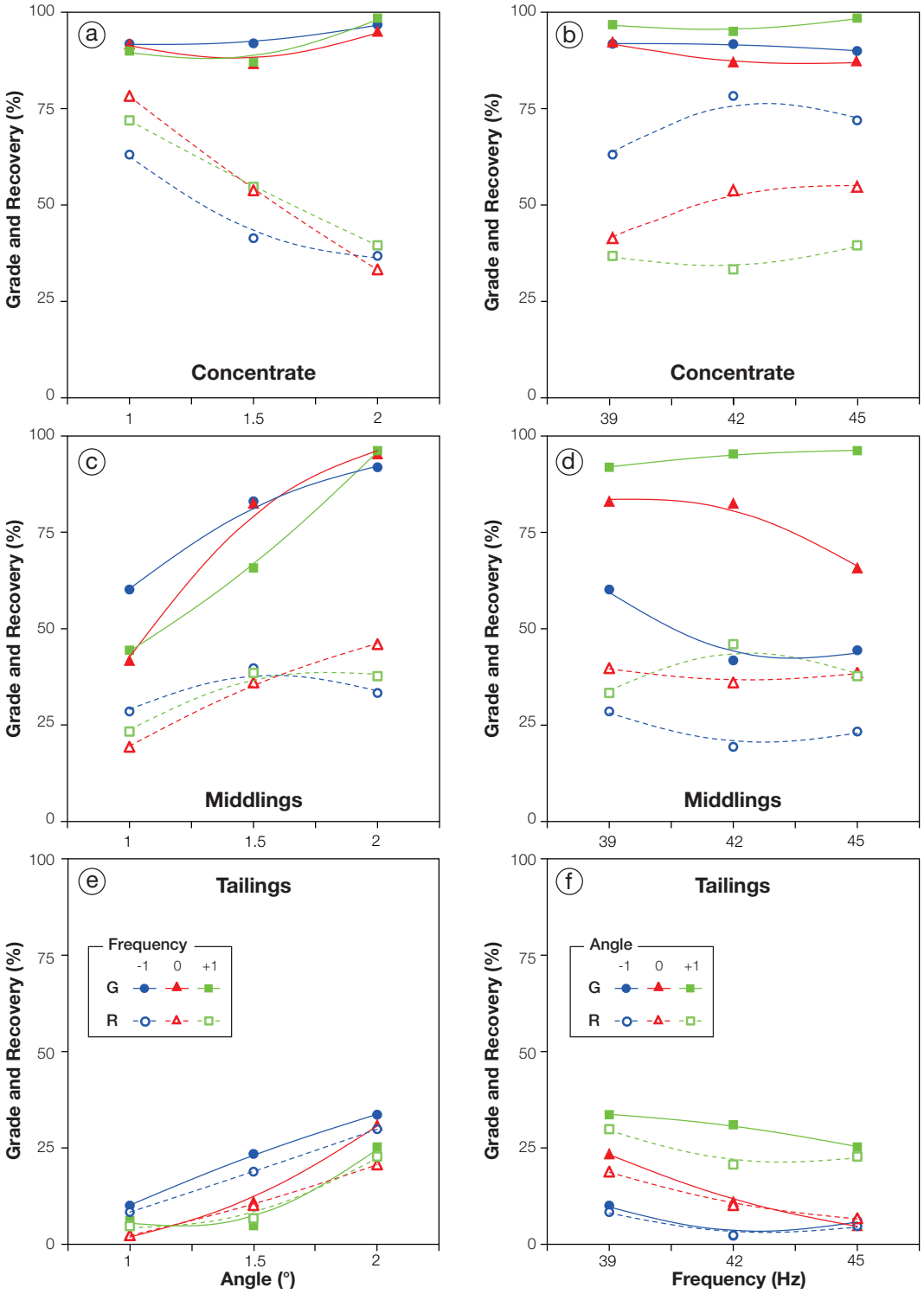


Figure 5.9: Effect of deck angle and motion frequency on shaking table performance. (a) and (b) Effect on grade and recovery of the concentrate. (c) and (d) Effect on grade and recovery of the middlings. (e) and (f) Effect on grade and recovery of the tailings.

too which result in a displacement of the concentrate/middling limit towards the tailing edge of the table. Considering a uniform grade within the concentrate band, this could explain why the heavy minerals grade remains constant in the concentrate offtakes

while the grade increases in the middlings offtakes. This also shows the limitation of a heavy minerals-based approach to analyse the separation with the shaking table, especially when treating a heavy minerals pre-concentrate.

As suggested by the ANOVA analysis, no obvious influence of the motion frequency neither on the grade nor the recovery. However the effect of motion frequency seems more significant on the tailings. Indeed both recovery and grade decrease with increasing frequency, indicating that motion frequency has potentially a more significant impact on the behaviour of the middlings/tailings boundary.

According to the experimental results, the primary objective of favouring the recovery could be achieved with a relatively low deck angle (1°) and a moderate motion frequency (42 Hz). These operating conditions allowed reaching a reasonable heavy minerals recovery (78.28 %) with a still high heavy minerals grade (91.73 %).

#### 5.1.3.3 Overall performance of the tested flowsheet for metal recovery

The ultimate objective of this heavy minerals concentration process applied to the micaceous residue is to recover as much LREE and rare-metal as possible, while simultaneously removing gangue minerals with a minimum processing cost in a saleable pre-concentrate to be sold as by-product. The grade-recovery relationship of LREE for spiral concentrates and shaking table concentrates (tests 7 to 9) are shown in Figure 5.10 with the effect of shaking table deck angle illustrated by a trend line. Figure 5.10 illustrates that low wash water and pulp density produce the best LREE recovery in spiral concentration whereas operating at high wash water and pulp density allow to obtain the best LREE grade which is in agreement with the observation made for heavy minerals grade and recovery. It can be observed that in the optimal recovery condition up to 70% LREE are recovered in only one pass. This means that even if less than 30% heavy minerals are recovered in the first pass and that mineralogical observation suggest that scavenging should comprise up to 3 passes, one or two passes are sufficient to recover the majority of monazite. However the behaviour of other metal-bearing minerals could be slightly different but given the very low grade in the initial sample these couldn't be assessed.

The effect of deck angle in shaking table concentration is illustrated in Figure 5.10 with suggest an increasing LREE grade as deck angle increases. The high deck angle test results in the highest LREE grade of 1.6% LREE (about 3% monazite) with a global LREE recovery of 43% (test n°9). Other tests display less clear results and back-calculated feed grade vary significantly from one test to another suggesting a poor homogenisation of the feed material which may be a consequence of some weakness of the experimental protocol (dry feed, sample mixing). However, in terms of performance the LREE grade reach is considerably higher than those obtained during the characterisation study (see Chapter 3). Nevertheless, LREE grade in the shaking table concentrate are relatively low to be considered directly as a marketable product but results are promising and higher LREE grade could probably be reached by further processing of shaking table concentrate. One major result of these beneficiation tests is that concentration of monazite is feasible even with very low feed grade around 100 ppm LREE. Conversely the recovery of rare metals such as Sn, Nb or W from the depleted micaceous residue samples has not been achieved suggesting that 100 ppm could be considered as a reasonable estimation of the minimum cut-off grade for these metals.

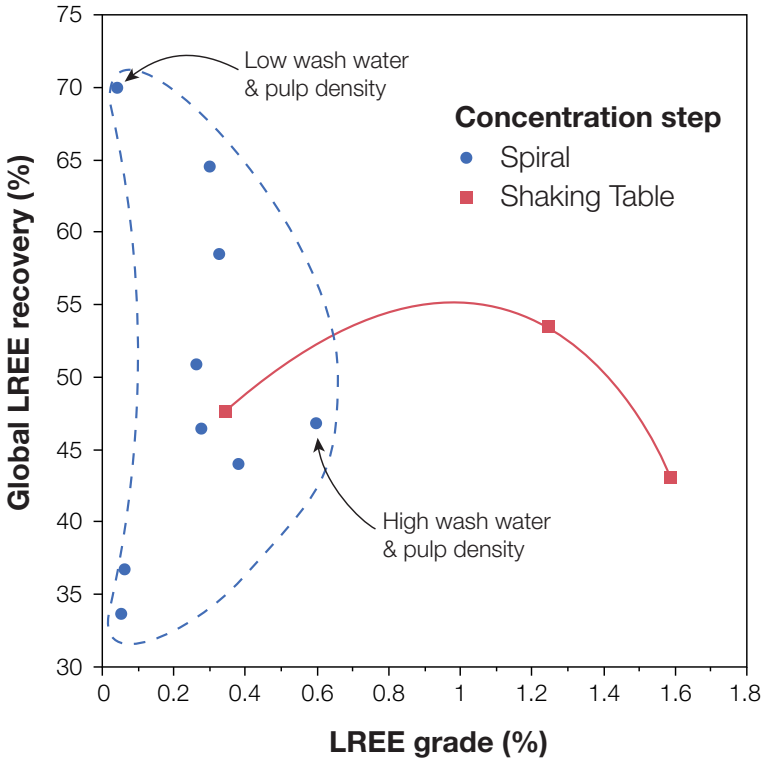


Figure 5.10: Cumulative LREE grade and recovery of gravity concentrates of all the spiral tests and shaking table tests 7 to 9 with trend line illustrating the effect of deck angle.

### 5.1.4 Conclusion

A multi-stage gravity concentration process involving spiral concentrator and shaking table has been developed with the objective of recovering the majority of the heavy minerals of the 53-180 µm fraction of the micaceous residue. Modelling of the influence of the operating parameters of the spiral concentrator through DOE methodology has allowed setting the required operating conditions to achieve the highest heavy minerals recovery. Scavenging tests indicate that up to 80% heavy minerals can be recovered. However mineralogical analysis of the concentrates indicates that middlings are recovered after 3 passes, suggesting that scavenging operations should not be further continued. Furthermore, LREE recoveries suggest that up to 70% monazite could be recovered in only one pass. Shaking table testing on spiral concentrates shows that heavy mineral concentrate with up to 98.5% heavy minerals can be recovered. However in terms of metals, the concentrate grades are still low for most metals (Sn, Nb and W) with the exception of LREE which reach up to 1.6% LREE grade in shaking table concentrate. Given the reasonable overall recoveries, the main reason for these low concentrate grades could be the very low grade of the feed material which is 2 to 3 times less enriched in metals (Sn, Nb and W) than average micaceous residues grades. This suggests that the cut-off grade for these metals should be above 100 ppm and points out the critical aspect of metal grades variability in the micaceous residue as one of the major issue when considering a potential industrial application.

## 5.2 Modelling heavy and gangue mineral size recovery curves in spiral concentration

### 5.2.1 Introduction

Spiral concentrators are high-capacity, low-cost units used for heavy mineral ore concentrations or coal cleaning (Wills and Napier-Munn, 2005). It can be illustrated as an inclined chute, which follows a downward helix that is wrapped around a column. It can encompass a variable degree of cross section complexity depending on the model (Falconer, 2003). The principle of separation is based on flowing film stratification in the vertical plane and centrifugal forces in the horizontal plane, as well as other hydrodynamic and friction forces (Kapur and Meloy, 1999). These forces jointly separate heavy minerals from gangue minerals based on their specific gravity differences. However, spiral separation efficiency is also impacted by the size and shape of the treated particles. Separation is also affected by the complex Bagnold force, which is sensitive to particle size rather than weight (Atasoy and Spottiswood, 1995; Burt, 1984b; Holtham, 1992a).

Despite the critical importance of particle size, most of published spiral studies focus on global recovery and few have investigated the recovery according to size-fraction (Atasoy and Spottiswood, 1995; Holland-Batt and Holtham, 1991; Richards et al., 2000). The size recovery curve (or partition curve) is a well-known tool used to analyse mineral processing equipment separation based on particles size. Recent iron ore processing studies have shown that heavy and gangue mineral partition curves can separately provide critical information related to spiral separation efficiency (Bazin et al., 2014; Sadeghi et al., 2014). However, these studies used chemical contents to determine the behaviour of heavy and gangue minerals. This may cause accuracy issues if significant number of middling particles are present in the treated material. The main operating parameters of a spiral separator, in addition to geometric parameters, are feed rate, feed solid pulp density, splitter positions and wash water flow rate. The effects of these parameters on the spiral efficiency have been extensively described in the literature (Atasoy and Spottiswood, 1995; Burt, 1984b; Sivamohan and Forssberg, 1985a). Many articles have explored the use of design of experiments (DOE) methodology to model the impacts of these parameters on spiral performance (Dixit et al., 2015; Honaker et al., 2007; Tripathy and Rama Murthy, 2012). However, few studies have combined this approach with a size recovery analysis based on different minerals in the treated material (Sadeghi et al., 2014).

This study investigates the influence of wash water flow rate and feed pulp density on the size recovery curves of heavy and gangue minerals in a spiral concentrate using DOE methodology. In addition, a method is proposed to model heavy and gangue mineral size recovery curves and assesses the best operating parameters for the spiral concentrator.

### 5.2.2 Materials and methods

#### 5.2.2.1 Materials

The feed material used in this study corresponds to a micaceous residue from the Imerys St Austell kaolin deposit in Cornwall, UK. This residue is seen as a potential

source of LREE (La, Ce and Nd) and Sn, which is linked to kaolin production. Figure 5.11 shows a typical particle size distribution of the raw micaceous residue and for 3 density fractions, *i.e.* heavy (SG > 2.89), middlings (2.79 < SG < 2.89) and gangue (SG < 2.79) minerals. Most of the heavy minerals are distributed in the fine fractions, especially in the 53-180 µm range. This size fraction of the micaceous residue, obtained after removing the +180 µm (∼25 wt.%) and -53 µm (∼18 wt.%) fractions by screening of the raw material, constitutes the feed material of this study.

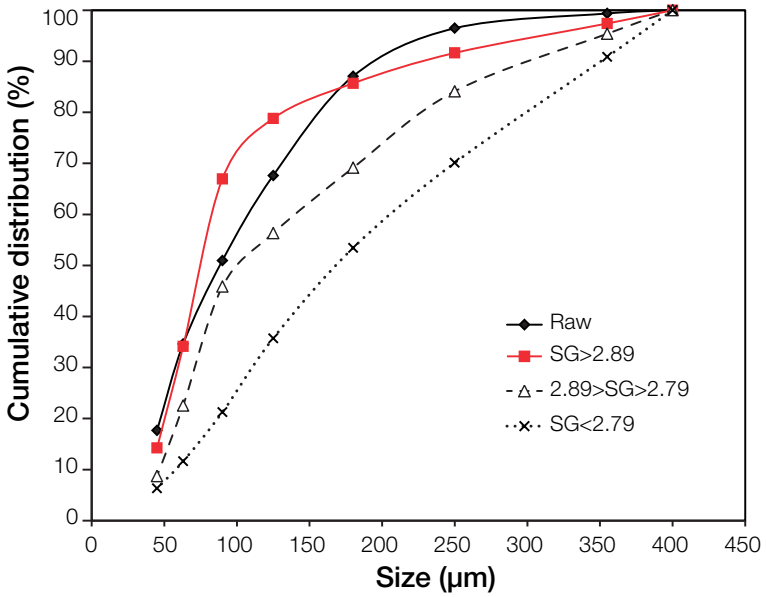


Figure 5.11: Typical particle size distribution of the raw micaceous residue and 3 specific gravity fractions.

The main LREE host mineral is monazite (SG=5.15), while the major Sn host is cassiterite (SG=6.90). The main gangue minerals are quartz, feldspar and micas, with relatively low specific gravities (SG=2.6-3). Significant amounts of accessory minerals are also present, including tourmaline (SG=3.12), topaz (SG=3.55) and Nb-rutile (SG=4.25), see Table 5.7. These accessory minerals have a medium SG, which is much higher than gangue minerals. Thus, they are often recovered in gravity concentrate and are considered heavy minerals in this study. In this study light-gangue and heavy minerals fractions are obtained by dense medium separation combined with centrifugation using bromoform (SG=2.89). The sample tube bases containing the heavy fractions were frozen using liquid nitrogen to avoid contamination between the heavy and light particles during the recovery of each fraction. Mineralogical observations and X-ray diffraction show that the resulting heavy mineral fraction mostly contains tourmaline, micas, topaz, rutile and all of the metal-bearing minerals, whereas the light fraction only contained gangue minerals, such as quartz, feldspar or micas and some remaining kaolinite.

#### 5.2.2.2 Spiral set-up

The spiral separator used in this paper is a 5 turn MKIIA Reichert spiral (Mineral Deposit Limited, Australia), with a 387 mm pitch, 2370 mm overall height and a 590 mm trough diameter. The dry sample is mixed with water in the mixing tank, forming

Table 5.7: Mineralogical composition of the micaceous residue and specific gravity data.

| Mineral | Estimated weight % | Mean SG |
|---|---|---|
| Kaolinite | 10.15 | 2.60 |
| Feldspar | 15.16 | 2.60 |
| Quartz | 29.79 | 2.62 |
| Muscovite | 14.81 | 2.82 |
| Chlorite | 1.13 | 2.95 |
| Biotite | 14.58 | 3.00 |
| Tourmaline | 9.90 | 3.12 |
| Apatite | 0.86 | 3.19 |
| Topaz | 1.50 | 3.55 |
| Rutile | 0.82 | 4.25 |
| Zircon | 0.64 | 4.65 |
| Monazite (Ce, La, Nd) | 0.07 | 5.15 |
| Fe oxides | 0.52 | 5.20 |
| Cassiterite | 0.08 | 6.90 |
| Wolframite | <0.01 | 7.30 |

pulp. The pulp is then pumped to the feed tank (see Figure 2.8 in Chapter 2). All spiral outputs discharge into the mixing tank via flexible pipes, which allow sample collection while operating in closed-circuit. All the outputs are systematically collected while the feed is back-calculated. Due to wash water additions, the feed pulp density decreases during the operation. This dilution can be controlled because the initial pulp density and wash water flow rates are known. Hence, samples can be collected at specific times during the operation to represent a given feed pulp density. The steady state is achieved when sampling is carried out. Because this stage is a roughing stage, the two middling offtakes were considered a single group. Wash water is supplied at each spiral turn via a washwater trough wrapped around the central column. The amount of wash water supplied to each wash water point on the spiral turns was adjusted by rotating the end of the wash water quill inserted in the polyurethane trough to ensure an even distribution of wash water to each turn. The concentrate splitter (cutters) positions were set at the beginning of the tests at a 3/4 aperture and remained fixed during the entire experiment.

#### 5.2.2.3 Particle size analysis and modelling

Each fraction (float and sinks) was separately analysed using laser light scattering to assess their particle size distributions. The particle size distributions presented in this article are the average of 5 successive analyses. Particle size analyses were performed using a Helium-Neon Laser Optical System Mastersizer 3000 (Malvern instruments Ltd.) coupled with a Hydro Extended Volume (EV) sample dispersion unit.

Particle size distribution is typically defined using several data points (passing or retained weight %), which represent potential responses to model using the DOE. However, particle size distributions can be modelled using statistically derived distribution models, which reduce the number of responses. The two most common methods used in mineral processing are the Gaudin-Schuhmann and the Rosin-Rammler models (Wills and Napier-Munn, 2005). However, these models are typically applied to comminution studies, which often deal with non-uniform size distributions. Thus, even if these models proved to be very accurate, comparisons with other distribution models suggest that a 2-parameter Gompertz model (Johnson and Kotz, 1994), which is a special case of

the more general logistic curve, provides the best fit to our data. The Gompertz model is generally applied to soil characterisation due to its superiority to the lognormal distribution (Hwang et al., 2002; Nemes et al., 1999). The mathematical formulation for the 2-parameter Gompertz cumulative size distribution ($F$) is:

$$F(x) = \exp\left[\exp\left(-\alpha(x-\beta)\right)\right] \tag{5.7}$$

where $\alpha$ and $\beta$ are the shape parameters of the curves. Gompertz model fitting typically displays high $R^2$>0.99 and low RMSE (<0.01), an example of the fitting procedure is given in Figure 5.12. Figure 5.12 illustrates that the residuals display a typical sine-like trend. This phenomenon is well known and cannot be easily modelled. The fine size range residuals can be reduced by a weighted fit, which favours the fine sizes. However, this provides poorer results for the other sizes fractions, which are more important for the studied phenomenon. Automatic curve fitting and data processing were conducted using Matlab® R2012a software.

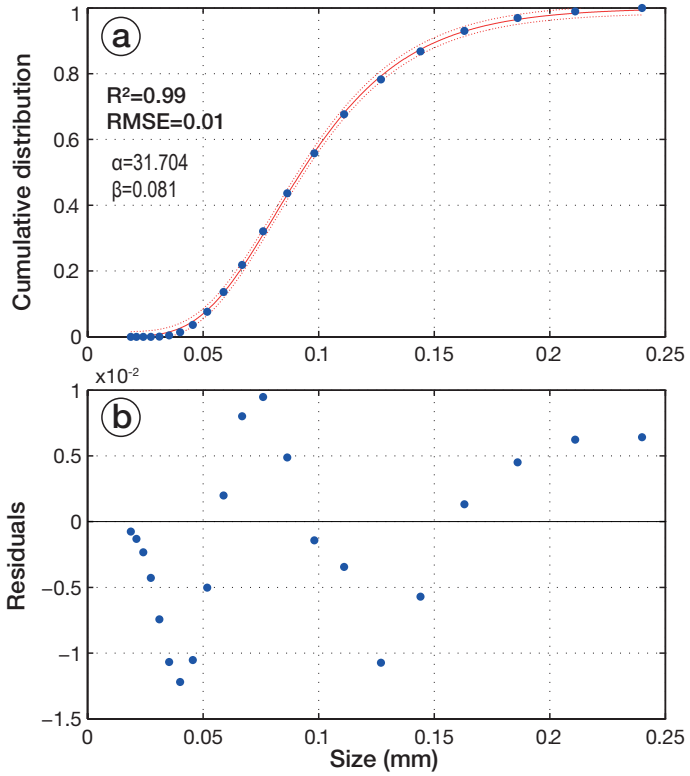


Figure 5.12: Illustration of the fitting procedure for particle size analysis data. (a) Gompertz fit with 95% confidence interval and model parameters $\alpha$ and $\beta$. (b) Residual plot showing a typical pattern.

#### 5.2.2.4 Partition curve calculation

After spiral testing, each product (concentrate, middlings and tailings) was treated via dense medium separation combined with centrifugation using pure bromoform (SG=2.89). The general formulation of the recovery of a family of particles within the density and size range $i$ and $j$, respectively, is expressed as:

$$(R_C)_{ij} = W_C \frac{(w_C)_i (g_C)_{ij}}{(w_F)_i (g_F)_{ij}} \tag{5.8}$$

where $W_C$ is the weight% of the concentrate, and $(w_C)_i$ and $(g_C)_{ij}$ are the weights retained in the size range and the weight% (or grade) of particles within the size-density range, $ij$, of the concentrate. Feed parameters $(w_F)_i$ and $(g_F)_{ij}$ are defined accordingly. This equation corresponds to the practical situation where samples are first screened into distinct size fractions and then treated via dense medium separation. In this study, the opposite methodology was used, *i.e.*, samples were first treated via dense medium separation to obtain a sink and float fraction and each fraction is then analysed by laser light scattering to obtain a higher particle size resolution. Therefore, a more appropriate expression can be used for this procedure:

$$(R_C)_{ij} = W_C \frac{(g_C)_j (w_C)_{ij}}{(g_F)_j (w_F)_{ij}} \tag{5.9}$$

leading to:

$$(R_C)_{ij} = (R_C)_j \frac{(w_C)_{ij}}{(w_F)_{ij}} \tag{5.10}$$

where $(R_C)_j$ is the global recovery of particles in the density range $j$, and $(w_C)_{ij}$ and $(w_F)_{ij}$ are the concentrate and feed particle weights retained from the size-density range $ij$. This is a more useful expression in this specific case, as $(R_C)_j$ is obtained by mass balance, whereas $(w_C)_{ij}$ and $(w_F)_{ij}$ are directly derived from the particle size analysis. This study considers only two density populations, *i.e.*, the heavy minerals (SG>2.89), denoted by $h$, and the gangue minerals (SG<2.89), denoted by $g$.

#### 5.2.2.5 Design of experiments

Tests were conducted using a $3^2$ full factorial design, where the wash water flow rate ($WW$) and feed solid pulp density (S) are independent variables. The levels for each factor were chosen in accordance with preliminary results and the operating range recommended by the manufacturers. The levels tested in this study are 10-2 Lpm for wash water flow rate and 25-15 solid wt.% for pulp density, corresponding to the high ($+1$) and low ($-1$) levels respectively. The recovery and two Gompertz size distribution fit parameters ($\alpha$ and $\beta$) are set as response variables for both heavy and gangue minerals. Test repeatability and experimental error estimation were assessed using randomly generated duplicate tests under the same experimental conditions (Montgomery, 2008). The responses, $y$, were modelled using typical second order models, which can be expressed in their general form as:

$$y = a_0 + a_1 WW + a_2 S + a_{12} S \cdot WW + a_{11} WW^2 + a_{22} S^2 + \varepsilon \tag{5.11}$$

where $a_0$, $a_1/a_2$, $a_{11}/a_{22}$ and $a_{12}$ are the unknown constant, linear, quadratic and interaction terms of the model, respectively, and $\varepsilon$ is a residual that groups the lack of fit (difference between the stated and true model) and random experimental error (Myers et al., 2009). The experimental design was generated using the JMP® statistical software (SAS institute) D-optimal design tool, per the procedures in Goupy and Creighton (2007).

### 5.2.3 Results

Spiral separation concentrate recoveries were calculated and particle size distributions were fitted for heavy and gangue minerals, as listed in Table 5.8. Since spiral was operating as a roughing unit, no clear distinctions were exhibited between the concentrate and middlings. Thus, the two outputs have been merged into one rough concentrate (noted C+M).

The highest heavy and gangue mineral recoveries were reached for low wash water additions. The pulp density effect was less significant, but increasing the solid pulp density decreased the recovery for a given wash water flow rate, especially for the heavy minerals. Partition curves were analysed to assess the sensitivity of each size fraction and understand the effects of the wash water flow rate. Experimental size recovery curves were calculated using the recoveries presented in Table 5.8 and the particle size analyses of each output. Appendix D.1 provides a size recovery calculation example for each spiral output and feed.

The partition curves for 20% solid pulp density tests are presented in Figure 5.13. Figure 5.13 illustrates the influence of wash water on size recovery curves, as the solid pulp density is set to a constant value (level 0). The heavy particle partition curves (Figure 5.13a) confirm that the wash water flow rate is the dominant parameter, as the overall recovery for each size fraction significantly decreased as the wash water flow rate increased. Note that the low wash water size recovery curves quickly plateau for particles above 100 µm. Conversely, medium and high wash water flow rate size recovery curves display a slightly decreased coarse particle recovery. The gangue mineral size recovery curves (Figure 5.13b) also exhibit decreased coarse particle recovery, even at low wash water addition rates. Similarly, increasing wash water additions lead to a significant decrease in the overall recovery for each size fraction, which is particularly prevalent in coarse to medium gangue particles.

Table 5.8: Results of heavy and gangue mineral recovery experiments as a function of wash water ($WW$) and solid pulp density ($S$) at high (+1), medium (0) and low (−1) levels. Notations are given in Equations (5.7), (5.10) and (5.11).

| Test # | $WW$ | $S$ | Heavy minerals | | | Gangue minerals | | |
|---|---|---|---|---|---|---|---|---|
| | | | $(R_{C+M})_h$ | $\alpha_h$ | $\beta_h$ | $(R_{C+M})_g$ | $\alpha_g$ | $\beta_g$ |
| Units | Lpm | wt.% | % | | $\mu m$ | % | | $\mu m$ |
| 1 | 10 (+ 1) | 15 (− 1) | 14.77 | 31.71 | 80.91 | 2.23 | 38.34 | 72.17 |
| 2 | 10 (+ 1) | 20 (0) | 8.28 | 31.65 | 79.98 | 1.27 | 40.40 | 69.06 |
| 3 | 10 (+ 1) | 25 (+ 1) | 6.18 | 33.63 | 78.07 | 1.20 | 38.79 | 68.85 |
| 4 | 6 (0) | 15 (− 1) | 15.73 | 30.58 | 83.82 | 3.38 | 35.55 | 75.72 |
| 5 | 6 (0) | 20 (0) | 12.26 | 29.89 | 82.17 | 2.60 | 37.05 | 71.94 |
| 6 | 6 (0) | 25 (+ 1) | 8.76 | 29.36 | 79.77 | 2.27 | 36.20 | 71.66 |
| 7 | 2 (− 1) | 15 (− 1) | 35.73 | 29.26 | 80.20 | 14.36 | 30.37 | 85.57 |
| 8 | 2 (− 1) | 20 (0) | 24.47 | 29.50 | 87.39 | 10.58 | 31.41 | 79.44 |
| 9 | 2 (− 1) | 25 (+ 1) | 20.21 | 29.09 | 84.85 | 9.01 | 32.21 | 79.83 |
| 10 | 2 (− 1) | 25 (+ 1) | 21.06 | 28.97 | 83.28 | 8.95 | 31.15 | 78.64 |
| 11 | 10 (+ 1) | 25 (+ 1) | 6.09 | 32.25 | 77.92 | 1.65 | 39.73 | 70.25 |

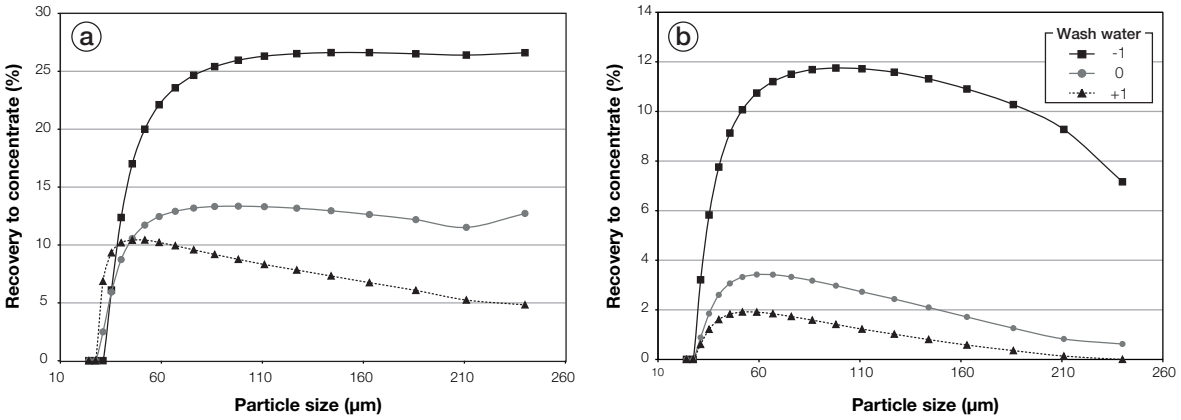


Figure 5.13: Effect of wash water flow rate on size recovery curves for a constant pulp density value (level 0). (a) Heavy particle size recovery curves. (b) Gangue particle size recovery curves.

The effect of solid pulp density on size recovery curves is illustrated in Figure 5.14. The overall recovery decreases when the solid pulp density increases, suggesting that this parameter exhibits a negative impact on recovery, as suggested by the global recoveries in Table 5.8. However, the shapes of the size recovery curves are unaffected by solid pulp density variations. The heavy and gangue mineral partition curve shapes at various pulp densities, which are nearly identical, indicate that the pulp density only affects the overall recovery.

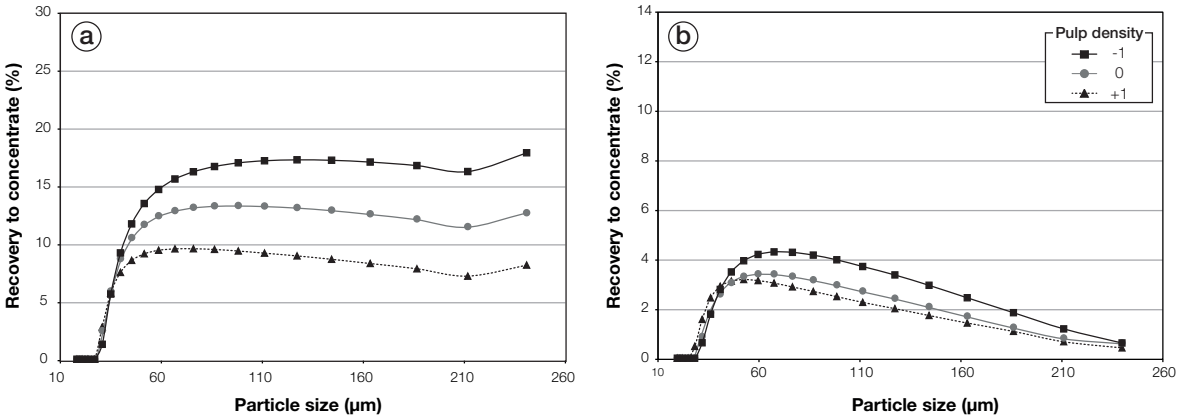


Figure 5.14: Effect of pulp density on size recovery curves for a constant wash water flow rate (level 0). (a) Heavy particle size recovery curves. (b) Gangue particle size recovery curves.

#### 5.2.3.1 Size recovery curve modelling

In total, 6 second order models were obtained from the 11 tests of the $3^2$ design. The second order heavy mineral recovery ($(R_{C+M})_{heavies}$) and gangue mineral recovery ($(R_{C+M})_{gangue}$) models that were obtained in the spiral concentrate as a function of wash water flow rate ($WW$) and solid pulp density ($S$) are presented below:

$$(R_{C+M})_{heavies} = 11.05 + 8.64WW - 5.20S + 1.55S \cdot WW + 5.98WW^2 \quad (5.12)$$

$$(R_{C+M})_{gangue} = 2.37 - 4.85WW - 1.26S + 1.12S \cdot WW + 3.68WW^2 \quad (5.13)$$

#### 5.2.3.1.1 Statistical validation of the obtained models

An Analysis of Variance (ANOVA) was conducted on each model to determine the regression coefficients and assess their significance (see Appendix D.2). According to the ANOVA analysis, all of the models are significant, which indicates that the observed variations for all of the responses are likely due to wash water flow rate and solid pulp density variations. Overall, the stated second order models appear to be sufficient, as all of the models display $F$-ratios above the critical values at the 0.05 significance level. However, the $\beta$-value heavy mineral model displayed a critical value at a 0.01 significance level. According to the $F$-test, most of the components of Equation (5.11) significantly influence all of the models, with the exception of the Gompertz fit parameters for the heavy mineral size distribution. The regression models for the $\alpha-$ and $\beta-$values are only influenced by the linear effect of wash water flow rate. All other independent variables and interactions display very high $p$-values. This can be explained by the fact that the shapes of the heavy mineral size recovery curves are only slightly affected by wash water flow rate variations (Figure 5.13a). Thus, $\alpha-$ and $\beta-$value variations are very small within the chosen experimental domain, as illustrated in Table 5.8. The quality of second order regression model fit is illustrated in Figure 5.15, which compares the experimental values to the fitted values and the corresponding $R^2$ values. The predicted values are in good agreement with the experimental results. The relationship between the observed and predicted values displays very high $R^2$ values, which are all above the recommended value of 0.80 (Montgomery, 2008), except the $\beta-$value heavy mineral model, which has an $R^2$ of 0.76.

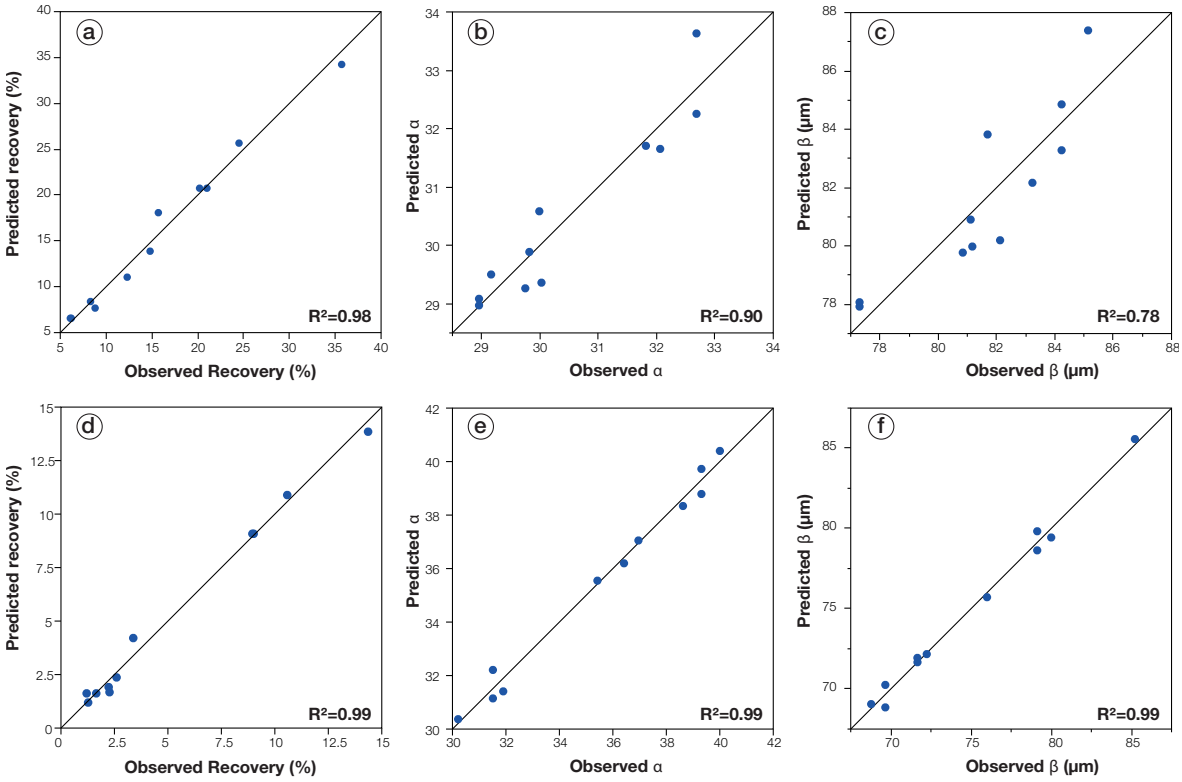


Figure 5.15: Relationship between observed and predicted heavy mineral recovery results. (a), $\alpha-$value (b) and $\beta-$value (c), and gangue mineral recovery (d), $\alpha-$value (e) and $\beta-$value (f).

From Equations (5.12) and (5.13), the heavy and gangue mineral recovery models are quite similar. This is because the linear effects of both the wash water flow rate and pulp density have a negative effect on the heavy and gangue mineral recoveries. However, the recoveries are positively affected by the second order wash water flow rate effect, as well as the interaction effect between the wash water and pulp density. The second order pulp density effects are not significant for the recoveries, as suggested by the ANOVA results in Appendix D.2. Parameter estimates and standard deviations for the six regression models are listed in Table 5.9.

Table 5.9: Parameter estimates for the recovery, $\alpha$- and $\beta$-values for heavy and gangue minerals as a function of the standardized parameters with standard errors (STD).

| Term | Recovery | | α-value | | β-value | |
|---|---|---|---|---|---|---|
| | Estimate | STD Error | Estimate | STD Error | Estimate | STD Error |
| Heavy minerals | | | | | | |
| Constant | 11.05 | 1.21 | 29.82 | 0.51 | 83.23 | 1.45 |
| *WW* | -8.64 | 0.61 | 1.45 | 0.26 | -1.98 | 0.73 |
| *S* | -5.20 | 0.61 | 0.02 | 0.26* | -0.43 | 0.72* |
| *WW*S* | 1.55 | 0.70 | 0.42 | 0.30* | -1.48 | 0.84* |
| $WW^2$ | 5.98 | 1.13 | 0.79 | 0.48* | -0.08 | 1.35* |
| $S^2$ | 1.83 | 1.13* | 0.19 | 0.48* | -1.96 | 1.35* |
| Gangue minerals | | | | | | |
| Constant | 2.37 | 0.44 | 36.96 | 0.42 | 71.65 | 0.51 |
| *WW* | -4.85 | 0.22 | 4.05 | 0.21 | -5.61 | 0.26 |
| *S* | -1.26 | 0.22 | 0.50 | 0.21 | -2.17 | 0.26 |
| *WW*S* | 1.12 | 0.25 | -0.15 | 0.24* | 0.88 | 0.30 |
| $WW^2$ | 3.68 | 0.41 | -1.00 | 0.39 | 2.73 | 0.48 |
| $S^2$ | 0.57 | 0.41* | -1.04 | 0.39 | 2.17 | 0.48 |

*Non-significant parameter.*

#### 5.2.3.1.2 Effect of wash water on size recovery curves

Rather than studying the influence of the operating parameters on the $\alpha-$ and $\beta-$values, it is more convenient to directly analyse their effect on the size recovery curves. Further investigation focused on the influence of wash water on heavy mineral particle size parameter models. Figure 5.16 shows the predicted heavy and gangue mineral size recoveries as a function of wash water flow rate using the obtained models.

The results suggest that the modelled partition curves are consistent with the experimental data, except for fine size ranges below 50 µm, for which the model overestimates the recoveries. This could be due to the limitation of the Gompertz particle size distribution, which displays higher residuals for fine particles. Thus, the obtained models are only valid for size fractions of 50 µm or larger. The relationship between the observed results (Figure 5.13) and the predicted results (Figure 5.16) can be described by the binary correlations presented in Figure 5.17. A positive correlation exists between the observed and predicted heavy and gangue mineral partition curves, with $R^2$ values of 0.97 and 0.99, respectively. Therefore, it can be assumed that the models are valid and the model predictions are adequate.

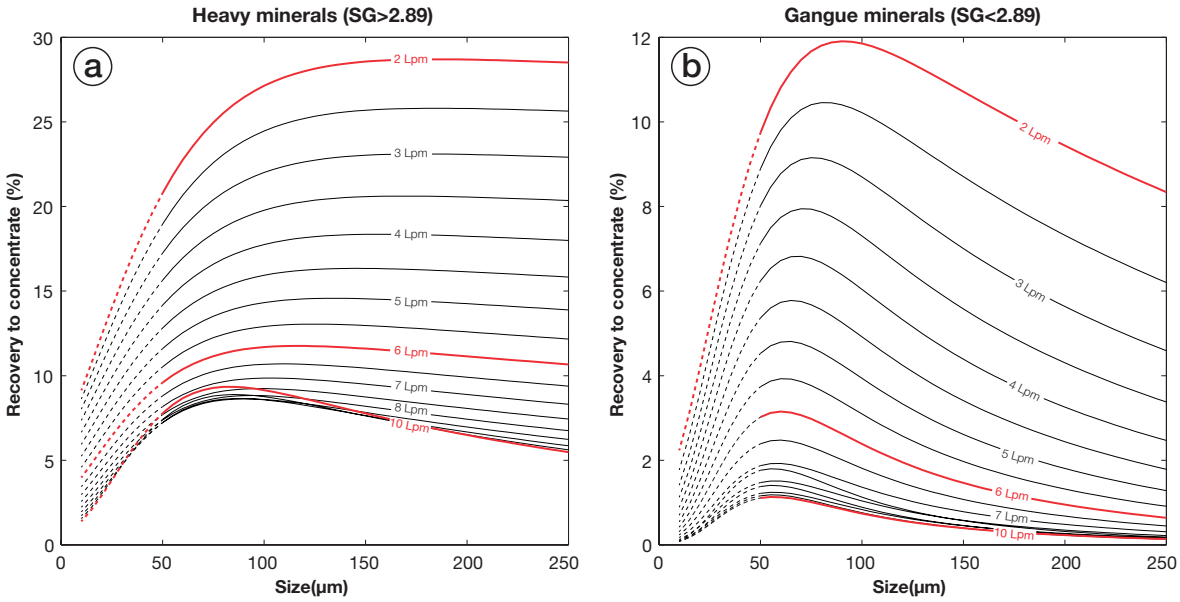


Figure 5.16: Heavy mineral (a) and gangue mineral (b) partition curve variations for increasing wash water flow rates with fixed pulp density (S=20%). Highlighted lines correspond to the experimental conditions tested in the experimental design and used for comparison. Dotted lines correspond to results outside the valid domain.

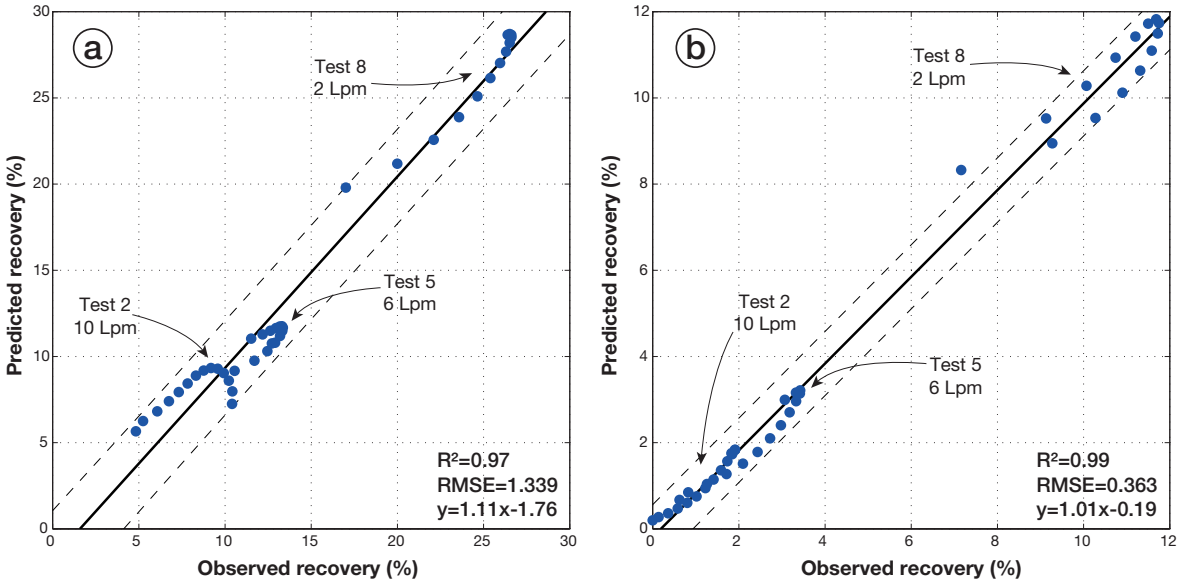


Figure 5.17: Comparison between observed and predicted size-by-size recoveries of heavy (a) and gangue (b) minerals for 3 solid pulp density centred tests 2, 5 and 8 (without points below 50 µm) with a 95% confidence interval

After verifying the models, the effect of wash water on heavy and gangue mineral partition curves was examined. As expected, the wash water flow rate negatively affects the overall recovery of all size fractions. However, the shape of the heavy minerals size recovery curves is minimally affected by wash water additions. Heavy mineral recovery increases with particle size and plateaus. This increase toward coarse particles is typical of gravity separator partition curves (Burt, 1984b). However, a slight heavy-coarse

particle recovery decrease can be observed for wash water rates above 6 Lpm. This phenomenon is less important than that observed in Sadeghi et al. (2014) and for most of the examples in Bazin et al. (2014) for iron-carrier recovery, which is likely due to the relatively fine grained and narrow size range material used in this study, as well as the relatively low wash water flow rates used. Conversely, the drop in recovery is much more important for gangue minerals (Figure 5.16b), which is consistent with observations of previous studies (Sadeghi et al., 2014; Bazin et al., 2014). Recovery is optimal for size ranges between 50 and 100 µm and then decreases for coarser size fractions.

The overall effect of wash water on heavy and gangue minerals size recovery curves can be summarised by plotting the 3D response surfaces of size recovery curves as a function of wash water flow rate (Figure 5.18). The standardized recovery for a given wash water flow rate captures the size-recovery distribution on the [-1 +1] interval for a given wash water value. The maximum heavy mineral recoveries exist for coarse size ranges and low wash water rates. The maximum recovery then shifts to the medium size range as the wash water flow rate increases (Figure 5.18a). This corresponds to the coarse particle recovery decrease observed for high wash water flow rates in Figure 5.16a. However, this coarse particle recovery decrease is observed for low to high wash water additions on the gangue mineral surface plot (Figure 5.18b). The steep slopes of both mineral fraction response surfaces along the wash water axis highlight the strong effect of wash water on recoveries.

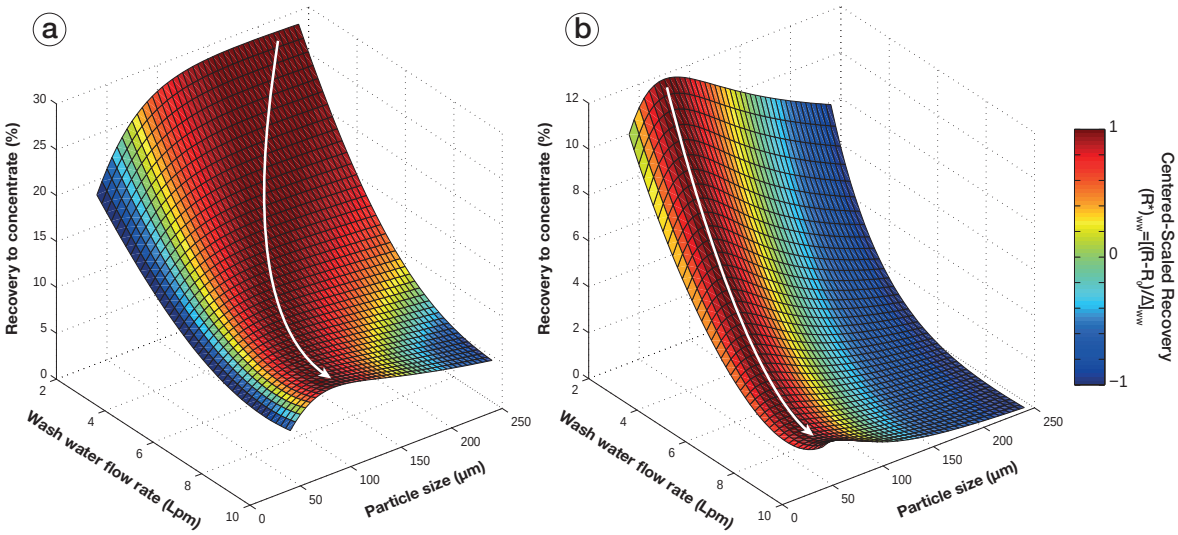


Figure 5.18: 3D surface plot of heavy (a) and gangue (b) mineral size recovery curves as a function of wash water flow rate. The colour bar represents the centred-scaled recovery for a given wash water value and represents the shift of maximum and minimum size-recovery locations with increasing wash water flow rate.

It is difficult to distinguish the effect of the wash water flow rate on the shape of the size recovery curves because the overall recovery effects decrease as the wash water flow rate increases. To only visualise partition curve shape variations, the global recovery effect can be deleted by replacing $(R_C)_j$ with 1 in Equation (5.10). The resulting value is not a real enrichment ratio, as the concentrate and feed mineral grades are not taken into account. However, it provides a size enrichment ratio for each mineral category.

The obtained curves are presented in Figure 5.19. Figure 5.19 indicates that the wash water flow rate decreases the coarse particle enrichment for heavy and gangue minerals. The opposite phenomenon occurs for medium size particles with increasing enrichment ratios between 50 and 100 µm as wash water flow rate increase. These variations are much more distinct for gangue minerals than for a heavy mineral, which explains why the coarse recovery decrease is less clear for heavy mineral partition curves.

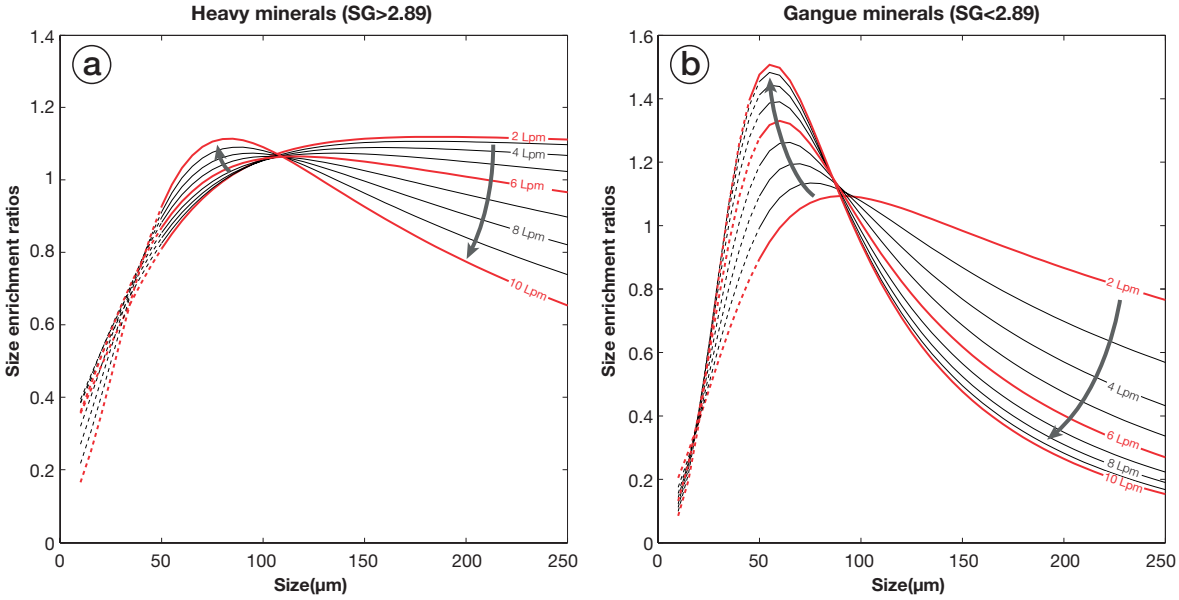


Figure 5.19: Heavy mineral (a) and gangue mineral (b) size enrichment ratio variations for increasing wash water flow rates with fixed pulp density (S=20%). Highlighted lines correspond to the experimental conditions tested in the experimental design and used for comparison. Dotted lines correspond to results outside the valid domain.

#### 5.2.3.1.3 Effect of pulp density on size recovery curves

Even if pulp density has no influence on heavy mineral partition curves, according to the ANOVA analysis, it has a significant influence on the $\alpha-$ and $\beta-$values for gangue minerals (Table 5.9). Figure 5.20 summarises the influence of pulp density on gangue mineral partition curves. Note that the partition curves are mainly affected by the global recovery of gangue minerals, as partition curve shapes stay relatively constant as the pulp density increases (Figure 5.20a). As both wash water and pulp density (and their interaction term) have a significant effect on the Gompertz fit parameters for gangue minerals, it is interesting to note the sensitivities of the gangue mineral partition curves when both factors vary (Figure 5.20b). The effect of pulp density is clearly more visible at low wash water flow rates, which may be related to the fact that the wash water dilution effect lowers the influence of pulp density at higher wash water flow rates. The influence of pulp density on size enrichment curves is presented in Figure 5.20c and can be compared to those obtained for various wash water flow rates (Figure 5.19b). Figure 5.20c shows that the pulp density has a similar, but minor, influence on the shape of the size recovery curves, which is consistent with the experimental observations. Figure 5.20d shows the relationship between the observed and predicted partition curves. Even if a good fit is observed ($R^2$=0.91), the model

precision is poor for low wash water flow rates. Thus, the obtained gangue mineral model is only valid for relatively high wash water flow rates, which are greater or equal to 6 Lpm.

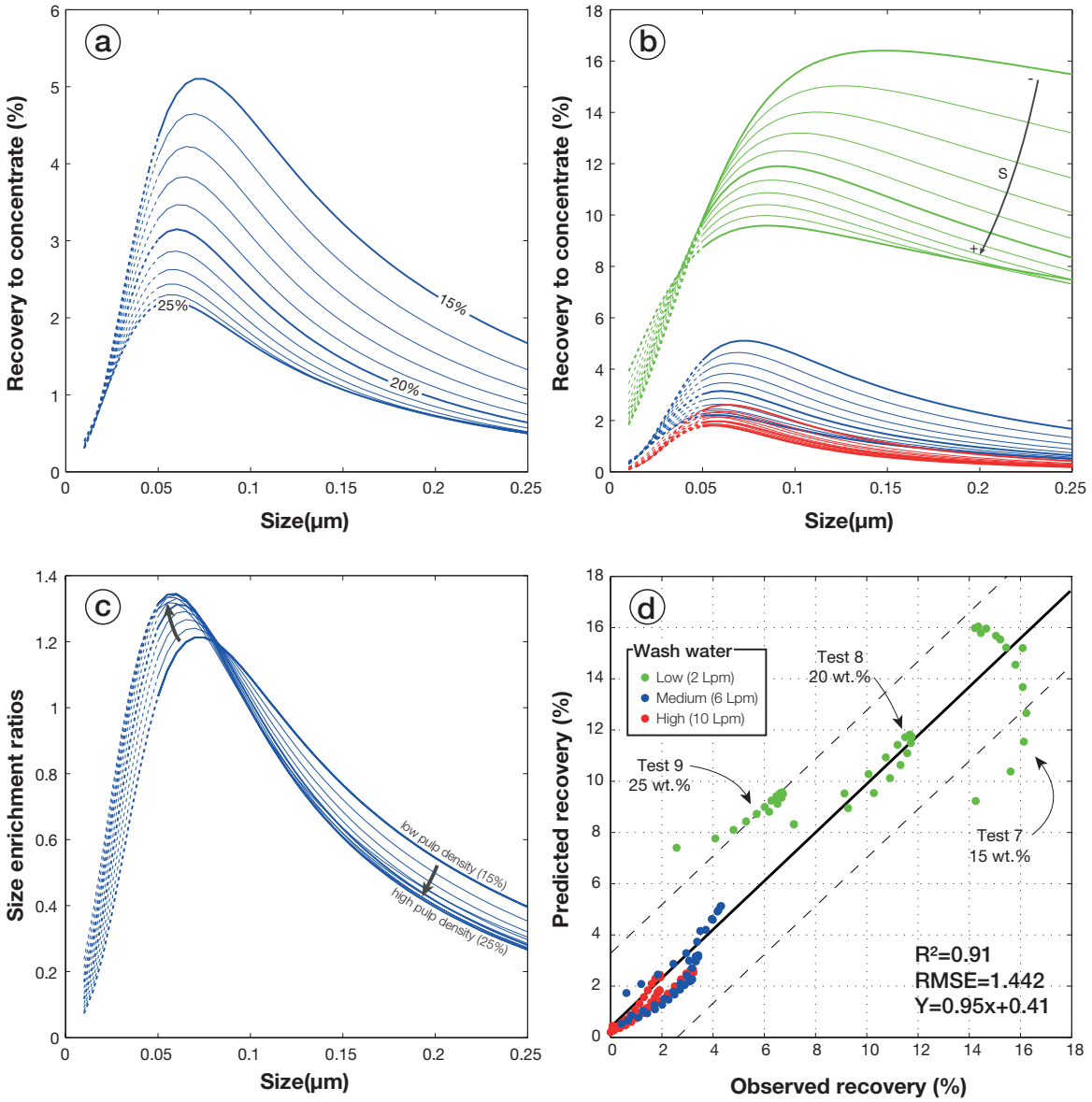


Figure 5.20: Summary of the pulp density influence on gangue mineral size recovery curves. (a) Influence of pulp density on size recovery curves with a fixed wash water rate (WW=6 Lpm). (b) Illustration of the combined effect of pulp density and wash water on gangue mineral partition curves. (c) Influence of pulp density on size enrichment ratios with a fixed wash water rate (WW=6 Lpm). (d) Comparison between observed and predicted size-by-size gangue mineral recoveries for tests 1 to 9 (without points below 50 µm) at a 95% confidence interval.

### 5.2.4 Discussion

A coarse particle recovery decrease has been previously observed for iron ore treatment in spiral concentrators (Bazin et al., 2014; Holland-Batt and Holtham, 1991; Hyma and Meech, 1989; Miller, 1991). This phenomenon has been attributed to the Bagnold force, which preferentially acts on coarse particles (Atasoy and Spottiswood, 1995; Burt, 1984b; Holtham, 1992a). The Bagnold force is a particle-particle interaction that significantly contributes to particle stratification in gravity concentration devices at high solid pulp densities (Holtham, 1992a). In a spiral concentrator, the pulp solid density increases from the outer zone to the inner concentrate zone as a result of the corresponding decrease in stream thickness, which is due to decreased particle velocities (Holtham, 1992b). This pulp density increase toward the inner spiral zone implies that a significant Bagnold stress can be expected in this zone, as illustrated by the particle size increase observed in Holtham (1992a). The Bagnold effect is due to the combined actions of wash water and secondary current flow (Holland-Batt and Holtham, 1991; Holtham, 1992b, 1990), which preferentially flush coarse particles toward the outer zone. This selective coarse particle entrainment causes recovery to decrease at high wash water flow rates (Figure 5.16). Bazin et al. (2014) suggested that difference in the intensity of the phenomenon between heavy and gangue minerals is due to the difference between the degree of coarse particle entrainment, which decreases with increasing particle specific gravity (Bazin et al., 2014). This phenomenon is also related to other components of the cross-sectional rotation (Burt, 1984b). The recovery is also controlled by settling rates and the inward movements in the middling zone of the spiral trough, which are induced by centrifugal forces, as observed with positron emission particle tracking (PEPT) technique in Boucher et al. (2014). Particle settling and inward movements are also selective, as the settling and inward movement velocities increase with increasing particle specific gravity. Therefore, it is a combination of these secondary circulation mechanisms that explains the coarse particles recovery decrease in spiral concentrate and the sensitivity variations between heavy and light particles, as observed in Figure 5.19.

These mechanisms are illustrated for relatively low wash water rate in Figure 5.21a. At low wash water flow rates, the secondary circulation of coarse particles is limited for heavy minerals, which stay in the inner zone of the spiral trough. However, gangue minerals are significantly entrained and cannot re-enter the concentrate zone. An increased wash water rate increases the intensity of the coarse particle flushing and the secondary circulation becomes more apparent, significantly decreasing the coarse gangue mineral recovery, as illustrated in Figure 5.21b. The selectivity of these secondary circulations through selective entrainment, settling time and inward movement velocities results in a contrast between the heavy and gangue mineral coarse particle distributions, favouring heavy mineral recovery.

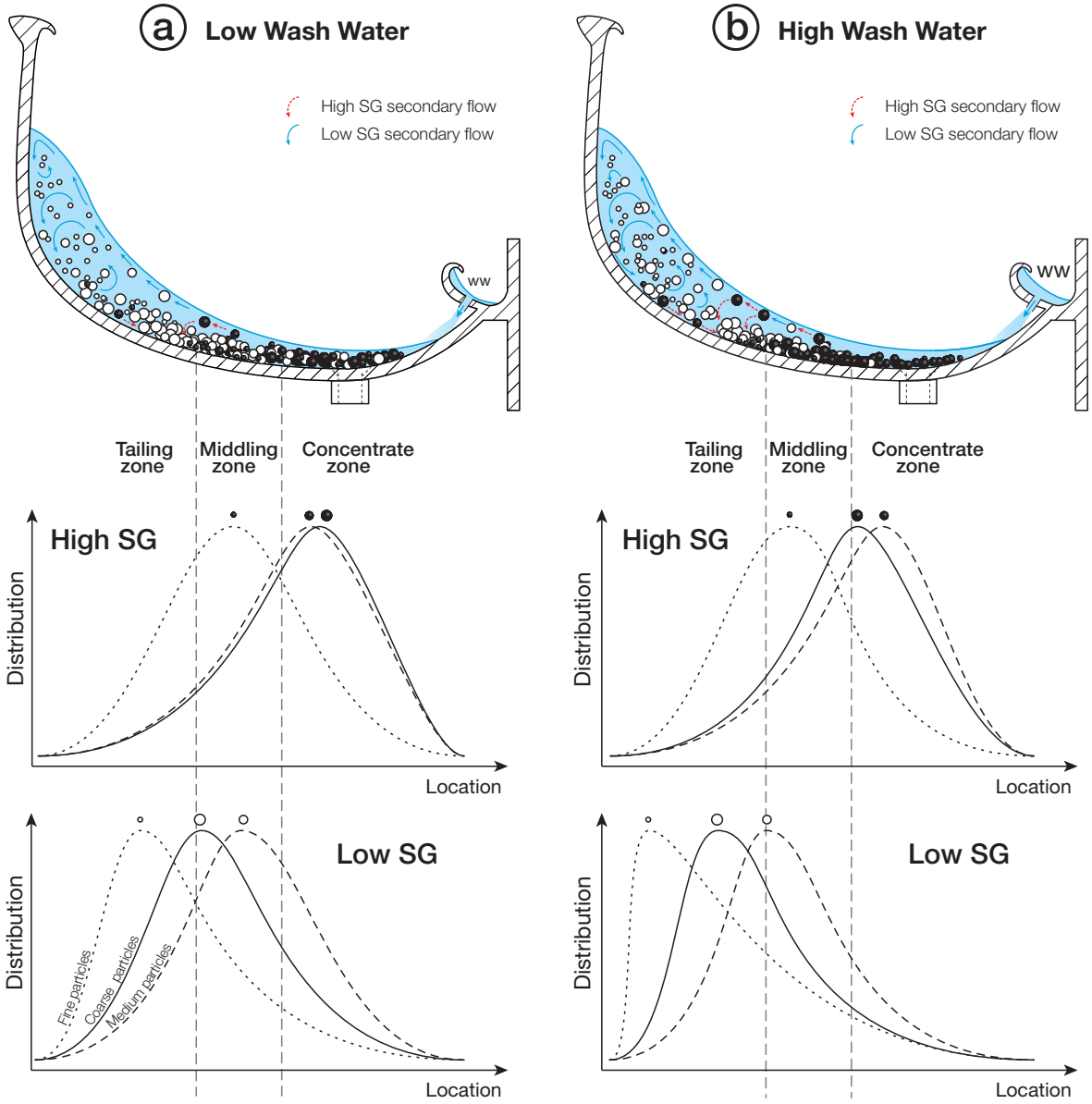


Figure 5.21: Schematic representation of the effect of wash water on particle distributions along the spiral trough flow with respect to their size and specific gravity. (a) Low wash water flow rate. (b) High wash water flow rate.

### 5.2.5 Conclusion

Pilot tests using heavy minerals-rich kaolin residue were used to investigate the effect of wash water additions and solid pulp density on spiral size recovery curves via a DOE methodology. Test results show that wash water is the most significant factor affecting global recovery. However, wash water additions also impact the partition curve shapes, especially for coarse gangue particles, the recovery of which decreases as the wash water flow rate increases. A heavy and gangue mineral partition curve model was derived based on regression models that exhibited satisfactory correlation with experimental data. These models show that both heavy and gangue mineral size recovery curves are impacted by wash water variations. More specifically, size recovery ratio curves indicate that a coarse particle decrease and medium particle increase occur

with increasing wash water flow rate. The wash water exhibits a more significant impact on the gangue mineral size recovery curve shape, which is likely due to selective migration phenomenon in secondary flows. The coarse particle recovery decrease in the spiral concentrator is a significant source of losses. A better understanding of this phenomenon and how it is affected by various operating parameters is fundamental for avoiding these losses.

# Chapter 6

# Processing of fines

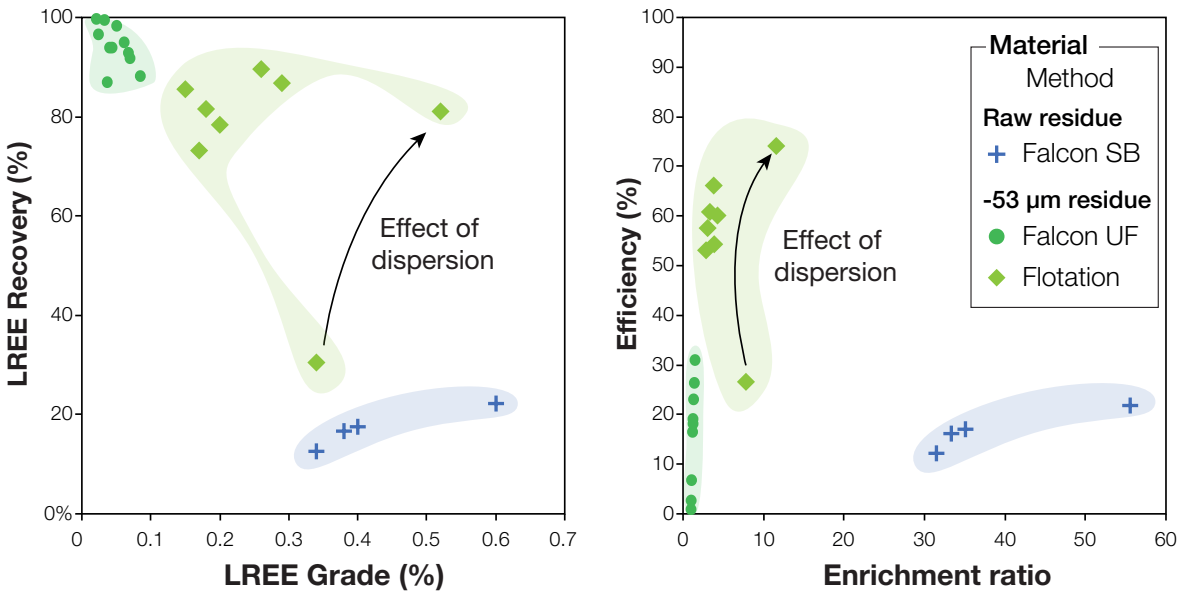

## Contents



# 6.1 Introduction

Despite the increasing developments and efforts in metal recycling, Rare Earth Elements (REE) still have low recycling rates and very few effective substitutes. For these strategic metals, future metal supplies will likely be dependent, in addition to classical ore deposits, on numerous unconventional resources among which low grade ores represent the next logical step for the mining industry (Laznicka, 2006). Industrial process residues often contain low REE concentrations, but volumes are large (Binnemans et al., 2015). A recent study has shown that Light Rare-Earth Elements (LREE) are pre-concentrated in the micaceous residue from the primary processing plant of St Austell kaolin deposits (Chapter 3). The main LREE in terms of grades are in decreasing order Ce, La, Nd, (Pr, Sm), with overall grades around 170 ppm LREE. Mineralogical observations suggest that monazite is the only LREE-bearing mineral which is found free in the micaceous residue stream but sometimes in association with rutile or micas (Chapter 3). Typical processing flowsheets of monazite start by physical beneficiation consisting mainly of high-capacity gravity separation steps, to take advantage of the high specific gravity (SG) of monazite which is between 4.98-5.43 (Jordens et al., 2013; Kumari et al., 2015). These steps are followed by additional gravity, magnetic and occasionally flotation steps (Ferron et al., 1991; Houot, 1982).

### 6.1.1 Froth flotation of monazite

Flotation of monazite has been investigated with many collectors such as sodium oleate (Cheng et al., 1993; Pavez et al., 1996; Sorensen and Lundgaard, 1966), fatty acids (Ferron et al., 1991; Wen Qi, 1993), hydroxamate (Pavez and Peres, 1994) and phosphoric acid esters (Ferron et al., 1991). However comparison between oleic acid and sodium oleate selectivity as collectors in monazite flotation indicates that sodium oleate show better floatabilites compared to oleic acid (Sorensen and Lundgaard, 1966). Adsorption of collectors onto monazite surface is pH-dependent as a consequence of varying monazite surface charge with different pH values. A wide range of values for the point of zero charge (PZC) of monazite have been reported as a consequence of varying chemical composition and crystal structure with different geological origin, presence or absence of impurities and distinct experimental conditions (Chelgani et al., 2015). However, the average PZC of monazite in the absence of collector is around pH 5 (Cheng et al., 1993; Pavez et al., 1996).

### 6.1.2 Falcon UF concentrator

The most common gravity concentration equipment used to treat fine particles are centrifugal separators, such as Knelson and Falcon concentrators (Falconer, 2003). In these separators, the slurry is introduced in a rotating bowl capable of operating at high rotation speed and hence high "G" force, enabling fine particles of different SG to be separated (Falconer, 2003). In addition, the bowls can be fluidized to avoid compaction by injection of high pressure water through the concentrate ridges. The Falcon Ultra-Fine (UF) concentrator are specifically designed to recover ultra-fine particles. No fluidisation is applied in these concentrators to prevent from flushing fine particles out the bowl. Since the concentrate is not continuously recovered, these separators are operated in semi-batch and must be stopped before saturation of the bowl to avoid concentrate erosion or by non-selective separation (Laplante, 1997).

Previous studies on Falcon concentrators have shown that 2 main mechanisms are involved in the separation process within the bowl: (1) differential particle settling in the flowing film along the wall of the bowl (Abela, 1997; Buonvino, 1993; Honaker et al., 1996; Laplante, 1997, 1993) and (2) reorganization of the particles in the retention zone (Ancia et al., 1997; Majumder and Barnwal, 2006). Which separation mechanism drives the separation depends mainly on the relative density of heavy minerals against the density of gangue particles. According to Abela (1997) with fine and low density particles such as coal, the first separation mechanism condition the probability that a particle reaches the particle bed during its relatively short residence time inside the bowl whereas with fine and dense particles such as gold, reorganisation of particles is the main separation mechanism as the heavy particles are centrifuged against the bowl even before they reach the retention zone (Kroll-Rabotin et al., 2010). Since Falcon UF are not fluidised the second separation mechanism does not occur in these smooth bowl as illustrated by the presence of a skin of higher grade material at the surface of the concentrate bed through the entire height of the bowl (Deveau, 2006). Hence, there is no reorganisation of particle in the concentrate bed and all particles entrapped before saturation report to the concentrate (Kroll-Rabotin et al., 2010).

### 6.1.3 Effect of clay slimes on mineral processing

The critical effect of phyllosilicate minerals in mineral processing and in particular in flotation performance is a well-known fact (Ndlovu et al., 2013). Phyllosilicate minerals are responsible for slimes coating (Tao et al., 2010), increasing reagent consumption and poorer selectivity, slimes entrainment into the concentrate during the roughing and scavenging stages (Jorjani et al., 2011), flocculation phenomenon which affect froth stability (Farrokhpay and Bradshaw, 2012) and increasing pulp viscosity (Arnold and Aplan, 1986; Genc et al., 2012). In addition, the efficiency of fine gravity concentration is also impacted by the clay content, due to high viscosity at low pH and greater negative potential at high pH which could cause greater mobility of all the particles keeping them in the upper part of the flowing film (Sivamohan and Forssberg, 1985c) or by entrainment of clay slimes (Luttrell et al., 1995).

In this paper we investigate the applicability and relative efficiency of centrifugal gravity concentration and flotation for the recovery of LREE from the fine fraction (-53 µm) of a kaolin residue.

## 6.2 Materials and methods

### 6.2.1 Material

All the samples used in this work were collected with the support of Imerys Minerals Ltd, UK. A large pulp sample (∼4 tons) was collected and aggregated from the secondary hydrocyclones underflow during the processing of highly kaolinised ore. The pulp samples were screened into three size fractions namely +180 µm, 53-180 µm and –53µm to follow distinct processing routes (see Section 2.5.1). The low grade +180 µm fraction was not considered for metal recovery, the 53-180 µm fraction was treated following a gravity processing route (see Chapter 5) and the -53 µm fraction constitute the feed material for the flotation and Falcon tests presented in this chapter. The estimated mineralogy of the -53 µm fraction is shown in Table 6.1. This fraction has been deslimed using a 2 inch Mozley C124 hydrocyclone with and without dispersant to test the influence of dispersion on flotation performance.

Table 6.1: Estimated mineralogical composition of the -53 µm micaceous residue fraction.

| Mineral | Formula | Estimated proportion (%) |
|---|---|---|
| **Kaolinite** | $Al_2Si_2O_5(OH)_4$ | 9.89 |
| **K-Feldspar** | $KAlSi_3O_8$ | 7.04 |
| **Quartz** | $SiO_2$ | 32.85 |
| **Micas (biotite, muscovite)** | $K(Fe, Mg)_3(AlSi_3)O_{10}(F,OH)_2$ , $KAl_2(Al\ Si_3)O_{10}(F,OH)_2$ | 28.48 |
| **Tourmaline (schorl, dravite)** | $NaMg_{3-z}Fe^{2+}{}_zAl_6(BO_3)_3Si_6O_{18}(OH)_4$ | 18.49 |
| **Topaz** | $Al_2SiO_4(F,OH)_2$ | 1.40 |
| **Rutile** | $TiO_2$ | 1.33 |
| **Monazite** | $(Ce, La, Nd, Th)PO_4$ | <0.20 |
| **Zircon** | $ZrSiO_4$ | <0.10 |
| **Cassiterite** | $SnO_2$ | <0.10 |
| **Wolframite** | $(Fe, Mn)WO_4$ | <0.10 |

### 6.2.2 Jar tests

The effect of dispersant type and dosage was tested using the jar test methodology in 1L beakers with a pulp solid density of 10 wt.%. The tests were performed on 110 g of -53 µm micaceous residue samples prior to desliming. The pulp was agitated for 3 min at 220 rpm followed by 5 min conditioning at 200 rpm after dispersant addition. Interface height was recorded every 5 min during the first hour and then at random for the most dispersed solution during 22 h. Five types of dispersant have been tested including sodium silicate ($Na_2SiO_3$), two Cyquest dispersants (CQ4000, CQ3223) supplied by Cytec, sodium polyacrylate solution Antiprex D (BASF, France) and 42%-purity Coatex GX TP supplied by Coatex (Arkema group, France). Three dispersant dosages at 10, 20 and 30 mg/L were tested, corresponding to a dosage of 90, 180 and 270 g/t of solid respectively. For each test a beaker containing only pulp with no dispersant was used as a reference.

### 6.2.3 Chemical analysis

Chemical analyses were carried out by Energy Dispersive X-Ray Fluorescence spectroscopy (ED-XRF) using a S2 Ranger (Bruker Corporation). Calibration of the XRF used results from Inductively Coupled Plasma Mass Spectrometry (ICP-MS) for the trace elements analyses performed at the *Service d'Analyses des Roches et des Minéraux* (SARM-CNRS, Nancy, France).

### 6.2.4 Zeta potential

Electrophoretic mobility measurements were carried out by timed image analysis with a Zetaphoremeter IV (CAD Instrumentation, France). The $\zeta$-potentials were evaluated after the Helmholtz–Smoluchowski and Hückel equations modified by Henry (Hiemenz and Rajagopalan, 1997). The experiments were performed on 30 µg of pure mineral samples grounded to -5 µm in an agate mortar and suspended in 300 mL KCl solution ($10^{-3}$ M). The pH of the solution was adjusted with drops of HCl or NaOH solutions to vary between 2 and 12 pH units.

### 6.2.5 Flotation

Figure 6.1 presents the flotation flowsheet investigated in this chapter consisting of one roughing stage followed by cleaning of the floated product and scavenging of the non-floated product. MIBC was used as a frother and sodium silicate (VWR BDH Prolabo), with $Na_2O/SiO_2$ ratio of 3.33, was used as depressant of silicate minerals. The frother dosage was 5 g/t in all experiments and sodium silicate dosage was 1000 g/t and 100 g/t for the roughing and cleaning stages respectively. Several collectors have been investigated in this study, including 98%-purity sodium oleate (Arcos Organics, France), hydroxamate (AC-3) purchased from Cytec (Solvay group, Belgium), and non-ionic reagent iso-tridecanol (PX4826) supplied by CECA (Arkema group, France). The flotation tests were carried out with deslimed –53 µm samples using a conventional Agitair LA-500 flotation cell (1.5 L). For each experiment, a pulp sample of ∼500 g dry micaceous residue was mixed into the cell with water at 1100 rpm for 10 min to obtain a 10 wt.% solid density. Sodium hydroxide (NaOH) was added to adjust the pH

of the slurry to 9.8-10 during the conditioning step, followed by frother, collector and depressant addition. The pulp was aerated and the froth product was collected for a total time of 7 to 13 mins.

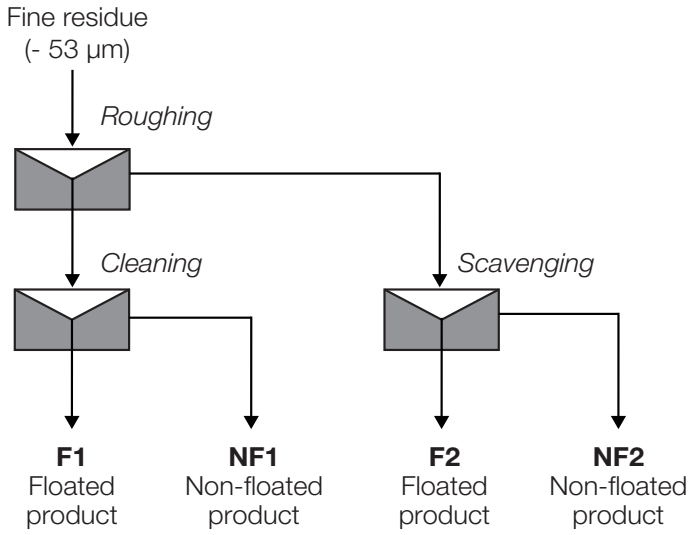


Figure 6.1: Flowsheet of the flotation experiments applied to the fine micaceous residue.

### 6.2.6 Falcon concentrator

The Falcon separator used in this work is a Falcon L40 laboratory model (Sepro Mineral Systems, Canada) with a solid capacity inferior at 300 kg/h producing a concentrate of 80-100 g. Tests on the raw micaceous residue product were conducted with the fluidised SB bowl and correspond to the experiments described in Chapter 3. For the processing of the -53 µm fraction the UF smooth-walled bowl were used with no fluidisation water. All Falcon UF tests were operated with a pulp density of 10 wt.% solid and a pulp flow rate of 1 kg/min. Saturation tests were performed using both raw and deslimed material to see the influence of desliming on Falcon UF performance and assess the critical feed mass. During these tests the Falcon was run at 63.89 Hz (200 G's) and stopped at distinct test durations (*i.e.* 30, 60, 90, 120 and 150 s) and both concentrate and tailings were recovered. Additionally, three rotary speeds were tested *i.e.*, 45, 50 and 65 Hz, corresponding to a centrifugal field around 100, 175 and 275 G's respectively, on deslimed samples.

## 6.3 Results

### 6.3.1 Selection of the dispersing agent

Sedimentation curves of the selected dispersing agents for the 3 selected dosages are presented in Figure 6.2. At low dosage (10 mg/L), the dispersion is limited for all dispersing agents and after 20 mins no difference with the reference test was observed. When dispersant dosage is increased to 20 mg/L, significant increase in dispersion is observed for Coatex and Antiprex which remains almost constant until the end of the test whereas other dispersants display only minor (CQ4000) to almost no difference

(CQ3223, $Na_2SiO_3$) from the previous test. Higher dispersant dosage (30 mg/L) does not significantly change the dispersion for most dispersants except for CQ3223 which is still below the dispersion observed with Coatex and Antiprex. Indeed, even after 22 h testing the standardized interface height with Coatex and Antiprex were still at 0.78 and 0.83 respectively. Hence, these two dispersants seem to be the most effective ones, especially at low dosage (20 mg/L). The contrasting results at 10 and 20 mg/L dosages for some dispersants, especially Coatex and Antiprex, suggests that either low dispersant dosage does not allow a good dispersion of the material, or the conditioning time were too short to observe the dispersion.

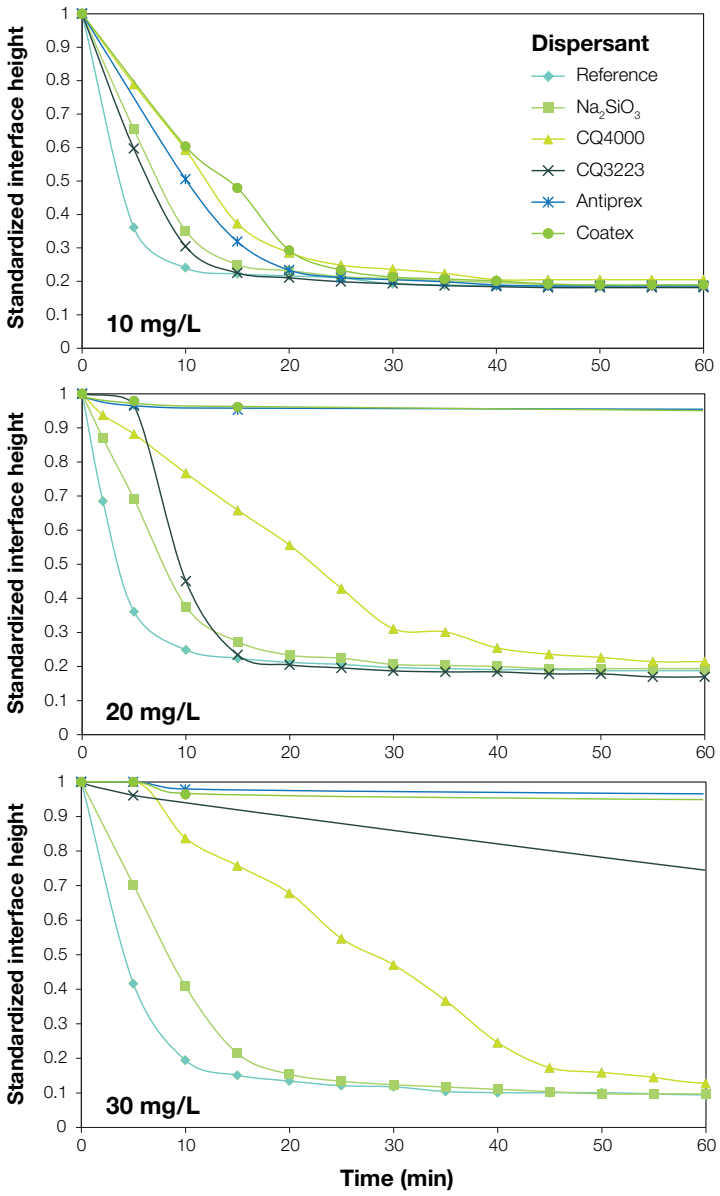


Figure 6.2: Effect of dispersant type and dosage on sedimentation curves at 10 mg/L, 20 mg/L and 30 mg/L.

Based on these results, Antiprex was selected for the dispersion of the -53 µm micaceous residue fraction prior to desliming operation. During conditioning, pulp was agitated for 10 min and another 15 min after dispersant addition (850 g/t dosage).

## 6.3.2 Flotation

### 6.3.2.1 Comparing flotation performance with different reagents

Figure 6.3 shows the LREE grade and recovery in the flotation products for different reagent types in the presence and absence of non-ionic reagent (PX4826). The highest LREE grades obtained in the cleaned product sodium oleate and hydroxamate alone were around 3370 ppm and 2500 ppm respectively. In terms of recovery, the best results were obtained with hydroxamate alone and with the mixture of sodium oleate and PX4826 at 88% and 83% respectively. In the case of sodium oleate the addition of non-ionic reagent resulted in increase in LREE recovery from 30% to 83% but at the expense of selectivity since the LREE grade in the obtained F1 floated product is twice lower than when PX4826 was not added. However, the low LREE recovery in the cleaned product is attributed only to the cleaning operation as 41% LREE are lost in the non-floated product at this stage which means that 74% of the LREE was recovered at the roughing stage. Non-ionic reagent mixing with hydroxamate did not improve the LREE flotation performance.

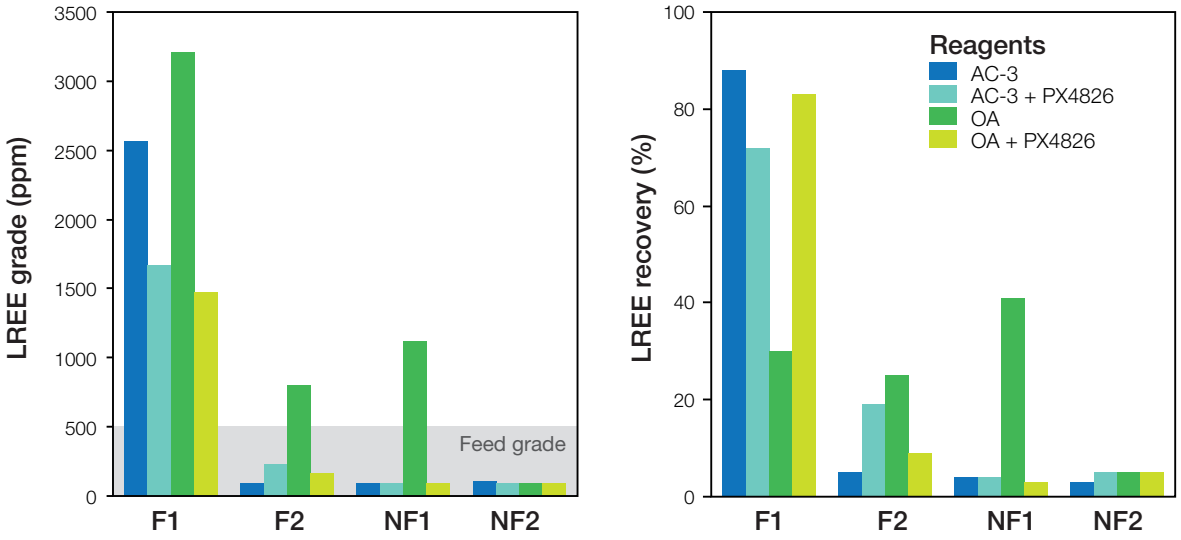


Figure 6.3: LREE grade and recovery in the flotation products using sodium oleate (OA) and hydroxamate (AC-3) in the presence or absence of non-ionic reagent (PX4826).

### 6.3.2.2 Enhancing flotation performance with dispersion

Replicate tests with the same operating conditions as the previous flotation experiments were carried out on a deslimed material with dispersant addition prior to hydrocycloning. Given the low LREE grades and recoveries in the scavenging step, the comparison of flotation performance with and without dispersion focused on the cleaned floated product (F1) only. Figure 6.4 shows the comparison of LREE grade and recovery in the concentrate in the presence or absence of dispersant. In all flotation experiments, dispersant addition resulted in a higher LREE grade in the floated product, especially when sodium oleate is used alone. Indeed LREE grade in the floated product obtained with sodium oleate increased from 3370 ppm without dispersion to 5350 ppm in the presence of dispersant. The effect of dispersion on LREE recovery was

also more pronounced for sodium oleate than for most reagents with an improvement in recovery from 30% to 80% in the presence of dispersant. LREE recovery was also improved by dispersion for the mixture of hydroxamate and non-ionic reagent (from 72% to 83%) whereas it slightly reduced the recovery for the two other experiments.

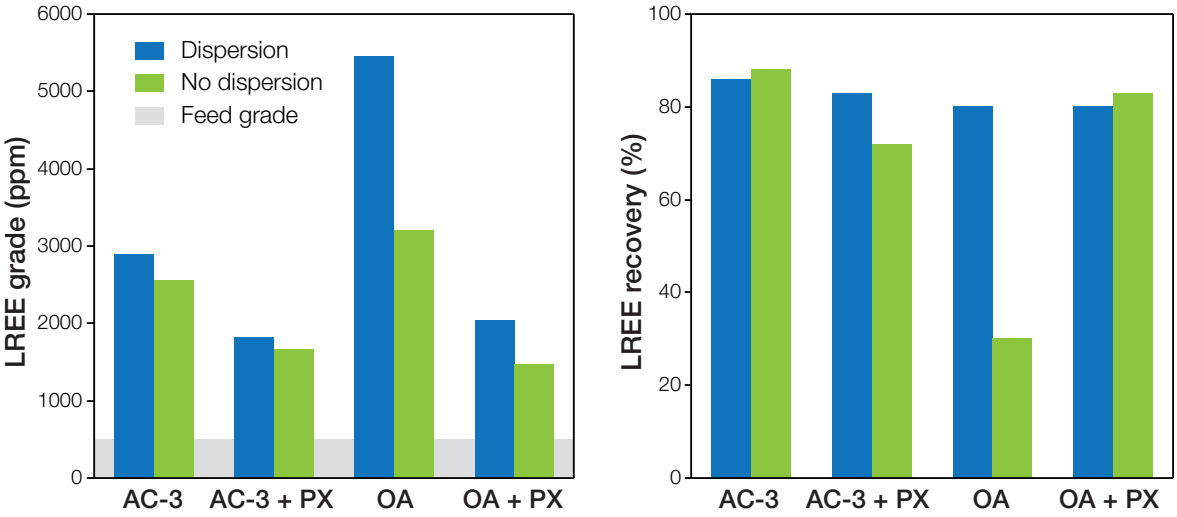


Figure 6.4: Comparison of LREE flotation performance with and without dispersion using sodium oleate (OA), hydroxamate (AC-3) in the presence or absence of non-ionic reagent (PX).

The overall superiority of sodium oleate observed in this study for the recovery of monazite, is mainly due to its higher selectivity in comparison with hydroxamate. Indeed, despite the low LREE grades of the floated products when hydroxamate was used as a reagent, the LREE recoveries were relatively high due to the yield of the flotation concentrate (between 18-28 wt.%). This could be explained by the high affinity of hydroxamate for some cationic sites, especially for those formed with transition metals such as $Fe^{3+}$ or $Al^{3+}$ as illustrated by the stability constant (K) of metal hydroxamates (Table 6.2). This is of primary importance for iron oxide mineral flotation for which hydroxamate have proven to be really effective (Fuerstenau et al., 1970, 1967). Mineralogical analyses have shown that both tourmaline and micas minerals belong to the Fe-rich group of their particular classification (Chapter 3). In addition, high proportion of tourmalines (∼19%), mainly schorl, and micas (∼30%), are present in the -53 µm fraction of the micaceous residue (see Table 6.1). Thus, it is highly probable that hydroxamate preferentially form stable complexes with cationic sites of tourmaline and micas, and in this regard, the selective flotation of monazite with hydroxamate is not feasible in the micaceous residue.

Table 6.2: Stability constants for metal hydroxamates at 20 °C (Miller et al., 2002).

| Cation | $H^+$ | $Ca^{2+}$ | $Fe^{2+}$ | $La^{3+}$ | $Ce^{3+}$ | $Sm^{3+}$ | $Gd^{3+}$ | $Dy^{3+}$ | $Yb^{3+}$ | $Al^{3+}$ | $Fe^{3+}$ |
|---|---|---|---|---|---|---|---|---|---|---|---|
| LogK | 9.35 | 2.4 | 4.8 | 5.16 | 5.45 | 5.96 | 6.1 | 6.52 | 6.61 | 7.95 | 11.42 |

The high contrast between flotation performance of sodium oleate with and without dispersion suggests that slimes coating is in part responsible for the low performance of sodium oleate observed in Figure 6.3. Indeed if lower flotation efficiency was only due to the action of clays on bubble coating, entrainment, pulp viscosity or even froth

stability, these issues would have been mitigated by desliming. The slimes coating is mainly attributed to electrostatic attractive forces between coarse minerals and fine clay particles of opposite surface charges (Del Giudice, 1934; Jorjani et al., 2011; Tao et al., 2010). Basal planes of clay minerals tend to be negatively charged, while the edges carry a charge that alters from positive to negative as a function of pH (Van Olphen, 1951). However, at neutral pH condition, in which the experiments where conducted, both monazite and kaolinite are negatively charged, as illustrated by their zeta potential in Figure 6.5.

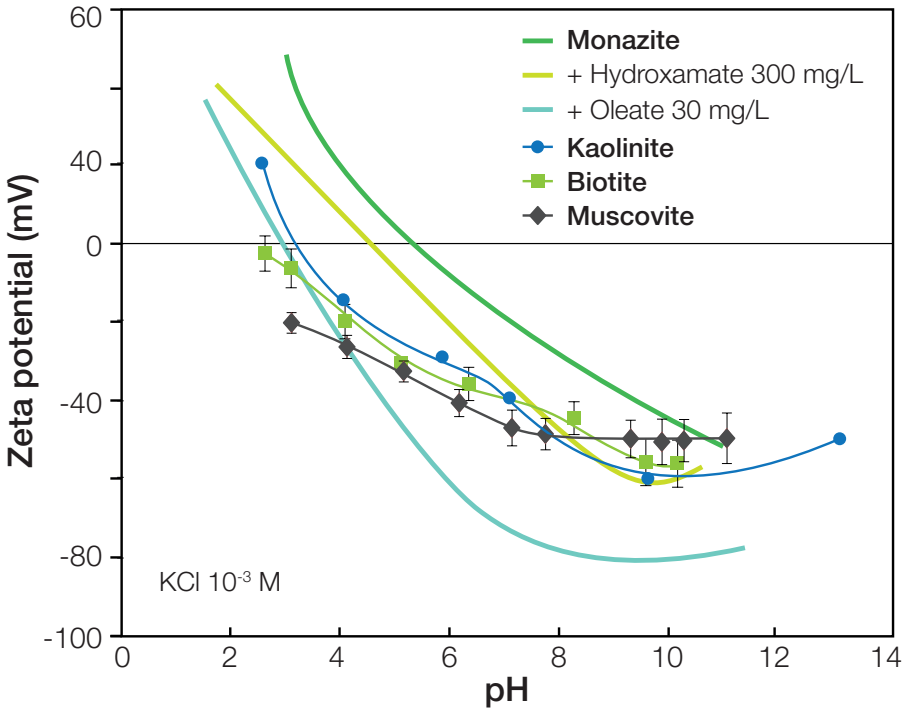


Figure 6.5: Zeta potential of kaolinite, biotite and muscovite, completed with zeta potential of monazite from Pavez et al. (1996).

In these conditions, clay coating cannot be attributed to pure electrostatic attraction since the electrical double-layer forces are repulsive. According to Lagaly (1989), kaolinite particles are linked at basic pH in banded structure through face/face contacts. These contacts are sensible to the presence of soluble cations such as $Ca^{2+}$, $Na^{+}$ or $Fe^{3+}$. In particular, calcium ions promote the formation of a central layer of counterions in face/face contacts and stabilize band-like structures. Hence sodium as counterion is repulsive at NaCl concentrations <0.1 M but is attractive for calcium counterions at calcium concentration from $10^{-5}$ M (Lagaly, 1989).

Table 6.3 shows the cationic composition of the process water from the micaceous residue pulp samples. The $Ca^{2+}$ content is largely above the required concentration to aggregate kaolin particles. Therefore it could be hypothesized that calcium counterion adsorption on kaolinite surface is likely to be the driving phenomenon that induce monazite coating. The addition of dispersant increase particles charge through the adsorption of multivalued cations such as $Ca^{2+}$ (He et al., 2004).This could also explain the differential response to dispersion of the sodium oleate and hydroxamate, illustrated by the important decrease of flotation efficiency with sodium oleate without dispersion whereas no significant changes are observable with hydroxamate. Indeed,

whereas sodium oleate is very sensible to the presence of cation such as $Ca^{2+}$ (Filippova et al., 2014), the calcium complex is the least stable complex for hydroxamate (Table 6.2). Thus it is likely that both liberation of monazite surface from clays coating and complexation of calcium by the dispersing agent are responsible for the higher performance of sodium oleate flotation with dispersion.

Table 6.3: Chemical analysis of flotation process water.

| Cation | $Na^{+}$ | $K^{+}$ | $Ca^{2+}$ | $Mg^{2+}$ | $Fe^{2+}/Fe^{3+}$ | $Al^{3+}$ |
|---|---|---|---|---|---|---|
| Content (mg/L) | 16.8 | 4.2 | 50.6 | 5.6 | <0.01 | <0.1 |

### 6.3.3 Falcon UF results

#### 6.3.3.1 Saturation tests

Saturation test were conducted using raw and deslimed (with dispersant) micaceous residue with the double objective of testing the influence of desliming on the saturation of the Falcon bowl and assessing the maximum sample mass for Falcon testing.

Figure 6.6 shows the effect of the mass fed to the Falcon UF on the concentrate mass and yield for both materials. A common trend is observed with an increase in concentrate mass with increasing feed mass until a maximum, followed by a decrease of concentrate mass indicating that the bowl is saturated and that erosion of the concentrate occurs. The results suggest that the bowl is saturated more rapidly when fed with deslimed material with a maximum concentrate mass of about 107 g reached after feeding the Falcon UF with 160 g of deslimed material. For the raw material, the maximum concentrate mass is about 125 g for a feed mass estimated at 215 g.

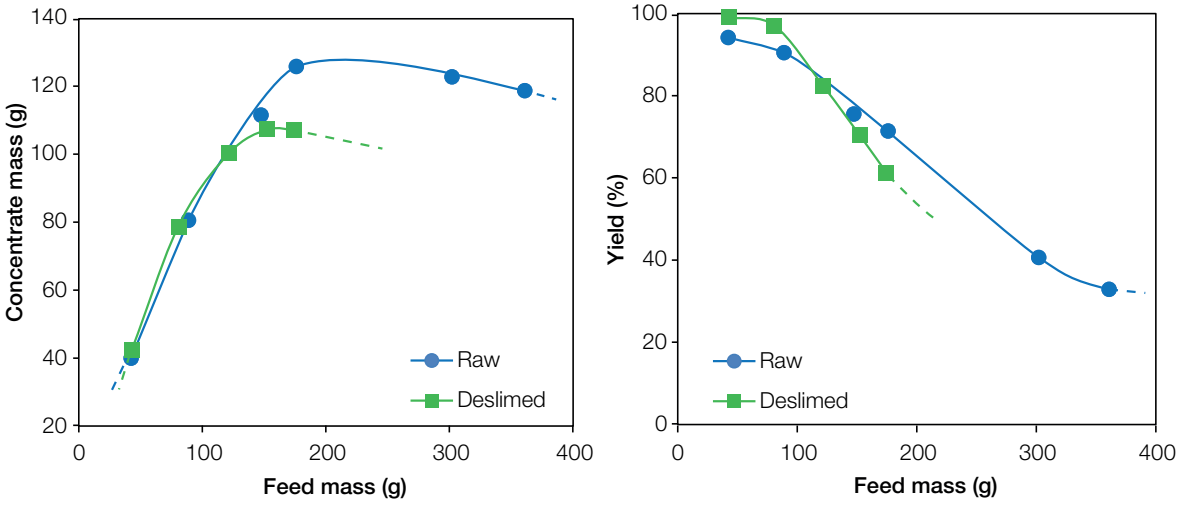


Figure 6.6: Effect of feed mass on Falcon UF concentrate mass (left) and yield (right) with raw and deslimed -53 µm residue samples.

The distinct maximum concentrate mass for raw and deslimed -53 µm residue could be explained by the fact that saturation is reached, independently from the material treated, when the captured volume is equal to the maximum recoverable volume. Hence

this means that the density of the concentrate is higher in presence of fine clays, *i.e.* that the concentrate bed is more compacted. This could be explained by the lower permeability of the concentrate bed and the surface coating phenomenon in presence of fine clay minerals which results in lower water content. However in terms of yield the results are quite similar for both materials as the aforementioned maximum concentrate masses correspond to yields of around 60% in each case.

Previous observations allow defining the critical feed mass for each material, defined as the feed mass above which the bowl is saturated. The percentage of critical mass can be estimated separately for each material by dividing the feed mass by the corresponding critical mass therefore reflecting the saturation rate of the Falcon bowl. The influence of the saturation rate of Falcon UF bowl on the separation performance is shown in Figure 6.7.

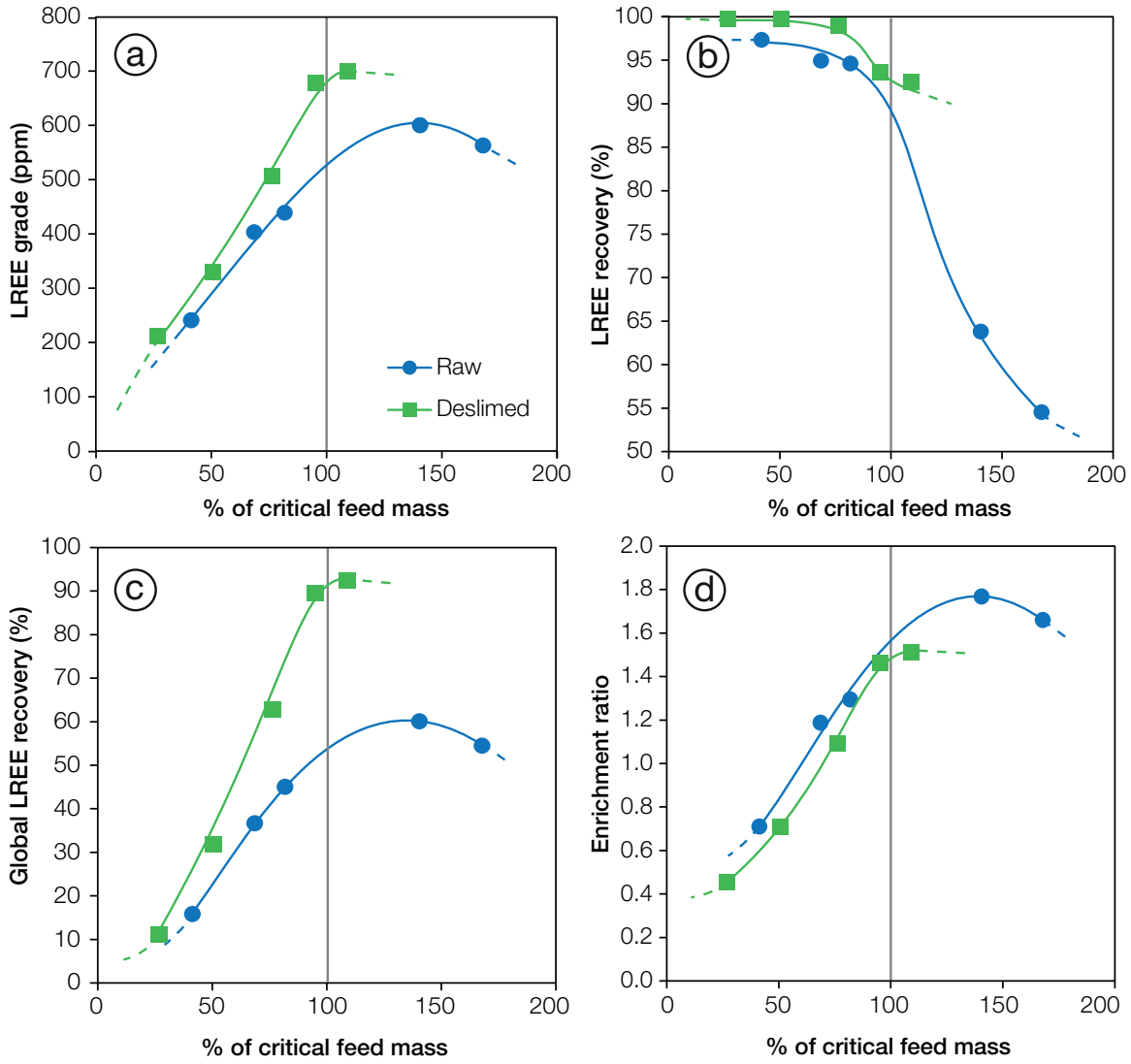


Figure 6.7: Effect of bowl saturation on Falcon UF separation performance on raw and deslimed -53 µm residue samples. (a) Effect of bowl saturation on concentrate LREE grade. (b) Effect of bowl saturation on final LREE recovery. (c) Evolution of global LREE recovery with increasing bowl saturation. (d) Effect of bowl saturation on LREE enrichment ratio.

LREE recovery slightly decreases with increasing feed mass and then drops drastically when the mass fed get close to the critical mass. This is consistent with previous observations that shows that when more material than which can be collected is fed to the bowl, the final recovery decreases (Laplante et al., 1994). Global LREE recovery is estimated by taking the last (largest) feed as a reference therefore reflecting the kinetic of the separation. As expected, LREE grade, global recovery and enrichment increase until the bowl became saturated for the deslimed material. However results are different for the raw material as LREE grade, global recovery and enrichment continue to increase after the bowl is saturated until around 150% saturation, and then decrease.

These results are surprising as previous works suggest that there is no further separation when the bowl became saturated (Deveau, 2006; Kroll-Rabotin et al., 2010). Hence two phenomena could be hypothesized: (1) selective erosion of the concentrate bed with preferred erosion of light gangue particles or (2) the non-selective erosion of the concentrate bed leading to vacancies which are in turn preferentially filled with heavy particles. These two phenomena are likely to be both responsible for the observed results.

Regarding the overall performance of Falcon UF separation, the benefit of desliming appears to be significant. Indeed the maximum LREE grade obtained with deslimed material is about 700 ppm against 600 ppm with raw material, with corresponding recoveries of 92% against 60% respectively.

This may appear consistent as desliming prior to gravity concentration is a well-proven technique for devices operating in normal gravitational field condition (1G). In addition, the presence of slimes is known to increase the pulp viscosity (Ndlovu et al., 2013; Sivamohan, 1990) which as a negative effect on Falcon UF separation efficiency has illustrated by recent studies on Falcon UF fluid dynamics based model by Kroll-Rabotin (Kroll-Rabotin et al., 2012, 2013). On the contrary some works have shown that slimes can improve centrifugal separation by acting as a quasi-heavy medium as illustrated by better performance obtained when treating cyclone feeds rather than cyclone underflows for gold and precious metals (Sprake and Mcalister, 2003). However, in the case of monazite which as a medium specific gravity (4.98-5.43) the negative effect of pulp viscosity is likely to be predominant comparing to the benefit of higher pulp density resulting in lower performance in presence of slimes.

#### 6.3.3.2 Effect of rotation speed

The effect of bowl rotation speed on Falcon UF performance has been tested on -53 µm deslimed residue samples with masses corresponding to the critical feed mass. Figure 6.8 shows the evolution of LREE grade and recovery obtained for the 3 tests at 45, 60 and 75 Hz plus those from the saturation test n°4 (95% of critical feed mass) operated at 63.89 Hz. Results suggest that LREE grade in the concentrate increases linearly with increasing rotation frequency whereas LREE recovery displays limited variations with a maximum LREE recovery of 95% obtained at medium rotation frequency at 60 Hz (175 G's).

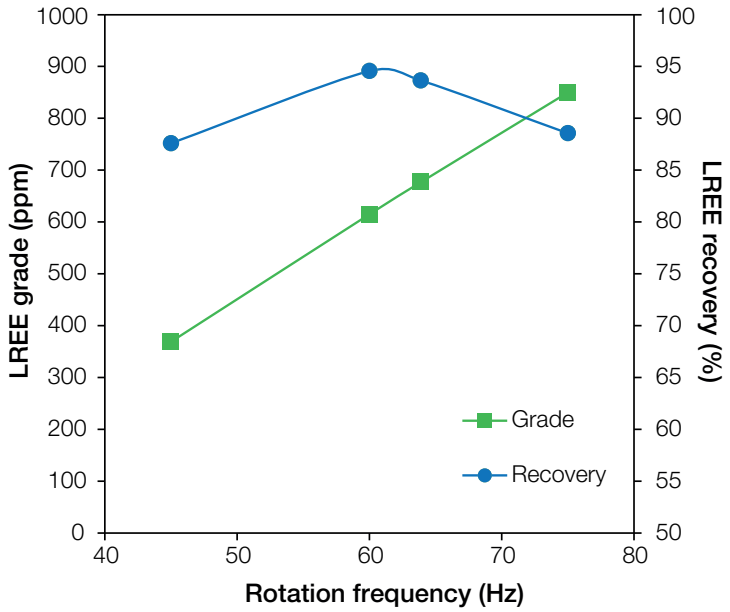


Figure 6.8: Effect of bowl rotation speed on LREE grade and recovery.

The low LREE grades (maximum 850 ppm) obtained with Falcon UF in one operation are much lower comparing to the ones obtained with froth flotation. However the high overall recoveries ($> 85\%$) suggest that the Falcon concentrate could be upgraded with reasonable recoveries in successive cleaning stages.

## 6.4 Discussion

Apart from the classical graphical grade-recovery curve, the best known definition of efficiency is that proposed by Hancock and Luyken defining the ratio between the "amount separated" and the amount separable" (Barsky and Barsky, 2006):

$$E = \frac{\varepsilon - \gamma}{\varepsilon_{max} - \gamma_{max}} \tag{6.1}$$

where $\varepsilon$ and $\gamma$ are the metal recovery and the concentrate yield respectively. However, the theoretical maximum recovery is equal to 1 and the maximum yield in the conditions of ideal separation is equal to the initial feed grade ($\alpha$). Consequently, Equation (6.1) may be written as follows:

$$E = \frac{\varepsilon - \gamma}{1 - \alpha} \tag{6.2}$$

Figure 6.9ab compares the performance of flotation and Falcon UF concentration of monazite from the -53 µm micaceous residue to previous results obtained with Falcon SB on the un-screened raw micaceous residue (Chapter 3). It is clear that the Falcon UF performance is low in terms of enrichment and separation efficiency. A similar conclusion have been reached by Jordens et al. (2014) for REE minerals concentration with a Falcon UF. This suggest that the Falcon UF is ineffective at concentrating fine medium SG minerals. However the high yields of Falcon UF concentrates (between 62-72 wt.%) are also an indication than the Falcon UF bowl became saturated too quickly.

Comparison of flotation performance to the Falcon SB in terms of grade and recovery shows that flotation achieved significantly higher LREE recoveries with concentrates grades similar to those obtained with the Falcon SB (for sodium oleate with dispersion). In terms of separation efficiency flotation is clearly superior with efficiencies up to 74 % whereas direct concentration of un-screened micaceous residue with Falcon SB only yielded efficiencies below 20%. However the enrichment ratios obtained with flotation (2.8-12) are much lower than those obtained with Falcon SB (32-56). The positive effect of dispersion on separation efficiency for flotation with sodium oleate is also clearly illustrated in Figure 6.9ab. Indeed the separation efficiency increased from a low separation efficiency of 26.6% to a very high efficiency of 74.10%, which is the highest efficiency of all the investigated methods for -53 µm residue beneficiation.

Figure 6.9c summarises the results of all the metallurgical tests performed on micaceous residue and presented in the present or previous chapters (Chapters 3 and 5). This representation allow highlighting the separation performances in terms of recovery, the objective being to be as close to the top left corner as possible, *i.e.* to reach the highest recovery with the lowest yield. Indeed, the main objective of this work was to assess the feasibility of LREE (La, Ce, Nd) and rare metals (Sn, Nb, W) recovery as potential by-product of kaolin production. Previous studies have proven that acceptable grades could be obtain but with significant losses (Shail et al., 2009). Hence the critical point was to produce a heavy-minerals pre-concentrate and to put emphasis on maximising the recovery. Unfortunately, the collected material used for metallurgical testing was depleted in most metals with the exception of LREE, so this assessment was only possible for the latter. As it can be seen in Figure 6.9c., there is a clear benefit in terms of recovery from treating screened material separately than treating directly the raw residue. It allows reducing monazite losses in the gravity concentration route especially in -53 µm size range and to effectively recover fine monazite using flotation.

The results are promising even if the overall LREE concentrate grades remain low for direct leaching via classical leaching route. However recent advances in leaching techniques raising from the need of recycling from lamp phosphors, magnet scrap or phosphoric acid industry have led to the development of new leaching technologies for material with REE grades as low as 0.1 to 1% (Peelman et al., 2016). In addition, even if the potentiality of metal recovery for the other considered metals (Sn, Nb, W) could not be assessed, the results from gravity concentration show that heavy minerals can effectively be recovered using simple two-stage gravity concentration. Given the high variability of metal grades in the micaceous residue (Chapter 4) and the relative high grades for some metals in some core sample assays, it is likely that the average metal grades suggested by the one week sampling in Chapter 3 are more representative of the average metal grades in the micaceous residue. Hence it is likely that, with a less depleted feed, effective metal recovery could be achieved as suggested by the relatively higher Sn grades obtained in previous studies (Scott et al., 1998; Shail et al., 2009).

With around 24 t LREE and 20 t Sn lost in the micaceous residue every year from biotite granite higher grade material only (Chapter 3), there is no doubt that total metal losses considering the whole kaolin deposits are significantly higher. This suggests that, in addition to current micaceous residue stream, the associated tailing dams could also be considered for metal recovery. Answering to the question of the potentiality of the considered metals as by-product of kaolin production requires economic assessment and proper resources estimation which is far beyond the scope of this study. However

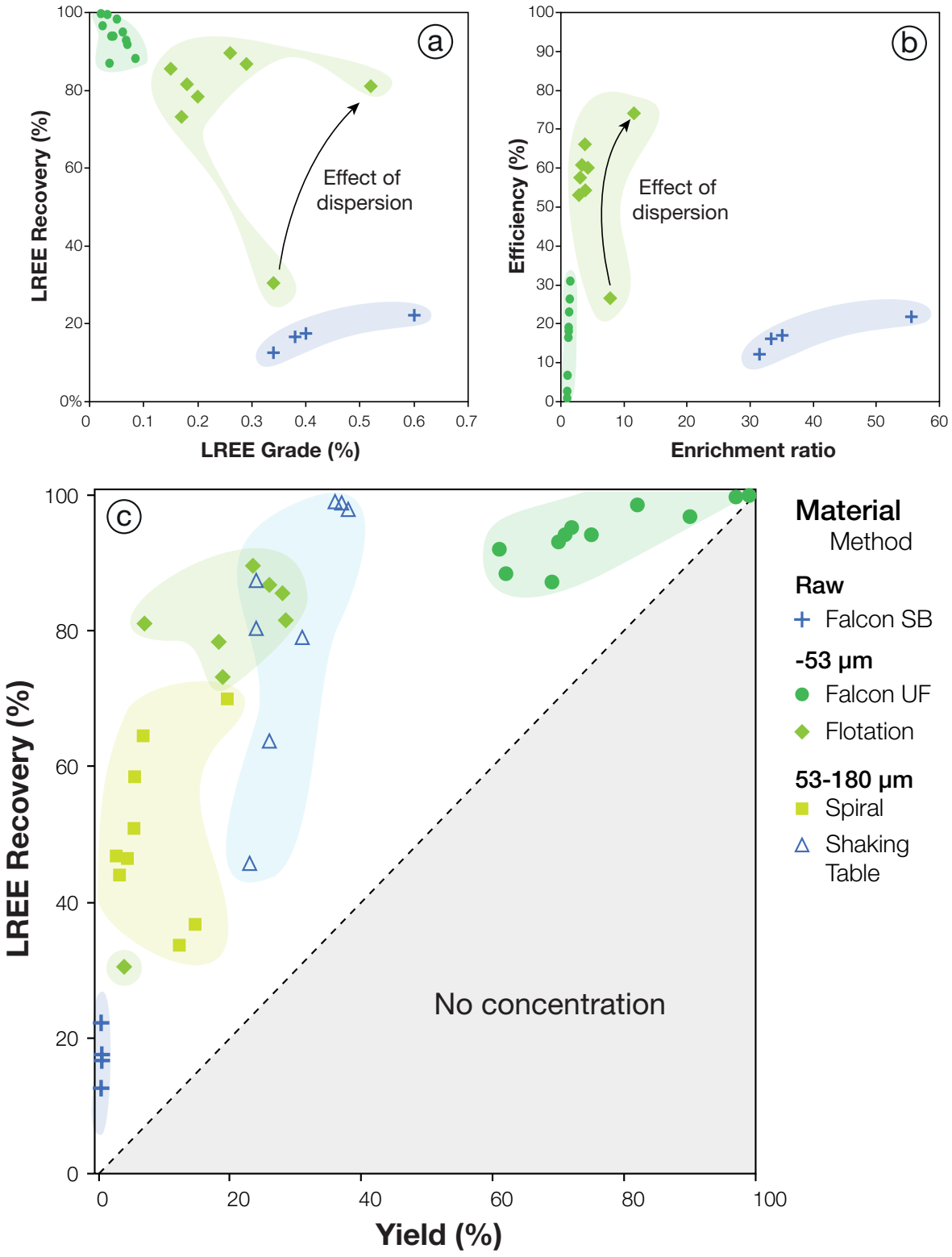


Figure 6.9: Comparison of the performance of the different beneficiation methods tested in this work. (a) LREE grade *vs.* recovery curve for beneficiation of the -53 µm residue. (b) Comparison of the efficiency of flotation and Falcon concentration. (c) Summary of the overall performance of all the methods investigated for the recovery of metals from the micaceous residue using data from feasibility tests as well as data from Chapters 3 and 5.

given the high recoveries obtained using what remain relatively low cost units, with a limited number of operations, that could be easily implemented on site to treat current residue stream and considering the high added values of some of the metals such as LREE, it is likely that kaolin residues could be considered as a potential source for these metals.

## 6.5 Conclusion

Recovery of monazite from kaolin micaceous residue using Falcon centrifugal separation and froth flotation as well as the effect of dispersion on separation efficiency, has been investigated. Results show that an effective dispersion of clay minerals is obtained with very low dosage (20 mg/L) using sodium polyacrylate dispersant (Antiprex D). The use of sodium oleate and hydroxamate in the presence and absence of non-ionic reagent (PX4826) has been investigated on material deslimed with or without dispersant. In the absence of dispersant, the best results obtained with sodium oleate and hydroxamate alone in terms of LREE grade in the cleaned product were around 3370 ppm and 2500 ppm respectively. LREE recovery with sodium oleate was very low at 30% but could be increased to 83% with the addition of non-ionic reagent at the expense of lower grade. The addition of dispersant significantly improved flotation efficiency. The LREE grade in the floated product obtained with sodium oleate increases from 3370 ppm to 5350 ppm while recovery improved from 30% to 80%.

Saturation tests performed on Falcon UF shows a positive effect of desliming on separation performance which provides higher LREE grades and recoveries. Comparison of the performance of flotation and Falcon UF concentration of monazite to previous results obtained with Falcon SB on the un-screened raw residue clearly shows that flotation of the fine residue is more efficient than Falcon UF and Falcon SB concentration.

Direct treatment of the un-screened material by Falcon SB gave very high enrichment rations (32-56) but the recoveries are low and beneficiation of screened material with a separate gravity route for the 53-180 µm fraction and combined flotation/gravity route for the -53 µm allows obtaining better recoveries. Even if the overall metal grades stay below usual concentrates grades (<50% REO), the high recoveries obtained with a limited number of operations, using relatively low cost techniques, suggest that kaolin residues could be considered as a potential source for these metals.

# Chapter 7

# Towards a geometallurgical model

*Forewords*

*The objective of this chapter is to propose and discuss some effective and inexpensive methods that could potentially be used for the establishment of a by-product resource estimation geometallurgical model that integrates results generated from ore characterisation and metallurgical testing to allow a more holistic evaluation of the by-product potentiality of CRMs.*

## Contents



# 7.1 Introduction

Geometallurgy combines geological and metallurgical information to create a spatial predictive model for mineral processing plants in order to reduce technical risk (Lamberg, 2011). This implies to document variability within the orebody and quantify the impact of some geological and mineralogical factors on metallurgical processes (grinding, recovery). The database thus generated can be readily integrated into a 3D model (Williams and Richardson, 2004).

Such an approach is fundamental for the unconventional 'resource' investigated in this work, not only because of its nature but also because the target metals must be considered as by-products.

Applying a geometallurgical approach to this case study is rather challenging for several reasons. First, there are no a priori certainties on the economic feasibility of CRM by-product recovery. Next, there is no processing plant operating on site for CRMs recovery from the micaceous residue stream. This causes an important lack of information for the establishment of a hypothetical geometallurgical model when most of geometallurgical program are applied to more conventional deposits already in operation for which a significant amount of data is available, with high number of geometallurgical variables allowing the use of multivariate modelling (Boisvert et al., 2013). In addition, most of the data available only concerns the main commodity. Given the complexity of the investigated deposits, this means that this approach could not consider the whole deposit but will have to focus on specific facies, ore-type or locations and that the representativeness of the results that will be obtained is a key feature for a potential application. Finally, the development of performance prediction

models for a hypothetical CRMs recovery process to assess the by-product potentiality is critical as no data is available on the required CRMs grade or recovery.

## 7.2 Materials and methods

### 7.2.1 Sampling

All the data used for trace element resource estimation in this work are from a sonic drilling campaign undertaken in 2011 by Imerys Ltd., UK. The dataset selected for this study covers only the Melbur-Virginia and Wheal Remfry pits located on biotite granite at the western part of the St Austell rare-metal granite and comprise around 1200 core samples collected every 3 meters over 100 drill holes.

#### 7.2.1.1 Sample processing protocol

The main objective of this sampling campaign was to assess kaolin resources and alternatively potential critical metals resources, in terms of yields and chemical composition of the potential end-product through a laboratory scale sample processing that mimics the industrial scale kaolin processing route (Figure 7.1). Samples were crushed to 15 mm if required (50 mm top size) in a jaw-crusher and then stirred/mixed with water to liberate any kaolin from the clay matrix. At this stage, the obtained material is equivalent to the output of the washing barrel of the WADM plant. The slurry is then classified on a vibrating 180 µm screen followed by a screening of the –180 µm material on a vibrating 53 µm screen corresponding to the classification stages realised by the bucket-wheel de-sander/ 660 mm cyclones and the primary cyclones respectively (see Figure 1.10 in Chapter 1).

The -53 µm material is then treated to remove the 15-53 µm material by sedimentation. If required, a magnetic separation was applied to the -15 µm material to improve brightness/colour as applied in the refining stages of the industrial process. Finally, the 5-15 µm fractions are removed by sedimentation and a -5 µm high quality kaolin product is recovered. In the end, 3 products are recovered, namely GT53 (53-180 µm), R15 (5-15 µm) and R5 (-5 µm) corresponding to a fine micaceous residue, a rough product and a fine product, respectively. Each product is weighed at each step of the sample processing, so that the yield of each final product is known. All the final products were then analysed by X-Ray fluorescence (XRF) for major elements whereas ProTrace (PT) XRF analyses (analyses for trace elements) were only carried out on the 180-53 µm and the -5 µm fractions. PT XRF analysis was carried out for a wide range of elements including 39 trace elements (Ag, As, Ba, Bi, Br, Cd, Ce, Co, Cr, Cs, Cu, Ga, Ge, Hf, I, La, Mo, Nb, Nd, Ni, Pb, Rb, Sb, Sc, Se, Sm, Sn, Sr, Ta, Te, Th, Tl, U, V, W, Y, Yb, Zn, Zr) and 9 major elements ($SiO_2$, $Al_2O_3$, $Fe_2O_3$, MnO, MgO, $TiO_2$, CaO, $K_2O$, $Na_2O$) plus loss on ignition (LOI).

#### 7.2.1.2 Sub-sampling of core samples for calibration

In order to control the accuracy of the PT XRF data for the LREE and other metals a set of 30 core samples from Melbur and Wheal Remfry pit have been selected to be re-analysed. The linear regression models for Nb and LREE prediction, obtained with process samples in Chapter 3, suggest that $TiO_2$ can be used as a "pathfinder"

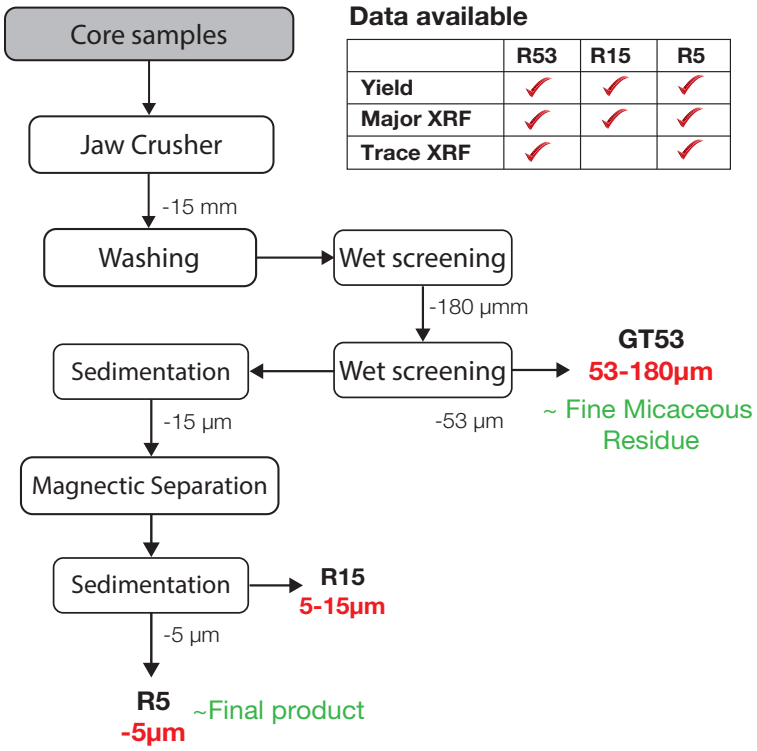


Figure 7.1: Sample treatment protocol of the geometallurgical program.

element for Nb and LREE. Moreover, $TiO_2$ is generally well quantified by XRF analysis. Hence sub-samples have been selected among all the available core samples based on their $TiO_2$ content to have a representative sub-set. The logarithmic transformation of PT $TiO_2$ values has a normal distribution and its cumulative distribution can be calculated, as shown in Figure 7.2ab. Then, 30 values where selected at random in the [0,1] interval and samples with the closest corresponding $x$-value (Log($TiO_2$) values) were selected. Following this procedure, the obtained sub-set has a normal distribution close to the one of the original dataset (Figure 7.2c). In the end, only 26 usable samples were recovered due to technical issues (contamination, losses).

### 7.2.2 Pilot-scale gravity concentration testing

The influence of the LREE grade in the feed material on the spiral concentration efficiency has been tested using the spiral setup in scavenging configuration (Figure 2.8 in Chapter 2). The feed grade decreases progressively as the spiral concentrate is recovered continuously and samples are collected at regular time interval. Operating condition are set at 2 Lpm wash water flow rate and 15% solid pulp density to favour recovery (see Chapter 5), concentrate splitters positions are adjusted visually for the first test but remains fixed for all the others.

### 7.2.3 Multivariate calibration/PLS regression

Multivariate calibration involves relating two sets of data, the independent data, called predictors (X) and the dependent data, *i.e.* responses (Y), by regression. It replaces the classical multiple linear regression and allows direct correlations to be

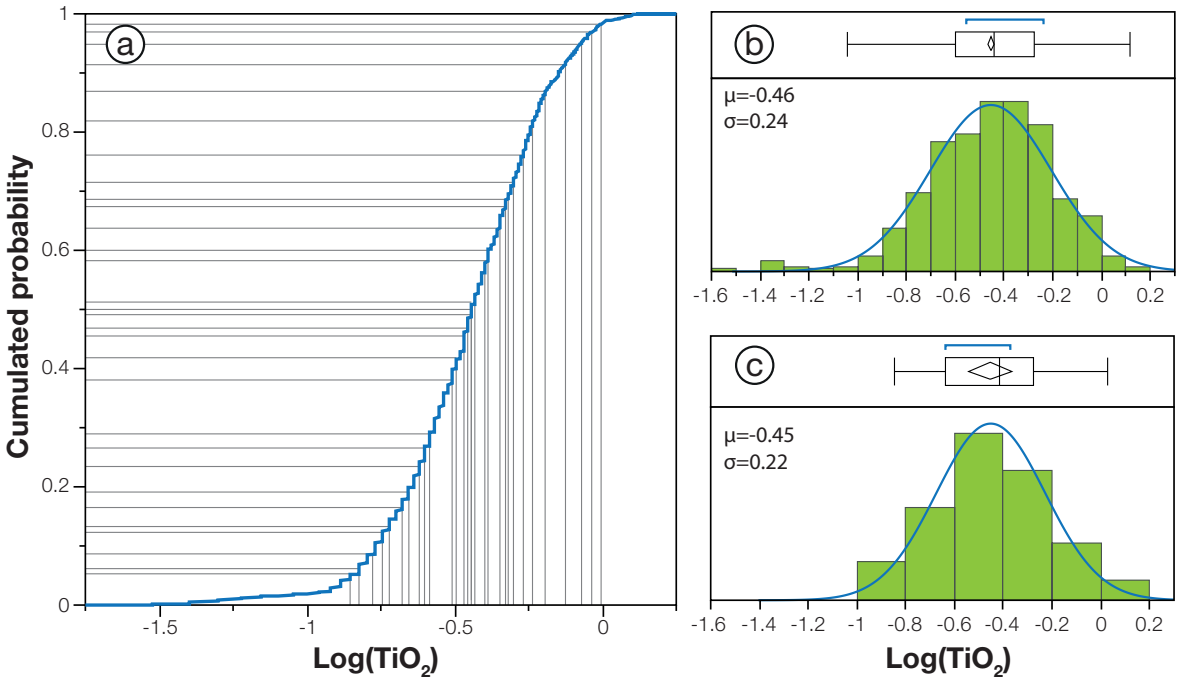


Figure 7.2: Subsampling procedure. (a) Cumulative distribution of Log($TiO_2$) of the GT53 fraction for the 1200 core samples and example of a random selection of 30 sub-samples uniformly distributed in the [0;1] interval. (b) Normal distribution of Log($TiO_2$) value in the original dataset. (c) Normal distribution of Log($TiO_2$) value in the selected sub-set.

modelled between a response y and a multivariate X data, among other compensating for debilitating co-linearity between x-variables (Esbensen et al., 2002). Partial Least Squares (PLS) models are based on principal components of both the predictors (X) and the responses (Y). PLS reduce the predictor variables dimensionality by extracting latent variables which are correlated to the responses while capturing a large amount of variation in the predictors therefore maximising the covariance between input and output variables (Wold et al., 2001). For more detailed about the mathematical procedure behind PLS regression, the interested reader is directed to Esbensen et al. (2002).

PLS regression model is usually developed from a training set of $N$ observations which is used to estimate the parameters of the model. For small datasets, like here where N=26, the common cross-validation method is the full cross validation or Leave-Out-One (LOO) method. LOO consist in making as many sub-models as there are objects, each time leaving out just one of the objects and only use this for testing. The squared difference between the predicted and the Y-value for each omitted sample is summed and averaged, giving the usual validation Y-variance (Esbensen et al., 2002).

The degree of prediction strength is evaluated using conventional modelling indices, *i.e.* trend line slope and regression coefficient ($R^2$), pertaining to a fitted linear regression model between predicted (y) versus reference (x) values which must both be as close to 1 as possible.

### 7.2.4 Methodology

The purpose of this work is to investigate and develop tools to help geometallurgical modelling and by-product resources estimation of LREE and rare metals within the St

Austell kaolin deposits. The methodology used in this study is presented in Figure 7.3. It follows two main steps which aim to populate the core sample database: (1) to control, and correct if necessary, the trace element grades using calibration or PLS-regression models based on duplicate ICP analyses on GT53 core samples and (2) to integrate metallurgical parameters through regression models (*e.g.* spiral performance prediction models) applied to the calibrated GT53 trace element data. These models will then be applied to core sample data to propose a simple geometallurgical model to help by-product resources estimation.

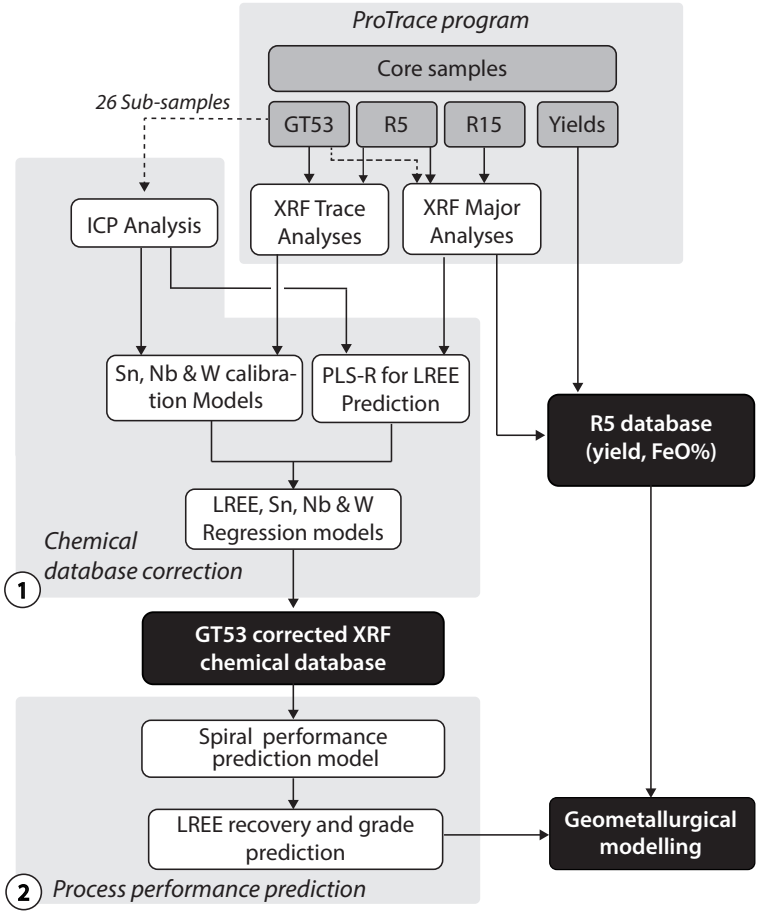


Figure 7.3: Outline of the methodology used in this work.

## 7.3 Chemical database correction

### 7.3.1 Metal grade calibration

Figure 7.4 shows the relationship between the LREE (Ce, La, Nd + Sm, Pr), Sn, Nb and W content of the 26 selected sub-samples measured by the PT XRF and ICP analysis. Results show that there is no correlation ($R^2$=0.24) between the LREE grade given by the PT XRF analysis and the grade given by the ICP analysis (Figure 7.4a). This is a consequence of the relative difficulty of quantifying LREE grades by XRF analysis without an extensive calibration, as it has been observed for our own XRF

analyses during this work (see Chapter 2). Hence it appears that LREE grades from PT data cannot be used directly to estimate the LREE resources. However comparison of PT XRF and ICP analysis for Sn, Nb and W shows good correlations, with high $R^2$ of 0.95, 0.96 and 0.87 respectively, suggesting that these metals may be easily corrected (Figure 7.4bcd). The slope of the regression trend lines, ranging from 1.16 to 1.57 indicates a potential systematic underestimation of the metal contents in the core samples which could result in significant resources underestimation of about 17% for Sn, 16% for Nb and 58% for W. More samples will be necessary to confirm these trends and refine the calibration models but they can be used as a first approximation to calibrate the PT data for these metals.

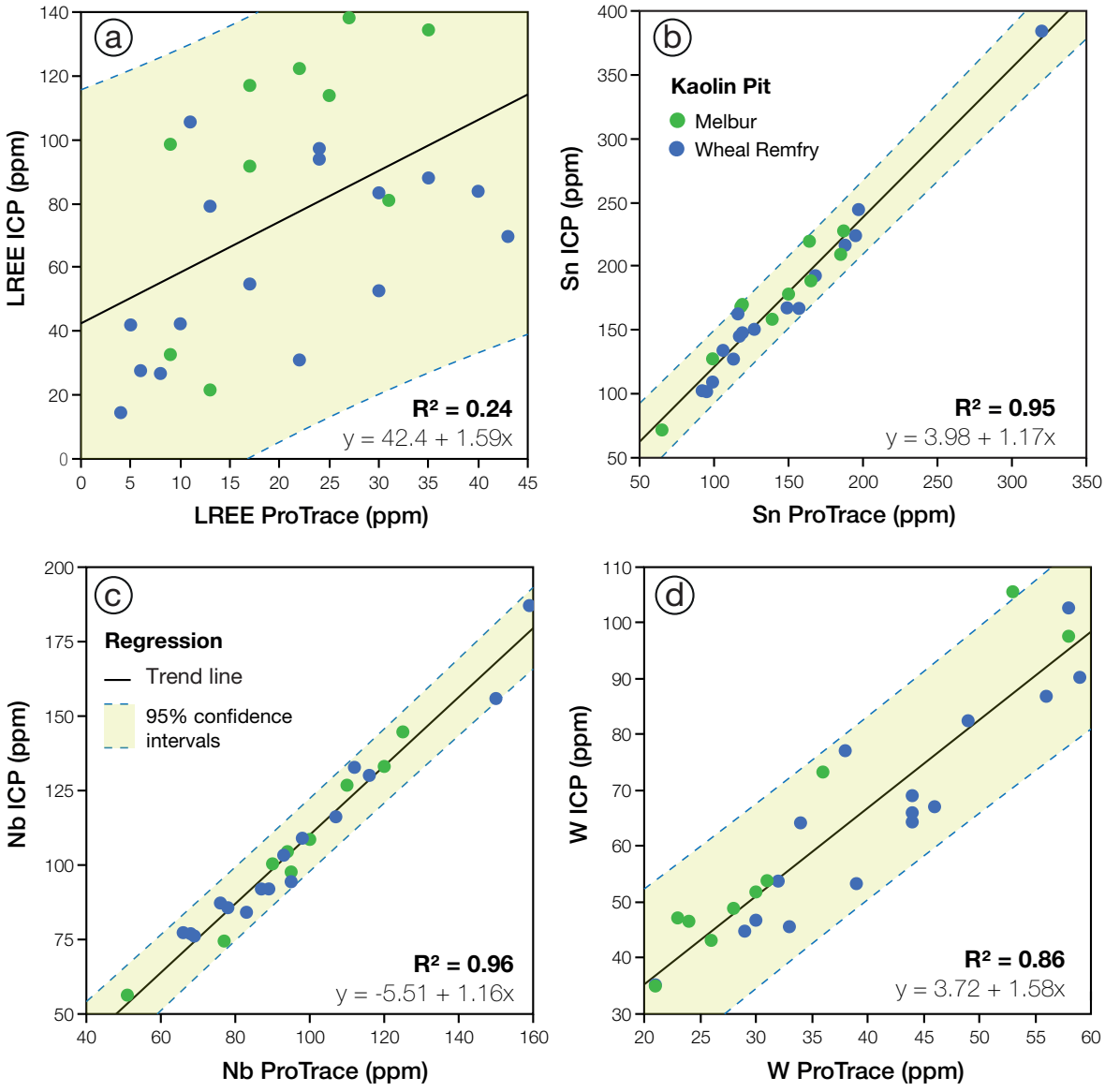


Figure 7.4: ICP *vs.* PT XRF analysis regressions plots for calibration. (a) LREE (La, Ce, Nd + Sm, Pr) plot display no correlation. (b, c, d) Sn, Nb and W correlations suggest that PT XRF data can be calibrated using linear regression models.

### 7.3.2 Multivariate LREE grade calibration

Multiple linear regression models presented in Chapter 3 suggest that LREE grade in process samples could be predicted using major element grades, $TiO_2$ and $SiO_2$ in particular, as a consequence of the separation process and mineral associations between monazite and other major minerals such as rutile. A more widely used technique for multivariate data calibration is the Partial Least Squares (PLS) regression. Results of the PLS-R applied to LREE grades given by ICP analysis ($y$-values) and to 21 factors including all major plus some trace elements (La, Ce, Nd, Th, Sn, Nb, W) from the PT XRF analyses ($X$-values) for the 27 GT53 samples is shown in Figure 7.5. The LOO cross-validation technique was applied within the PLS framework to extract the latent variables out of the 21 factors. Results suggest that the minimum predicted residual sum of squares (PRESS) is obtained for a 3 component model with a cumulated $y$-modelled variance of 84.4% (Figure 7.5c). Therefore, a 3 component model was considered as the benefit of adding further component was insignificant.

No clear difference is observable between chemical properties of Wheal Remfry and Melbur pit samples (Figure 7.5a). This indicates that both pits display similar X-Y data structures (covariance relationship) suggesting a quite homogeneous distribution of major elements within the kaolinised biotite granite.

A three-components PLS model applied to the full dataset predicts the LREE grade with satisfactory correlation ($R^2$=0.84, slope=0.84) to the reference LREE grade given by the ICP analysis (Figure 7.5d). Thus the PLS model leads to better LREE grade estimates than normally achieved with PT XRF analysis for the two pits studied. The LREE grade prediction model is primarily carried by a positive correlation with Th, and to a lesser extent by MnO and Ce grades of the PT data (Figure 7.5b). The strong positive correlation with Th is clearly due to monazite being the host mineral for LREE as Th is also present in monazite and is better quantified by XRF analysis than LREE. The role of MnO is hard to interpret, especially given the low variation displayed by MnO values ranging from 0.1 to 0.5 % and the low resolution of the analyses (0.1% increments). Contrary to what was previously observed with process samples, neither $TiO_2$ nor $SiO_2$ PT grades are correlated to LREE grades. This could be due to biases in $TiO_2$ and $SiO_2$ measurements from the PT XRF analysis. This may also suggest that the regression models presented in Chapter 3 are mainly a consequence of the separation process and hence could not be extended to the deposit itself. Since monazite is pre-concentrated in the hydrocyclone underflow along with rutile and other accessory minerals, gangue minerals are removed in the other residues. The positive correlation of LREE with $TiO_2$ and negative correlation with $SiO_2$ may reflect this separation phenomenon between accessory ($\sim TiO_2$) and gangue ($\sim SiO_2$) minerals in the kaolin processing route.

The results obtained with LREE prediction model are promising and can be used as first approximation to estimate the LREE grade in the GT53 core samples. However, the accuracy of the models could be increased by adding more data points to complete the training set and, even more important, to make a proper validation set which is the necessary condition to use validation statistics (Esbensen and Geladi, 2010). Given the importance of PT Th in the PLS regression model the new sub-samples selection should be based on PT Th grade rather than the PT $TiO_2$ grade in order to work with a representative sample set regarding LREE grade.

Table 7.1 shows the summary statistics of the GT53 data before and after cali-

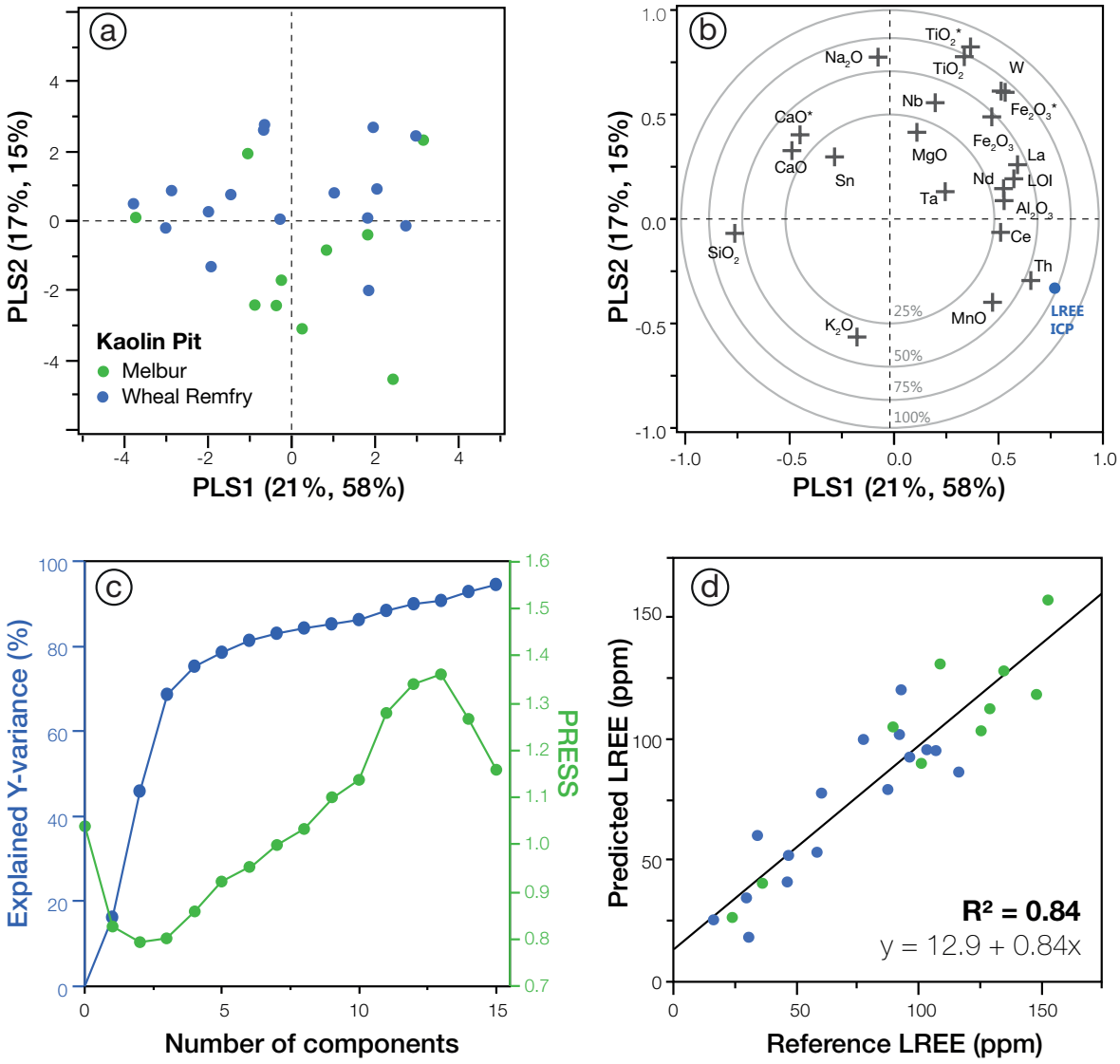


Figure 7.5: PLS Regression model for LREE prediction. (a) PLS score plot and loading plot (b) for Melbur and Wheal Remfry pit with proportions of total data variance modelled shown as (X%, Y%). Oxides with a '*' are from an additional major element analysis of the PT program. (c) Plot of Y-variance and PRESS values illustrating the cumulative contribution of the principal components to the model performance. (d) Prediction *vs.* reference plot for LREE, using a three-component model. One outlier was deleted from the original dataset.

bration for the values covered by the above-mentioned regression models. In order to be representative of the disseminated mineralisations within the St Austell rare metal granite only, outliers were removed from the original dataset (Appendix E.1). Indeed these outliers are likely to correspond to higher metal grade veins or lode-type mineralisations which occur throughout the St Austell kaolin deposits. Based on the Box and Whisker plots, the outlier threshold of the Nb, Sn and W is around 170, 250 and 100 ppm respectively (Appendix E.1). The mean CRM grades obtained after calibration are 83 ppm LREE, 106 ppm Sn, 73 ppm Nb and 38 ppm W (Table 7.1). Apart from LREE which are calibrated using the PLS regression model, the calibrated data display the same distribution asymmetry (skewness) and flatness (kurtosis).

Table 7.1: Summary statistics of the initial and calibrated GT53 content for LREE, Sn, Nb and W without outliers.

| Variable | Count* | Mean | Median | Standard deviation | Minimum | Maximum | Kurtosis | Skewness |
|---|---|---|---|---|---|---|---|---|
| *Initial data* | | | | | | | | |
| LREE | 886 | 25.07 | 20.00 | 17.59 | 1.00 | 132.00 | 4.81 | 1.79 |
| Sn | 1122 | 88.20 | 73.5 | 50.84 | 8.00 | 237.00 | 0.17 | 0.96 |
| Nb | 1165 | 68.01 | 68.87 | 32.25 | 3.75 | 161.00 | -0.35 | 0.55 |
| W | 1137 | 22.27 | 20.00 | 11.87 | 2.00 | 58.00 | 0.05 | 0.78 |
| *After calibration* | | | | | | | | |
| LREE | 880 | 83.44 | 80.83 | 38.64 | 0.29 | 239.79 | 0.10 | 0.34 |
| Sn | 1122 | 105.66 | 88.27 | 60.13 | 10.80 | 281.66 | 0.17 | 0.96 |
| Nb | 1165 | 73.27 | 68.35 | 37.20 | 1.50 | 180.67 | -0.35 | 0.55 |
| W | 1137 | 38.05 | 34.40 | 19.12 | 5.41 | 95.62 | 0.05 | 0.78 |

* Only the data points within the domain investigated for the establishment of the PLS regression/ calibration models were considered

### 7.3.3 Relationship between some elements and oxides

The relationship between the $TiO_2$ and Nb content obtained by ICP analysis is presented in Figure 7.6a. $TiO_2$ and Nb seem correlated ($R^2$=0.7) which is consistent with the previous observations made on process samples (Chapter 3). The variation of the $Nb/TiO_2$, highlighted by the dispersion of the data point along the regression trend line, is in agreement with the scanning electron microprobe analysis on Nb-rutile. This suggests that rutile is likely to be the major Nb-bearing mineral within the biotite granite and that the Nb content in rutile may vary. Figure 7.6b shows the relationship between each LREE based on the ICP analysis of the GT53 core samples. Similarly, results are in accordance with the observations made at the macroscopic sale on process samples and at the microscopic scale on monazite grains (see Chapter 3). Indeed the ratios between each LREE are similar to those previously observed which confirms that monazite is the only LREE-bearing within the St Austell biotite granite.

## 7.4 Prediction of process performance

Spiral concentration is the first and one of the most crucial step of the investigated beneficiation process for the 53-180 µm micaceous residue fractions. The following results present an attempt to predict spiral separation performance using the available core sample data.

### 7.4.1 Effect of feed grade

Since the effects of operating parameters on spiral performance have been investigated and optimum operating conditions are known, one remaining task is to study the influence of the characteristics of the materials treated on separation performance. Spiral concentrators are based on gravity separation principle by differentiating the minerals based on particle size, density and shape (Burt, 1984b). In addition, some other important factor such as feed grade or liberation degree may play an important role (Sivamohan and Forssberg, 1985a). The first few parameters (particle size, density and

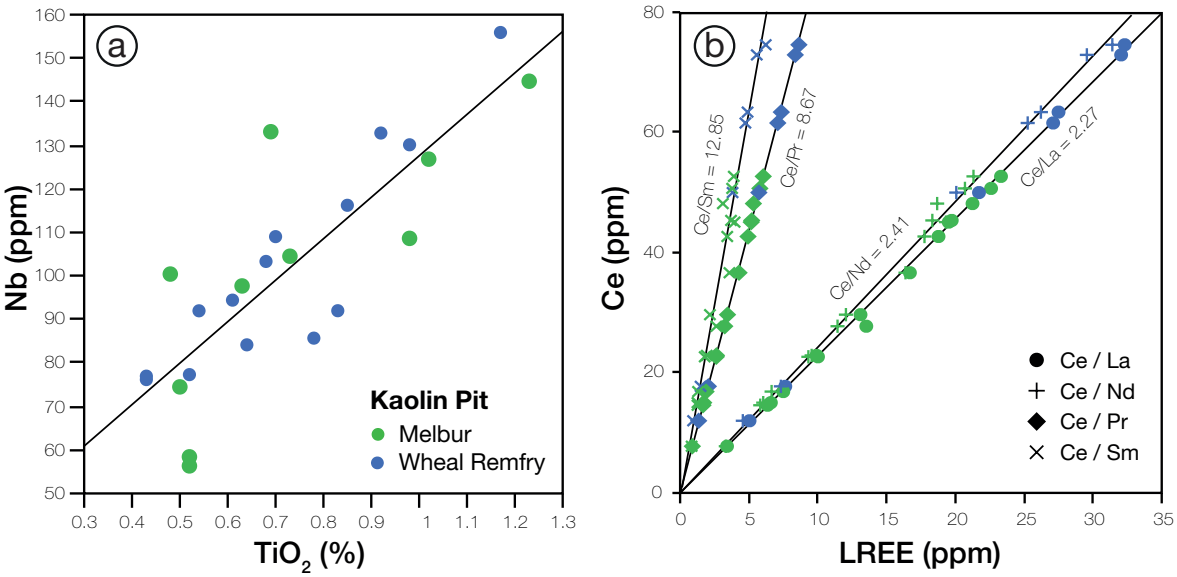


Figure 7.6: Binary linear correlation plots and trend lines between elements using ICP analysis chemical data. (a) Good correlation ($R^2$=0.70) suggesting a proportional relationship between $TiO_2$ and Nb. (b) Strong correlations ($R^2$>0.99) suggesting a proportional relationship between each LREE similar to the one observed on process samples and at the microscopic scale on monazite grains.

shape) can only be assessed by systematic mineralogical and textural analysis or other additional analyses and no data is available from the core sampling program. However the grade of the spiral feed is known as the feed material of the spiral concentration tests consist in the 53-180 µm fraction of the micaceous residue which corresponds to the GT53 fraction analysed for trace elements.

The influence of the LREE grade in the feed material on the spiral concentration efficiency has been tested using the spiral setup in scavenging configuration. The initial feed material was relatively "enriched" in LREE with a grade of 225 ppm close to the maximum LREE grade suggested by the PT data calibration (Table 7.1). Hence this allows covering the whole range of LREE values potentially displayed by the GT53 core samples data. To reflect this, the LREE feed grade is normalised using the minimum and maximum values displayed in Table 7.1, as follows:

$$G_F^* = \frac{G_F - 0.29}{239.79 - 0.29} \tag{7.1}$$

Figure 7.7 shows the influence of the normalised LREE grade ($G_F^*$) in the feed material on the performance of spiral concentration which reveals some interesting trends. As expected, spiral performance is found to improve with increasing feed grade. Indeed, LREE recovery and concentrate grade increase with LREE content in the feed, with a maximum recovery and grade of 55% and 1000 ppm respectively. However LREE enrichment degree reaches a plateau at 4.5 for LREE normalised feed grade higher than 0.6-0.7 (∼150 ppm LREE). All performance indexes trend lines suggest that below 0.2 LREE normalised feed grade (around 60 ppm LREE) no separation should be expected (Figure 7.7). Hence, this value could be considered as an estimation of the minimum cut-off grade of the GT53 fraction that should be considered for LREE recovery within

the St Austell biotite granite. This suggested cut-off grade is of the same order of magnitude as that of other metals (*i.e.* ∼100 ppm) suggested by the feasibility studies (see Chapter 5).

The relationship between spiral performance indexes and normalised LREE feed grade, shown in Figure 7.7, exhibits clear trends that can be fitted by an empirical model, using the equation:

$$y = a + b \times \exp(c \times G_F^*) \tag{7.2}$$

where $a, b$ and $c$ are the asymptote, scale and growth rate terms respectively.

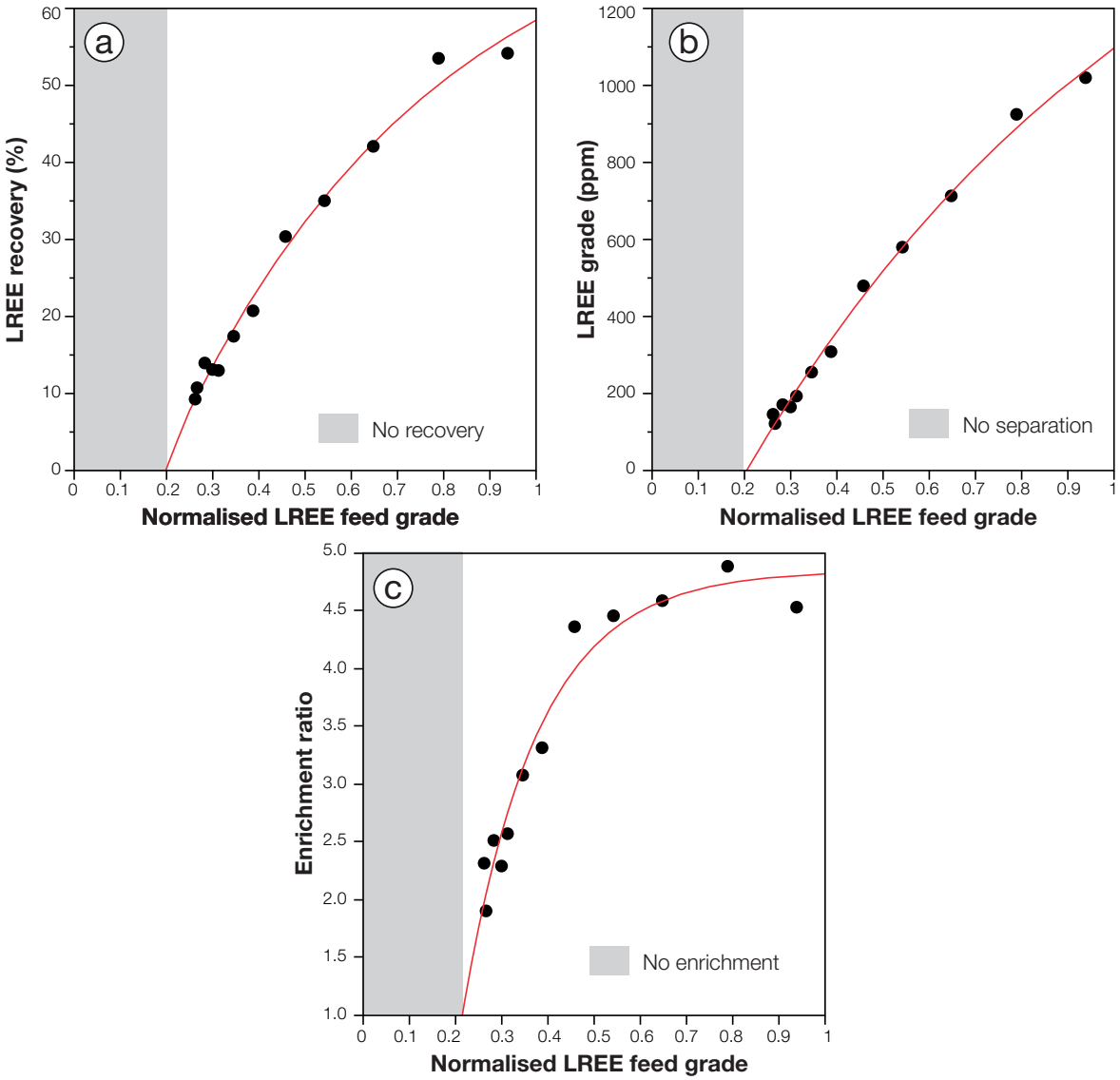


Figure 7.7: Prediction of the performance of the rougher spiral concentration process for LREE as a function of LREE feed grade normalised according to Table 7.1. (a) LREE recovery, (b) LREE grade and (c) LREE enrichment ratio.

The parameters $a, b$ and $c$ are fitted, and have no physical meaning. However, it is expected that they would be linked to changes in mineralogy or liberation degree which consequently affects spiral performance. The values of the fitted parameters are given

in Table 7.2. Comparison between the observed and predicted values in Figure 7.8 shows a good agreement with high regression coefficient values ($R^2$>0.9) and trend line slopes close to 1, suggesting that the models can reasonably be used to estimate spiral performance.

Table 7.2: Values of fitted parameters $a, b$ and $c$ in Equation (7.2) for the models shown in Figure 7.7.

| Performance index\Coefficient | a | b | c |
|---|---|---|---|
| Recovery | 0.77 | -1.07 | -1.74 |
| Grade | 1921.17 | -2386.91 | -1.06 |
| Enrichment | 4.85 | -14.51 | -6.19 |

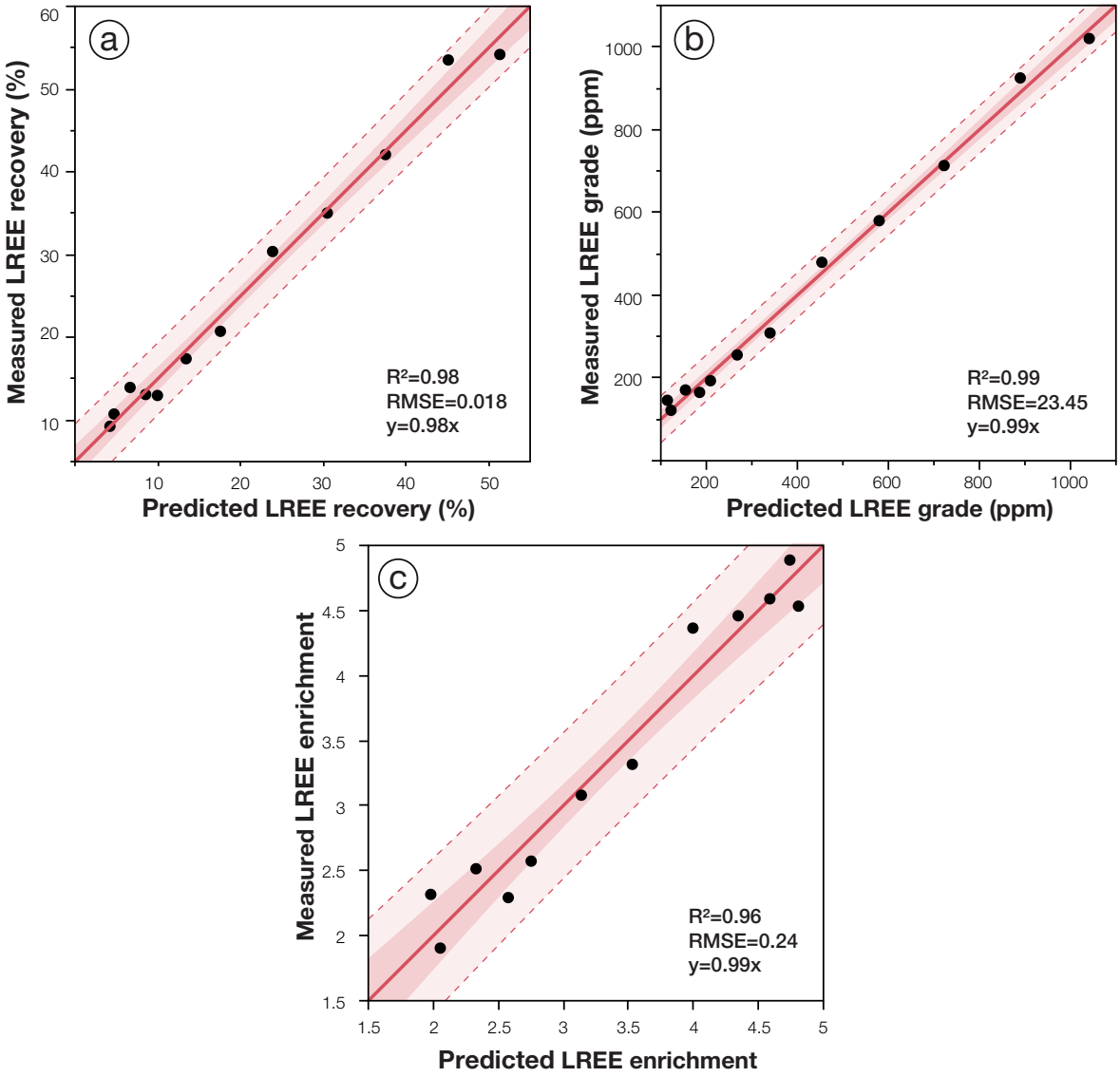


Figure 7.8: Comparison between predicted and measured spiral performance with trend lines and 95% confidence intervals. (a) LREE recovery, (b) LREE grade and (c) LREE enrichment ratio.

The aforementioned results suggest that the regression models proposed to predict spiral performance for LREE can reasonably been applied to the GT53 core sample data. In addition, the range of LREE feed grade used to calibrate the models covers most of the LREE grade interval suggested by the calibrated PT data (Table 7.1). Hence, prediction of spiral performance using PT core sample database can be undertaken using the following equation (with coefficient values given in Table 7.2):

$$y = \begin{cases} a + b \times \exp(c \times G_F^*) & , \quad G_F^* \geq 0.2 \\ 0 & , \quad G_F^* < 0.2 \end{cases} \tag{7.3}$$

### 7.4.2 Effect of particle size

Particle size is a critical parameter to take into account as variations in particle size distribution of the spiral feed may significantly impact the performance of the separation with the spiral concentrator.

The influence of particle size on spiral performance in terms of heavy minerals (SG>2.89) recovery has been investigated in Chapter 5. It has been observed that at the low wash water and pulp density conditions used in tests, the variation of heavy minerals recovery as a function of particle size is limited and only decreases for particle size below 50 µm. Given the discrepancies between the performance in terms of heavy minerals and monazite (LREE) recovery (see Chapter 5), most likely due to the higher specific gravity of monazite (4.98-5.43) compared to the bulk of the "heavy minerals", this phenomenon should be even more pronounced for monazite.

Particle size analysis of the 26 GT53 core samples shows that the mean particle size distribution is very close to the one of the spiral feeds (Figure 7.9). This suggests that GT53 samples are in average representative, in terms of particle size, of 53-180µm size fraction of the micaceous residue obtained with similar sample treatment. It can be observed that the variation in particle size distribution of the GT53 fraction is relatively limited and is more important in the 10-50 µm size range. This may be surprising given the high short range variability displayed by the multivariogram of the size distribution properties (mainly accounted to the D90) of the micaceous residue stream in Chapter 4. However, these results were obtained from raw micaceous residue, and these variations may be less visible on the screened spiral feed as a consequence of the screening operations. In addition, the overall limited variations displayed by the core samples may also be explained by the fact that the sample set is only composed of kaolin grade IV-V samples and that more variations (toward the coarser fractions) should be observed with lower grade samples. The variations in particle size distribution of spiral feed are more limited and almost always included into the variations interval of the GT53 particle size distribution. These variations, however, do not seem to affect the performance of the separation as illustrated by the rather small variations of spiral concentrate particle size distribution (Figure 7.9). In addition, it can be seen that particles in the finer size ranges below 40-50 µm, for which the spiral feed particle size variations are more important, are not recovered in the spiral concentrate. This result is in agreement with the results from partition curve analyses presented in Chapter 5, and suggests that variations in particle sizes, at least for the finer size range, is unlikely to influence the performance of the separation.

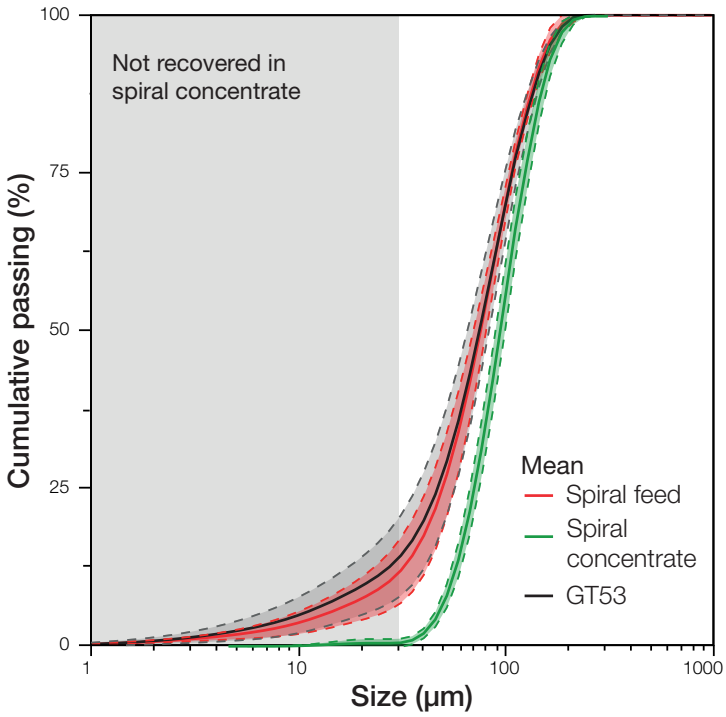


Figure 7.9: Mean particle size distribution of the GT53 core samples, the spiral feed (53-180 µm micaceous residue) and the spiral concentrate. The dashed lines represent the mean $\pm 1\sigma$.

Unfortunately no systematic measurements of the particle size distribution of the GT53 samples were performed during the sampling campaign which means that particle size cannot be taken into account for the spiral performance prediction model without an extensive particle size analyses campaign of all GT53 samples. However, particle size is likely to vary with variation of kaolinisation grade within the deposit. Hence, without additional analyses on GT53 core samples the relationship between the kaolin grade and the particle size distribution should be investigated. Furthermore, the liberation degree of the CRM-bearing minerals is likely to change with the kaolinisation grade of the kaolin ore.

For all these reasons the spiral performance models previously introduced can only be used as a first approximation to predict spiral performance if:

- The plant is processing high grade kaolin ore (IV-V) with a particle size distribution within the spiral feed interval shown in Figure 7.9,
- The kaolin ore treated is from Melbur-Virginia or Wheal Remfry pits or other deposits located on biotite granite,
- The LREE grade of the GT53 fraction is below 240 ppm, which is the maximum LREE grade predicted by the PLS regression model (Table 7.1),
- The micaceous residue is processed with the same flowsheet and the same equipment (5 turn Reichert MKIIA spiral), under similar operating conditions (pulp density, wash water, splitter positions, etc.).

These make a lot of necessary conditions for the direct application of the predictive models and it is unlikely that if a similar gravity concentration route is ever imple-

mented on site, the performance will be exactly as predicted by the aforementioned models. However the methodology is valid and the trends observed reflect a true phenomenon. Hence for the purpose of illustrating the benefit of such models for resources estimation, they could be applied as a first approximation, to core samples that respect the required conditions.

## 7.5 Potential application to core sample data

The interest of the data calibration and process performance prediction models developed in this work is that they could be directly applied to the GT53 core sample database. This could help assessing the potential resources in CRMs within the kaolin deposits by giving estimated process performances as illustrated in Figure 7.10 for LREE recovery. It gives quantitative information of what performance could be expected if the area would be exploited for CRMs thereby defining locations of interest for CRMs recovery, which in this simple univariate case is directly link to the CRM grades. For instance, regarding the LREE recovery the results suggest that Melbur pit have more potential than Wheal Remfry.

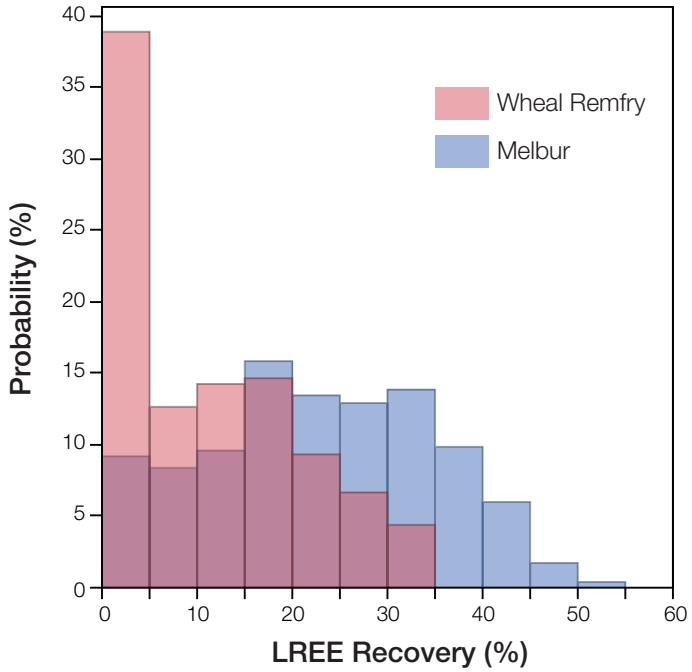


Figure 7.10: Distribution of LREE Recovery applied to GT53 core samples for Melbur and Wheal Remfry pits.

However, since the CRMs are considered as potential *by-product*, the resource must primarily valuable for the main commodity, *i.e.* kaolin, which means that both kaolin and CRMs must be taken into account in the geometallurgical model. Hence, in order to evaluate the potential of the metals as by-product of kaolin production, both kaolin resources using R5 data and potential metal resources using the GT53 data must be considered.

A proposal for the establishment of a geometallurgical model to evaluate the by-product potential of CRMs is shown in Figure 7.11.

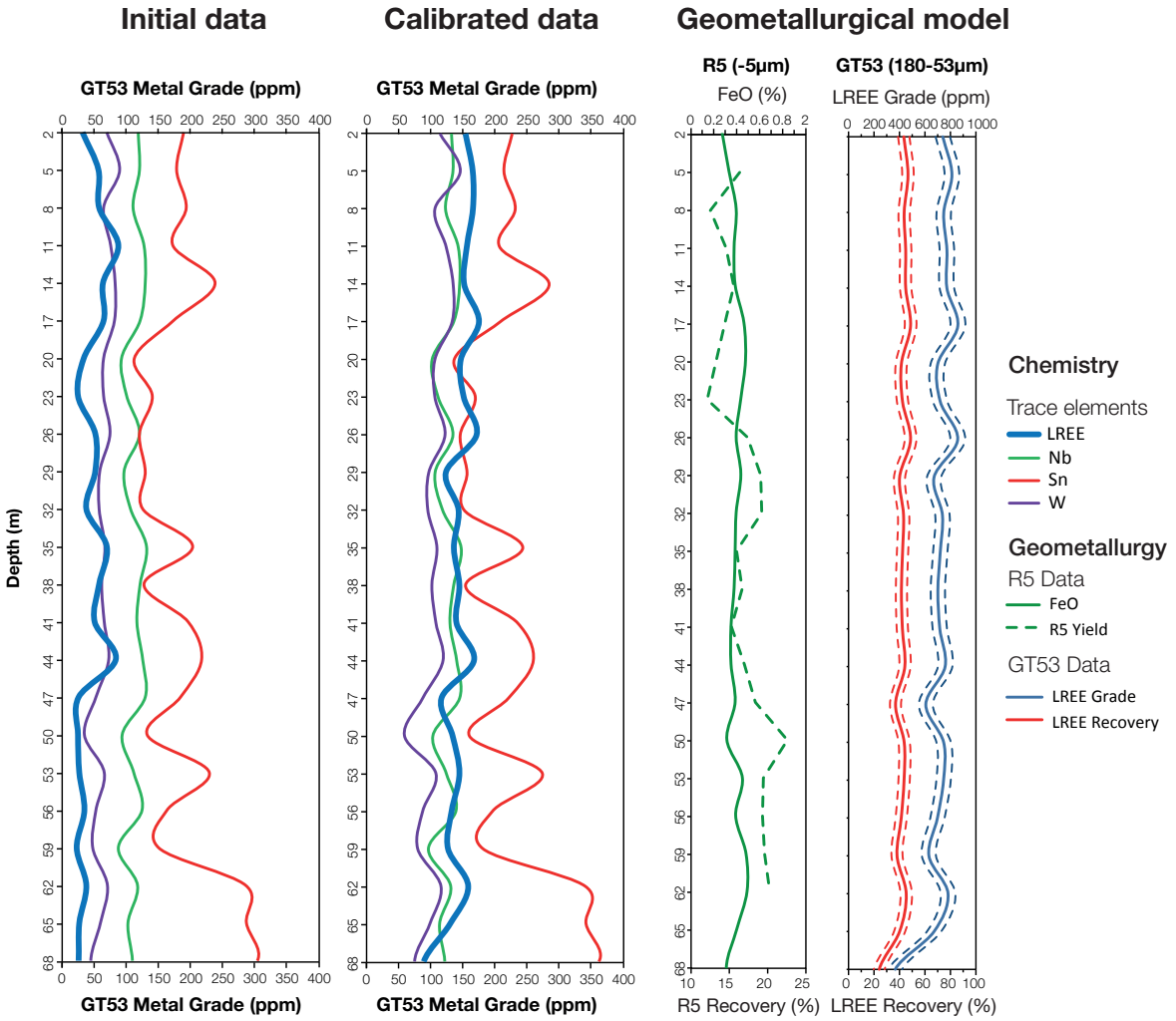


Figure 7.11: Graphic log showing the application of the data calibration and process performance prediction models to the ML11S041 drill core from Melbur pit. The proposed data processing method allow developing a geometallurgical and resources estimation model by giving both quantitative (yield) and qualitative (whiteness) information about the (main) kaolin product, as well as quantitative evaluation of by-product potential of CRMs in terms of LREE grade and recovery in spiral concentrate.

It can be seen that according to the calibration models, the original data tends to underestimate the metal grades which could potentially lead to bad resource estimation. For instance according to the original dataset all the LREE grades within the ML11S041 core samples are below the cut-off grade which could lead to erroneously consider this zone as non-valuable whereas the estimated LREE grade using the PLS regression model is largely above the empirical cut-off.

Kaolin resources can be estimated on textural and alteration based classification schemes or estimated using quantitative indicators such as the yield of the R5 (-5 µm) fraction. Other indicators could also reflect the quality of the kaolin product such as the iron content (FeO) which gives insight about the kaolin whiteness. These indicators can be used to define the zones of interest for kaolin recovery in the first hand, and then to see if these zones are also of interest for metal recovery. The spiral

performance prediction models (Equation (7.3)) could then be used to predict LREE grade and recovery in the spiral concentrate and see if the predicted performance fit the requirements.

## 7.6 Conclusion

In this study, effective and inexpensive methods have been developed to calibrate metal grades of the GT53 (53-180 µm fraction) core sample database. Comparison with ICP analyses shows that rare-metals (Sn, Nb and W) grades are underestimated by the PT XRF analyses but could be calibrated using linear regression models whereas LREE grades are seriously biased and display no correlation with ICP results. A PLS regression applied to some major and trace XRF analyses allowed to predict the LREE grade accurately with satisfactory validation results ($R^2 = 0.88$). These regression models are promising; however the potential of these results worth to perform more analyses on core samples to complete the models validation.

Pilot scale tests using 53-180 µm micaceous residue samples suggest that spiral performance in terms of LREE grade, recovery and enrichment could be predicted as a function of LREE feed grade. Even if particle size distribution of the feed material is likely to influence spiral separation performance, results show that, for the investigated high grade sample, the variation of particle size distribution is rather limited and does not seem to affect the efficiency of the separation if the operating parameters are maintained fixed.

Application of the aforementioned models to the GT53 core sample data in parallel with R5 (-5 µm) core sample data allows targeting potential zones of interest for CRMs recovery as by product of kaolin production.

# Chapter 8

# General discussion

## Contents



## 8.1 CRM recovery process proposal

Before carrying out a preliminary economic feasibility for CRMs recovery, a tentative process flowsheet is given showing the unit operations and materials required. Figure 8.1 and Figure 8.2 show suggested qualitative and quantitative flowsheets for the recovery of heavy minerals and CRMs from the micaceous residue. This is a preliminary flow diagram based on the best results obtained in this work from metallurgical testing with laboratory and pilot scale units available at the STEVAL pilot plant of the Georessources laboratory and thus it is subject to modifications. The proposed flowsheet uses the micaceous residue stream from secondary cyclones underflow as a primary feed. It comprises three main stages: (1) classification, (2) gravity concentration of 53-180 µm fraction and (3) flotation of -53 µm fractions.

*Classification*

The classification stages are essential as they allow providing a sized (53-180 µm) feed for the gravity processing route which increase the efficiency of the separation and provide a fine (-53 µm) feed for the flotation route. These stages were realised at the pilot scale using vibratory screens but screening operations at these cut-size are usually performed by hydrocyclones on-site for the main kaolin processing route. If these classification stages were to be performed by hydrocyclones, pre-concentration of heavy minerals in the underflow streams may occur as this is the reason why metals are pre-concentrated in the micaceous residue. It must be noted that these cut-size also correspond to the one used for core sample treatment and resources estimation (see Chapter 7).

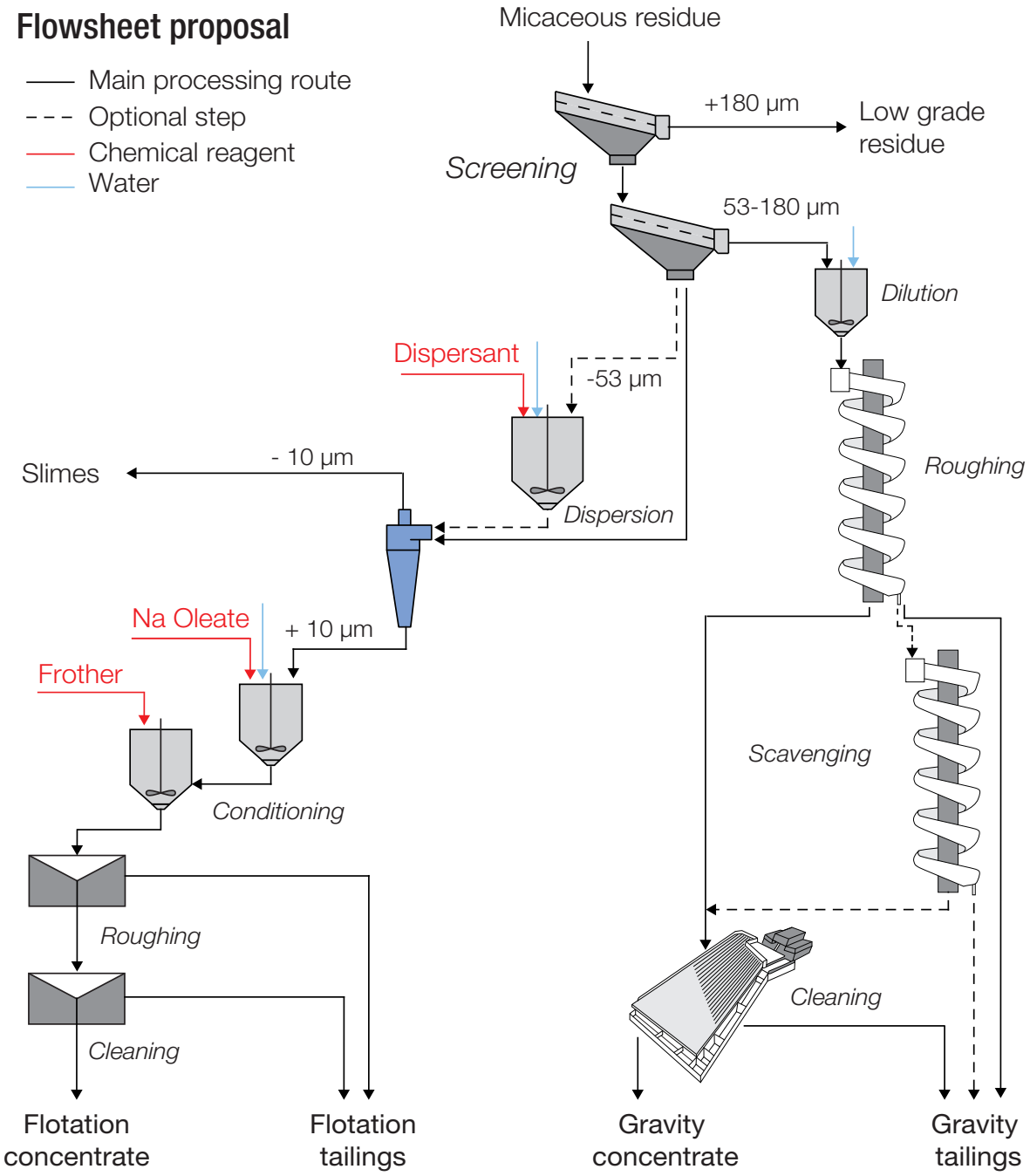


Figure 8.1: Flowsheet proposal for the beneficiation of CRMs from micaceous residue using gravity concentration and flotation.

*Gravity processing*

The suggested gravity processing route is composed of one rouging stage of spiral concentration followed by a cleaning stage of the spiral concentrate using a shaking table. As results have shown that low wash water and low pulp density favour heavy mineral recovery (Chapter 5), the spiral should operate accordingly and a pulp dilution stage may be necessary. The exact number of spiral concentration steps required may vary depending on the feed grade and one or two scavenging operations may be neces-

sary. The cleaning operation could be performed by a shaking table or a similar device, and as the preliminary design proceeds toward completion and if detailed information on flow quantities and equipment performance become available, other equipment could be investigated (Mozley table, MGS).

*Flotation*

A desliming operation for the -53 µm residue is recommended before feeding the flotation circuit. Prior to desliming a conditioning step with dispersant addition is suggested as it improves the flotation performance which is impacted by clay coating (Chapter 6). Sodium polyacrylate solutions could be used as dispersant as they prove to be effective at low dosage (180 g/t). The deslimed residue passes then through two conditioning steps (frother addition, reagents addition). The flotation circuit comprises one roughing and one cleaning step as the scavenging operation was found to be unnecessary (Chapter 6). However more cleaning stages may be necessary to improve the concentrate grade. Results suggest that sodium oleate at 200 g/t dosage should be used if dispersant were used during the desliming step. Otherwise the LREE recovery is low with sodium oleate and hydroxamate should be used instead.

Figure 8.2 shows a quantitative flowsheet for the beneficiation of the micaceous residue with an arbitrary feed flowrate of 15 t/h. This quantitative flowsheet was obtained using results from different tests performed on samples from different batches which were sometimes analysed with distinct techniques (ICP or XRF). Hence the values given in Figure 8.2 are only indicative of possible process performance. Again, as the design proceeds toward completion and the detailed information on flow quantities and equipment specifications become available, a combined-detail flow diagram could be prepared. Data reconciliation was done with the BILCO™ software (Caspeo, France) dedicated to data reconciliation by material balance. Estimation errors were computed taking into account analytical errors and errors on stream distribution estimation (set at 20%). The results of the material balance are shown in Figure 8.3 and detailed material balance can be found in Appendix F.1. As it can be seen, the material balance suggests that up to 40% of the LREE are recovered in the gravity concentrate whereas 22.3% LREE are recovered in the cleaned flotation concentrate. Most of the lost occurred in the gravity tailings (24.14% LREE) and the coarse residue (6.80% LREE). The slimes do not contain significant amount of LREE confirming that clays have been effectively removed during the hydrocycloning. Surprisingly, most of the LREE goes into the gravity feed stream (53-180 µm) instead of the flotation feed stream (-53 µm). Note that the characterisation results suggest that most of the LREE are in the fine fraction (see Chapter 3). This could be explained by the fact that parts of fine monazite could be recovered in +53 µm fraction which remain in the screen oversize, by variation in the particle size distribution of monazite within the deposit or by the accumulation of analytical errors.

However these results are promising as they suggest that up to 62.3% of the LREE within the micaceous residue could potentially be recovered with concentrates grades about 0.5-1.4% LREE.

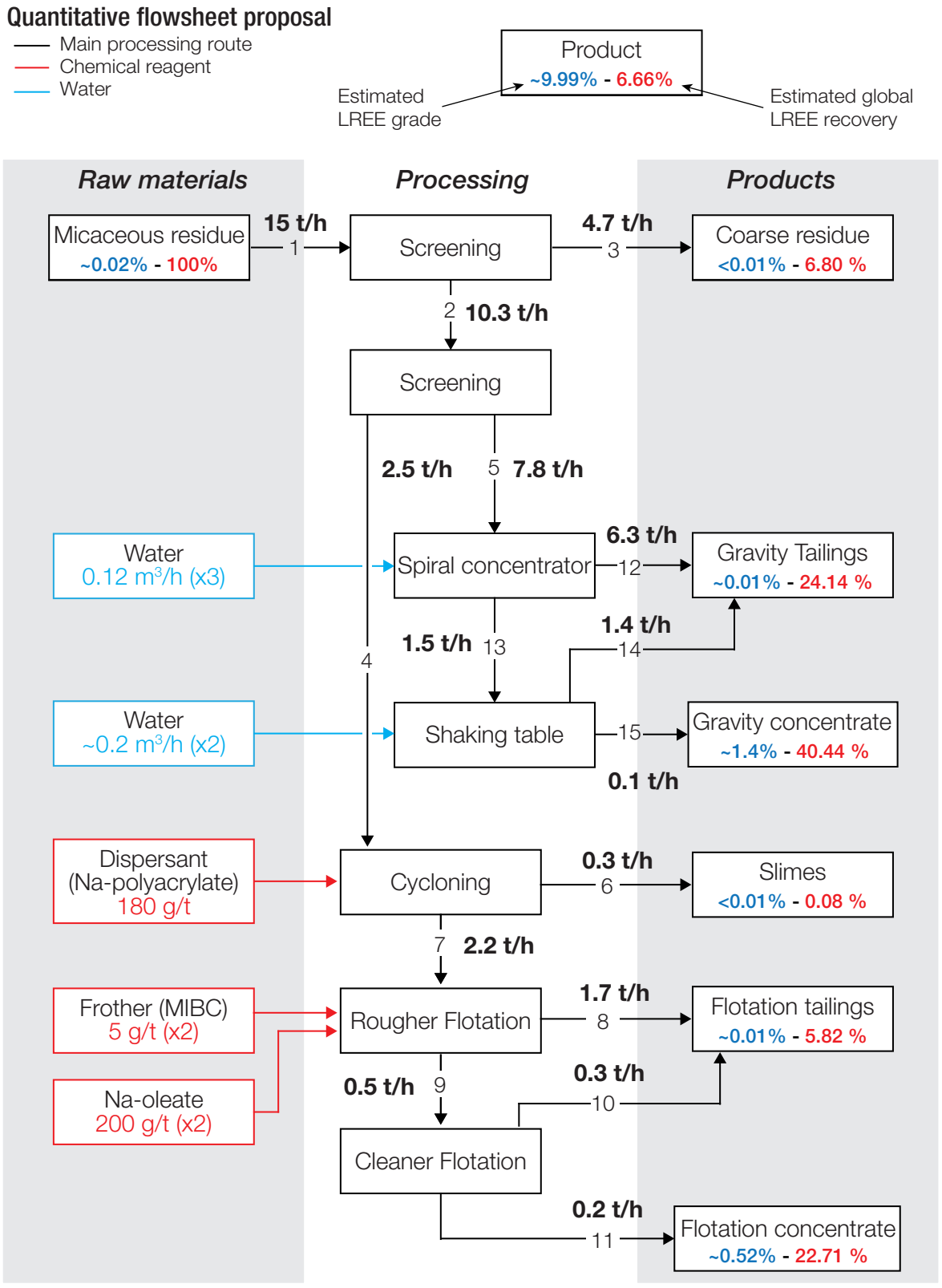


Figure 8.2: Quantitative flowsheet proposal for the beneficiation of CRMs from micaceous residue using gravity concentration and flotation based on the pilot/ laboratory scale tests results. Solid flowrates are obtained by data reconciliation using the BILCO™ software based on a treatment of 15t/h micaceous residue.

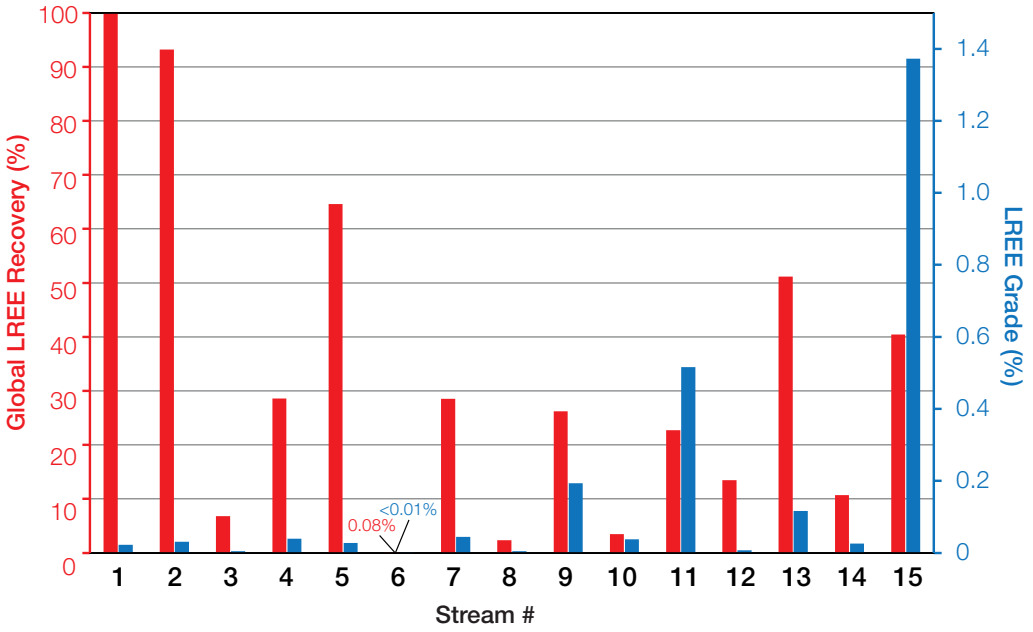


Figure 8.3: Estimated material balance of the micaceous residue beneficiation process. Stream numbers correspond to those of Figure 8.2.

## 8.2 Evaluating project profitability

In order to define the profitability of any plant design, one must assess if the proposed process is capable of operating under conditions that will yield a profit. Thus it is necessary to evaluate quantitatively all expenses involved in the mining, manufacturing process and all the possible incomes generated. In the case of CRMs as by-product, the cost of mining is already covered by the sale of the kaolin product. Since the material treated in this work is regarded as waste and is not valorised, only cost incurred in setting up the hypothetical plant and running the process will be evaluated. The total investment is the sum of two major sources of expanses, *i.e.* the fixed-capital investment (capital expenditure CAPEX), for the equipments and facilities in the plant, and the operational expenditure (or expense) OPEX (salaries, raw materials and products storage, etc.). The capital expenditure is the major source of expense and will be evaluated in the following section.

### 8.2.1 Capital costs estimation

Costs estimation is provided by the USIM PAC™ software based on simulation results and scaling the units making up the process (Caspeo, 2013). The whole process must be simulated with satisfactory correspondence to observed process performance prior to direct cost estimation which is far beyond the scope of this study. However all unit capital cost (UCC) estimations are made on the basis of the work of Mular (1982) and more recently Mular and Poulin (1998) which provide equipment cost estimates (C) as a function of a critical parameter (X) following the general form:

$$C = aX^b \tag{8.1}$$

where a and $b$ are constants determined graphically based on C *vs.* X graphs.

This method only gives an estimate with an overall accuracy of 20% which is sufficient to give an order of magnitude of the investment costs. Therefore all the following expressions are defined in common currency at that time (*i.e.* Canadian Dollar in 1982 or 1998) and thus need to be updated and converted. The price is updated using the Marshall and Swift cost index (Mining & milling) of 1759.5 at the 4$^{th}$ trimester 2015. The costs are then converted in euros using the current exchange ratio (currently 0.630424).

Table 8.1 shows the estimation of all unit capital costs (UCC) without the two screening stages as cost equipment models for screens are based on their sizes and that the equipment used for the screening operations don't have industrial equivalent (although the use of hydrocyclones could be suggested). The detailed calculation of the capital cost estimation for all units can be found in Appendix F.2. The UCC estimated using the aforementioned methodology is 182 657 €. It could be noted that this UCC is mainly impacted by the fine fraction beneficiation route (desliming and flotation) as the gravity processing equipment only account for 81 785 €.

Table 8.1: All unit capital cost (UCC) estimations (without the two screening stages).

| Equipment | Number of units | Unit cost (€) | Total cost (€) |
|---|---|---|---|
| Spiral | 1 | 14 761 | 14 761 |
| Shaking table | 1 | 52 263 | 67 024 |
| Hydrocyclone | 5 | 4 084 | 71 108 |
| Flotation roughing | 3 | 82 405 | 153 513 |
| Flotation cleaning | 3 | 29 144 | 182 657 |
| Total | | | 182 657 |

The estimation of the total investment coast (TIC) for the whole process is then performed using the method described in Vilbrandt and Dryden (1959). These costs are estimated as fraction of the UCC previously calculated. The default ratios are the mean values which are adjusted according to the type of installation (gravity, flotation, etc.) and to the installation site (Caspeo, 2013). Table 8.2 shows the detailed calculation of the TIC for the hypothetical CRM recovery plant. The fixed capital cost estimated using this method is 601 452 €. This is of course a rough estimation but it gives the order of magnitude of what the fixed capital cost could be if the proposed CRMs beneficiation process is ever implemented on site.

### 8.2.2 Revenue

The evaluation of the potential revenue associated with the commercialisation of the heavy minerals concentrate from the St Austell kaolin residues is relatively difficult as it is a rather atypical product. Indeed, it is a polymetallic concentrate (LREE, Sn, Nb, W) with relatively low grades and with no equivalent in the market. The only comparable product is the heavy minerals concentrate sold as a by-product of Beauvoir kaolin which contains cassiterite, columbo-tantalite and microlite. The Beauvoir heavy minerals concentrate is sold on the basis of its Sn and Ta content. Also Nb is present in the concentrates, it is not beneficiated for this type of mineral concentrate (Negroni,

Table 8.2: Estimation of the total investment cost (TIC) for the hypothetical CRM recovery plant.

| Item | Ratio | Item cost (€) | Cumulated cost (€) |
|---|---|---|---|
| *Main Equipment* | | | 182 657 € |
| Installation | 0.4 | 73 063 € | |
| *Equipment (installed cost)* | | | 255 720 € |
| Process piping | 0.1 | 25 572 € | |
| Instrumentation | 0.05 | 12 786 € | |
| Site development | 0.35 | 89 502 € | |
| Auxiliaries | 0.1 | 25 572 € | |
| Outside lines | 0.08 | 20 458 € | |
| *Total plant construction* | | | 429 609 € |
| Engineering | 0.25 | 107 402 € | |
| Contingencies | 0.1 | 42 961 € | |
| Size factor | 0.05 | 21 480 € | |
| *Fixed capital* | | | 601 452 € |

2015). The major parameters that are taken into account to sell the Beauvoir heavy mineral concentrate are (Negroni, 2015):

- The price of tin, given daily and officially by the London Metal Exchange (LME), currently 13 325 US$/tonne (Cash buyer, LME (2015)),
- The price of tantalum which is not officially released, even if some sites provide information or trends, the market remains opaque,
- The concentrate is atypical of conventional tin concentrate and tantalum,
- Metallurgists buy concentrates based on metal content and apply discounts that can split the metals prices by 4 or 5 (Terms of the contracts are confidential),
- The levels of radioactive elements (U, Th), often associated with Ta ore, pose marketing and transportation problems (Class-7 radioactive material) and decreases the market value of the concentrate.

Such parameters are likely to be applicable to the heavy mineral concentrate obtained in this work. However, trying to assess the price of the low grade concentrates obtained in this work appears to be in vain until a higher concentration rate is reached. For instance, typical monazite-rich concentrates are at 50% REO and are sold at an average price of 2-4 US$/kg (Kingsnorth, 2014b). Hence LREE, and all the other metals in general, must be further concentrated (with reasonable recovery) to consider a potential commercialisation. However this could pose some technical feasibility issues at the lab scale (large sample size required to lead to a reasonable primary concentrate size, radioactivity due to monazite) that will be discussed in the perspectives (see Chapter 8).

The production of micaceous residue from the WADM kaolin plant is about 145 000 tonnes per year (Imerys, personal communication). Considering the average CRMs

grades of the micaceous residue obtained in Chapter 3 as representative in first approximation, it is possible to roughly estimate the amount of CRMs which are lost every year in the micaceous residues (Table 8.3). This suggests that around 25 t LREE, 20 t Sn, 14 t Nb and 10 t W are lost every year in the micaceous residue going to waste. Applying a yield of 0.2 for the micaceous residue and a recovery factor of 0.63 for the LREE as suggested by the material balance (Appendix F.1), it is possible to estimate the annual concentrate tonnage and LREE production (Table 8.3). This rough estimation suggests that annual productions could be around 2 393 t/y and 15.5 t/y for the raw pre-concentrate and the LREE respectively. This includes 8.4 t/y Ce, 3.7 t/y La and 3.4 t/y Nd.

Table 8.3: Estimation of the potential CRMs production for the WADM plant only.

| **CRM** | **Residue grade (g/t)** | **Tonnage (t/y)** | **Recovery Factor** | **Concentrate production (t/y)** |
|---|---|---|---|---|
| Raw | - | 145 000 | 0.02 | 2 393 |
| LREE | 168.8 | 24.5 | 0.63 | 15.5 |
| Ce | 91.4 | 13.3 | 0.63 | 8.4 |
| La | 40.0 | 5.8 | 0.63 | 3.7 |
| Nd | 37.3 | 5.4 | 0.63 | 3.4 |
| Sn | 139.4 | 20.2 | ? | ? |
| Nb | 93.7 | 13.6 | ? | ? |
| W | 69.2 | 10.0 | ? | ? |

## 8.3 On the micaceous residue commercial potential

Answering to that question is not an easy task even after all the work performed in the previous (Scott et al., 1998; Shail et al., 2009) and present studies. Table 8.4 summarize all the findings, observations or general conclusions described in this work that are in favour or against an implementation of a CRMs recovery process from micaceous residue and that should be taken into account while attempting to answer to that question.

From a resources point of view, the CRMs grades within the deposit are low, most of them are actually below the suggested cut-off grade for Sn, Nb and W (see Chapter 7). However, the volumes are large and mineralisations disseminated. In addition, the data from the GT53 fraction only account for 53-180 µm fraction of the micaceous residue, which is less enriched than the -53 µm fraction.

Whilst this work has demonstrated that heavy minerals can be recovered and concentrated from the micaceous residue of the WADM plant using a simple processing route with a limited number of operations, the CRM grades are low. The effectiveness of the heavy mineral recovery is accounted to the complexity of the considered material which is low grade, fine grained, contains high proportions of medium density minerals and clay minerals. However, the recovery is relatively higher than those previously obtained, which is encouraging as this was pointed out as the most critical point in the previous studies (Shail et al., 2009).

Table 8.4: Summary of the arguments in favour or against the by-product recovery of CRMs.

| In Favour | Against |
|---|---|
| **Resources** | |
| Large volumes (tailing dams) | Low grade ore |
| Magmatic disseminated mineralisations thorough the kaolin deposits | Most of CRMs grades of the 53-180 m core samples are below the suggested cut-off grade (*i.e.* 100 ppm for Sn, Nb, W) for the gravity concentration route |
| Resources already mined for kaolin | Limited amount of data available |
| **Processing aspects** | |
| No need for additional grinding (CRM-bearing minerals are (partially) liberated) | Low grade material |
| Simple and few separation steps required | Fine grain size distribution of heavy minerals |
| Heavy accessory minerals can effectively be recovered in the gravity concentrate (87 to 98% heavy minerals (SG>2.89)) | High proportion of accessory minerals (tourmaline, micas, topaz) with medium SG close to SG of monazite, rutile |
| High CRMs enrichment ratios (10-60) | High variability of CRMs grades in the micaceous residue |
| Reasonable recovery, at least for LREE (~60%) | Clay rich material (~10% Kaolinite) |
| **Environmental aspects** | |
| Reduce waste production | Material displacement (if historic tailing dams are considered) |
| Potential use for historic tailing dams | |
| Better waste management | |
| Low environmental footprint | |
| Few/No additional energy consumption (Gravity concentration) | |
| Environmental-friendly chemical reagent (Flotation) | |
| **Economic aspects** | |
| No extra mining costs (except if tailing dams are considered) | Atypical concentrate with no equivalent (no reference for the terms of the contract) |
| High market value products (cassiterite, monazite) | Low concentrate grade (<50% REO) |
| Low UCC and TIC (~ 601 452 €) | Multi-metallic concentrate (penalties) |
| Few/No additional energy consumption (low operating cost) | Th negative aspect (storage, transport, marketing) |

From an environmental point of view, only benefits could arise from a potential processing of micaceous residue as the proposed processing route has a low environmental footprint with low energy consumption (gravity concentration) and environmental friendly chemical reagents (dispersion, flotation). In addition processing the micaceous

residue will result in a reduced waste production (and even more if historical tailing dams are considered) and a better waste management (sized wastes).

From an economic point of view the arguments are more balanced. Indeed the obtained concentrate is rather atypical with no equivalent on the market (the Beauvoir heavy mineral concentrate is not sell for LREE) and thus there is no reference for the terms of a potential contract. In addition, for the time being the concentrate grades are low to be considered as a marketable product. Another limitation is the application of penalties due to the presence of several CRMs-bearing minerals that would impaired the value of the concentrate. The more restrictive issue facing potential LREE production is associated with the potential radioactive activity of the concentrate due to the presence of Th in monazite (Zhu et al., 2015). This means that a limitation in terms of LREE concentration should be accepted above which some special dispositions must be taken. The proposed CRMs recovery process requires an initial fixed-capital investment of 601 452 €. The annual income cannot be estimated but an assessment of the annual production for the WADM plant suggests that around 15.5 t/y LREE could be recovered in CRMs pre-concentrates. Although the current concentrate grade is low, the annual tonnage is high and total capital investment is low. With demand for Neodymium (Nd) and Cerium (Ce) expected to grow in the future due to their use in permanent magnets (Kingsnorth, 2014b), micaceous residue beneficiation is probably a worthwhile future investment.

# Chapter 9

# Conclusions and Perspectives

## 9.1 General Conclusion

A metallurgical balance applied on all the output streams of 3 kaolin extraction processes have shown that CRMs are mostly concentrated and distributed in the micaceous residue stream as a consequence of the pre-concentration of the accessory minerals from the host granite in the hydrocyclone underflow. The CRMs grades and distribution patterns vary depending on the source granite and are also likely to be influenced by the degree of kaolinisation of the kaolin ore.

From the 3 investigated locations, treating material from biotite, tourmaline or topaz granite, the micaceous residue from the WADM pant (biotite granite) displays the higher grades with 168.8 ± 8.4 ppm LREE (including 40 ± 2 ppm La, 91.4 ± 4.6 ppm Ce, 37.3 ± 1.9 ppm Nd), 139.4 ± 7 ppm Sn, 93.7 ± 4.7 ppm Nb and 69.2 ± 3.5 ppm W. The distributions of the metals in the plant outputs are less contrasted but the micaceous residue clearly accounts for a major proportion of the mass of metal entering the plant, closely followed by the sand stream and the "product" stream for the LREE only.

The mineralogy of the micaceous residue from biotite granite (WADM plant) is dominated by quartz, unaltered K-feldspar, and micas. Two types of micas are present: biotite (siderophyllite-annite), and muscovite which is less abundant. Tourmaline (schorl-dravite) is the main accessory mineral with rutile and some remaining kaolinite is also present.

The overall CRMs grade increases with decreasing particle size within the micaceous residue. Overall, 95% of LREE, 84% of Sn, 87% of Nb, and 83% of W are present in the size fraction below 100 µm.

A combined statistical/mineralogical approach has allowed highlighting the mineralogical associations and identifying monazite as the only LREE-bearing minerals as well as cassiterite, wolframite and rutile as the major host for Sn, Nb and W respectively. Monazite, rutile and cassiterite are interpreted as magmatic mineralisations which shared mineralogical associations with rutile, tourmaline or micas whereas wolframite which is always found free in the gravity concentrates is believed to have a hydrothermal origin.

Conservation of the LREE ratio from macroscopic (whole rock analyses on residue or core samples) to microscopic scale (*in situ* analyses on monazite grains) indicates

that monazite is the only LREE-bearing mineral within St Austell biotite granite.

A multivariate approach of process variograms have been investigated to address the issue of sampling representativeness when several critical properties must be taken into account as for metallurgical testing. This approach has proven to be a powerful tool when the overall time-variability of process streams must be summarized in terms of a large set of properties. It describes the multivariate aspect of heterogeneity by considering all of the properties of interest instead of focusing on the individual property with the highest variability. This approach provides an opportunity to choose all of the material properties that are critical for given objectives and to use multivariograms as a summarising tool to handle $p$ simultaneous properties.

In the case of the micaceous residue process stream from the WADM plant, most of the variability is due to the LREE concentration on an individual scale, whereas the aforementioned multivariate approach indicates that size distribution is the most important contribution.

A two-stage gravity concentration process involving spiral concentrator and shaking table has been developed for the 53-180 µm fraction of the micaceous residue. Modelling of the influence of the operating parameters of the spiral concentrator through DOE methodology has allowed setting the required operating conditions to achieve the highest heavy minerals recovery, *i.e.* low wash water flow rate (2 Lpm) and low pulp density (15 wt.% solid). Scavenging tests suggest that up to 80% heavy minerals can be recovered in 4 passes. However, mineralogical analysis of the concentrates indicates that middlings are recovered after 3 passes, suggesting that scavenging operations should not be further continued.

Furthermore LREE recoveries show that up to 70% monazite could be recovered in only one pass. Shaking table testing on spiral concentrates shows that heavy mineral concentrate with up to 98.5% heavy minerals can be recovered. However in terms of metals, the concentrate grades are still low for most metals (Sn, Nb and W) with the exception of LREE which reach up to 1.6% LREE grade in shaking table concentrate.

The results suggest that the cut-off grade for Sn, Nb and W should be above 100 ppm and above 60 ppm for LREE. These values are close to the average grades suggested by the various sampling campaigns and point out the critical aspect of metal grades variability in the micaceous residue as one of the major issue if a potential industrial application is to be considered.

The effect of wash water additions and solid pulp density on spiral size recovery curves has been investigated via the DOE methodology. The experimental results suggest that wash water is the most significant factor affecting global recovery. However, wash water addition also impact the partition curve shapes, especially for coarse gangue particles, the recovery of which decreases as the wash water flow rate increases.

A heavy and gangue mineral partition curve model was derived based on regression models that exhibited satisfactory correlation with experimental data. These models show that both heavy and gangue minerals size recovery curves are impacted by wash water variations. More specifically, size recovery ratio curves indicate that a coarse particle decrease and medium particle increase occur with increasing wash water flow rate. The wash water exhibits a more significant impact on the gangue minerals size

recovery curve shape, which is likely due to selective migration phenomenon in secondary flows.

Processing of the fine fraction (-53 µm) of the micaceous residue for monazite recovery has been investigated using Falcon centrifugal separation and froth flotation. Saturation tests performed on Falcon UF shows a positive effect of desliming on separation performance which provides higher LREE grades and recoveries.

The best flotation results on the deslimed -53 µm residue are obtained with sodium oleate and hydroxamate alone with around 3370 ppm and 2500 ppm LREE in the cleaned product respectively. LREE recovery with sodium oleate is very low (30%) but could be increased to 83% with the addition of non-ionic reagent at the expanse of LREE grade which is divided by 2.

The effect of dispersion on separation efficiency has also been investigated. Results show that an effective dispersion of clay minerals is obtained with very low dosage (20 mg/L) using sodium polyacrylate dispersant (Antiprex D). The addition of dispersant allows improving significantly flotation efficiency by eliminating the negative effect of clay-coating. The grade in the floated product obtained with sodium oleate increase from 3370 ppm LREE to 5350 ppm LREE and LREE recovery from 30% to 80% with the addition of dispersant during the desliming step.

Comparison of the performance of flotation and Falcon UF concentration of monazite to previous results obtained with Falcon SB on the unsized raw residue clearly shows that flotation of the fine residue is most efficient than Falcon UF and Falcon SB concentration.

Direct treatment of the unsized material by Falcon SB gives very high enrichment ratios (32-56) but the recoveries are low. The beneficiation of sized material with a separate gravity route for the 53-180 µm fraction and combined flotation/gravity route for the -53 µm allow obtaining better recoveries. This shows the benefit of treating different size-fractions of the residue with dedicated processing routes.

Inexpensive methods have been developed to calibrate metal grades of the 53-180 µm fraction core sample database. Comparison with ICP analyses shows that rare-metals XRF analyses (Sn, Nb and W) grades are underestimated but could be calibrated using linear regression models whereas LREE XRF grades are seriously biased and display no correlation with ICP results. A PLS regression applied to some major and trace XRF analyses allowed to predict the LREE grade accurately with satisfactory validation results ($R^2 = 0.88$).

Pilot scale tests using 53-180 µm micaceous residue samples suggest that spiral performance in terms of LREE grade, recovery and enrichment could be predicted as a function of LREE feed grade. Even if particle size distribution of the feed material is likely to influence spiral separation performance, results show that for the investigated high kaolin grade sample the variation of particle size distribution is rather limited and does not seem to affect the separation if the operating parameters are maintained fixed.

An illustration of potential application of the aforementioned models to core sample data is shown. It allows targeting potential zones of interest for CRMs recovery as by product of kaolin production.

## 9.2 Perspectives

The following section provides a list of bullet points for recommended future work on the different aspects of CRMs by-product potentiality evaluation that have been investigated in this work.

*Processing*

One of the most detrimental results is the low CRMs grade of the heavy minerals concentrates obtained in this work. To address this issue the following could be recommended:

- Performing tests on non-depleted residue samples with CRMs grades above the suggested cut-off,
- Gravity concentrate: The previous studies have shown that higher grades could be obtained with fine gravity separators such as Mozley table or Multi-Gravity Separator (MGS). Since the low recoveries obtained in the previous works were accounted to the primary gravity concentration stages (Shail et al., 2009), which is not the case in the developed process using a spiral for preliminary concentration, the use of these techniques to improve the grade of the gravity concentrate should be investigated,
- Flotation concentrate: The flotation results display high recoveries (>80% for LREE) and enrichment ratios (>10 for LREE) with a two-stage operation. Hence the use of additional cleaning stages should be investigated.

One other detrimental aspect is the fact that all metals are concentrated together in the gravity concentrate. Separation of CRMs from each other should also be investigated using the following techniques:

- High and/or medium intensity magnetic separation to take advantage of the paramagnetic properties of monazite and wolframite followed by a specific flotation route,
- Electrostatic separation to recover cassiterite.

Other difficulties linked with the processing of the primary concentrate is the need for very large micaceous residue samples as the obtained primary concentrate from the low grade residue are small in size (about few grams to a hundred grams). Finally, as monazite concentration rate will increase, Th content and thus radioactivity of the concentrate will increase too which, after a certain concentration rate, will require safety measures and dedicated facilities. Hence the determination of the required and maximum LREE grade to achieve must be considered prior to any processing of the primary concentrate.

*Long-term variability of micaceous residue properties*

The results from the variographic analysis suggest a low frequency phenomenon with a period of approximately 23-25 lags whereas the data only contains 50 lags.

Hence the estimation of the sill values and length of periods is uncertain. To confirm this phenomenon, the length of the variographic experiment should be extended over 3 work shifts (6-9 h). In addition the low grades of the large sample collected for metallurgical testing relative to the weekly sample suggest an important long-term variability of metal contents in the micaceous residue stream which should also be assessed by performing a variographic study at a larger scale (weeks or months).

*Combining multivariogram with DOE*

Even when choosing carefully the properties of interest for the process tested to avoid unnecessary variance increase, and combining multivariogram with PCA analysis, the required number of increments to sample for metallurgical testing is high. Hence there is a need to reduce the sampling variance further. In particular, some properties which contribute to a major proportion of the global (multivariate) variability could potentially be less important for the process tested than other properties having a lower variability. To address this issue, one could try to combine the multivariogram approach with DOE methodology. Indeed, considering the case where a separation performance could be linked to the material properties (independent variables) through the heterogeneity vector $H$ by simple linear models such as:

$$Y = H \cdot A \tag{9.1}$$

where $Y$ is a matrix containing the process responses/performance indexes (recovery, grade) and $A$ is the matrix containing the coefficients of each model obtained using the DOE methodology, which can be seen in this case as a "weights matrix". The multivariogram of $Y$ can be expressed as:

$$V_{Y_j} = \frac{1}{2(N-j)} \sum_{i=1}^{N-j} (Y_i - Y_{i+j}) M (Y_i - Y_{i+j})^t, \quad j = 1, \ldots, N/2 \tag{9.2}$$

where $M$ is the Mahalanobis metric (MD) defined as the inverse of the variance-covariance matrix of $Y$. Using the relationship defined in Equation (9.1), it follows:

$$V_{Y_j} = \frac{1}{2(N-j)} \sum_{i=1}^{N-j} (H_i - H_{i+j}) A M A^t (H_i - H_{i+j})^t, \quad j = 1, \ldots, N/2 \tag{9.3}$$

where

$$M = [Cov(Y)]^{-1} = [Cov(H \cdot A)]^{-1} = A^{-1} [Cov(H)]^{-1} \tag{9.4}$$

leading to

$$V_{Y_j} = \frac{1}{2(N-j)} \sum_{i=1}^{N-j} (H_i - H_{i+j}) A A^{-1} [Cov(H)]^{-1} A^t (H_i - H_{i+j})^t, \quad j = 1, \ldots, N/2$$

$$V_{Y_j} = \frac{1}{2(N-j)} \sum_{i=1}^{N-j} (H_i - H_{i+j}) [Cov(H)]^{-1} A^t (H_i - H_{i+j})^t, \quad j = 1, \ldots, N/2 \tag{9.5}$$

The last expression of the multivariogram of $Y$ actually corresponds to the multivariogram of $H$ with a new metric $M'$, corresponding to MD metric weighted by the matrix $A^t$:

$$V_Y = V_H, \text{with } M' = [Cov(H)]^{-1} A^t \tag{9.6}$$

This new metric could potentially lead to a reduction of the overall variance suggested by the multivariogram as the individual variability contribution of each property will be weighted according to their importance/significance for the responses of the process.

*Geometallurgy*

The obtained regression models for trace elements grade calibration are promising. However the potential of these results worth to perform more analyses on core samples to complete the models validation.

For XRF data calibration, collection of an independent test set of core samples (about 30 samples) would allow validating the regression models using proper validation. Indeed cross validation is only a simulation of the ideal test set validation and can never be a complete alternative (Esbensen et al., 2002). In addition, a second data set (test/validation set) is critically necessary for the inclusion of the sampling errors incurred in all 'future' situations in which the validated model must perform (Esbensen and Geladi, 2010). The validated models could then be used as external calibration models for the whole XRF database from Melbur-Virginia and Wheal-Remfry pits. To apply this methodology to other kaolin deposits, covering other granite types, it will be necessary to repeat the work realised for biotite granite at least for each granite type, as results of XRF analysis are sensible to matrix effects.

Regarding the development of process prediction models, the results need to be confirmed by comparing the results predicted with those obtained after processing the micaceous residue samples which were collected when treating a block/ore for which the GT53 grades are known. This may be very difficult for several technical reasons including ore traceability, contamination, large sample collection, etc. In most geometallurgical approaches, process performance prediction models are built using production data comprising a large dataset collected after months of production.

Hence implementation on site of a primary concentration process (spiral concentrators for instance) seems to be the next logical step. Indeed, it would give the opportunity to collect enough data for developing similar process performance prediction models and could also allow assessing the effect of the ore variability in terms of CRMs grades, alteration grade and lithology (granite type) which is fundamental for the development of a proper geometallurgical model. In addition, it would allow recovering directly some primary concentrate samples for metallurgical testing, therefore removing the need for large residue samples collection.

# Bibliography


Abela, R. L. (1997). Centrifugal concentrators in gold recovery and coal processing. *Extraction Metallurgy Africa*.

Abzalov, M. (2013). Representativiness of bulk samples. In Beniscelli, J., Felipe Costa, J., Domínguez, O., Duggan, S., Esbensen, K., Lyman, G., and Sanfurgo, B., editors, *Proceedings of the 6th World Conference on Sampling and Blending*, pages 257–264, Lima.

Alderton, D., Pearce, J., and Potts, P. (1980). Rare earth element mobility during granite alteration: Evidence from southwest England. *Earth and Planetary Science Letters*, 49(1):149–165.

Alderton, D. and Rankin, A. H. (1983). The character and evolution of hydrothermal fluids associated with the kaolinized St. Austell granite, SW England. *Journal of the Geological Society*, 140(2):297–309.

Allminerall (2015). Allmineral products brochure. http://www.allmineral.com/gb/download/productinfos/allmineral_productinfo_gb.pdf. Last accessed: 2015-11-21.

Ancia, P., Frenay, J., and Dandois, P. (1997). Comparison of Knelson and Falcon centrifugal separators. In Mozeley, R., editor, *Innovation in Physical Separation Technologies*, pages 53 – 62, Falmouth, UK.

Angadi, S., Sreenivas, T., Jeon, H.-S., Baek, S.-H., and Mishra, B. (2015). A review of cassiterite beneficiation fundamentals and plant practices. *Minerals Engineering*, 70:178–200.

Anthony, J. W., Bideaux, R. A., W., K., Bladh, and Nichols, M. C. (2001). *Handbook of mineralogy*, volume 10. Mineralogical Society of America, Chantilly, VA, USA.

Arnold, B. and Aplan, F. (1986). The effect of clay slimes on coal flotation, part I: The nature of the clay. *International Journal of Mineral Processing*, 17(3-4):225–242.

Atasoy, Y. and Spottiswood, D. (1995). A study of particle separation in a spiral concentrator. *Minerals Engineering*, 8(10):1197–1208.

Ayanda, O. and Adekola, F. (2011). A review of niobium-tantalum separation in hydrometallurgy. *Journal of Minerals and Materials Characterization and Engineering*, 10(3):245–256.

Barbery, G. (1983). Engineering Aspects of Flotation in the Minerals Industry: Flotation Machines, Circuits and their Simulation. In Ives, K. J., editor, *Scientific Basis of Flotation*, pages 289–348. Springer Netherlands, Cambridge, UK.

Barsky, E. and Barsky, M. (2006). *Cascade separation of powders*. Cambridge International Science Publishing, Cambridge, UK.

Bazin, C., Sadeghi, M., Bourassa, M., Roy, P., Lavoie, F., Cataford, D., Rochefort, C., and Gosselin, C. (2014). Size recovery curves of minerals in industrial spirals for processing iron oxide ores. *Minerals Engineering*, 65:115–123.

Belkasmi, M., Cuney, M., Pollard, P., and Bastoul, A. (2000). Chemistry of the Ta-Nb-Sn-W oxide minerals from the Yichun rare metal granite (SE China): genetic implications and comparison with Moroccan and French Hercynian examples. *Mineralogical Magazine*, 64(3):507–523.

Binnemans, K., Jones, P. T., Blanpain, B., Van Gerven, T., and Pontikes, Y. (2015). Towards zero-waste valorisation of rare-earth-containing industrial process residues: a critical review. *Journal of Cleaner Production*, 99:17–38.

Bo, Q., Dan, F., Tao, S., Xudong, Z., Jie, Z., Chongjie, Z., Kun, L., Xiaoyang, L., Yuzhu, Y., Qiang, L. Y., Jiawei, H., Shaodong, W., Lin, B., Guo, J. S. Y., and Joan, K. (2011). Method for recovering tin by centrifugal concentration. Pantent N° CN102172560 A, China.

Boisvert, J. B., Rossi, M. E., Ehrig, K., and Deutsch, C. V. (2013). Geometallurgical Modeling at Olympic Dam Mine, South Australia. *Mathematical Geosciences*, 45(8):901–925.

Bose, D. K. and Gupta, C. K. (2002). Extractive Metallurgy of Tantalum. *Mineral Processing and Extractive Metallurgy Review*, 22(4-6):389–412.

Boucher, D., Deng, Z., Leadbeater, T., Langlois, R., Renaud, M., and Waters, K. E. (2014). PEPT studies of heavy particle flow within a spiral concentrator. *Minerals Engineering*, 62:120–128.

Bourgault, G. and Marcotte, D. (1991). Multivariable variogram and its application to the linear model of coregionalization. *Mathematical Geology*, 23(7):899–928.

Bourgault, G., Marcotte, D., and Legendre, P. (1992). The multivariate (co)variogram as a spatial weighting function in classification methods. *Mathematical Geology*, 24(5):463–478.

Bray, C. J. and Spooner, E. T. C. (1983). Sheeted vein Sn-W mineralization and greisenization associated with economic kaolinization, Goonbarrow china clay pit, St. Austell, Cornwall, England: geologic relationships and geochronology. *Economic Geology*, 78(6):1064–1089.

Breiter, K., Škoda, R., and Uher, P. (2007). Nb-Ta-Ti-W-Sn-oxide minerals as indicators of a peraluminous P- and F-rich granitic system evolution: Podlesí, Czech Republic. *Mineralogy and Petrology*, 91(3-4):225–248.

BRGM (2011). Mineral deposits of Europe. http://promine.gtk.fi/main_mineral_deposits_of_europa.pdf. Last accessed: 2015-10-21.

British Geological Survey (1997). Mineral Resources map for Cornwall. Technical report, British Geological Survey.

Bruker (2015). S2 RANGER user manual. Technical report, Bruker AXS Microanalysis GmbH, Berlin, Germany.

Bulatovic, S. M. (2010). Flotation of Tantalum/Niobium Ores. In *Handbook of Flotation Reagents: Chemistry, Theory and Practice*, chapter 23, pages 127–149.

Buonvino, M. (1993). *A study of the Falcon concentrator*. Phd thesis, McGill University.

Burt, R. (1984a). Cornish tin processing. In Fuerstenau, D., editor, *Gravity concentration technology*, chapter 26, pages 193–504. Elsevier Science Publishers, New York, NY.

Burt, R. (1984b). *Gravity Concentration Technology*. Developments in mineral processing. Elsevier Science Publishers, New York, NY.

Burt, R. (1984c). The treatment of tungsten ores. In Fuerstenau, D., editor, *Gravity concentration technology*, chapter 28, pages 521–533. Elsevier Science Publishers, New York, NY.

Burt, R. (1988). A review of gravity concentration techniques for processing fines. In The Canadian Institute of Mining and Metallurgy, editor, *Proceedings of the International Symposium on the Production and Processing of Fine Particles*, pages 375–385, Montreal. Elsevier Science Publishers.

Burt, R. (1999). The role of gravity concentration in modern processing plants. *Minerals Engineering*, 12(11):1291–1300.

Burt, R. (2000). Gravity Concentration. In *Ullmann's Encyclopedia of Industrial Chemistry*, pages 11275–11282. Wiley-VCH Verlag GmbH & Co. KGaA, Weinheim, Germany.

Burt, R., Korinek, G., Young, S., and Deveau, C. (1995). Ultrafine tantalum recovery strategies. *Minerals Engineering*, 8(8):859–870.

Burt, R. and Ottley, D. J. (1974). Fine gravity concentration using the Bartles-Mozley concentrator. *International Journal of Mineral Processing*, 1(4):347–366.

Camm, G. and Dominy, S. (1999). Tin Mineralization and Structure at Treliver, St. Austell, mid-Cornwall. *Geoscience in South West England*, 9(4):370–373.

Camm, G. and Moon, C. J. (2001). Surficial geochemical signatures of tin and tungsten deposits north of the St. Austell Granite. *Geoscience in South West England*, 10(2):215–220.

Carignan, J., Hild, P., Mevelle, G., Morel, J., and Yeghicheyan, D. (2001). Routine Analyses of Trace Elements in Geological Samples using Flow Injection and Low Pressure On-Line Liquid Chromatography Coupled to ICP-MS: A Study of Geochemical Reference Materials BR, DR-N, UB-N, AN-G and GH. *Geostandards and Geoanalytical Research*, 25(2-3):187–198.

Caspeo (2013). UsimPac Reference Guide. Technical report.

Černý, P., Blevin, P., Cuney, M., and London, D. (2005). Granite-Related Ore Deposits. In Hedenquist, J. W., Thompson, J. F. H., Goldfarb, R. J., and Richards, J. P., editors, *Economic geology 100th Anniversary Volume*, chapter 11, pages 337–370. Littleton, Colorado.

Chan, B., Mozley, R., and Childs, G. (1991). Extended trials with the high tonnage multi-gravity separator. *Minerals Engineering*, 4(3-4):489–496.

Chelgani, S. C., Rudolph, M., Leistner, T., Gutzmer, J., and Peuker, U. A. (2015). A review of rare earth minerals flotation: Monazite and xenotime. *International Journal of Mining Science and Technology*, 25(6):877–883.

Chen, Z. (2011). Global rare earth resources and scenarios of future rare earth industry. *Journal of Rare Earths*, 29(1):1–6.

Cheng, T.-W., Holtham, P., and Tran, T. (1993). Froth flotation of monazite and xenotime. *Minerals Engineering*, 6(4):341–351.

Christian, J., Singh Gaur, R., Wolfe, T., and Trasorras, J. R. (2011). Tungsten Chemicals and their Applications. Technical report, International Tungsten Industry Association, Towanda, PA, USA.

Clemente, D., Newling, P., Botelho de Sousa, A., LeJeune, G., Barber, S., and Tucker, P. (1993). Reprocessing slimes tailings from a tungsten mine. *Minerals Engineering*, 6(8-10):831–839.

Committee on Critical Mineral Impacts of the US Economy (2008). Minerals, critical minerals, and the US economy. Technical report, Washington.

Cuney, M., Marignac, C., and Weisbrod, A. (1992). The Beauvoir topaz-lepidolite albite granite (Massif Central, France): the disseminated magmatic Sn-Li-Ta-Nb-Be mineralization. *Economic Geology*, 87(7):1766–1794.

De Cuyper, J. and Delwasse, A. (1999). *Métallurgie et recyclage de l'étain*. Techniques de l'Ingénieur, Paris.

De Maesschalck, R., Jouan-Rimbaud, D., and Massart, D. (2000). The Mahalanobis distance. *Chemometrics and Intelligent Laboratory Systems*, 50(1):1–18.

Deister (2015). Deister shaking tables brochure. http://www.deisterconcentrator.com/pdf/tables.pdf. Last accessed: 2015-11-20.

Del Giudice, G. R. M. (1934). A Study of Slime-coatings in Flotation. *Transactions of the Society of Mining Engineers of AIME*, 112:398–410.

Deveau, C. (2006). Improving fine particle gravity recovery through equipment behavior modification. In *38th Annual Meeting of the Canadian Mineral Processors, Paper*, volume 31, pages 501–517.

Dixit, P., Tiwari, R., Mukherjee, A. K., and Banerjee, P. K. (2015). Application of response surface methodology for modeling and optimization of spiral separator for processing of iron ore slime. *Powder Technology*, 275:105–112.

Dreyer, J. (1976). Note: The development of AGIT AIR flotation machines. *Journal of the South African Institute of Mining and Metallurgy*, 26(11):445–447.

Eriez (2012). DensitySort, Sorts Nonferrous "Fines" By Gravity. http://en-us.eriez.com. Last accessed: 2015-11-21.

Esbensen, K. H. and Geladi, P. (2010). Principles of proper validation: Use and abuse of re-sampling for validation. *Journal of Chemometrics*, 24(3-4):168–187.

Esbensen, K. H., Guyot, D., Westad, F., and Houmoller, L. P. (2002). *Multivariate Data Analysis - in Practice: An Introduction to Multivariate Data Analysis and Experimental Design*. CAMO AS, Oslo, 5th edition.

Esbensen, K. H., Paoletti, C., and Minkkinen, P. O. (2012). Representative sampling of large kernel lots I. Theory of Sampling and variographic analysis. *TrAC Trends in Analytical Chemistry*, 32:154–164.

EU (2015). Stoicism website. http://www.stoicism.eu/. Last accessed: 2015-10-18.

European Commission (2008). The raw materials initiative–meeting our critical needs for growth and jobs in Europe. Communication from the Commission to the European Parliament and the Council, COM (2008) 699. Technical report.

European Commission (2010). Critical raw materials for the EU. Report of the Ad-hoc Working Group on Definning Critical Raw Materials. Technical report, European Commission.

European Commission (2014). Report on Critical Raw Materials for the EU, Report of the Ad hoc Working Group on defining critical raw materials. Technical Report May, European Comision, DG Enterprise and Industry, Brussels.

Falcon, L. (1982). The Gravity Recovery of Cassiterite. *Journal Of The South African Institute Of Mining And Metallurgy*, 82(4):112–117.

Falcon Concentrators Inc. (2007). FALCON L40 operations and maintenance manual. Technical report.

Falconer, A. (2003). Gravity Separation: Old Technique/New Methods. *Physical Separation in Science and Engineering*, 12(1):31–48.

Farrokhpay, S. and Bradshaw, D. (2012). Effect of clay minerals on froth stability in mineral flotation: a review. In *26th International Mineral Processing Congress, IMPC 2012: Innovative Processing for Sustainable Growth - Conference Proceedings*, pages 4601–4611, New Delhi, India. Technowrites.

Ferron, C. J., Bulatovic, S. M., and Salter, R. S. (1991). Beneficiation of rare earth oxide minerals. In *Materials Science Forum*, volume 70, pages 251–270. Trans Tech Publ.

Fetherston, J. (2004). *Tantalum in Western Australia, Mineral Resources*. Geological Survey of Western Australia, Bulletin 22, Perth, WA.

Fields, R. and Bally, P. (1967). Beneficiation of tantalum-and columbium-bearing tin slags. Patent N° US3300297 A, United States.

Filippova, I., Filippov, L. O., Duverger, A., and Severov, V. (2014). Synergetic effect of a mixture of anionic and nonionic reagents: Ca mineral contrast separation by flotation at neutral pH. *Minerals Engineering*, 66-68:135–144.

Floyd, P., Exley, C., and Styles, M. (1993). *Igneous Rocks of South-West England*. Springer Science & Business Media, London.

FLSmidth (2015). FLSmidth Knelson's website. http://www.flsmidth.com/en-US/About+FLSmidth/Our+History/Our+Product+Brands/Knelson. Last accessed: 2015-11-19.

François-Bongarçon, D. (2004). Theory of sampling and geostatistics: an intimate link. *Chemometrics and Intelligent Laboratory Systems*, 74(1):143–148.

Fuerstenau, M. C., Harper, R. W., and Miller, J. (1970). Hydroxamate vs. fatty-acid flotation of iron oxide. *Transactions of the Society of Mining Engineers of AIME*, 247(1):69–73.

Fuerstenau, M. C., Miller, J., and Gutierrez, G. (1967). Selective flotation of iron oxide. *Transactions of the Society of Mining Engineers of AIME*, 238:200–203.

Fuerstenau, M. C. and Somasundaran, P. (2003). Flotation Machines. In Fuerstenau, M. C. and Han, K. N., editors, *Principles of Mineral Processing*, pages 292–307. Society for Mining, Metallurgy, and Exploration.

Gekko (2015). Inline pressure jig website. http://www.gekkos.com/equipment/inline-pressure-jig. Last accessed: 2015-11-20.

Genc, A. M., Kilickaplan, I., and Laskowski, J. S. (2012). Effect of pulp rheology on flotation of nickel sulphide ore with fibrous gangue particles. *Canadian Metallurgical Quarterly*, 51(4):368–375.

Gibson, C., Kelebek, S., and Aghamirian, M. (2015). Niobium oxide mineral flotation: A review of relevant literature and the current state of industrial operations. *International Journal of Mineral Processing*, 137:82–97.

Golev, A., Scott, M., Erskine, P. D., Ali, S. H., and Ballantyne, G. R. (2014). Rare earths supply chains: Current status, constraints and opportunities. *Resources Policy*, 41:52–59.

Gorain, B., Franzidis, J.-P., and Manlapig, E. (1995). Studies on impeller type, impeller speed and air flow rate in an industrial scale flotation cell — Part 1: Effect on bubble size distribution. *Minerals Engineering*, 8(6):615–635.

Goupy, J. and Creighton, L. (2007). *Introduction to Design of Experiments with JMP Examples*. SAS Publishing, Cary, NC, USA, 3rd edition.

Gupta, C. K. and Krishnamurthy, N. (2004). *Extractive metallurgy of rare earths*. CRC Press, Boca Raton.

Gy, P. (1971). *L'Echantillonnage des Minerais en Vrac*. Revue de l'Industrie Minérale, St Etienne.

Gy, P. (1992). *Sampling of Heterogeneous and Dynamic Material Systems: Theories of Heterogeneity, Sampling and Homogenizing*. Elsevier, Amsterdam.

Gy, P. (1998). *Sampling for Analytical Purposes*. John Wiley & Sons, Chichester, UK, 1st edition.

Gy, P. (2004a). Sampling of discrete materials. *Chemometrics and Intelligent Laboratory Systems*, 74(1):39–47.

Gy, P. (2004b). Sampling of discrete materials II. Quantitative approach—sampling of zero-dimensional objects. *Chemometrics and Intelligent Laboratory Systems*, 74(1):25–38.

Gy, P. (2004c). Sampling of discrete materials—a new introduction to the theory of sampling I. Qualitative approach. *Chemometrics and Intelligent Laboratory Systems*, 74(1):7–24.

He, M., Wang, Y., and Forssberg, E. (2004). Slurry rheology in wet ultrafine grinding of industrial minerals: a review. *Powder Technology*, 147(1-3):94–112.

Heikka, R. and Minkkinen, P. O. (1997). Comparison of some methods to estimate the limiting value of the variogram, vh(j), for the sampling interval j=0 in sampling error estimation. *Analytica Chimica Acta*, 346(3):277–283.

Hiemenz, P. C. and Rajagopalan, R. (1997). *Principles of Colloid and Surface Chemistry*, volume 14. CRC press, New York, 3rd edition.

Highley, D., Brown, T., Harrison, D. J., Lusty, P., Cameron, D., and Cowley, J. (2009). Mineral Planning Factsheet: kaolin. Technical report, British Geological Survey, Nottingham.

Hill, P. and Manning, D. (1987). Multiple intrusions and pervasive hydrothermal alteration in the St Austell Granite, Cornwall. *Proceedings of the Ussher Society*, 6(4):447–453.

Holl, C. and Bromley, A. (1988). Application of mineralogy to the beneficiation of a tin-sulphide ore. *Minerals Engineering*, 1(1):19–30.

Holland-Batt, A. and Holtham, P. (1991). Particle and fluid motion on spiral separators. *Minerals Engineering*, 4(3-4):457–482.

Holman Wilfley Ltd. (2014). Products - Holman Wilfley Shaking Tables for Metal and Mineral Separation. http://www.holmanwilfley.co.uk/shaking-table-products.htm. Last accessed: 2015-10-29.

Holmes, R. J. (2004). Correct sampling and measurement—the foundation of accurate metallurgical accounting. *Chemometrics and Intelligent Laboratory Systems*, 74(1):71–83.

Holtham, P. (1990). Flow visualisation of secondary currents on spiral separators. *Minerals Engineering*, 3(3-4):279–286.

Holtham, P. (1992a). Particle transport in gravity concentrators and the Bagnold effect. *Minerals Engineering*, 5(2):205–221.

Holtham, P. (1992b). Primary and secondary fluid velocities on spiral separators. *Minerals Engineering*, 5(1):79–91.

Honaker, R., Jain, M., Parekh, B., and Saracoglu, M. (2007). Ultrafine coal cleaning using spiral concentrators. *Minerals Engineering*, 20(14):1315–1319.

Honaker, R., Wang, D., and Ho, K. (1996). Application of the Falcon Concentrator for fine coal cleaning. *Minerals Engineering*, 9(11):1143–1156.

Houot, R. (1982). Beneficiation of phosphatic ores through flotation: Review of industrial applications and potential developments. *International Journal of Mineral Processing*, 9(4):353–384.

Hwang, S. I., Lee, K. P., Lee, D. S., and Powers, S. E. (2002). Models for estimating soil particle-size distributions. *Soil Science Society of America Journal*, 66(4):1143–1150.

Hyma, D. and Meech, J. (1989). Preliminary tests to improve the iron recovery from the -212 micron fraction of new spiral feed at Quebec Cartier mining company. *Minerals Engineering*, 2(4):481–488.

Imerys Ltd (2008). Dry mining of china clay. *CFI – Ceramic Forum International/Ber. der DKG*, 85(9):67–69.

Ito, S., Yotsumoto, H., and Sakamoto, H. (1991). Magnetic Separation of Monazite and Xenotime. *Materials Science Forum*, 70-72:279–300.

ITRI (2010). Tin Use, International Tin Research Institute (ITRI) website. https://www.itri.co.uk/index.php?option=com_zoo&task=item&item_id=9&Itemid=65. Last accessed: 2015-11-30.

Jackson, N. J., Willis-Richards, J., Manning, D., and Sams, M. S. (1989). Evolution of the Cornubian ore field, Southwest England; Part II, Mineral deposits and ore-forming processes. *Economic Geology*, 84(5):1101–1133.

Jakhu, M. R. and Ray, S. (1996). Degana tungsten project—present plant practice and future scenario. *Bulletin of Materials Science*, 19(2):313–329.

Jébrak, M. and Marcoux, É. (2008). *Géologie des ressources minérales*. Ministère des Ressources Minérales et Faune du Québec.

Jefferies, N. (1985). The distribution of the rare earth elements within the Carnmenellis Pluton, Cornwall. *Mineralogical Magazine*, 49(4):495–504.

Johnson, L. J., Chu, C. H., and Hussey, G. A. (1985). Quantitative clay mineral analysis using simultaneous linear equations. *Clays and Clay Minerals*, 33(2):107–117.

Johnson, N. L. and Kotz, S. (1994). Continuous Univariate Distributions. In *Discrete Distributions*, chapter 12, pages 25–26. John Wiley & Sons, 2nd edition.

Jolliffe, I. T. (2002). *Principal Component Analysis*. Springer-Verlag, New York.

Jordens, A., Cheng, Y. P., and Waters, K. E. (2013). A review of the beneficiation of rare earth element bearing minerals. *Minerals Engineering*, 41:97–114.

Jordens, A., Sheridan, R. S., Rowson, N. A., and Waters, K. E. (2014). Processing a rare earth mineral deposit using gravity and magnetic separation. *Minerals Engineering*, 62:9–18.

Jorjani, E., Barkhordari, H., Tayebi Khorami, M., and Fazeli, A. (2011). Effects of aluminosilicate minerals on copper–molybdenum flotation from Sarcheshmeh porphyry ores. *Minerals Engineering*, 24(8):754–759.

Kapur, P. C. and Meloy, T. P. (1999). Industrial modeling of spirals for optimal configuration and design: spiral geometry, fluid flow and forces on particles. *Powder Technology*, 102(3):244–252.

Kardanpour, Z., Jacobsen, O. S., and Esbensen, K. H. (2014). Soil heterogeneity characterization using PCA (Xvariogram) - Multivariate analysis of spatial signatures for optimal sampling purposes. *Chemometrics and Intelligent Laboratory Systems*, 136:24–35.

Kerry, R. and Oliver, M. A. (2003). Variograms of Ancillary Data to Aid Sampling for Soil Surveys. *Precision Agriculture*, 4(3):261–278.

Kingsnorth, D. J. (2014a). Personnal communication.

Kingsnorth, D. J. (2014b). Rare Earths Supply & Demand to 2020: Opportunities for Australia & France. In *France-Australia Rare Earths workshop*, Perth, Australia.

Klimpel, R. (1999). The selection of wet grinding chemical additives based on slurry rheology control. *Powder Technology*, 105(1-3):430–435.

Koch, I. (2013). *Analysis of Multivariate and High-Dimensional Data*. Cambridge University Press., Cambridge.

Kroll-Rabotin, J.-S. (2010). *Analyse physique et modélisation de la séparation centrifuge de particules ultrafies en film fluant: application au séparateur industriel Falcon*. Phd thesis, Université de Toulouse.

Kroll-Rabotin, J.-S., Bourgeois, F., and Climent, É. (2010). Fluid dynamics based modelling of the Falcon concentrator for ultrafine particle beneficiation. *Minerals Engineering*, 23(4):313–320.

Kroll-Rabotin, J.-S., Bourgeois, F., and Climent, É. (2012). Experimental validation of a fluid dynamics based model of the UF Falcon concentrator in the ultrafine range. *Separation and Purification Technology*, 92:129–135.

Kroll-Rabotin, J.-S., Bourgeois, F., and Climent, É. (2013). Physical analysis and modeling of the Falcon concentrator for beneficiation of ultrafine particles. *International Journal of Mineral Processing*, 121:39–50.

Kumari, A., Panda, R., Jha, M. K., Kumar, J. R., and Lee, J. Y. (2015). Process development to recover rare earth metals from monazite mineral: A review. *Minerals Engineering*, 79:102–115.

Lach, P., Mercadier, J., Dubessy, J., Boiron, M.-C., and Cuney, M. (2013). In Situ Quantitative Measurement of Rare Earth Elements in Uranium Oxides by Laser Ablation-Inductively Coupled Plasma-Mass Spectrometry. *Geostandards and Geoanalytical Research*, 37(3):277–296.

Lagaly, G. (1989). Principles of flow of kaolin and bentonite dispersions. *Applied Clay Science*, 4(2):105–123.

Lamberg, P. (2011). Particles – the bridge between geology and metallurgy. In *Proceedings of the Conference in mineral engineering*, pages 1–16, Luleå.

Laplante, A. R. (1993). A comparative study of two centrifugal concentrators. In *Canadian Mineral Processors' Conference*, Ottawa, Canada.

Laplante, A. R. (1997). Validation of a Falcon model with a synthetic ore. *Canadian Metallurgical Quarterly*, 36(I):7–13.

Laplante, A. R., Buonvino, M., Veltmeyer, A., Robitaille, J., and Naud, G. (1994). A Study of the Falcon Concentrator. *Canadian Metallurgical Quarterly*, 33(4):279–288.

Laznicka, P. (2006). Future metal supplies. In *Giant Metallic Deposits*, pages 15–29. Springer, Berlin, Heidelberg.

Lepetic, V. M. (1987). Cassiterite flotation: a review. In Somasundaran, P., editor, *Advances in Mineral Processing: A Half-century of Progress in Application of Theory to Practice : Proceedings of a Symposium Honoring Nathaniel Arbiter on His 75th Birthday*, chapter 19, pages 343–350. SME Inc., New Orleans, Louisiana.

Lessard, J., de Bakker, J., and McHugh, L. (2014). Development of ore sorting and its impact on mineral processing economics. *Minerals Engineering*, 65:88–97.

Linnen, R. and Cuney, M. (2005). Granite-related rare-element deposits and experimental constraints on Ta-Nb-W-Sn-Zr-Hf mineralization. *Rare-Element Geochemistry and Mineral Deposits*, pages 45–68.

LME (2015). London Metal Exchange: Tin. http://www.lme.com/metals/non-ferrous/tin. Last accessed: 2016-01-20.

Long, K. R., Bradley S., V. G., Nora K., F., and Daniel, C. (2010). The Principal Rare Earth Elements Deposits of the United States - A Summary of Domestic Deposits and a Global Perspective. Technical Report 5220, US Geological Survey, Reston, Virginia, USA.

Longerich, H., Jackson, S., and Günther, D. (1996). Inter-laboratory note. Laser ablation inductively coupled plasma mass spectrometric transient signal data acquisition and analyte concentration calculation. *Journal of Analytical Atomic Spectrometry*, 11:899–904.

Luttrell, G. H., Honaker, R., and Phillips, D. (1995). Enhanced Gravity Separators: New Alternatives for Fine Coal Cleaning. In *12th International Coal Preparation Conference*, pages 281–292.

Lynas Corporation Ltd. (2010). Will there be sufficient rare earths to meet demand from clean energy technology? In *Presentation at International Minor Metals Conference*, London.

Majumder, A. K. and Barnwal, J. P. (2006). Modeling of enhanced gravity concentrators - Present status. *Mineral Processing and Extractive Metallurgy Review*, 27(1):61–86.

Manning, D. and Exley, C. (1984). The origins of late-stage rocks in the St Austell granite - a re-interpretation. *Journal of the Geological Society*, 141(3):581–591.

Manning, D. and Hill, P. (1990). The petrogenetic and metallogenetic significance of topaz granite from the southwest England orefield. *Geological Society of America Special Papers*, 246:51–70.

Manning, D., Hill, P., and Howe, J. (1996). Primary lithological variation in the kaolinized St Austell Granite, Cornwall, England. *Journal of the Geological Society*, 153(6):827–838.

Manser, R., Barley, R., and Wills, B. A. (1991). The shaking table concentrator — The influence of operating conditions and table parameters on mineral separation — The development of a mathematical model for normal operating conditions. *Minerals Engineering*, 4(3-4):369–381.

Marques, D. M. and Costa, J. F. C. (2014). Choosing a proper sampling interval for the ore feeding a processing plant: A geostatistical solution. *International Journal of Mineral Processing*, 131:31–42.

Massari, S. and Ruberti, M. (2013). Rare earth elements as critical raw materials: Focus on international markets and future strategies. *Resources Policy*, 38(1):36–43.

McAlister, S. and Armstrong, K. (1998). Development of the Falcon concentrators. In *Society for Mining, Metallurgy and Exploration Annual Meeting*, Orlando, Florida.

Metso (2010). *Basics in minerals processing.* Metso Corporation, 10th edition.

Meyer-Joly, M.-C. (1988). *Valorisation du concentré mixte d'Échassières (Allier).* Phd thesis, Institut National Polytechnique de Lorraine.

Miller, D. (1991). Design and operating experience with the Goldsworthy Mining Limited BATAC Jig and spiral separator iron ore beneficiation plant. *Minerals Engineering*, 4(3-4):411–435.

Miller, J., Wang, X., and Li, M. (2002). Selective flotation of phosphate minerals with hydroxamate collectors. Pantent N° US 6341697, United States.

Mineral Technologies (2015). Centrifugal Jig Technology. http://www.mineraltechnologies.com/process-solutions/equipment-design-selection/centrifugal-jig-technology. Last accessed: 2015-11-19.

Mining Magazine (2014). Buyers' guide: 2014-15.

Minkkinen, P. O. (2013). Properties of process variograms. In Beniscelli, J., Felipe Costa, J., Domínguez, O., Duggan, S., Esbensen, K., Lyman, G., and Sanfurgo, B., editors, *Proceedings of the 6th World Conference on Sampling and Blending*, pages 241–247, Lima.

Minkkinen, P. O. and Esbensen, K. H. (2009). Grab vs. composite sampling of particulate materials with significant spatial heterogeneity - a simulation study of "correct sampling errors". *Analytica chimica acta*, 653(1):59–70.

Minkkinen, P. O. and Esbensen, K. H. (2014). Multivariate variographic versus bilinear data modeling. *Journal of Chemometrics*, 28(5):395–410.

Montgomery, D. C. (2008). *Design and Analysis of Experiments*. John Wiley & Sons.

Moon, C. J. (2010). Geochemical exploration in Cornwall and Devon: a review. *Geochemistry: Exploration, Environment, Analysis*, 10(3):331–351.

Mudd, G. M. (2009). The Sustainability of Mining in Australia: Key Production Trends and Their Environmental Implications for the Future. Technical Report October 2007.

Mueller, S., Scott, P. W., and Evans, M. (1999). Kaolinisation, mineralisation and structures in biotite granite at Bodelva, St. Austell, Cornwall. *Proceedings of the Ussher Society*, 9(4):310–317.

Mukhtar, S., Haswell, S. J., Ellis, A. T., and Hawke, D. T. (1991). Application of total-reflection X-ray fluorescence spectrometry to elemental determinations in water, soil and sewage sludge samples. *The Analyst*, 116(4):333.

Mular, A. (1982). *Mining and mineral processing equipment costs and preliminary capital cost estimations*. Canadian Institute of Mining and Metallurgy.

Mular, A. L. and Poulin, R. (1998). *CAPCOSTS: a handbook for estimating mining and mineral processing equipment costs and capital expenditures and aiding mineral project evaluations*. Canadian Mineral Processors Division of Canadian Institute of Mining, Metallurgy and Petroleum, Montreal.

Müller, A. and Halls, C. (2005). Rutile — the tin-tungsten host in the intrusive tourmaline breccia at Wheal Remfry, SW England. In Mao, J. and Bierlein, F., editors, *Mineral Deposit Research: Meeting the Global Challenge SE - 115*, chapter 4, pages 441–444. Springer, Berlin.

Multotec (2015). Heavy Mineral Concentrators brochure. http://www.multotec.com/public/uploads/fileLibrary/heavy-mineral-spiral-concentrators-brochure-d6d30.pdf. Last accessed: 2015-11-20.

Myers, R. H., Montgomery, D. C., and Anderson-Cook, C. M. (2009). *Response Surface Methodology: Process and Product Optimization Using Designed Experiments*. John Wiley & Sons.

Ndlovu, B., Farrokhpay, S., and Bradshaw, D. (2013). The effect of phyllosilicate minerals on mineral processing industry. *International Journal of Mineral Processing*, 125:149–156.

Negroni, J.-m. (2015). Valorisation de la cassitérite associée au gisement de kaolin de Beauvoir. Orléans, France. Presented at Journée Mines en France 2015.

Nemes, A., Wösten, J., Lilly, A., and Oude Voshaar, J. (1999). Evaluation of different procedures to interpolate particle-size distributions to achieve compatibility within soil databases. *Geoderma*, 90(3-4):187–202.

Nguyen, A. (2007). Flotation. In Wilson, I. D., Cooke, M., and Poole, C., editors, *Encyclopedia of Separation Science*, pages 1–27. Elsevier, Oxford,UK.

Norgate, T. and Jahanshahi, S. (2006). Energy and greenhouse gas implications of deteriorating quality ore reserves. In *5th Australian Conference on Life Cycle Assessment*, page 10, Melbourne.

Norgate, T. and Jahanshahi, S. (2010). Low grade ores – Smelt, leach or concentrate? *Minerals Engineering*, 23(2):65–73.

Oakdene Hollins and Faunhofer ISI (2014). Study on Critical Raw Materials at EU level Final Report. Technical Report December, Concil of the European Union, Brussels.

Oliver, M. A. and Webster, R. (1989). A geostatistical basis for spatial weighting in multivariate classification. *Mathematical Geology*, 21(1):15–35.

Outotec (2015). Spiral concentrators.

Özbayoğlu, G. and Ümit Atalay, M. (2000). Beneficiation of bastnaesite by a multi-gravity separator. *Journal of Alloys and Compounds*, 303-304:520–523.

Paakkunainen, M., Kilpeläinen, J., Reinikainen, S.-P., and Minkkinen, P. O. (2007). Effect of missing values in estimation of mean of auto-correlated measurement series. *Analytica chimica acta*, 595(1-2):209–15.

Paton, C., Hellstrom, J., Paul, B., Woodhead, J., and Hergt, J. (2011). Iolite: Freeware for the visualisation and processing of mass spectrometric data. *Journal of Analytical Atomic Spectrometry*, 26(12):2508.

Pavez, O., Brandao, P., and Peres, A. (1996). Adsorption of oleate and octylhydroxamate on to rare-earths minerals. *Minerals Engineering*, 9(3):357–366.

Pavez, O. and Peres, A. (1994). Technical note bench scale flotation of a brazilian monazite ore. *Minerals Engineering*, 7(12):1561–1564.

Peelman, S., Sun, Z. H., Sietsma, J., and Yang, Y. (2016). Leaching of Rare Earth Elements: Review of Past and Present Technologies. In *Rare Earths Industry*, chapter 21, pages 319–334. Elsevier, Oxford,UK.

Petersen, L., Dahl, C. K., and Esbensen, K. H. (2004). Representative mass reduction in sampling—a critical survey of techniques and hardware. *Chemometrics and Intelligent Laboratory Systems*, 74(1):95–114.

Petersen, L. and Esbensen, K. H. (2005). Representative process sampling for reliable data analysis—a tutorial. *Journal of Chemometrics*, 19(11-12):625–647.

Petersen, L., Minkkinen, P. O., and Esbensen, K. H. (2005). Representative sampling for reliable data analysis: Theory of Sampling. *Chemometrics and Intelligent Laboratory Systems*, 77(1-2):261–277.

Pitard, F. F. (1993). *Pierre Gy's Sampling Theory and Sampling Practice, Second Edition: Heterogeneity, Sampling Correctness, and Statistical Process Control*. CRC Press, Boca Raton.

Pitfield, P. and Brown, T. (2011). Tungsten - Commodity Profile. Technical Report January, British Geological Survey, Keyworth, UK.

Pohl, W. L. (2011). Economic Geology of Metals. In Wiley-Blackwell, editor, *Economic Geology Principles and Practice: Metals, Minerals, Coal and Hydrocarbons - Introduction to Formation and Sustainable Exploitation of Mineral Deposits*, chapter 2, pages 149–284. Oxford,UK.

Pradip (1996). Recent advances in the recovery of tungsten values in the fine and ultrafine size range. *Bulletin of Materials Science*, 19(2):267–293.

Psyrillos, A., Manning, D., and Burley, S. D. (1998). Geochemical constraints on kaolinization in the St Austell Granite, Cornwall, England. *Journal of the Geological Society*, 155(5):829–840.

Raimbault, L., Cuney, M., Azencott, C., Duthou, J.-L., and Joron, J. L. (1995). Geochemical evidence for a multistage magmatic genesis of Ta-Sn-Li mineralization in the granite at Beauvoir, French Massif Central. *Economic Geology*, 90(3):548–576.

Rankin, W. J. (1986). The slag-metal equilibrium in tin smelting. *Metallurgical Transactions B*, 17(1):61–68.

Rao, G. M. and Satynarayana (1987). The processing of tungsten ores processes available – challenges – a critical review. *Physicochemical Problems of Mineral Processing*, pages 183–193.

Richards, R., MacHunter, D., Gates, P., and Palmer, M. (2000). Gravity separation of ultra-fine (-0.1mm) minerals using spiral separators. *Minerals Engineering*, 13(1):65–77.

Rockenbauer, W. (1984). Production of niobium metal and compounds from tantalite-columbite natural ores and synthetic tantalum-niobium concentrates. In Stuart, H., editor, *Niobium - Proceedings of the international symposium*, pages 133–152. Pittsburg.

Roethe, G. (1989). Processing of Tantalum and Niobium Ores. In Möller, P., Černý, P., and Saupé, F., editors, *Lanthanides, Tantalum and Niobium*, pages 331–341. Springer, Berlin, Heidelberg.

Rosenau-Tornow, D., Buchholz, P., Riemann, A., and Wagner, M. (2009). Assessing the long-term supply risks for mineral raw materials—a combined evaluation of past and future trends. *Resources Policy*, 34(4):161–175.

Rosenblum, S. and Brownfield, I. K. (1999). Magnetic Susceptibilities of Minerals - Report for U.S. Geological Survey. Technical report, US Geological Survey.

Roskill Consulting Group (2010). A custom study of the market for tungsten. Commissioned. Technical report, Commissioned by Wolf Minerals Ltd., London, UK.

Sadeghi, M., Bazin, C., and Renaud, M. (2014). Effect of wash water on the mineral size recovery curves in a spiral concentrator used for iron ore processing. *International Journal of Mineral Processing*, 129:22–26.

Salter Cyclones Ltd (2015). Multi-Gravity Separators brochure. http://www.saltercyclones.com/files/6814/4231/3314/multi-gravity_separation_systems_june_2015.pdf. Last accessed: 2015-11-19.

Saunders, I. W. and Robinson, G. K. (1989). Restricted stratified random sampling. *International Journal of Mineral Processing*, 25(3-4):159–166.

Saunders, I. W., Robinson, G. K., Lwin, T., and Holmes, R. J. (1989). A simplified variogram method for determining the estimation error variance in sampling from a continuous stream. *International Journal of Mineral Processing*, 25(3-4):175–198.

Schuiling, R. D. (1967). Tin belts on the continents around the Atlantic Ocean. *Economic Geology*, 62(4):540–550.

Schwanghart, W. (2009). Variogramfit, MATLAB Central File Exchange. http://www.mathworks.com/matlabcentral/fileexchange/25948-variogramfit. Last accessed: 2015-05-15.

Schwartz, M. (1992). Geochemical criteria for distinguishing magmatic and metasomatic albite-enrichment in granitoids: examples from the Ta-Li granite Yichun (China) and the Sn-W deposit Tikus (Indonesia). *Mineralium Deposita*, 27(2):101–108.

Schwela, U. (2010). TIC Statistics and transport project. *Tantalum-Niobium International Study Center bulletin*, (N° 145):2–8.

Scott, P. W. and Bristow, C. M. (2002). Field excursion to study aspects of the St. Austell Granite and its related kaolinization and other mineralization, January, 2002. *Geoscience in south-west England*, 10(3):370–372.

Scott, P. W., Bristow, C. M., and of London, G. S. (2002). *Industrial Minerals and Extractive Industry Geology: Based on Papers Presented at the Combined 36th Forum on the Geology of Industrial Minerals and 11th Extractive Industry Geology Conference, Bath, England, 7th-12th May, 2000*. Geological Society of London.

Scott, P. W., Pascoe, R., and Hart, F. W. (1998). Columbite-tantalite, rutlie and other accessory minerals from the St Austell topaz granite, Cornwall. *Geoscience in south-west England*, 9(3):165–170.

Scrivener, R. C., Highley, D., Cameron, D. G., Linley, K. A., and White, R. (1997). Mineral Resource Information for Development Plans Phase One, Cornwall: Resources and Constraints. Technical report, Keyworth, Nottingham.

Sepro (2015a). Falcon SB Gravity Concentrators brochure. http://www.seprosystems.com/images/brochures/sepro-falcon-sb-concentrators.pdf. Last accessed: 2015-11-19.

Sepro (2015b). Falcon UF Gravity Concentrators brochure. http://www.seprosystems.com/images/brochures/sepro-falcon-uf-concentrators.pdf. Last accessed: 2015-11-19.

Sepro (2015c). Sepro Condor Multi-stage Dense Medium Separators brochure. http://www.seprosystems.com/images/brochures/sepro-condor-multi-stage-dms.pdf. Last accessed: 2015-11-21.

Shail, R., Pascoe, R., and Rollinson, G. (2009). Mineral potential of china clay waste streams, initial scoping study. Technical Report February, UEC Enterprises Ltd, Project 710.

Shaw, R. and Goodenough, K. (2011). Niobium–tantalum - Commodity Profile. Technical Report April, British Geological Survey, Keyworth, UK.

Sheppard, S. M. F. (1977). The Cornubian batholith, SW England: D/H and 18O/16O studies of kaolinite and other alteration minerals. *Journal of the Geological Society*, 133(6):573–591.

Singh, A. K., Ananda, M. M., and Sparks, A. R. (1993). Superfund site characterization using non-parametric variogram modeling. *Analytica Chimica Acta*, 277(2):255–266.

Singh, R., Bhattacharyya, K. K., and Maulik, S. C. (1997). Gravity concentration of fines and ultrafines. In *Processing of fines: Proceedings of the national seminar*, pages 40–56, Jamshedpur. NML.

Sivamohan, R. (1990). The problem of recovering very fine particles in mineral processing — A review. *International Journal of Mineral Processing*, 28(3-4):247–288.

Sivamohan, R. and Forssberg, E. (1985a). Principles of spiral concentration. *International Journal of Mineral Processing*, 15(3):173–181.

Sivamohan, R. and Forssberg, E. (1985b). Principles of tabling. *International Journal of Mineral Processing*, 15(4):281–295.

Sivamohan, R. and Forssberg, E. (1985c). Recovery of heavy minerals from slimes. *International Journal of Mineral Processing*, 15(4):297–314.

Somasundaran, P. (1986). An Overview of the Ultrafine Problem. In Wills, B. A. and Barley, R. W., editors, *Mineral Processing at a Crossroads*, pages 1–36. Springer Netherlands, Dordrecht.

Sorensen, E. and Lundgaard, T. (1966). Selective flotation of steenstrupine and monazite from Kvanefjeld Lujavrite – report for the Danish atomic energy commission. Technical report, Roskilde.

Sprake, C. and Mcalister, S. (2003). Enhanced Gravity Concentration for Precious Metal Recovery. Technical report, Falcon Concentrators Inc., Langley.

Suri, A. K., Subramanian, C., and Gupta, C. K. (1992). Investigations on Flowsheet Development for the Treatment of Niobium-Tantalum Bearing Cassiterite. *Mineral Processing and Extractive Metallurgy Review*, 9(1-4):293–303.

Tantalum-Niobium International Study Center (2013). Tantalum - Raw Materials and Processing. http://tanb.org/tantalum. Last accessed: 2013-05-16.

Tao, D., Dopico, P., Hines, J., and Kennedy, D. (2010). An experimental study of clay binders in fine coal froth flotation. In *International Coal Preparation Congress 2010 Conference Proceedings*, pages 478–487, Lexington, USA. SME.

Towett, E. K., Shepherd, K. D., and Cadisch, G. (2013). Quantification of total element concentrations in soils using total X-ray fluorescence spectroscopy (TXRF). *The Science of the total environment*, 463-464:374–88.

Tripathy, S. K. and Rama Murthy, Y. (2012). Modeling and optimization of spiral concentrator for separation of ultrafine chromite. *Powder Technology*, 221:387–394.

Turner, J. and Hallewell, M. (1993). Process improvements for fine cassiterite recovery at Wheal Jane. *Minerals Engineering*, 6(8-10):817–829.

US Geological Survey (2010). Mineral Commodity Summaries 2010. Technical report, United States Geological Survey, Reston, Virginia, USA.

US Geological Survey (2013). Mineral Commodity Summaries 2013. Technical report, United States Geological Survey, Reston, Virginia, USA.

US Geological Survey (2015). Mineral Commodity Summaries 2015. Technical report, United States Geological Survey, Reston, Virginia, USA.

Van Olphen, H. (1951). Rheological phenomena of clay sols in connection with the charge distribution on the micelles. *Discussions of the Faraday Society*, 11:82–84.

Veasey, T., Penhallow, A., and Elliott, A. (1989). Mineralogy and mill performance optimization- a case study of south crofty tin mine. *Minerals Engineering*, 2(4):471–480.

Vilbrandt, F. C. and Dryden, C. E. (1959). *Chemical Engineering Plant Design*. McGraw-Hill, New York, NY, 4th edition.

Walters, A. and Lusty, P. (2011). Rare earth elements - Commodity Profile. Technical report, British Geological Survey, Keyworth, UK.

Webster, R. and Oliver, M. A. (2007). *Geostatistics for Environmental Scientists*. Statistics in Practice. John Wiley & Sons, Ltd, Chichester, UK, 2nd edition.

Wen Qi, G. (1993). Use of the QEMSEM analysis in flotation testwork on a phosphate ore containing monazite. *International Journal of Mineral Processing*, 37(1-2):89–108.

Williams, S. R. and Richardson, J. M. (2004). Geometallurgical mapping: a new approach that reduces technical risks. In *Proceedings of 36th Annual Meeting of the Canadian Mineral Processors Conference*, pages 241–268, Ottawa, ON, Canada. CIM.

Willis-Richards, J. and Jackson, N. J. (1989). Evolution of the Cornubian ore field, Southwest England; Part I, Batholith modeling and ore distribution. *Economic Geology*, 84:1078–1100.

Wills, B. A. and Napier-Munn, T. (2005). *Wills' Mineral Processing Technology*. Elsevier Science & Technology Books, 7th edition.

Wilson, I., Halls, C., and Spiro, B. (1997). A comparaison between the china clay deposits of China and Cornwall. *Proceedings of the Usher Society*, 9(2):195–200.

Wilson, I. and Jiranek, J. (1995). Kaolin deposits of the Czech Republic and some comparisons with south-west England. *Proceedings of the Usher Society*, 8(4):357–362.

Wold, S., Esbensen, K., and Geladi, P. (1987). Principal component analysis. *Chemometrics and Intelligent Laboratory Systems*, 2(1-3):37–52.

Wold, S., Sjöström, M., and Eriksson, L. (2001). PLS-regression: a basic tool of chemometrics. *Chemometrics and Intelligent Laboratory Systems*, 58(2):109–130.

Wright, P. A. (1982). *Extractive metallurgy of tin*. Elsevier Science Ltd, Oxford, UK, 2nd edition.

Yin, L., Pollard, P., Shouxi, H., and Taylor, R. (1995). Geologic and Geochemical Characteristics of the Yichun Ta-Nb-Li Deposit, Jiangxi Province, South China. *Economic Geology*, 90:577–585.

Zhou, Y. (1976). *Recent Advances in Mining and Processing of Low-Grade and Submarginal Mineral Deposits*. Elsevier, New York, NY.

Zhu, Z., Pranolo, Y., and Cheng, C. Y. (2015). Separation of uranium and thorium from rare earths for rare earth production – A review. *Minerals Engineering*, 77:185–196.

# Appendices

# Appendix A

# Introduction appendices

# A.1 CRMs applications and uses

Table A.1: Principal industrial applications of the CRMs of interest and Sn (Christian et al., 2011; Long et al., 2010; Shaw and Goodenough, 2011).

| CRM | Industry | Application |
|---|---|---|
| **LREE** | Ceramics | Capacitors, sensors, colourants, scintillators, refractories |
| | Electrical | Permanent magnets, motors, disc drives, MRI, power generation, microphones and speakers, magnetic refrigeration, batteries (*e.g.*, NiMH batteries) |
| | Metallurgical | Fuel cells, steel, lighter flints, super alloys, Aluminium/Magnesium |
| | Plastic | Glass polishing, Glass (*e.g.*, U.V. resistant glass), X-ray imaging |
| | Electronics | Phosphors, phosphors display (CRT, LPD, LCD), fluorescent lighting, lasers, fibre optics |
| | Chemicals | Chemical processing catalyst |
| | Automotive-petroleum | Catalytic converter, diesel additives, Catalyst (*e.g.*, petroleum refining) |
| | Others | Nuclear (Ce, Y, Sm), defence (Nd, Pr, La, Sm), water treatment, pigments (Ce), fertilisers |
| **Sn** | Metallurgy | Tinplate or steel coated (packaging), brass, bronze |
| | Electronics | Solder |
| | Chemical | Chemicals, pigments, organic compounds |
| | Plastic | Float glass |
| **Nb** | Automotive | Vehicles bodies |
| | Ceramics | Capacitors, glass coatings and camera lenses |
| | Chemicals | Chemical processing equipment and oil and gas pipelines |
| | Construction | Architectural steels and cathode protection systems for large steel structures |
| | Engineering | Cutting tools, railway tracks and ship hulls |
| | Electronics | Capacitors, street lighting systems and surface acoustic wave filters for sensor and touchscreen technologies |
| | Medicine | Superconducting magnetic coils in MRI scanners and magnetoencephalography (brain activity mapping) |
| | Metallurgical | Superalloys for jet engines and turbine blades |
| **Ta** | Automotive | Anti-lock brake systems, airbag activation systems and engine management modules |
| | Ceramics | Ceramic capacitors, glass coatings, camera lenses and X-ray film |
| | Chemicals | Chemical processing equipment |
| | Construction | Cathode protection systems for large steel structures such as oil platforms and corrosion resistant fasteners such as screws, and nuts and bolts |
| | Engineering | Cutting tools |
| | Electronics | Capacitors, surface acoustic wave filters for sensor and touchscreen technologies, hard disc drives, and LED lights |
| | Medicine | Pace makers, hearing aids and prosthetic devices such as hip joints |
| | Metallurgical | Furnace parts, superalloys for jet engines and rocket engine nozzles |
| | Military | Missile parts, ignition systems, night vision goggles and Global Positioning Systems (GPS) |
| **W** | Metallurgical | Superalloys, steel |
| | Enginering-Mining-Petroleum | Hard metals, tungsten carbides (WC), mining and stone-cutting tools, drilling and wear-resistant parts or coatings. |
| | Electrical- Electronics | Incandescent light bulb filaments, vacuum tubes, electronic circuit interconnects, filaments in vacuum-metallising furnaces, and for electrical contacts, metallizing of semiconductors |
| | Chemicals | Colouring agent, phosphors, absorbent gels , catalyst, pigment in ceramics |
| | Medical | Filament and target of medical X-ray tubes, dental filling materials |

# Appendix B

# Materials and methods appendices

# B.1 Rotational divider setups

Figure B.1: Rotational divider setups. (a) Side and top view of the dry sample rotational divider. This apparatus divides the sample into four representative sub-samples (2*1/9 and 2*7/18). (b) Side and top view of the pulp sample rotational divider. This apparatus divides the slurry into six representative sub-samples.

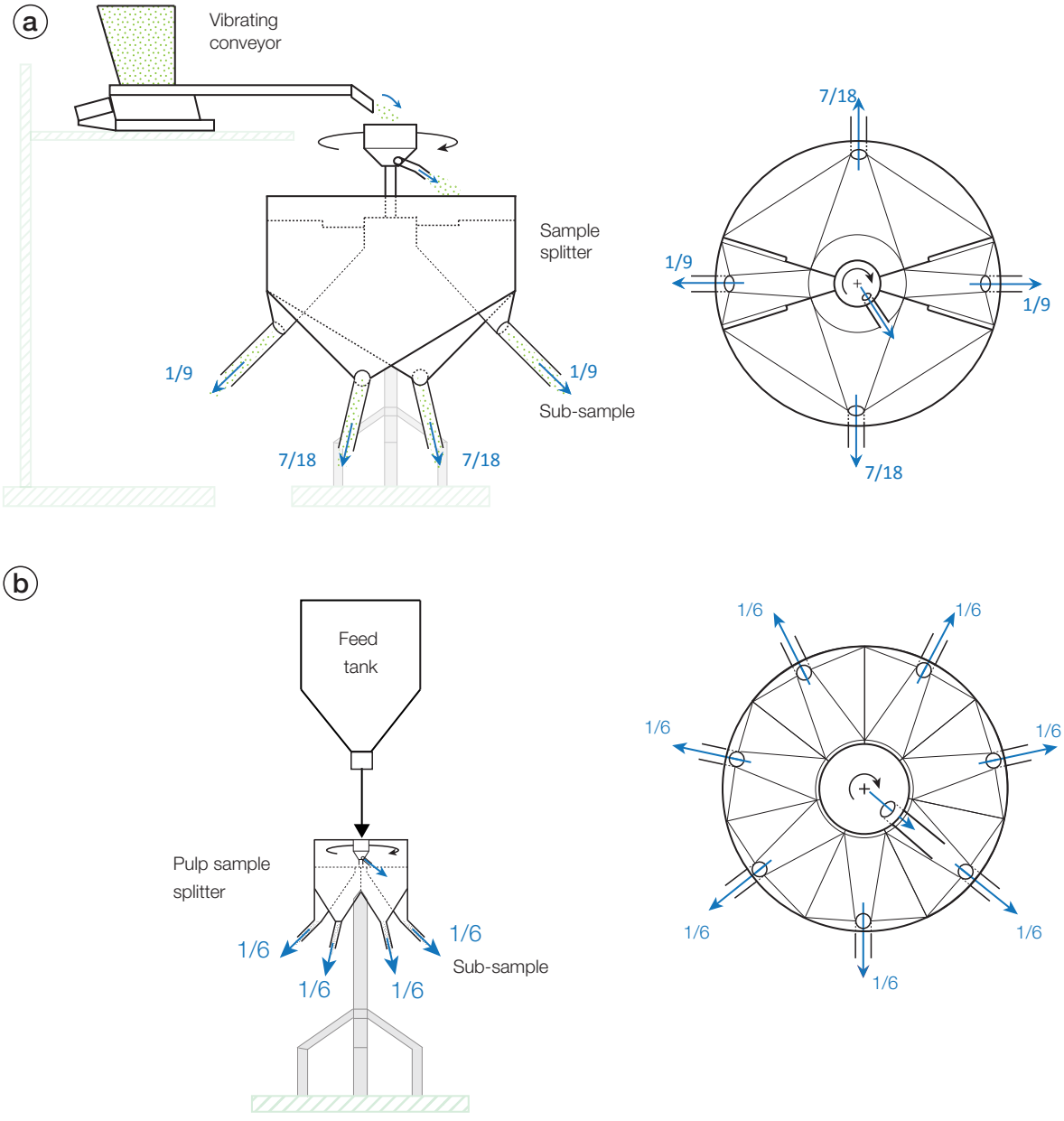

# B.2 ICP analysis uncertainties

Figure B.2: Uncertainties and limits of detection (LOD) for trace and major element analysis by ICP (SARM-CNRS, Nancy, France).

| | >50 ppm | >10 ppm | >1 ppm | >0.1 ppm | >0.01 ppm | LOD ppm |
|---|---|---|---|---|---|---|
| As | <5% | <10% | | | | 1.50 |
| Ba | <5% | <10% | | | | 1.60 |
| Be | <5% | <10% | | | | 0.40 |
| Bi | | <5% | <10% | | | 0.10 |
| Cd | | <5% | <15% | | | 0.12 |
| Ce | | <5% | <10% | | | 0.14 |
| Co | <5% | <10% | <15% | | | 0.40 |
| Cr | <5% | <10% | | | | 4.00 |
| Cs | | <5% | <10% | | | 0.10 |
| Cu | <5% | <10% | | | | 5.00 |
| Dy | | | <5% | <10% | <15% | 0.01 |
| Er | | | <5% | <10% | | 0.01 |
| Eu | | | | <5% | <10% | 0.005 |
| Ga | | <5% | <8% | | | 0.20 |
| Gd | | | | <5% | <10% | 0.013 |
| Ge | | <5% | <8% | | | 0.15 |
| Hf | | <5% | <10% | <15% | | 0.03 |
| Ho | | | <5% | <10% | | 0.002 |
| In | | | <5% | | | 0.07 |
| La | | | <5% | <10% | | 0.09 |
| Lu | | | | <5% | <10% | 0.003 |
| Mo | | <5% | <10% | | | 0.50 |

| | >50 ppm | >10 ppm | >1 ppm | >0.1 ppm | >0.01 ppm | LOD ppm |
|---|---|---|---|---|---|---|
| Nb | | <5% | <10% | <15% | | 0.09 |
| Nd | | | <5% | <10% | | 0.06 |
| Ni | <5% | | | | | 5.00 |
| Pb | | <5% | <10% | | | 0.70 |
| Pr | | | <5% | <10% | | 0.015 |
| Rb | | <5% | <10% | | | 0.40 |
| Sb | | <5% | <10% | | | 0.20 |
| Sc | <5% | <15% | | | | 1.00 |
| Sm | | | <5% | <10% | | 0.015 |
| Sn | <5% | <10% | <15% | | | 0.45 |
| Sr | <5% | <10% | | | | 2.00 |
| Ta | | <5% | <10% | <15% | | 0.01 |
| Tb | | | | <5% | <10% | 0.003 |
| Th | | <5% | <10% | <15% | | 0.06 |
| Tm | | | <5% | <10% | | 0.001 |
| U | <5% | <10% | | <15% | | 0.03 |
| V | <5% | <10% | | | | 0.70 |
| W | <5% | <10% | <15% | | | 0.25 |
| Y | | <5% | | | | 0.20 |
| Yb | | | <5% | <10% | | 0.007 |
| Zn | <10% | | | | | 11.00 |
| Zr | <8% | <15% | | | | 1.00 |

| Oxides | >10% | >5% | >1% | >0.5% | >0.1% | >0.05% | >0.01% | LOD (%) |
|---|---|---|---|---|---|---|---|---|
| $SiO_2$ | <1% | | <5% | | | <15% | | 0.02 |
| $Al_2O_3$ | <1% | | | <10% | | <15% | | 0.02 |
| $Fe_2O_3$ | | | <2% | | <5% | <15% | | 0.02 |
| MnO | | | <1% | | <5% | | <10% | 0.0002 |
| MgO | | <2% | <5% | | | <10% | | 0.015 |
| CaO | | <2% | | <5% | | <15% | | 0.03 |
| $Na_2O$ | | <2% | | <5% | | <15% | | 0.01 |
| $K_2O$ | | <2% | | <5% | <10% | <15% | | 0.01 |
| $TiO_2$ | | | | <5% | <10% | | | 0.02 |
| $P_2O_5$ | | | <5% | | <10% | | | 0.04 |

## B.3 XRF analysis calibration (major elements)

Figure B.3: Relationship between the estimated concentrations obtained by XRF analysis against concentration measured by ICP-OES analysis for major elements. Most of the major elements display high R squared ($R^2$) above 0.8, suggesting that XRF analysis accurately determined the concentration of these elements. Other elements are estimated with an acceptable accuracy ($0.7<R^2<0.8$) such as $SiO_2$ which display only $R^2$ of 0.77 and large confidence intervals suggesting a less accurate estimation. Although $MnO$ and $MgO$ display $R^2>0.8$, the small number of data points for MnO and the large confidence intervals for both major elements indicate only an acceptable accuracy.

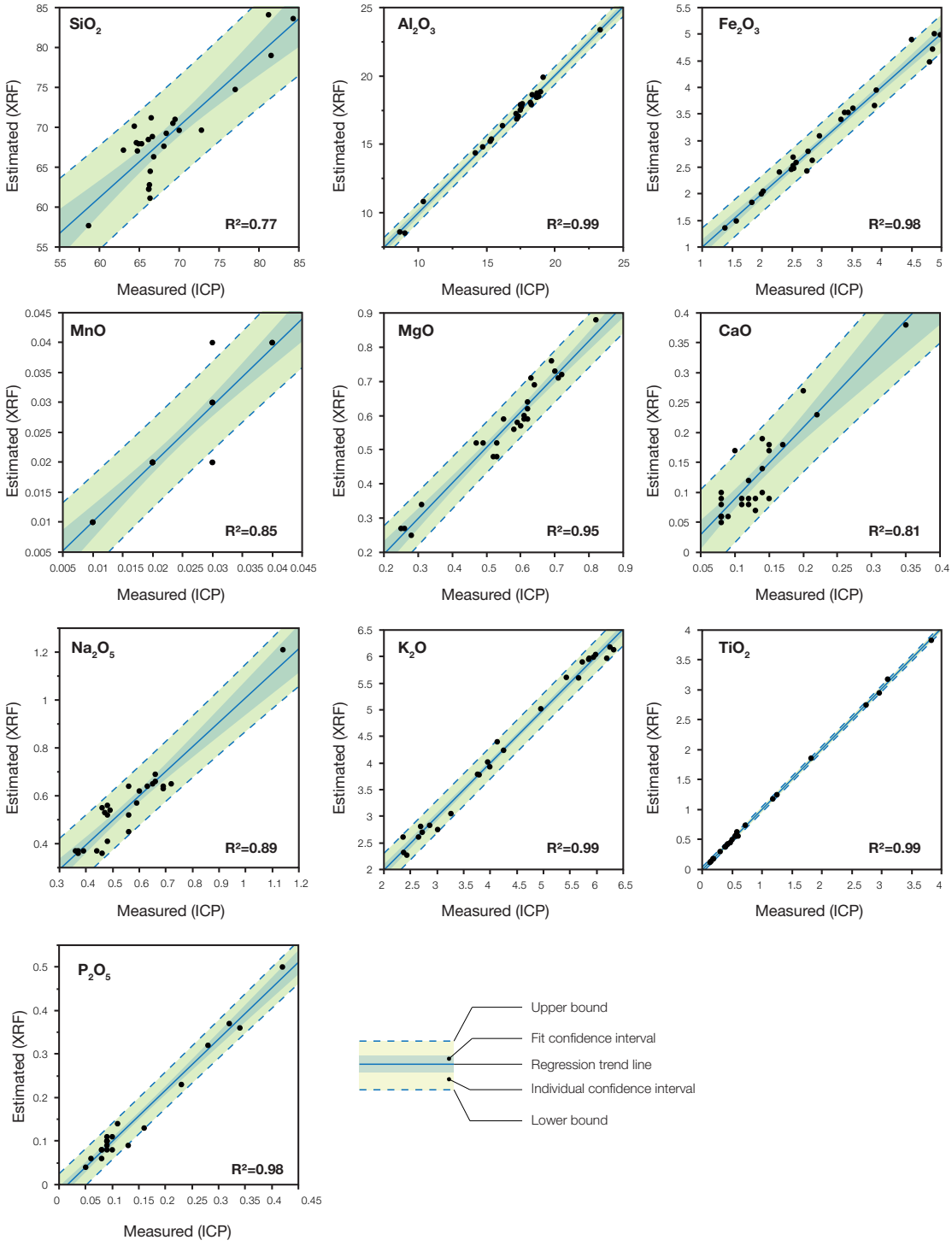

# B.4 XRF analysis calibration (trace elements)

Figure B.4: Relationship between the estimated concentrations obtained by XRF analysis against concentrations measured by ICP-MS for trace elements using the classical method (a to g) and a dedicated method for Ce-La (h and i). For each metal, regression trend lines, confidence intervals as well as a summary of fit comprising R squared ($R^2$), Root Mean Square Error (RMSE) and number of data points (n) are presented. All metals display strong correlations ($R^2$>0.9) with slope close to 1:1 (except for La and Ce with the classical method), suggesting that XRF analysis accurately determined the concentration of these metals.

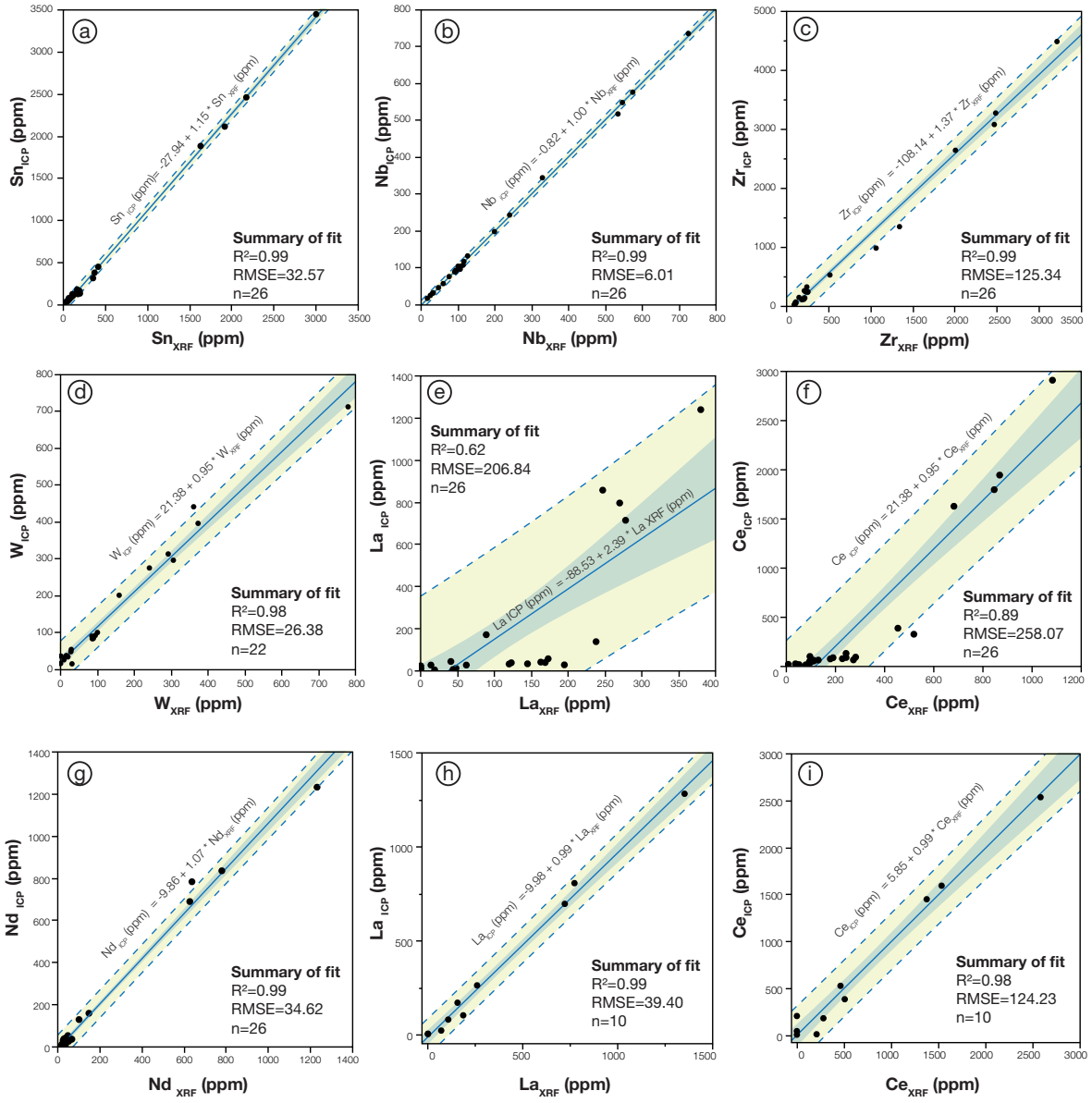

## B.5 Comparison of particle size analysis techniques

Figure B.5: Comparison between particle size analysis obtained with the Rotap apparatus (seiving) and with laser light scattering on a micaceous residue sample.

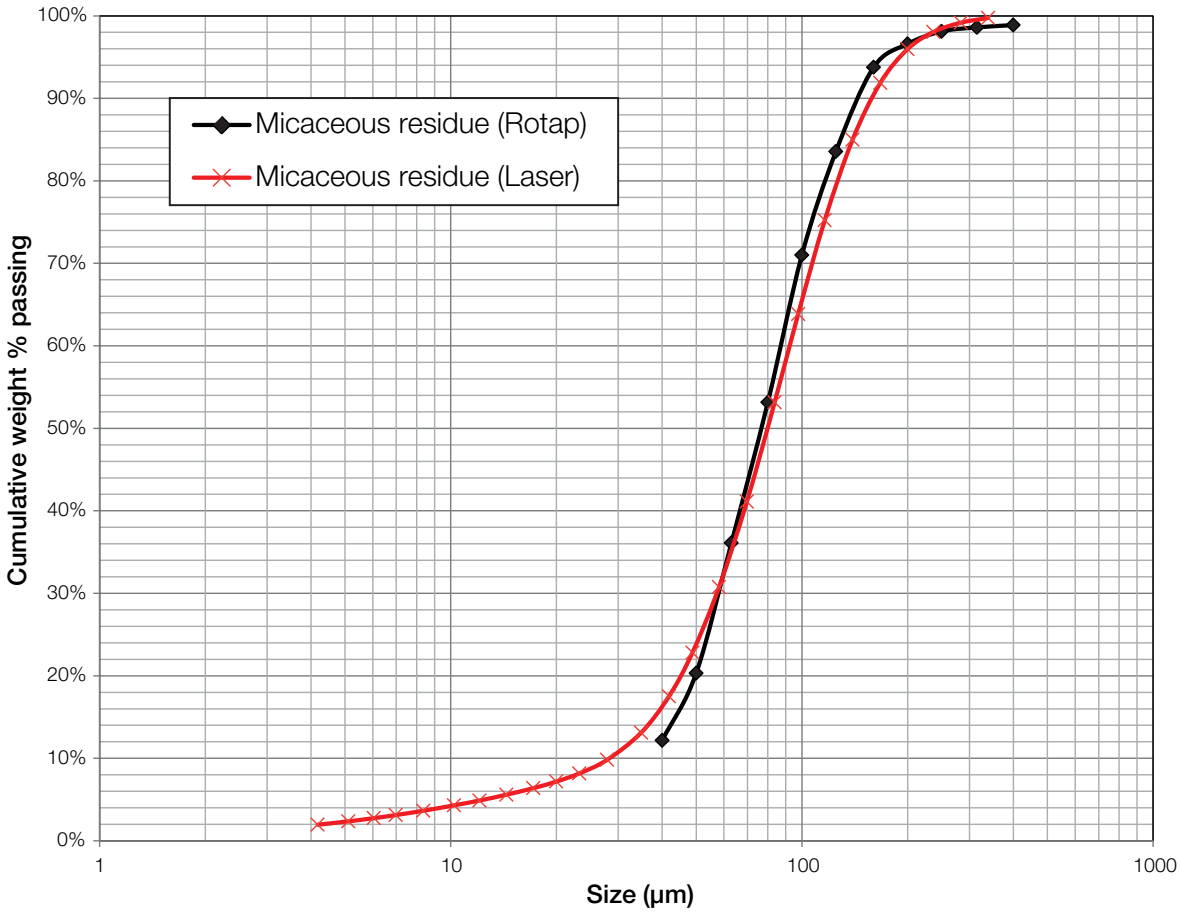

# B.6 Operating conditions of flotation tests

Table B.1: Operating conditions for the flotation tests using MIBC as a frother, sodium hydroxide (NaOH) to adjust pH at 9.8-10, sodium silicate ($Na_2SiO_3$) as depressant, and several collectors such as sodium oleate (OA), hydroxamate (AC-3) in the presence or absence of non-ionic reagent (PX4826).

| Dispersion | Test # | Operation | Reagents | Concentration (%) | Volume (mL) | Dosage (g/t) | Impeller speed (rpm) | Time (min) | Air flowrate (L/h) |
|---|---|---|---|---|---|---|---|---|---|
| No | 1 | **Conditioning** | NaOH | 1 | 8 | 160 | 1100 | 10 | |
| | | **Roughing** | $Na_2SiO_3$ | 5 | 10.06 | 1008 | 1100 | 8 | |
| | | | Na-Oleate | 1 | 10.06 | 202 | 900 | 2 | |
| | | | MIBC | 1 | 0.25 | 5 | 900 | 1 | |
| | | | NaOH | 1 | 8 | 160 | | | |
| | | | *Flotation* | | | | *900* | *13* | *50* |
| | | **Scavenging** | Na-Oleate | 1 | 10.06 | 202 | 900 | 2 | |
| | | | MIBC | 1 | 0.25 | 5 | 900 | 1 | |
| | | | NaOH | 1 | | | | | |
| | | | *Flotation* | | | | *900* | *7* | *50* |
| | | **Cleaning** | $Na_2SiO_3$ | 5 | 1 | 100 | 900 | 2 | |
| | | | NaOH | 1 | | | | | |
| | | | MIBC | 1 | 0.25 | 5 | 900 | 1 | |
| | | | *Flotation* | | | | *900* | *9* | *50* |
| Yes | 2 | **Conditioning** | NaOH | 1 | 7.2 | 141 | 1100 | 12 | |
| | | **Roughing** | $Na_2SiO_3$ | 5 | 10.03 | 985 | 1100 | 8 | |
| | | | Na-Oleate | 1 | 10.03 | 197 | 900 | 2 | |
| | | | MIBC | 1 | 0.25 | 5 | 900 | 1 | |
| | | | NaOH | 1 | 9 | 177 | | | |
| | | | *Flotation* | | | | *900* | *13* | *50* |
| | | **Scavenging** | Na-Oleate | 1 | 10.03 | 197 | 900 | 2 | |
| | | | MIBC | 1 | 0.25 | 5 | 900 | 1 | |
| | | | NaOH | 1 | 7.8 | 153 | | | |
| | | | *Flotation* | | | | *900* | *7* | *50* |
| | | **Cleaning** | $Na_2SiO_3$ | 5 | 1 | 98 | 900 | 2 | |
| | | | NaOH | 1 | | | | | |
| | | | MIBC | 1 | 0.25 | 5 | 900 | 1 | |
| | | | *Flotation* | | | | *900* | *9* | *50* |
| No | 3 | **Conditioning** | NaOH | 1 | 11 | 224 | 1100 | 10 | |
| | | **Roughing** | $Na_2SiO_3$ | 5 | 10.1 | 1026 | 1100 | 8 | |
| | | | Na-Oleate | 1 | 10.1 | 205 | 900 | 2 | |
| | | | PX4826 | 10 | 0.5 | 102 | 900 | 2 | |
| | | | MIBC | 1 | 0.25 | 5 | 900 | 1 | |
| | | | NaOH | 1 | 10.5 | 213 | | | |
| | | | *Flotation* | | | | *900* | *13* | *50* |
| | | **Scavenging** | Na-Oleate | 1 | 10.1 | 205 | 900 | 2 | |
| | | | PX4826 | 10 | 0.5 | 102 | 900 | 2 | |
| | | | MIBC | 1 | 0.25 | 5 | 900 | 1 | |
| | | | NaOH | 1 | 5.2 | 106 | | | |
| | | | *Flotation* | | | | *900* | *7* | *50* |
| | | **Cleaning** | $Na_2SiO_3$ | 5 | 1 | 102 | 900 | 2 | |
| | | | MIBC | 1 | 0.25 | 5 | 900 | 1 | |
| | | | NaOH | 1 | 10 | 203 | | | |
| | | | *Flotation* | | | | *900* | *9* | *50* |
| Yes | 4 | **Conditioning** | NaOH | 1 | 11 | 220 | 1100 | 10 | |
| | | **Roughing** | $Na_2SiO_3$ | 5 | 10.22 | 1022 | 1100 | 8 | |
| | | | Na-Oleate | 1 | 10.22 | 204 | 900 | 2 | |
| | | | PX4826 | 10 | 0.5 | 100 | 900 | 2 | |
| | | | MIBC | 1 | 0.25 | 5 | 900 | 1 | |
| | | | NaOH | 1 | 14 | 280 | | | |
| | | | *Flotation* | | | | *900* | *13* | *50* |
| | | **Scavenging** | Na-Oleate | 1 | 10.22 | 204 | 900 | 2 | |
| | | | PX4826 | 10 | 0.5 | 100 | 900 | 2 | |
| | | | MIBC | 1 | 0.25 | 5 | 900 | 1 | |
| | | | NaOH | 1 | 7 | 140 | | | |
| | | | *Flotation* | | | | *900* | *7* | *50* |
| | | **Cleaning** | $Na_2SiO_3$ | 5 | 1 | 100 | 900 | 2 | |
| | | | MIBC | 1 | 0.25 | 5 | 900 | 1 | |
| | | | NaOH | 1 | 3 | 60 | | | |
| | | | *Flotation* | | | | *900* | *9* | *50* |

| Dispersion | Test # | Operation | Reagents | Concentration (%) | Volume (mL) | Dosage (g/t) | Impeller speed (rpm) | Time (min) | Air flowrate (L/h) |
|---|---|---|---|---|---|---|---|---|---|
| Yes | 5 | **Conditioning** | NaOH | 1 | 7 | 138 | 1100 | 10 | |
| | | **Roughing** | $Na_2SiO_3$ | 5 | 10.16 | 999 | 1100 | 8 | |
| | | | AC-3 | 100 | 0.1 | 197 | 900 | 2 | |
| | | | MIBC | 1 | 0.25 | 5 | 900 | 1 | |
| | | | NaOH | 1 | 15 | 295 | | | |
| | | | *Flotation* | | | | *900* | *13* | *50* |
| | | **Scavenging** | AC-3 | 100 | 0.1 | 197 | 900 | 2 | |
| | | | MIBC | 1 | 0.25 | 5 | 900 | 1 | |
| | | | NaOH | 1 | 12 | 236 | | | |
| | | | *Flotation* | | | | *900* | *7* | *50* |
| | | **Cleaning** | $Na_2SiO_3$ | 5 | 1 | 98 | 900 | 2 | |
| | | | NaOH | 1 | 10 | 197 | | | |
| | | | MIBC | 1 | 0.25 | 5 | 900 | 1 | |
| | | | *Flotation* | | | | *900* | *9* | *50* |
| No | 6 | **Conditioning** | NaOH | 1 | 10 | 198 | 1100 | 10 | |
| | | **Roughing** | $Na_2SiO_3$ | 5 | 10.1 | 999 | 1100 | 8 | |
| | | | AC-3 | 100 | 0.1 | 198 | 900 | 2 | |
| | | | MIBC | 1 | 0.25 | 5 | 900 | 1 | |
| | | | NaOH | 1 | 14 | 277 | | | |
| | | | *Flotation* | | | | *900* | *13* | *50* |
| | | **Scavenging** | AC-3 | 100 | 0.1 | 198 | 900 | 2 | |
| | | | MIBC | 1 | 0.25 | 5 | 900 | 1 | |
| | | | NaOH | 1 | 9 | 178 | | | |
| | | | *Flotation* | | | | *900* | *7* | *50* |
| | | **Cleaning** | $Na_2SiO_3$ | 5 | 1 | 99 | 900 | 2 | |
| | | | MIBC | 1 | 0.25 | 5 | 900 | 1 | |
| | | | NaOH | | 8 | 0 | | | |
| | | | *Flotation* | | | | *900* | *9* | *50* |
| No | 7 | **Conditioning** | NaOH | 1 | 9 | 177 | 1100 | 10 | |
| | | **Roughing** | $Na_2SiO_3$ | 5 | 10.24 | 1007 | 1100 | 8 | |
| | | | AC-3 | 100 | 0.1 | 197 | 900 | 2 | |
| | | | PX4826 | 10 | 0.5 | 98 | 900 | 2 | |
| | | | MIBC | 1 | 0.25 | 5 | 900 | 1 | |
| | | | NaOH | 1 | 16 | 315 | | | |
| | | | *Flotation* | | | | *900* | *13* | *50* |
| | | **Scavenging** | AC-3 | 1 | 0.1 | 2 | 900 | 2 | |
| | | | PX4826 | 10 | 0.5 | 98 | 900 | 2 | |
| | | | MIBC | 1 | 0.25 | 5 | 900 | 1 | |
| | | | NaOH | 1 | 8 | 157 | | | |
| | | | *Flotation* | | | | *900* | *7* | *50* |
| | | **Cleaning** | $Na_2SiO_3$ | 5 | 1 | 98 | 900 | 2 | |
| | | | MIBC | 1 | 0.25 | 5 | 900 | 1 | |
| | | | NaOH | 1 | 9 | 177 | | | |
| | | | *Flotation* | | | | *900* | *9* | *50* |
| Yes | 8 | **Conditioning** | NaOH | 1 | 9 | 178 | 1100 | 10 | |
| | | **Roughing** | $Na_2SiO_3$ | 5 | 10.11 | 1001 | 1100 | 8 | |
| | | | AC-3 | 1 | 0.1 | 2 | 900 | 2 | |
| | | | PX4826 | 10 | 0.5 | 99 | 900 | 2 | |
| | | | MIBC | 1 | 0.25 | 5 | 900 | 1 | |
| | | | NaOH | 1 | 16 | 317 | | | |
| | | | *Flotation* | | | | *900* | *13* | *50* |
| | | **Scavenging** | AC-3 | 1 | 0.1 | 2 | 900 | 2 | |
| | | | PX4826 | 10 | 0.5 | 99 | 900 | 2 | |
| | | | MIBC | 1 | 0.25 | 5 | 900 | 1 | |
| | | | NaOH | 1 | 8 | 158 | | | |
| | | | *Flotation* | | | | *900* | *7* | *50* |
| | | **Cleaning** | $Na_2SiO_3$ | 5 | 1 | 99 | 900 | 2 | |
| | | | MIBC | 1 | 0.25 | 5 | 900 | 1 | |
| | | | NaOH | 1 | 8 | | | | |
| | | | *Flotation* | | | | *900* | *9* | *50* |

# Appendix C

# Multivariate variographic study appendices

# C.1 Summary statistics of variogram model fitting

Table C.1: Summary statistics and characteristics (range $a$, sill $s$ and nugget $n$) of the theoretical models that were fitted to the (multi)variogram curves. The models with the highest $R^2$ and lowest $RMSE$ are highlighted in bold.

| **Variogram** | **Size Distribution** | | | | | **Metal Content** | | | | | **Pulp Density** | | | | | **Global** | | | | |
|---|---|---|---|---|---|---|---|---|---|---|---|---|---|---|---|---|---|---|---|---|
| **Model** | $a$ | $s$ | $n$ | $R^2$ | $RMSE$ | $a$ | $s$ | $n$ | $R^2$ | $RMSE$ | $a$ | $s$ | $n$ | $R^2$ | $RMSE$ | $a$ | $s$ | $n$ | $R^2$ | $RMSE$ |
| **Blinear** | **14** | **1.68** | **2.24** | **0.83** | **0.248** | **9** | **1.61** | **1.71** | **0.94** | **0.127** | **6** | **0.69** | **0.36** | **0.69** | **0.114** | 13 | 3.1 | 5.4 | 0.91 | 0.332 |
| **Circular** | 16 | 1.73 | 2.18 | 0.82 | 0.250 | 10 | 1.64 | 1.68 | 0.93 | 0.135 | 7 | 0.71 | 0.34 | 0.68 | 0.115 | 15 | 3.2 | 5.3 | 0.92 | 0.306 |
| **Spherical** | 17 | 1.76 | 2.15 | 0.82 | 0.253 | 12 | 1.65 | 1.69 | 0.93 | 0.138 | 8 | 0.72 | 0.33 | 0.68 | 0.115 | 17 | 3.3 | 5.2 | 0.93 | 0.297 |
| **Pentaspherical** | 20 | 1.79 | 2.12 | 0.81 | 0.256 | 14 | 1.66 | 1.68 | 0.92 | 0.141 | 9 | 0.72 | 0.33 | 0.67 | 0.115 | **20** | **3.4** | **5.1** | **0.93** | **0.292** |
| **Exponential** | 7 | 2.04 | 1.99 | 0.79 | 0.267 | 5 | 1.80 | 1.62 | 0.89 | 0.166 | 3 | 0.77 | 0.29 | 0.64 | 0.118 | 7 | 3.9 | 4.8 | 0.93 | 0.301 |

# Appendix D

# Size recovery curves modelling appendices

# D.1 Example of size recovery curve calculation

Table D.1: Illustration of the heavy mineral fraction $(R_X)_{ih}$ size recovery calculation for the test n°1 using data from Table 5.8 and particle size analysis data $(w_X)_{ih}$. Feed is back-calculated from concentrate, middlings and tailings.

| Size | Feed | Concentrate | | Middlings | | Tailings | | Conc.+Mid. |
|---|---|---|---|---|---|---|---|---|
| $i$ | $(w_F)_{ih}$ | $(w_F)_{ih}$ | $(R_C)_{ih}$ | $(w_M)_{ih}$ | $(R_M)_{ih}$ | $(w_T)_{ih}$ | $(R_T)_{ih}$ | $(R_{C+M})_{ih}$ |
| m | % | % | % | % | % | % | % | % |
| 18.70 | 0.00 | 0.00 | 0.00 | 0.00 | 0.00 | 0.22 | 100.00 | 0.00 |
| 21.20 | 0.14 | 0.00 | 0.00 | 0.00 | 0.00 | 0.16 | 98.99 | 0.00 |
| 24.10 | 0.09 | 0.00 | 0.00 | 0.00 | 0.00 | 0.10 | 98.99 | 0.00 |
| 27.40 | 0.09 | 0.00 | 0.00 | 0.00 | 0.00 | 0.10 | 98.99 | 0.00 |
| 31.10 | 0.21 | 0.08 | 3.76 | 0.00 | 0.00 | 0.24 | 95.26 | 3.76 |
| 35.30 | 0.58 | 0.42 | 7.21 | 0.23 | 1.93 | 0.62 | 89.90 | 9.14 |
| 40.10 | 1.27 | 1.20 | 9.44 | 0.84 | 3.22 | 1.30 | 86.39 | 12.67 |
| 45.60 | 2.35 | 2.50 | 10.63 | 1.96 | 4.07 | 2.35 | 84.37 | 14.70 |
| 51.80 | 3.80 | 4.27 | 11.20 | 3.61 | 4.62 | 3.76 | 83.25 | 15.82 |
| 58.90 | 5.54 | 6.38 | 11.48 | 5.66 | 4.97 | 5.44 | 82.62 | 16.45 |
| 66.90 | 7.40 | 8.53 | 11.50 | 7.88 | 5.18 | 7.24 | 82.39 | 16.69 |
| 76.00 | 9.13 | 10.41 | 11.37 | 9.94 | 5.30 | 8.94 | 82.41 | 16.67 |
| 86.40 | 10.48 | 11.68 | 11.12 | 11.49 | 5.34 | 10.28 | 82.61 | 16.46 |
| 98.10 | 11.21 | 12.10 | 10.77 | 12.25 | 5.32 | 11.05 | 82.98 | 16.08 |
| 111.00 | 11.17 | 11.57 | 10.33 | 12.03 | 5.24 | 11.08 | 83.50 | 15.57 |
| 127.00 | 10.35 | 10.16 | 9.80 | 10.86 | 5.11 | 10.34 | 84.16 | 14.90 |
| 144.00 | 8.84 | 8.12 | 9.16 | 8.93 | 4.92 | 8.92 | 84.98 | 14.08 |
| 163.00 | 6.90 | 5.80 | 8.39 | 6.60 | 4.66 | 7.04 | 86.00 | 13.05 |
| 186.00 | 4.82 | 3.61 | 7.48 | 4.27 | 4.31 | 4.99 | 87.26 | 11.79 |
| 211.00 | 2.93 | 1.84 | 6.27 | 2.30 | 3.82 | 3.09 | 88.94 | 10.09 |
| 240.00 | 1.44 | 0.69 | 4.77 | 0.93 | 3.14 | 1.56 | 91.12 | 7.91 |

## D.2 Analyses of variance (ANOVA)

An Analysis of Variance (ANOVA) was conducted on each model to determine the regression coefficients and to assess their significance. According to the degrees of freedom (DF) of the models and residuals, the $F$-values (F) of all models are above the critical value for the 0.05 significance level, with the exception of the $\beta$-value model for heavy minerals, which is only acceptable at the 0.1 significance level. This indicates that the observed disparities are likely due to wash water flowrate and solid pulp density variations. Accordingly, $p$-values (P) are very low, $<0.0002$ for all of the models except the $\beta$-value heavy minerals model, which has a $p$-values of 0.0986. This indicates that there is a small probability (below 10 %) that the obtained model is only due to the effect of the mean.

Table D.2: Analyses of variance (ANOVA) for heavy minerals recovery and Gompertz parameters models with degrees of freedom (DF), sum of squares ($SS$), $F$-ratios ($F$) and $p$-values ($P$).

| Source of variation | DF | Recovery | | | α-value | | | β-value | | |
|---|---|---|---|---|---|---|---|---|---|---|
| | | *SS* | *F* * | *P* | *SS* | *F* * | *P* | *SS* | *F* * | *P* |
| Model | 5 | 809.31 | 59.74 | 0.0002 | 21.77 | 8.96 | 0.0155 | 67.18 | 3.48 | 0.0986 |
| *WW* | 1 | 546.97 | 201.86 | <.0001 | 15.40 | 31.69 | 0.0025 | 546.97 | 201.86 | 0.0410 |
| *S* | 1 | 199.84 | 73.75 | 0.0004 | 0.01 | 0.01 | 0.9456** | 199.84 | 73.75 | 0.5820** |
| *WW*S* | 1 | 13.14 | 4.85 | 0.0789 | 0.94 | 1.95 | 0.2214** | 13.14 | 4.85 | 0.1376** |
| $WW^2$ | 1 | 76.32 | 28.17 | 0.0032 | 1.34 | 1.34 | 0.1572** | 76.32 | 28.17 | 0.9573** |
| $S^2$ | 1 | 7.15 | 2.64 | 0.1651** | 0.08 | 0.16 | 0.7083** | 7.15 | 2.64 | 0.2043** |
| Residuals | 5 | 13.55 | | | 13.55 | | | 29.29 | | |
| Total | 10 | 822.57 | | | 24.20 | | | 86.46 | | |
| Lack of fit | 3 | 13.22 | 27.12 | 0.0358 | 1.47 | 1.03 | 0.5275** | 18.04 | 9.64 | 0.0954 |
| Pure error | 2 | 0.33 | | | 0.95 | | | 1.25 | | |
| Total | 5 | 13.55 | | | 2.43 | | | 19.29 | | |

* *Critical F-value for the 0.05 and 0.1 significance levels is $F_{0.05}(5,5)=5.05$ and $F_{0.1}(5,5)=3.45$ respectively.*

** *Non-significant parameter.*

Table D.3: Analyses of variance (ANOVA) for gangue minerals recovery and Gompertz parameters models with degrees of freedom (DF), sum of squares ($SS$), $F$-ratios ($F$) and $p$-values ($P$).

| Source of variation | DF | Recovery | | | α-value | | | β-value | | |
|---|---|---|---|---|---|---|---|---|---|---|
| | | *SS* | *F* * | *P* | *SS* | *F* * | *P* | *SS* | *F* * | *P* |
| Model | 5 | 211.19 | 120.41 | <.0001 | 134.75 | 82.20 | <.0001 | 289.89 | 120.15 | <.0001 |
| *WW* | 1 | 172.40 | 461.47 | 0.0021 | 120.43 | 367.34 | <.0001 | 230.93 | 478.56 | <.0001 |
| *S* | 1 | 11.82 | 33.70 | 0.0021 | 1.83 | 5.58 | 0.0647 | 34.72 | 71.96 | 0.0004 |
| *WW*S* | 1 | 6.89 | 19.65 | 0.0068 | 0.13 | 0.39 | 0.5589** | 4.23 | 8.77 | 0.0315 |
| $WW^2$ | 1 | 28.81 | 82.12 | 0.0003 | 2.15 | 6.57 | 0.0504 | 15.90 | 32.95 | 0.0022 |
| $S^2$ | 1 | 0.71 | 2.01 | 0.2156** | 2.30 | 6.99 | 0.0458 | 10.08 | 20.89 | 0.0060 |
| Residuals | 5 | 1.75 | | | 1.64 | | | 2.41 | | |
| Total | 10 | 212.95 | | | 136.39 | | | 292.30 | | |
| Lack of fit | 3 | 1.65 | 10.68 | 0.0868 | 0.63 | 0.42 | 0.7594** | 0.72 | 0.29 | 0.9942** |
| Pure error | 2 | 0.10 | | | 1.00 | | | 1.69 | | |
| Total | 5 | 1.75 | | | 1.64 | | | 2.41 | | |

* *Critical F-value for the 0.05 and 0.1 significance levels is $F_{0.05}(5,5)=5.05$ and $F_{0.1}(5,5)=3.45$ respectively.*

** *Non-significant parameter.*

# Appendix E

# Geometallurgical modelling appendices

# E.1 Calibrated GT53 core sample data

Figure E.1: Distribution and Box and Whisker plots of calibrated GT53 Nb, Sn and W grades with and without outliers.

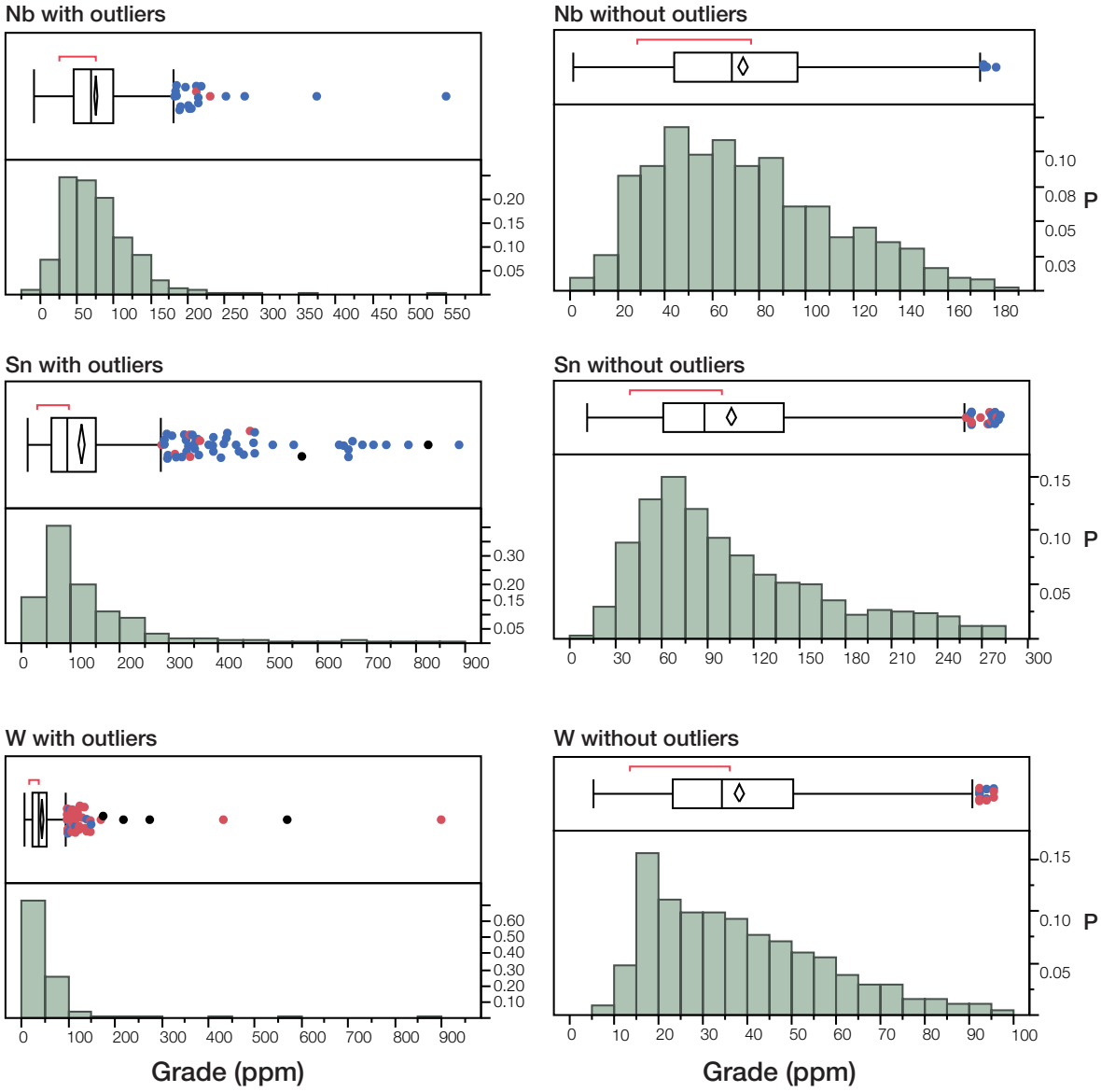

# Appendix F

# Discussion appendices

# F.1 Global material balance

Table F.1: Simulated material balance of the CRMs recovery process.

| N° | Stream definition: | Flowrate (t/h) | Yield (%) | LREE Grade (%) | LREE Recovery (%) |
|---|---|---|---|---|---|
| **1** | Micaceous residue | 15.00 | 100.00 | 0.02 | 100.00 |
| **2** | -180 µm Residue | 10.26 | 68.40 | 0.03 | 93.20 |
| **3** | Coarse Residue | 4.74 | 31.60 | 0.00 | 6.80 |
| **4** | -53 µm Residue | 2.45 | 16.34 | 0.04 | 28.61 |
| **5** | 53-180 µm Residue | 7.81 | 52.06 | 0.03 | 64.58 |
| **6** | Slimes | 0.27 | 1.78 | <0.01 | 0.08 |
| **7** | Flotation feed | 2.18 | 14.56 | 0.04 | 28.53 |
| **8** | Rougher tailings | 1.73 | 11.50 | <0.01 | 2.33 |
| **9** | Rougher concentrate | 0.46 | 3.05 | 0.19 | 26.20 |
| **10** | Cleaner tailings | 0.31 | 2.06 | 0.04 | 3.49 |
| **11** | Cleaner concentrate | 0.15 | 0.99 | 0.52 | 22.71 |
| **12** | Flotation tailings | 2.03 | 13.56 | 0.01 | 5.82 |
| **13** | Spiral tailings | 6.33 | 42.19 | 0.01 | 13.44 |
| **14** | Spiral concentrate | 1.48 | 9.88 | 0.12 | 51.14 |
| **15** | Table tailings | 1.38 | 9.21 | 0.03 | 10.70 |
| **16** | Table concentrate | 0.10 | 0.66 | 1.37 | 40.44 |
| **17** | Gravity tailings | 7.71 | 51.40 | 0.01 | 24.14 |

## F.2 Process equipment selection and costs estimations

The capital cost (UCC) estimations are made on the basis of the work of (Mular and Poulin, 1998). Therefore all the following expressions are defined in common currency at that time (*i.e.* Canadian Dollar in 1998) and thus need to be updated and converted. The price is updated using the Marshall and Swift economic index ($I_m = 1400$, at that time) which is regularly updated online (currently $I_n = 1759.5$) and then converted using the current exchange ratio (currently $r$=0.630424) as follows:

$$C_n = (I_n/I_m) \times C_n \times r \tag{F.1}$$

The following assumptions were used to assess the expected unit treatment capacity:

- The average micaceous residue solid flowrate is around 15 t/h,
- The estimated flowrates given in Figure 8.2 are considered as close to the real expected values,
- The specific gravity of the solid is around 2.7.

*Spiral*

The capital cost ($C$) of a spiral concentrator mainly depends on its nominal capacity ($Q$) and on the type of material used for the inclined chute. The capital cost is estimated using the following formula for a 5-turn spiral (Mular and Poulin, 1998):

$$C = aQ^b \tag{F.2}$$

where

| Material | Q (st/h) | $a$ | $b$ |
|---|---|---|---|
| Steel | 1.5≤Q≤3000 | 3600 | 0.87 |
| Fiberglass | 1≤Q≤3000 | 2165 | 1 |

The spiral used in this work is in fiberglass and the nominal capacity required, in agreement to spiral solid feed flowrate given by the material balance, is around 7.8 t/h corresponding to 8.61 st/h. Hence, the estimated capital cost for the spiral is around 14 761 €.

*Shaking table*

The capital cost ($C$) of a shaking table mainly depends on the surface area of the deck ($A$), on its shape (rectangular, diagonal) and on the number of decks (single, double, etc.). The capital cost is estimated using the following formula (Mular and Poulin, 1998):

$$C = KaA^b \tag{F.3}$$

where

| Shape | A ($ft^2$) | $a$ | $b$ | $K$ | | |
|---|---|---|---|---|---|---|
| | | | | *single* | *double* | *triple* |
| Rectangular | 5≤A≤93 | 7041 | 0.3619 | 1 | 2.35 | 3.55 |
| Diagonal | 5≤A≤90 | 7698 | 0.2147 | | | |

In this work, the shaking table used is a Wilfley shaking (rectangular) table equipped with a single rectangular deck. However according to the material balance presented previously, the required nominal capacity of the shaking table is around 1.5 t/h. The corresponding shaking table model in terms of capacity in the Wilfley product range is the Wilfley 7000 with a deck surface area of 71.3 $ft^2$ (Holman Wilfley Ltd., 2014). According to the formula the estimated shaking table cost would be around 26 131 €.

*Hydrocyclone*

The capital cost ($C$) of a hydrocyclone depends on its diameter ($D$), following the formula (Mular and Poulin, 1998):

$$C = aD^b \tag{F.4}$$

where

| D (in) | $a$ | $b$ |
|---|---|---|
| 1≤D≤13.46 | 609.5 | 0.7582 |
| 13.46≤D≤50 | 103.3 | 1.43 |

The hydrocyclone used for the desliming operation is a 2 inch Mozley hydrocyclone with a nominal capacity ranging from 1 to 4 $m^3/h$. However the solid feed rate of the desliming operation is estimated at 2.45 t/h, at 15 wt.% solid dilution which means a pulp flowrate of around 14.8 $m^3/h$. Assuming an optimal feed flowrate of 3 $m^3/h$, a 5-hydrocyclone bank will be required which raise the cost of the desliming equipment to $5 \times 817 = 4084$ €.

*Flotation*

Selection of the flotation equipment is based on the practical methodology described in Metso (2010). It follows 3 steps: (1) Determination of total flotation cell volume, (2) election of the number of cells per bank and (3) select the bank arrangement.

The total flotation volume required ($V_T$) can be assessed using the following equation:

$$V_T = \frac{Q \times Tr \times S}{60 \times C_a} \tag{F.5}$$

where $Q$ is the feed flow rate (in $m^3/h$), $Tr$ is the residence time (in minutes), $S$ is a scale-up factor for residence time (typically equal to 2.5 for laboratory scale testworks

using conventional mechanical cells) and $C_a$ is an aeration factor that takes into account gas holdup difference at lab and industrial scales (typically $C_a$=0.85). The experiments were carried out at 10 wt.% solid pulp density with residence time of 13 min for the roughing stage and 9 min for the cleaning stage (see Appendix B.6). The estimated solid flowrate for the roughing and cleaning operations are around 2.2 t/h and 0.2 t/h corresponding to a pulp flowrate of 20.46 $m^3$/h and 1.89 $m^3$/h respectively. Hence, the total volume required for the roughing and cleaning stages are around 13.04 $m^3$ and 1.89 $m^3$ respectively.

Typical cell configuration (volume, feed rate and maximum cells per bank) are displayed below (Metso, 2010):

| Model | Volume ($m^3$) | Maximum bank feed rate ($m^3$/h) | Maximum cells per bank |
|---|---|---|---|
| RCS 0.8 | 0.8 | 25 | 4 |
| RCS 3 | 3 | 240 | 4-5 |
| RCS 5 | 5 | 320 | 4-5 |
| RCS 10 | 10 | 540 | 4 |
| RCS 15 | 15 | 730 | 4 |

According to the pulp flowrates and total volumes required, an adapted configuration for the roughing stage could be a 3-RCS 5 cells bank while the cleaning stage could be ensured by a 3-RCS 0.8 cells bank.

The capital cost ($C$) of a flotation bank depends on the number of cells ($N$) and the cells volume ($V$), following the formula (Mular and Poulin, 1998):

$$C = aV^b \tag{F.6}$$

where

| V ($ft^3$) | $a$ | $b$ |
|---|---|---|
| 9≤V≤450 | 3223 | 0.3999 |
| 450≤V≤1000 | 264.2 | 0.0809 |

Hence, for the 3-cells bank configuration suggested above, with cells volume of 106 $ft^3$ and 28 $ft^3$, *i.e.* for the roughing and the cleaning stages, the estimated capital costs are 82 2405 € and 29 144 € respectively.

# Appendix G

# List of publications

## G.1 Articles

*Peer reviewed international journals*

1. **Dehaine, Q.**, Filippov, L., (2015). Rare earth (La, Ce, Nd) and rare metals (Sn, Nb, W) as by-product of kaolin production, Cornwall: Part1: Selection and characterisation of the valuable stream. *Minerals Engineering*, 76:141–153. doi: http://dx.doi.org/10.1016/j.mineng.2014.10.006

2. **Dehaine, Q.**, Filippov, L., Royer, J.J., (2016). Comparing univariate and multivariate approaches for process variograms: A case study. *Chemometrics and Intelligent Laboratory Systems*, (In press). doi: http://dx.doi.org/10.1016/j.chemolab.2016.01.016

3. **Dehaine, Q.**, Filippov L., (2016). Modelling heavy and gangue mineral size recovery curves using the spiral concentration of heavy minerals from kaolin residues. *Powder Technology*, (In press). doi: http://dx.doi.org/10.1016/j.powtec.2016.02.005

*Peer reviewed national journal*

1. **Dehaine, Q.**, Filippov, L., (2015). Métaux critiques (terres rares légères, niobium, tungstène) et étain comme co-produits de la production de kaolin, *Mines & Carrières*, Hors Série. 16:99–111.

## G.2 Conference papers

1. **Dehaine, Q.**, Filippov, L., (2014). Distribution of critical raw materials (LREE Nb, Ta, W) and Sn within waste streams of china clay production plants, Cornwall, in: A., Nzihou, S., Guerreiro, E.S., Lora (Eds.), *Proceedings of the 5th International Conference on Engineering for Waste and Biomass Valorisation*. Rio de Janeiro, pp. 1264–1275. ISBN: 979-10-91526-03-6

2. **Dehaine, Q.**, Filippov, L., (2015). A multivariate approach for process variograms, in: Esbensen, K.H, Wagner, C. (Eds.), TOS Forum - *Proceedings of the 7th World Conference on Sampling and Blending*. IM Publishers, Bordeaux, pp. 169 –174. doi:10.1255/tosf.76

3. Filippov, L., **Dehaine, Q.**, (2015). Gravity processing of a low grade kaolin residue for the recovery of Rare Earth Elements (La, Ce, Nd) and rare metals (Sn, Nb, W), in: *13th SGA Biennial Meeting "Mineral Resources in a Sustainable World."* Nancy, pp. 1359–1360.

4. **Dehaine, Q.**, Filippov, L., (2015). From plant to mine: a reverse approach to help LREE and rare metals by-product resource estimation and geometallurgical modelling, in: *13th SGA Biennial Meeting "Mineral Resources in a Sustainable World"*. Nancy, pp. 1399–1401.

## Récupération des Terres Rares (La, Ce, Nd) et métaux rares (Sn, Nb, W) à partir de résidus micacés issus de la production de kaolin

L'approvisionnement en matières premières critiques minérales (CRMs), est un sujet préoccupant pour l'industrie européenne. Les granites à métaux rares, en raison de leurs faibles teneurs en métaux, ont toujours été considérés comme ayant une faible valeur économique mais, lorsqu'ils sont altérés, ils sont souvent exploités pour les minéraux industriels. L'objectif du présent travail est d'évaluer la potentialité des résidus micacés issus de la production de kaolin pour la récupération des Terres Rares légères (LREE), Nb, W et Sn, au travers du développement d'un procédé de valorisation de ces résidus dans le cas des kaolins de St Austell. Le granite de St Austell, à l'origine des dépôts de kaolin, est composé de 6 types de granites ayant chacun leur propre cortège de minéraux accessoires. Ces derniers, libérés par le processus de kaolinisation, sont majoritairement pré-concentrés dans le résidu micacé du procédé de traitement de kaolin, notamment pour les zones couvrant le granite à biotite. Les teneurs en CRMs atteignent 170 ppm LREE (Ce, La, Nd), 140 ppm Sn, 94 ppm Nb et 70 ppm W, ceux-ci étant principalement distribués dans les fractions fines (-100 µm). Une approche statistique combinée aux observations minéralogiques a montré que les LREE sont uniquement portés par la monazite et que Sn, Nb et W sont respectivement portés par la cassiterite, le rutile et la wolframite. La prise en compte de la variabilité des propriétés du flux de résidu considéré, tels que les teneurs, la granularité, etc., est primordiale. Le développement du multivariogramme a permis de résumer la variabilité globale de l'ensemble des propriétés considérées en une fonction unique soulignant les structures communes à ces propriétés. Un procédé de traitement du résidu micacé combinant concentration gravimétrique (spirale, table à secousses, Falcon) et flottation a été testé sur les fractions 53-180 µm et -53 µm. Une modélisation par la méthode des plans d'expériences montre que le débit d'eau de lavage de la spirale est le facteur le plus significatif pour la récupération des minéraux denses. De la même manière, la modélisation des courbes de distribution par taille via des modèles de régression permet de mieux comprendre les mécanismes de séparation ayant lieu au sein de la spirale (effet de Bagnold, circulations secondaires). Jusqu'à 70% des minéraux denses peuvent être récupérés après trois passages de spirale tandis que le même niveau de récupération pour les LREE est obtenu en un seul passage. Le traitement du concentré de spirale par table à secousses permet d'obtenir un concentré à 1.6% LREE. La flottation de la monazite dans la fraction -53 µm est globalement plus performante que la séparation centrifuge (Falcon UF). L'utilisation de dispersant lors du deschlammage élimine l'effet néfaste des argiles et augmente l'efficacité de la flottation, en particulier avec l'oléate de sodium, permettant de récupérer jusqu'à 80% des LREE avec une teneur de 0.54% LREE. Une méthode d'évaluation des ressources, intégrant les résultats de caractérisation et des tests de valorisation, est proposée afin de prédire les performances du procédé de récupération des CRMs, ce qui permettra d'aller vers l'établissement d'un modèle géométallurgique.

**Mots-clés:** Résidu de kaolin, Terres Rares, Minerais à faible teneur, Théorie de l'échantillonnage, Concentration gravimétrique, Flottation

---

## Rare Earths (La, Ce, Nd) and rare metals (Sn, Nb, W) recovery from micaceous waste of china clay production

During the last few years the supply of some critical raw materials (CRMs) such as the Light Rare Earth Elements (LREE) became a concern for the European industry. Rare metals granites have always been considered of poor economic value due to their low grades but, when altered, they are often exploited for their industrial minerals. This work addresses the recovery of LREE (La, Ce, Nd) and rare metals (Sn, Nb, W) from St Austell (UK) kaolin residues though the development of a dedicated beneficiation process. The St Austell granite is composed of six major granite types, each one having its own accessory mineral assemblage. As a consequence of the kaolinisation process, these accessory minerals are partially liberated from the gangue which allows their pre-concentration in some residues of the kaolin production route. Results shows that when processing material from biotite granite, 40% to 60% of the CRMs goes to the micaceous residue stream with CRM grades around 170 ppm LREE, 140 ppm Sn, 94 ppm Nb et 70 ppm W. The overall CRMs grade increases in the fines fractions of the residue in which the majority of the CRMs are distributed. A combined statistical/mineralogical approach has allowed identifying monazite as the only LREE-bearing mineral as well as cassiterite, wolframite and rutile as the major host for Sn, Nb and W respectively. Taking into account the variability of the properties of the residue treated such as grade or particle sizes is essential. A multivariate variographic approach has been developed to summarize the overall spatial variability of a set of properties by one structural function and thus highlight their common spatial structures. A CRMs beneficiation process combining gravity (spiral, shaking table, Falcon) and flotation has been tested on the 53-180 µm and –53 µm fractions of the micaceous residue. Modelling of the influence of the operating parameters on spiral performance using the design of experiments methodology (DOE) shows that wash water flow rate as the most significant effect on heavy minerals recovery. Similarly, modelling size recovery curves through particle size distribution and DOE regression model fitting allow a better understanding of the effect of wash water on separation mechanism (Bagnold effect and secondary flows). Up to 70% heavy minerals recovery is achieved after three spiral passes at low wash water addition whereas the same recoveries are obtained for the LREE in only one pass. Processing of spiral concentrate by shaking table allow to obtain a 1.6% LREE concentrate. Froth flotation of monazite in the -53 µm fraction is generally more efficient than centrifugal separation (Falcon UF). The use of dispersant in the desliming step eliminates the negative effect of clay-coating and increases flotation efficiency, especially with sodium oleate, allowing to recover 80% of the LREE in the floated product with a 0.54% LREE grade. A resources evaluation method, using results from characterisation and metallurgical testing, is proposed to predict the performance of spiral concentration and goes towards the development of a geometallurgical model.

**Keywords:** Kaolin residue, Rare earths, Low grade ores, Theory of Sampling (TOS), Gravity processing, Flotation